**University of Reading**

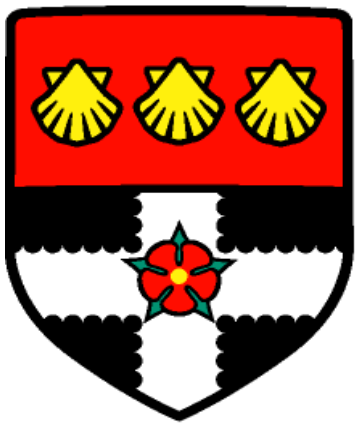

# Novel nanostructured materials with 3D architecture

By

***Nassar Abdelrahim***

A thesis submitted in partial fulfilment of the requirements for the degree of Doctor of Philosophy

**Supervisors:**
**Dr Adam M. Squires**
**Dr Joanne M. Elliott**

Department of Chemistry

School of Chemistry, Food and Pharmacy

**June 2016**

# DECLARATION

I confirm that this is my own work and the use of all material from other sources has been properly and fully acknowledged.

**Signed:**…….

**Date:**…….

# ACKNOWLEDGEMENTS

First of all, I would like to express my deep love and my special thanks to my wife (**Wafaa**), who has continuously helped, encouraged and supported me to overcome all the difficulties I have faced during my stay in England.

Second, I would especially like to thank my supervisors, Dr Adam Squires and Joanne Elliott for their guidance, help and patience over the last four years.

My deep thanks to the previous member of lab G69, Kaleem Ashgar and to my fellow postgraduates in lab G13, Sam Richardson, Eleonore Mason, Ben Eves who helped and encouraged me a lot during my work.

Thanks due to our collaborators: Stephen Tay, (Department of Chemistry, Imperial College London, UK) for providing me the recipe of the nickel deposition solution, staff of beamline I07 (Diamond, UK), staff of ESRF (France), staff of MAX-lab (Sweden) and staff of SAXS lab (Physics Department, Bristol University).

I would like to thank all the people in CAF lab (Department of Chemistry, University of Reading, UK) who helped me a lot over the last few years, specially, Nick Spencer and Nicholas Michael. All thanks to Peter Harris and Amanpreet Kaur (CfAM Electron Microscopy laboratory, University of Reading, UK) for preforming the electron microscopy analysis.

Finally, I would like to express my deep and special thanks to my mum and all my brothers and sisters for their love, kindness and prayers which helped me to overcome the difficulties during my mission in England.

# SUMMARY

Herein, we report for the first time the fabrication of novel 3-D mesoporous nickel with single diamond morphology using direct templating through bicontinuous cubic phases of monoolein (Rylo) via the electrodeposition route. Mesoporous nickel was successfully electrodeposited from nickel electrolyte at room temperature through the bicontinuous cubic phases of monoolein (Rylo) at a potential of -0.95 V vs. Ag/AgCl. The structure of the fabricated nickel films was confirmed by small angle X-ray scattering (SAXS) analysis and the calculated lattice parameter of the fabricated films was found to be (175 ± 2.5 Å). Transmission electron microscopy (TEM) of the fabricated nickel films confirmed the deposition of nickel in a 3-D network of interconnected nanowires. The electrochemical surface area of the nickel films deposited in the presence of monoolein template was estimated to be ~266 fold higher than that of the nickel films deposited in the absence of the template. Furthermore, the specific surface area of the templated nickel films was calculated to be (~13 $m^2$/g). In addition, the templated nickel films were found to exhibit high electrochemical stability. This makes these films very promising to be used as capacitors in batteries and fuel cells. These results validate the use of monoolein as a structure directing agent for fabrication of 3-D mesoporous materials via the electrodeposition route.

Mesoporous platinum was electrodeposited for the first time from hexachloroplatinic acid (HCPA) solution through the bicontinuous cubic phases of monoolein (Cithrol) at potential of -0.25 V vs. Ag/AgCl. Cyclic voltammetry confirmed the presence of nanostructured platinum in the deposited films. Furthermore, a clear SAXS peak was observed. The lattice parameter for this peak was calculated to be 456 Å. However, the structure of the deposited platinum films could not be revealed from the SAXS analysis. Therefore, further investigations are required in order to reveal the structure of the fabricated platinum films.

For the first time, we report the fabrication of Pt/Ni and Ni/Pt composites by electrodeposition of platinum and nickel onto 3-D Ni and Pt scaffolds, respectively. The 3-D Ni and Pt scaffolds were fabricated by direct templating through cubic phases of monoolein and phytantriol, respectively. The fabricated Pt/Ni, Ni/Pt films could be promising as electrode materials for batteries, fuel cells, sensors and other applications.

Some of the physicochemical properties of monoolein products, Rylo and Cithrol were studied using different analytical techniques. Both cross polarised light microscopy (CPLM) and SAXS analysis revealed the formation of stable cubic phases of Rylo and Cithrol at room temperature under excess water. CPLM analysis demonstrated that the phase transition from cubic phase ($Q_{II}$) to hexagonal ($H_{II}$) occurred at 65 $^oC$ for Rylo and at a lower temperature for Cithrol (52.3 $^oC$). Consistently, SAXS patterns of Rylo and Cithrol at full hydration at different temperatures showed a phase transition from diamond cubic phase ($Q_{II}^D$) to hexagonal ($H_{II}$) at 65 $^oC$ for Rylo and at 55 $^oC$ for Cithrol. The phase transition was accompanied with a decrease in the lattice parameter with both materials. SAXS analysis also revealed an increase in the lattice parameters of the cubic phases of both monoolein types (Rylo and Cithrol) by increasing the concentration of Brij-56 up to 20% (wt/wt), indicating a swelling of monoolein cubic phases. Therefore, Brij-56 is promising for tuning the structural parameters of monoolein-water system which is potentially important for many applications such as membrane protein crystallization, drug delivery and electrodeposition templating of nanostructured materials.

# TABLE OF CONTENTS

# ABBREVIATIONS

| | |
|---|---|
| ***a*** | Lattice parameter |
| **Å** | Ångström |
| **AAO** | Anodic aluminum oxide |
| **°C** | Degrees centigrade |
| **CE** | Counter electrode |
| **CMC** | Critical micelle concentration |
| **CPLM** | Cross polarised light microscopy |
| **CTAB** | Hexadecyltrimethylammonium bromide |
| **CV** | Cyclic voltammetry |
| **1D/1-D** | One dimension |
| **2D/2-D** | Two dimensions |
| **3D/3-D** | Three dimensions |
| **DSC** | Differential scanning calorimetry |
| **DSPG** | Distearoylphosphatidylglycerol |
| **E** | Potential |
| **ECSA** | Electrochemically active surface area |
| **$F_I$** | Fluid isotropic phase |
| ***Fd3m*** | Single network diamond structure, $Q_{227}$ |
| **FFT** | Fast Fourier Transform |
| **FT-IR** | Fourier transform infrared spectroscopy |
| **FT-Raman** | Fourier transform Raman spectroscopy |
| **g** | Gram |
| **$H_I$** | Hexagonal phase |
| **$H_{II}$** | Inverse hexagonal phase |

| | |
|---|---|
| **HEPES** | 4-(2-hydroxyethyl)-1-piperazineethanesulfonic acid |
| **HCPA** | Hexachloroplatinic acid |
| **HIPE** | High internal phase emulsion |
| **HLB** | Hydrophilic lipophilic balance |
| **HPAEC** | High-performance anion-exchange chromatography |
| **i** | Current |
| **Ia3d** | Single network gyroid structure, $Q_{230}$ |
| **IUPAC** | International union of pure and applied chemistry |
| **KOH** | Potassium hydroxide |
| ***Lα*** | Lamellar phase |
| $L_I$ | Micellar phase |
| $L_{II}$ | Inverse micellar phase |
| **LCs** | Liquid crystals |
| **LCT** | Liquid crystal templating |
| **LLC/LLCs** | Lyotropic liquid crystal/s |
| **LPD** | Liquid phase deposition |
| **min** | Minute |
| **mg** | Milligram |
| **mL** | Millilitre |
| **MPD** | 2-methyl-2,4-pentanediol |
| **µm** | Micrometre |
| **σm** | Specific surface area |
| **nm** | Nanometre |
| **pH** | Potential of Hydrogen |
| **PED** | Preferential pulsed electrodeposition |

| | |
|---|---|
| ***Pm3m*** | Single network primitive structure, $Q_{221}$ |
| **PS-PLLA** | Polystyrene-b-poly(L-lactide) |
| ***Q*** | Charge density |
| $Q_I$ | Bicontinuous cubic phase |
| $Q_{II}$ | Inverse bicontinuous cubic phase |
| $Q_{II}^D$ | Inverse bicontinuous cubic phase of diamond morphology, Pn3m, $Q_{224}$ |
| $Q_{II}^G$ | Inverse bicontinuous cubic phase of gyroid morphology, Ia3d, $Q_{230}$ |
| $Q_{II}^P$ | Inverse bicontinuous cubic phase of primitive morphology, Im3m, $Q_{229}$ |
| **R** | Principle radius |
| **RE** | Reference electrode |
| **Rf** | Roughness factor |
| **sec or s** | Second |
| **SAXS** | Small angle X-ray scattering |
| **SEM** | Scanning electron microscope |
| **t** | Time |
| **T** | Temperature |
| **TEM** | Transmission electron microscope |
| **TLCs** | Thermotropic liquid crystals |
| **UK** | United Kingdom |
| **ν** | Scan rate |
| **WE** | Working electrode |
| **Wt** | Weight |
| **XRD** | X-ray diffraction |

# THESIS STRUCTURE

This thesis consists of six chapters; a brief description of the contents of each chapter is stated in the following paragraphs:

**Chapter 1** discusses, briefly, the applications of mesoporous materials, their preparation methods, some examples of mesoporous materials, in particular nickel and platinum and their applications as well as liquid crystals and their phases. It also discusses in detail the liquid crystalline systems used in this study.

**Chapter 2** describes, in detail, all the analytical techniques used to collect the data in this work. It also describes the materials, chemicals, techniques and instruments that have been used in this work as well as the sample preparation. It also describes how the data had been analysed.

**Chapter 3** investigates the optimum conditions needed for electrodeposition of mesoporous nickel as well as the preparation of electrodeposited nickel films. It also reports the electrochemical, structural and morphological characterisation of the deposited nickel films.

**Chapter 4** investigates the experimental conditions required for electrodeposition of mesoporous platinum. It also studies the preparation of electrodeposited platinum films and the electrochemical as well as the structural characterisation of the fabricated platinum films.

**Chapter 5** studies the use of mesoporous 3-D nickel films and mesoporous 3-D platinum films as hard templates for fabrication of Ni/Pt and Pt/Ni composites via electrodeposition route. It also reports the electrochemical characterisation of the fabricated composites.

**Chapter 6** studies some physico-chemical properties of monoolein products, namely Rylo and Cithrol. It also studies the phase behavior of monoolein. In addition it studies the effect of Brij-65 on the phase behavior of monoolein.

**Chapter 7** includes the general conclusions of the important findings obtained in this work. It also includes the possible suggestions for future work.

# Chapter 1: Introduction

## 1.1 Liquid crystals and their phases

Matter exists in four different forms, or phases. These phases are solid, liquid, gas, and plasma. A delicate state of matter which is stable thermodynamically and exists between the solid and liquid phase is called liquid crystals (*LC*s). According to the physico-chemical parameters responsible for the phase transitions, liquid crystals can be classified into two main groups, thermotropic liquid crystals (*TLC*s) and lyotropic liquid crystals (*LLC*s). Thermotropic liquid crystals exhibit a phase transition into the liquid crystal phases with temperature and pressure changes[1]. However, lyotropic liquid crystals exhibit phase transitions as a function of both temperature and concentration of the liquid crystal molecules. Here in our work we are interested in *LLC*s. Details about *LLC*s and their phases are described in the following section.

### 1.1.1 Lyotropic liquid crystal (*LLC*s)

Lyotropic liquid crystals are made from surfactants which form lyotropic liquid crystalline phases when they are mixed with a polar solvent, such as water[2,3]. Surfactants are amphiphilic molecules. An amphiphilic molecule consists of two parts, a polar head and one or more non polar tails. The head and the tail are attached together to make a surfactant. If the amphiphilic molecules are dissolved in an aqueous solvent, the amphiphilic molecules form groupings, for example in spherical shapes called micelles where the polar heads protect the non-polar chains. This process is called a self-assembly process. In a micelle, a polar head forms an outer shell in contact with an aqueous solvent, while the non-polar tails are hidden inside the shell. Hence, the core of a micelle, being formed of long non-polar tails, resembles

an oil drop. This structure is stable thermodynamically. Micelle aggregates form only when the concentration of the amphiphilic molecule reaches a given concentration called critical micelle concentration (CMC). The self-assembly process is an important characteristic feature of lyotropic liquid crystals (*LLCs*) which makes them different from thermotropics.

Under suitable conditions of temperature and relative concentrations, mixtures of surfactants and solvents self-assemble in different structures known as lyotropic mesophases. Based on the dimensional range (2.5-25 nm), the lyotropic phases are also known as liquid crystalline nanostructures[4]. Lyotropic liquid crystalline (*LLC*) phases have been identified by different analytical methods, such as polarized light microscopy, X-ray scattering and Raman spectroscopy[5,6,7]. These phases are lamellar *L*, cubic *Q*, hexagonal *H*, and some intermediate ones.

According to the direction of the curvature, the *LLC* phases can be classified into type I (normal phases) and type II (inverse phases). Type I can be micellar ($L_I$), hexagonal ($H_I$), or bicontinuous cubic ($Q_I$), while type II can be inverse micellar ($L_{II}$), inverse hexagonal ($H_{II}$), or inverse bicontinuous cubic ($Q_{II}$) (Figure 1.1). There are three different morphologies of the inverse bicontinuous cubic phase ($Q_{II}$) are: G (gyroid, space group Ia3d ($Q_{230}$)), D (double diamond, space group Pn3m ($Q_{224}$)) and P (primitive, space group Im3m ($Q_{229}$). These phases are complex symmetrical three-dimensional structures[8] consisting of two intertwined water channels separated by a single continuous lipid bilayer (Figure 1.1).

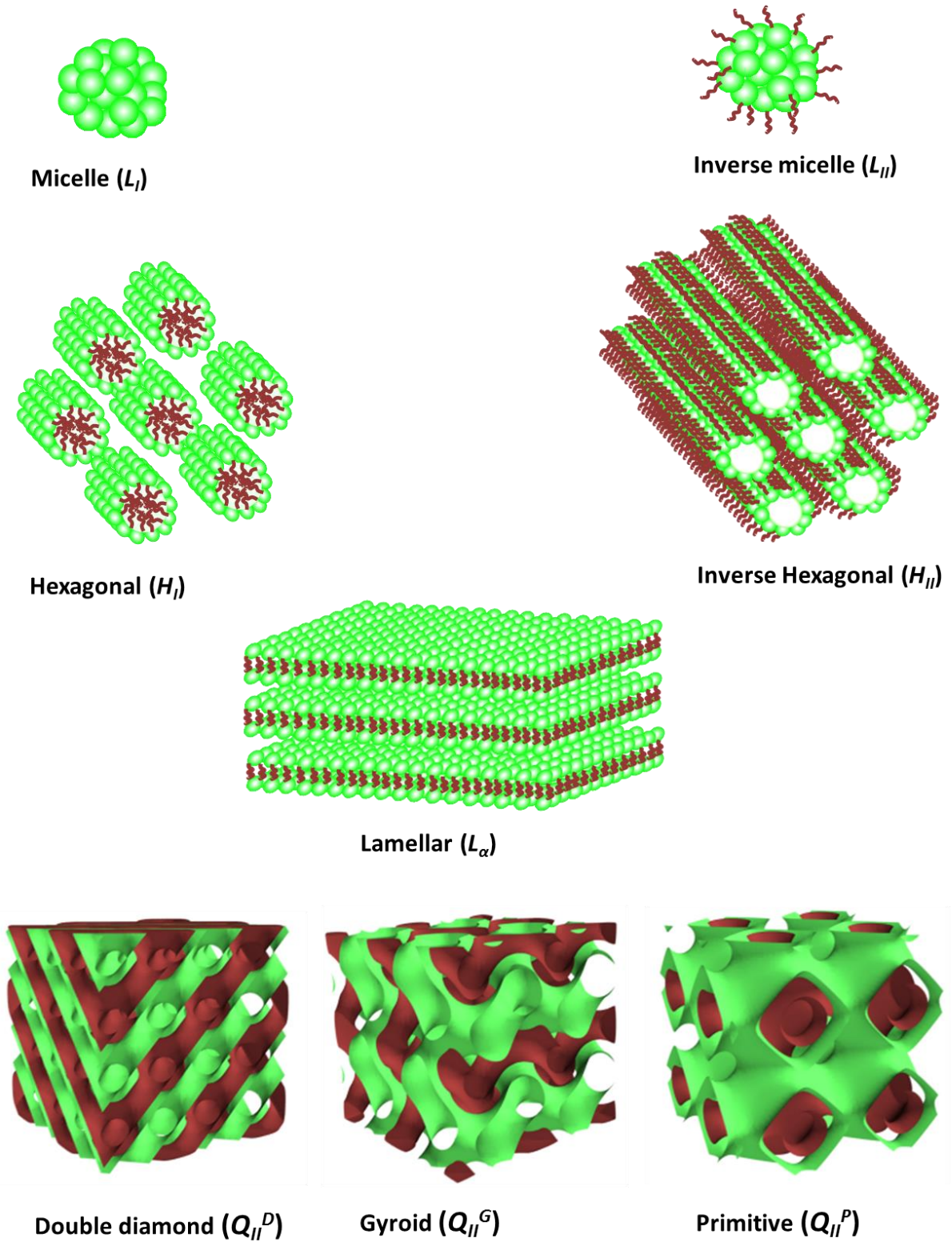


**Figure 1.1 Different phases of lyotropic liquid crystal.** The inverse bicontinuous cubic ($Q_{II}$) phases were designed using Enthought Canopy Python software.

## 1.2 Liquid crystalline systems used in this study

Monoolein-water and phytantriol-water are the liquid crystalline systems used in this study. More details of these two systems are described below.

### 1.2.1 Monoolein-water system

#### 1.2.1.1 Chemical and physical properties of monoolein

Monoolein (1-(cis-9-octadecenoyl)-rac-glycerol) is a viscous liquid with a characteristic odor[9]. It is pale yellow or clear amber in colour[9]. On the molecular level, monoolein is an amphiphilic material (it contains hydrophilic and lipophilic moieties) consisting of a 18-C hydrocarbon chain and a glycerol backbone which are joined together at the first position (1-monoolein) via an ester bond with one cis double bond at the ninth position as shown in Figure 1.2. The glycerol moiety (known as the 'head') is responsible for the hydrophilic characteristics of the molecule. This is due to the presence of hydroxyl groups in this part. While the C18 hydrocarbon chain (called the 'tail') is strongly hydrophobic[9].

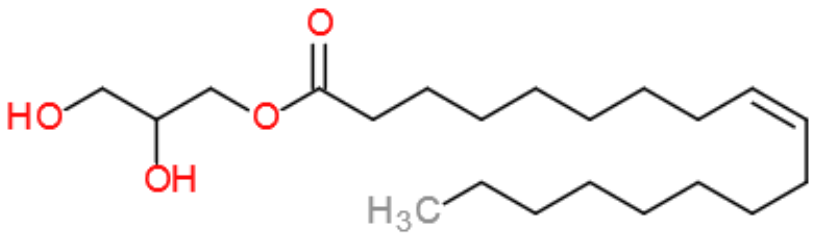


**Figure 1.2 Chemical structure of monoolein, (1-(cis-9-octadecenoyl)-rac-glycerol).**

Monoolein is insoluble in water and cold alcohol; however it is very soluble in oil, and other solvents such as petroleum ether or chloroform[10]. Besides its high oil solubility, it is a non-toxic, biodegradable and biocompatible material. This makes monoolein and its commercial

forms suitable for a wide range of applications including, pharmaceuticals, food, cosmetics, agriculture and protein crystallization[4]. Some of these applications include biological applications, in particular for drug delivery applications[11], biosensors, emulsifiers, solubility enhancers and others. Furthermore, monoolein bicontinuous cubic phases have been useful for many applications including gene therapy, crystallization of membrane proteins, fabrication of metal nanoparticles and for soap industry [4].

### 1.2.1.2 Lyotropic phases formed by monoolein

As amphiphilic material, monoolein shows different phases in the presence of water including, lamellar, hexagonal and bicontinuous cubic phases (double diamond, space group *Pn3m* ($Q_{224}$) and gyroid, space group *Ia3d* ($Q_{230}$))[4], which assemble in 1, 2 and 3 dimensional structures. In addition, monoolein exhibits more phases in the presence of additives such as lipids, salts, detergents and others. These additional phases include bicontinuous cubic phase (*Im3m*), micellar cubic (*Fd3m*), sponge phase, vesicles and bicelles (Figure 1.3).

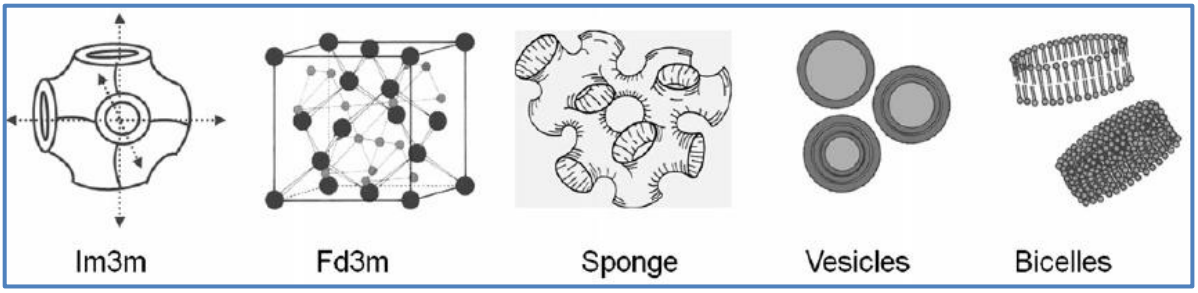


**Figure 1.3 Additional phases of monoolein occurring in the presence of different additives:** Bicontinuous cubic (primitive, space group *(Im3m)*), micellar cubic (*Fd3m*) phase, sponge phase, vesicles and bicelles. Adapted from Kulkarni et al.[4].

### 1.2.1.3 Phase behavior of monoolein

Many studies have reported the phase behaviour of monoolein-water mixtures[12,6,13,7]. Small angle X-ray scattering (SAXS) has been used to investigate the phase behaviour of monoolein/water system[6]. Figure 1.4 shows the phase diagram for monoolein-water system.

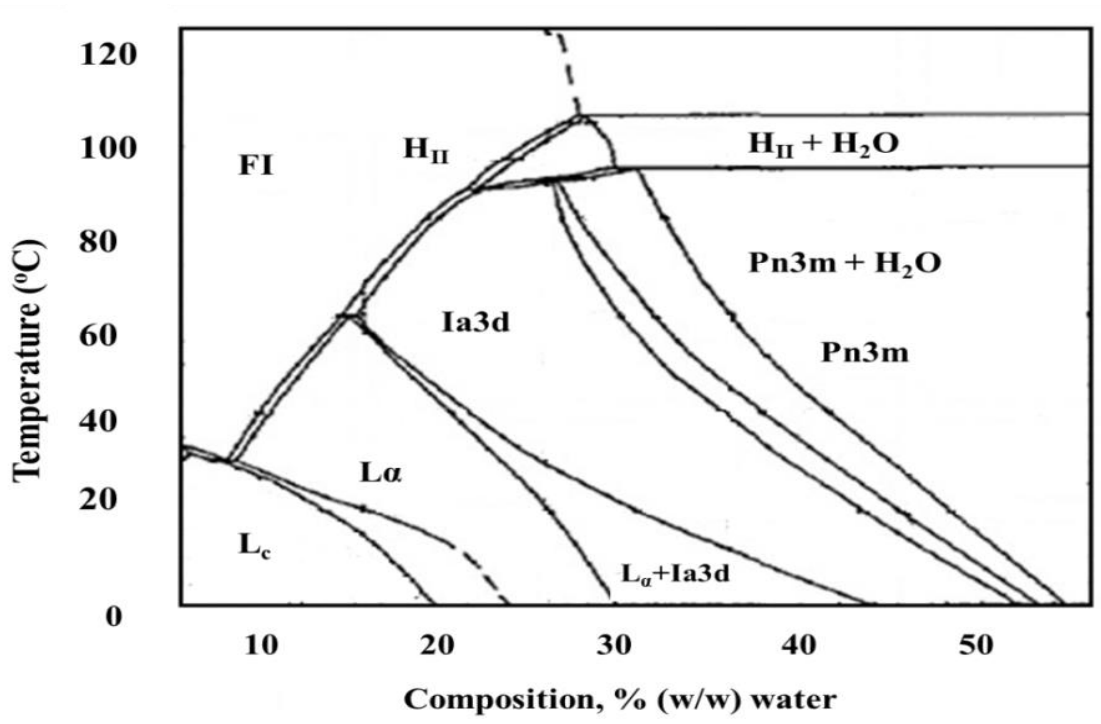


**Figure 1.4 Phase diagram of monoolein-water system.** The diagram is adapted from Briggs et al.[6].

In the phase diagram, the boundaries and coexistence regions are shown. The type of structure formed depends on water content or/and temperature. The phases observed in monoolein aqueous system are lamellar crystalline phase ($L_c$), lamellar liquid crystalline phase ($L_\alpha$), fluid isotropic phase ($F_I$), inverse hexagonal phase ($H_{II}$), and inverse cubic of space groups *Ia3d* ($Q_{II}^G$, gyroid) and *Pn3m* ($Q_{II}^D$, diamond).

Under excess water, monoolein exhibits two different types of bicontinuous cubic phases ($Q_{II}$) depending on the water content[7,14]. These cubic phases assemble with two distinct morphologies: $Q_{II}^{G}$ (gyroid type, space group *Ia3d)* and $Q_{II}^{D}$ (diamond type, space group *Pn3m*)[6] and complemented by the cubic phase $Q_{II}^{P}$ (primitive, space group *Im3m*). These phases are complex symmetrical three-dimensional structures[8] consisting of two intertwined water channels separated by a single continuous lipid bilayer. Also the cubic phases are characterised by high surface area[15], high solubility in both hydrophilic and hydrophobic materials[16]. This makes the bicontinuous cubic phases of monoolein very attractive for many applications including for the crystallization of membrane protein[17,18,19], for the solubilisation of different molecules such as vitamins[20], drugs[21] and essential oils[22] and for the synthesis of metal nanoparticles[4] and metal oxides such as alumina[23]. In this work bicontinuous cubic phases of monoolein were used as templates for preparation of high surface area nickel and platinum at room temperature via electrochemical deposition route.

The classical phase behavior of monoolein/water system could be modulated by several environmental factors including, temperature[6,24], pressure[25], magnetic fields[26] and electrostatic fields[27]. In addition, the presence of additives could modulate the lyotropic behavior of monoolien/water system[4,28]. The additives could alter the molecular structure of monoolein resulting in different phase behavior in the presence of water. Many additives have been reported to modulate the phase behavior of monoolein/water systems including hydrophilic, hydrophobic or amphiphilic molecules[4]. Examples of such additives are lipids[29,30,31], detergents[32,33,34], electrolytes,[35,36] sugars[37,28], glycerol[38] and others.

## 1.2.2 Phytantriol-water system

### 1.2.2.1 Chemical structure of phytantriol

Phytantriol (3,7,11,15-tetramethyl-1,2,3-hexadecanetriol) (Figure 1.5) has been used in many applications including, cosmetics[16], drug delivery[39,40] and only recently for metal deposition[41].

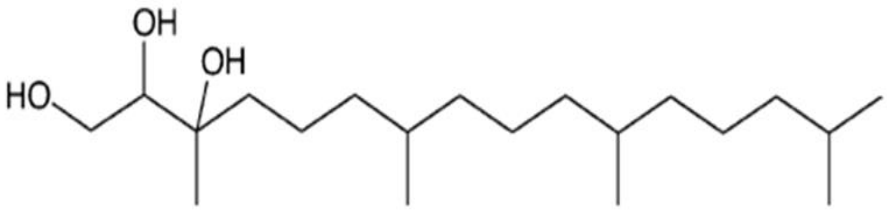


**Figure 1.5 Chemical structure of phytantriol (3,7,11,15-tetramethyl-1,2,3-hexadecanetriol).**

Phytantriol contains a polar head and a non-polar tail. The three hydroxyl groups in the head are responsible for hydrophilic properties of the molecule (polar head), while the alkyl chain is responsible for the hydrophobic properties (non-polar tail). This means that the phytantriol is an amphiphilic molecule when dissolved in a solvent such as water. The intermolecular forces make phytantriol self-assemble in many mesophases as the polar heads protect the non-polar chains. The structure and geometry of these mesophases depend on the concentration and temperature of the phytantriol[5].

### 1.2.2.2 Phase behavior of phytantriol

The phase behavior of phytantriol was first reported by Barauskas et al.[5]. Studying of the phase diagram of phytantriol provides the basis of many technical applications, especially

cubic liquid crystalline phases. The investigation of the phase behavior of aqueous phytantriol has been done by X-ray diffraction and polarised microscopy. The phase diagram of phytantriol is shown in Figure 1.6.

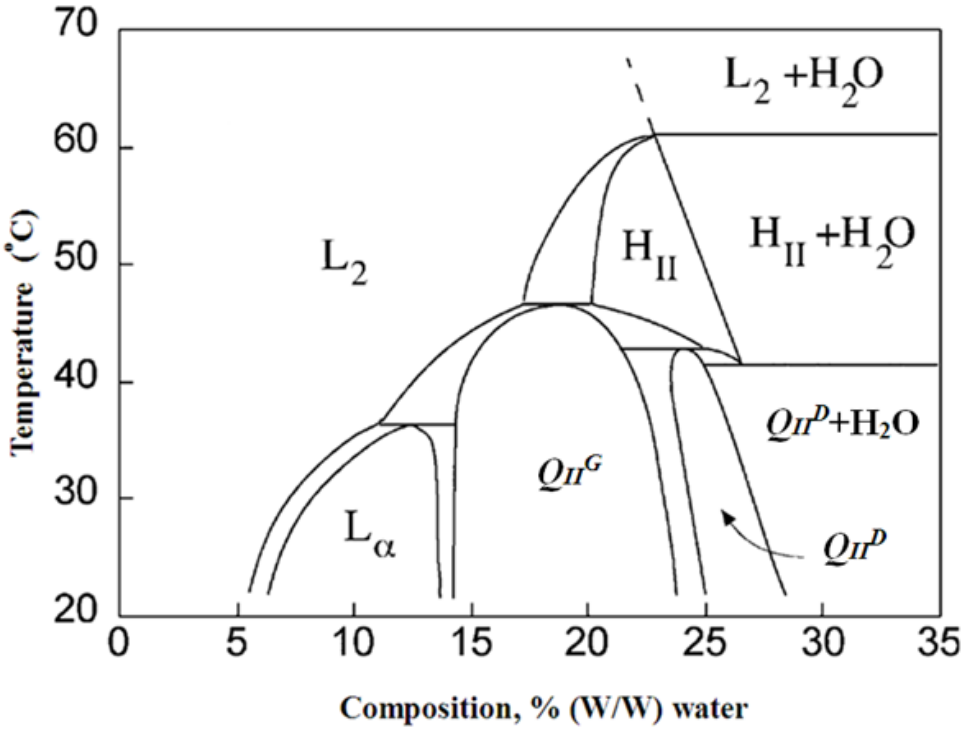


**Figure 1.6 Phase diagram of phytantriol-water system.** Adapted from Barauskas et al.[5].

According to Barauskas et al.[5], several phases in the phytantriol-water system have been observed including, inverse micellar ($L_{II}$), inverse hexagonal ($H_{II}$), lamellar ($L_{\alpha}$), and inverse cubic of space groups *Ia3d* ($Q_{II}^{G}$, gyroid) and *Pn3m* ($Q_{II}^{D}$, diamond) (Figure 1.6). Other phases were observed from phytantriol-water system but in the presence of additives. The cubic phase with the space group *Im3m* ($Q_{II}^{P}$, primitive) was observed in the presence of distearoylphosphatidylglycerol (DSPG) and the sponge phase was observed in the presence of 2-methyl-2,4-pentanediol (MPD)[42].

Cubic phases of phytantriol are in equilibrium in excess water and they are formed at a temperature range of (4-40 °C)[5]. This makes the family of cubic phases of phytantriol very important and attracts the scientific and industrial attention in various fields ranging from biophysics to drug delivery[5,16,40]. Akbar et al.[41] reported recently the fabrication of 3-D mesoporous platinum networks by direct liquid crystal templating approach via electrodeposition route. In their work, Pt was electrodeposited from HCPA solution the double diamond cubic phases of phytantriol/water system as templates. Electrodeposition of Pt films was carried out using potentiostatic controller at room temperature at potential of -0.25 V vs. Ag/AgCl. The fabricated 3-D Pt films were found to have single diamond morphology with a double lattice parameter (130 Å). Also the fabricated 3-D Pt films were found to exhibit extremely high surface area and high electrochemical stability[41]. In this thesis, we used the cubic phases formed by phytantriol/water system at room temperature as templates for fabrication of 3-D mesoporous platinum films with high surface area. The fabricated 3-D mesoporous platinum films were then used as hard templates for electrodeposition of Ni to form high surface area Ni/Pt composite.

## 1.3 Mesoporous materials

Mesoporous materials have been defined by the international union of pure and applied chemistry (IUPAC) as the materials which have pores in the size range of 2-50 nm[43]. Moreover, these materials were found to exhibit high surface areas[44]. They are widely used in many technological applications such as catalysis, sensors, selective separation and others[45]. Therefore, research interest in the synthesis and characterisation of these materials has increased. The synthesis of mesoporous materials is more complicated than the synthesis of conventional materials. Thus new approaches have been developed for synthesis of mesoporous materials[46,41]. In 1992, the first successful synthesis of mesoporous silica and aluminosiicates was reported at the Mobil Corporation[47]. This approach was based on the self-assembly of a cationic surfactant into micelles which was used as a template for the formation of a porous oxide network. Since 1992, the mesostructural templating techniques have been widely developed including the use of other template materials such as block copolymers[48], primary amines[49], and poly(ethylene oxide) surfactants[50] to produce a range of silicate and non-silicate oxides[50]. Moreover, Attard et al.[46,51] developed a different approach for organic structural templating. In this approach, a high concentration of surfactant (>30 wt % surfactant) was used to form a homogeneous self-assembled liquid crystal template. This approach enabled production of thin mesoporous films for metals using electrodeposition. Later, this approach was successfully used to produce nanostructured thin films of platinum[52,53,41], tin[54], nickel[55] and others via electrodeposition route using different liquid crystal templates.

Mesoporous materials possessing ordered porous networks have an advantage over mesoporous materials with non-ordered porous networks such as nanoparticles. The former are expected to possess superior mass transport properties and larger surface areas[56], which

make these materials potentially important in many applications such as catalysis, selective separation, and electrochemical devices such as batteries and fuel cells[57]. Consequently, the interest in materials having ordered porous networks with uniform pore diameters in the nanometer range has increased massively in order to replace conventional porous materials (nanoparticles).

There are a wide range of mesoporous materials synthesised by different approaches, however, in this study we are interested in synthesising nickel and platinum with 3-D structures. Details about mesoporous nickel and platinum materials as well as the different methods used to prepare mesoporous materials are summarised in the following sections.

### 1.3.1 Mesoporous nickel

Nickel is used in many applications such as an electrode material in batteries [58] (cadmium-nickel oxide, zinc-nickel oxide, metal hydride-nickel oxide, and hydrogen-nickel oxide), fuel cells[59,60] electrochemical hydrogenation of organic species[61], in alkaline water electrolysis[62] and in sensors[63]. Enhancing the sensitivity of electrochemical sensors is highly desirable. This can be achieved by increasing of the surface area of an electrode. Therefore, recently, electrochemical electrodes have been developed from conventional flat electrodes (e.g., glassy carbon, gold, and platinum) to 2-D or 3-D nanostructured materials such as porous films of Pt[64,65], Au[66,67] and Ni[55,68]. Nickel electrodes with high surface area have been prepared using many methods. The production of porous nickel films involves either a thermal treatment step or leaching with concentrated alkali solutions. For example, synthesis of sintered microporous nickel films involves thermal decomposition and sintering of a mixture of nickel powder, consisting of micrometer-sized particles, and an organic binder. Also nickel has been electrodeposited into the voids of a microporous polymer matrix

template. Then the polymer is burn out by heat treatment to produce micro-porous nickel coatings[69]. A highly porous large surface area nickel film was prepared from a high internal phase emulsion (HIPE) template[70]. Moreover, nanoporous Raney nickel was prepared using cathodic co-deposition of the Raney nickel precursor alloys (Ni/Al or Ni/Zn) on a conducting support. However, the materials obtained in all these trials have disordered, and non-uniform pores. This feature together with the high surface area acts to delay or inhibit the movement of gas and liquid species through the pore network. In contrary, materials with a uniform, ordered pore network and high surface area facilitate the movement of gas and liquid through the pore network and in turn exhibit superior performance in electrochemical systems which rely on gas or liquid diffusion within the electrode material. Therefore interest has increased towards the fabrication of mesoporous nickel with a uniform, ordered pore network. New approaches have been developed to prepare mesoporous nickel via the liquid crystal templating route. The first synthesis of mesoporous nickel using the liquid crystal templating via the electrodeposition route was reported by Nelson et al.[55]. They reported the electrodeposition of metallic nickel from aqueous nickel (II) acetate through the hexagonal ($H_I$) lyotropic liquid crystalline phases of polyoxyethylene (10) cetyl ether (Brij-56) and polyethylene glycol octadecyl ether (Brij-78) surfactant templates to form nickel films with hexagonal arrays of nanometer-sized channels[55]. The fabricated nickel films contained a well-ordered pore network with spacings between 5 and 8 nm. The estimated accessible surface area of the templated nickel films was found to be 100 times greater than samples fabricated without a template. Later, several attempts have been conducted to prepare mesoporous Ni with uniform, ordered pore networks (Table 1.1).

**Table 1.1** Mesoporous nickel materials fabricated using different methods

| **Product** | **Structure** | **Method** | **Pore size** | **References** |
|---|---|---|---|---|
| **NiO** | $H_I$ | Direct soft templating through Brij-56 and Brij-78 surfactants via the electrodeposition route | 5 -8 nm | Nelson et al.[55] |
| **Ni** | $H_I$ | Direct soft templating through a hexagonal liquid crystalline phase prepared from ternary mixture of Triton X-100, poly(acrylic acid) and water via the electrodeposition route | ~ 17 - 25 nm | Ganesh et al.[71,58] |
| **Ni** | $H_I$ | Electroless deposition using Brij-56 ($C_{16}$ $EO_{10}$) as a template | NA | Yamauchi et al.[72] |
| **NiO** | NA | Thermal treatment of $Ni(OH)_2$ using sodium dodecyl sulfate and urea as a hydrolysis controlling agent | 3-7 nm | Xing et al.[73] |
| **Ni/Co alloy** | $H_I$ | Electroless deposition using Brij-56 a template | NA | Yamauchi et al.[74] |
| **NiO** | $H_I$ | Hard templating using SBA-15 silica as template | 3-7 nm | Wang and Xia[75] |
| **Ni $(OH)_2$** | $H_I$ | Direct soft templating through a hexagonal liquid crystalline phase prepared from Brij-56 via the electrodeposition route | 7 nm | Zhao et al.[76] |
| **$Ni(OH)_2$** | $H_I$ | Direct soft templating through a hexagonal liquid crystalline phase prepared using 50 wt. % Brij-56 via the electrodeposition route | 2.5 nm | Zhao et al.[77] |

**Continue Table 1.1**

| | | | | |
|---|---|---|---|---|
| **α-Ni(OH)$_2$** | $H_I$ | Liquid phase deposition (LPD) method | varied | Deki et al.[78] |
| **Ni** | 3-D nanoporous gyroid | Electroless Plating using a nanoporous block copolymer with gyroid nanochannels as a template | NA | Hsueh et al.[79] |
| **Ni/Co** | $H_I$ | Electrodeposition using hexagonal phase of cetyltrimethylammonium bromide surfactant | ~ 2 nm | Bartlett et al.[80] |
| **Ni Co S** | Nanosheet arrays | Electrodeposition on carbon cloth | 2-10 nm | Chen et al.[81] |
| **MnO$_2$/Ni** | 3-D porous network | Ni was deposited chemically on planar conducting substrate with thermal treatment, followed by electrodeposition of Mn | NA | Xiao et al.[56] |
| **Ni-NiO$_2$** | 3-D nanorod array | Electrodeposition using aluminium oxide template | NA | Wang et al.[63] |
| **Ni** | Porous Ni | Electrodeposition using polystyrene sphere templates | 280 nm | Li et al.[82] |

$H_I$ = hexagonal, NA = not applicable

### 1.3.2 Mesoporous platinum

Mesoporous platinum materials have attracted attention due to their fascinating properties for a variety of applications, including sensing, cathode materials for fuel cells, batteries, electro analysis, electrodes for electrochemical biosensors (including, free hydrogen peroxide biosensor as well as non-enzymatic glucose sensing[57]. For example, mesoporous ($H_I$-ePt) platinum microelectrodes electrodeposited from the hexagonal ($H_I$) lyotropic liquid crystalline phase were synthesised and investigated for the detection of hydrogen peroxide. The fabricated electrodes exhibited excellent potential to be used as amperometric sensors for the detection of hydrogen peroxide[83]. Recently, a new method based on mesoporous platinum (Pt) electrodes has been developed for the detection of sugars (glucose, fructose, and sucrose) with high-performance anion-exchange chromatography (HPAEC). In this approach, the detection is based on the direct oxidation of sugars on mesoporous Pt films deposited on a gold electrode[84]. Moreover, mesoporous platinum nanowires have been synthesised and tested as a biosensor for the detection of glucose[85,86]. In fuel cells, platinum can be used as a catalyst which facilitates the reactions at the cathode (oxygen reduction reaction)[87] and the anode (methanol oxidation reaction). However, the majority of platinum catalysts consist of carbon-supported Pt nanoparticles which are subjected to carbon corrosion and aggregation during the electrochemical reaction of the fuel cell[88]. In order to overcome these problems, fabrication of nanoporous platinum is required to replace the carbon-supported Pt nanoparticles. Therefore, a wide range of nanoporous platinum materials with various shapes and sizes were fabricated for this purpose such as Pt-nanowires[87] nanotubes[89], nanodendrites[90] and others. Many attempts have been reported to fabricate nanostructured platinum with controlled size and shapes using different methods, some of these attempts are summarized in Table 1.2.

**Table 1.2** Nanostructured platinum materials fabricated with different methods.

| **Nanostructured Pt materials** | **Preparation method** | **Pore size** | **References** |
|---|---|---|---|
| **Nanoporous Pt films ($H_I$-ePt)** | Direct soft templating through hexagonal phase of octaethyleneglycol monohexadecyl ether ($C_{16}EO_8$) via the electrodeposition route | 2-15 nm | Attard et al.[51] |
| **lamellar Pt nanostructures** | Direct soft templating through lamellar phase of tetraethylene glycol monododecyl ether ($C_{12}EO_4$) surfactant using the electrodeposition route | NA | Zhao et al.[91] |
| **Pt nanocubes and nanospheres** | Substrate enhanced electroless deposition process | varied | Qu et al.[92] |
| **Pt nanowires** | Photochemical reduction of platinum ions | 40 ± 5 nm | Kundu et al.[93] |
| **Pt nanowires** | Using cetyltrimethylammonium bromide as a phase transfer agent | 2.2 nm | Song et al. [94] |
| **Pt nanowires** | Using n-dodecyl-trimethylammonium bromide as phase transfer agent | 2.3 nm | Teng et al.[95] |
| **Pt nanowires** | Hard templating using anodic aluminum oxide template | 50-60 nm | Napolskii et al.[96] |
| **Pt nanotubes** | Electroless synthesis | varied | Muench et al.[97] |

**Continue Table 1.2**

| | | | |
|---|---|---|---|
| **Hexagonal Pt array** | Direct soft templating through the hexagonal phase of octaethylene glycol monohexadecyl ether ($C_{16}EO_8$) via the electrodeposition route | 1.8 - 4 nm | Elliott et al.[52] |
| **Hexagonal PtRu** | Hard templating using 3-D mesoporous silica template | 2.4 nm | Jiang and Kucernak[98] |
| **Pt nanosponges and nanonetwork (PNNs)** | By galvanic replacement reactions with Te nanowires | NA | Lin et al.[99] |
| **3-D Pt nanoflowers** | Chemically using carbon nanospheres support | NA | Sun et al.[100] |
| **Nanostructured platinum** | Preferential pulsed electrodeposition (PED) from a dilute solution of chloroplatinic acid | varied | Rajalakshmi and Dhathathreyan[101] |
| **3-D Pt networks with a gyroid morphology** | Using nanostructured MCM-48 and SBA-15 silica materials as a structure directing agents | NA | Shin et al.[102] |
| **3-D mesoporous Pt network with a double gyroid morphology** | Using electrodeposition of Pt into a double gyroid mesoporous silica film as a template | 3-4 nm | Kibsgaard et al.[103] |
| **3-D mesoporous Pt network with a double gyroid morphology** | By vapor infiltration of a reducing agent using double gyroid mesoporous silica (KIT-6) template | > 10 nm | Doi et al.[104] |

**Continue Table 1.2**

| | | | |
|---|---|---|---|
| **Free-Standing Pt nanowires** | By casting using Te (Te@C) nanocables | 12 nm | Liang et al. [87] |
| **Hexagonal mesoporous Pt** | Direct soft templating through hexagonal phase of $C_{16}EO_{10}$ surfactant via the electrodeposition route | NA | Asghar et al.[53] |
| **3-D Pt with single diamond morphology** | Direct soft templating through phytantriol cubic phase via the electrodeposition route | 10 nm | Akbar et al.[41] |
| **3-D mesoporous Pt nanocubes** | A novel meso-crystal self-assembly mechanism | ~50 nm | Cao et al.[105] |
| **Mesoporous Pt nanospheres** | Using triblock copolymer [poly(styrene-*b*-2-vinylpyridine-*b*-ethylene oxide), PS-*b*-P2VP-*b*-PEO] as template | varied | Li et al.[106] |
| **3-D nanoporous gyroid Pt** | By electroless plating using polystyrene-b-poly(L-lactide) (PS-PLLA) block copolymer as a template | 20 nm | Cheng et al. [107] |
| **Mesoporous Pt/Ni with double gyroid morphology** | By co-electrodeposition of Pt and Ni into a mesoporous silica | 3-4 nm | Kibsgaard et al.[108] |

$H_I$ = hexagonal, NA = not applicable

## 1.4 Preparation of mesoporous materials

Mesoporous materials with well-defined pore sizes can be prepared by various approaches in which different templates are utilised. Hard templating and soft templating are the main approaches used for the preparation of mesoporous materials[46,51,109]. The structure and the shape of the mesoporous material depend on both the template and the method used in the preparation. A wide variety of templates ranging from 2-D hexagonal to 3-D structures are available. In the hard templating method, templates with predefined and non-flexible channels are used. The common templates used for hard templating methods include mesoporous silica[75,110,109], anodic aluminium oxide[111,112], and others. However, in the soft templating method, templates with flexible shapes and structures are used. Examples of these soft templates are surfactants[113,51,41], amphiphilic block copolymers[50,114], emulsions[115,116,117], polymer latex spheres[118,119] and others. Details about both hard templating and soft templating methods are described in the following sections.

### 1.4.1 Hard templating approach

In this approach, hard templates are used in the preparation of mesoporous materials. Mesoporous silica materials are the most common templates used for the preparation of mesoporous materials. The hard templating process is carried out in two stages; the first stage is the annealing of the materials with the silica template. The second stage is the removal of the parent silica template using concentrated NaOH or HF[109]. There are many silica templates with different structures, for example, the SBA-15 silica template has 2-D hexagonal symmetry, while the KIT-6 silica template has 3-D cubic symmetry. Mesoporous silica materials have been involved in the preparation of a wide range of mesoporous materials with different structures including, C[120], Pt[110,121], Sn[109] and many others. Anodic aluminium oxide

(AAO) templates have been also widely used in the preparation of mesoporous materials[122]. AAO templates have 2-D hexagonal pores. A wide variety of metal nanowires have been prepared in AAO templates using different routes including casting, chemical, electro-electrochemical, and photochemical depositions[122]. Metallic nanowires of Ni[123], (Ni, Cu, Co, Fe)[124], Co [125] and others have been prepared onto AAO templates via electrodeposition route.

Although the hard templating method is a highly reproducible method, it has some limitations including, high cost, long time scale, multiple-step procedure, as well as the difficulty to remove the parent templates[126].

### 1.4.2 Soft templating approach

In this approach, many soft templates can be used for the fabrication of nanostructured materials as mention in Section 1.4. Among these templates the lyotropic liquid crystals (LLC) which are characterised by high structural deformations as well as flow properties. Therefore, they have been used either directly or indirectly for preparations of nanostructure materials with different mesoporous structures. LLCs have been used directly as templates for fabrication of nanostructured materials. This method called true liquid crystal templating. Details about this method will be discussed later in the following section. In addition, LLCs have been used indirectly for the preparation of mesoporous materials through the preparation of mesoporous silica materials which are commonly used as hard templates for fabrication of other mesoporous materials (via hard templating method). Mesoporous silica materials were prepared using the surfactants hexadecyltrimethylammonium bromide (CTAB) and polyoxyethylene-10-cetyl ether (Brij-56) aligned under an extremely high magnetic field of 30 Tesla[127].

Another set of soft templates which are commonly used for the fabrication of mesoporous materials are block copolymers. For example, the triblock copolymer [poly(styrene-*b*-2-vinylpyridine-*b*-ethylene oxide), PS-*b*-P2VP-*b*-PEO] was used as a pore-directing agent for the fabrication of mesoporous Pt nanospheres with variable pore size[106]. Chen et al.[107] have reported the fabrication of a 3-D mesoporous platinum via electroless plating using the block copolymer, polystyrene-b-poly(L-lactide) (PS-PLLA) as a template. The soft templating approach has some advantages over hard templating including; low cost, simple processing and easy to remove templates[128].

### 1.4.3 Liquid crystal templating

This approach is one of the soft templating techniques used for fabrication of nanostructured materials. In this approach, lyotropic liquid crystalline phases are used directly as templates and the electrodeposition through them is a versatile route for fabrication of nanostructured materials[51]. This approach overcomes the problems associated with the hard templating route such as fabrication and removal of the hard templates. Furthermore, lyotropic liquid crystalline phases are ideal systems for the synthesis of nanomaterials due to their periodic architecture with lattice parameters in nanometers.

The first synthesis of nanostructure material using a lyotropic liquid crystalline phase as a direct template was reported by Attard et al.[51]. They reported a successful electrodeposition of highly ordered nanoporous platinum films with high surface area using a lyotropic liquid crystalline phase as a template. Since that time, this technique is used as a general synthetic technique for the fabrication of nanostructured materials. This approach involves electrodeposition of materials directly through the channels provided by the template in the electrolyte to access the conductive substrate. Therefore, the substrate needs to be coated with

the lyotropic liquid crystal template before electrodeposition. This approach is known as true lyotropic liquid crystal templating. Successful fabrication of a wide range of 2-D mesoporous materials has been reported using direct liquid crystal templating via electrodeposition route including platinum[51,52], tin[54] and nickel[55,71,76,77,80]. Recently this approach was successfully modified and extended to produce 2-D hexagonal mesoporous Pt with biaxially aligned mesopores[53] and 3-D nanostructured Pt with a single diamond morphology[41].

## 1.5 Aims and objectives

This work aimed to develop and extend methods for the fabrication of mesoporous metals with 3-D structures at room temperature using liquid crystal templating approach via the electrodeposition route. This work can be broken down into several separate points.

- To determine whether it is possible to electrodeposit nickel with single diamond morphology using monoolein as a template (Chapter 3).
- To determine whether it is possible to electrodeposit platinum with single diamond morphology using monoolein as a template (Chapter 4).
- To determine whether it is possible to utilise the platinum and nickel nanowires as hard templates for fabrication of Ni/Pt and Pt/Ni composites, respectively via electrodeposition route (Chapter 5).
- To investigate the physico-chemical properties of monoolein and its phase behavior (Chapter 6).

# Chapter 2: Materials and Methods

## 2.1 Introduction

This chapter describes all the analytical techniques and methods used to collect the data in this work. The theoretical bases of these techniques are briefly described. Details of the materials used in this work, sample preparations and experimental conditions are also included.

## 2.2 Materials

Nickel sulphate ($NiSO_4.6H_2O$), nickel chloride ($NiCl_2.6H_2O$), concentrated sulfuric acid ($H_2SO_4$) and hexachloroplatinic acid (HCPA) ($H_2PtCl_6$) solution (8 wt % in water) were purchased from Sigma Aldrich (UK). Monoolein product Rylo (95%) was sourced from Danisco A/S (UK) and monoolein product Cithrol was sourced from CRODA, Croda International Plc, UK. Boric acid (4%) was purchased from Fluka (UK). Phytantriol (3,7,11,15-tetramethyl-1,2,3-hexadecanetriol ($C_2H_{42}O_3$)) was a gift from Adina Cosmetics Ingredients UK (purity > 98.3 %). Potasium hydroxide was purchased from Fisher Chemical (UK), 0.5 M aqueous sulfuric acid ($H_2SO_4$) solution was prepared from Merck p.a.-grade. Butyl rubber (Miccro XP-2000) (red polymer) was sourced from Hi-Tek Products Ltd, UK. Ethanol ($C_2H_5OH$) was purchased from Fischer Scientific (UK). Brij-56 (polyethylene glycol hexadecyl ether ($C_{16}EO_{10}$)) was purchased from Aldrich (UK). Alumina powder in three grades (25, 1.0, 0.3 μm) and polishing pads (microcloth PSA) were purchased from Buehler (UK). Gold wire electrodes and platinum wire electrodes were purchased from Goodfellow, Cambridge Limited (UK). Gold-coated glass slides were purchased from EMF, evaporated metal films (UK). Gold-coated foil slides were purchased from Goodfellow, Cambridge

Limited. DVDs were sourced from Delkin Devices (UK). A glass capillary tube (diameter 1.5 mm, thickness 10 μm) was purchased from Capillary Tube Supplies Ltd, Reading, UK. All compounds were used as received. All aqueous solutions were prepared in Milli-Q water.

## 2.3 Sample preparations

### 2.3.1 Preparation of Liquid crystal ethanolic solutions

Solutions of monoolein/ethanol wt/wt % (1:1) and phytantriol/ethanol wt/wt % (1:1) were prepared by dissolving the appropriate weights of lipids in ethanol in eppendorf tubes. The eppendorf tubes were immediately sealed to avoid the loss of ethanol. The mixture was mixed manually for 10 min in order to obtain homogenous samples.

### 2.3.2 Nickel deposition solution

Nickel deposition solution consisting of (0.856 M $NiSO_4.6H_2O$, 0.158 M of $NiCl_2.6H_2O$ and 0.539 M of boric acid) was used as an aqueous phase for electrodeposition of nickel. The mixture was prepared by dissolving 135 g of $NiSO_4.6H_2O$, 22.5 g of $NiCl_2.6H_2O$ and 20 g of boric acid in 600 mL in Milli-Q water. The solutions were prepared in a fume cupboard. The final mixture has a pH of 4.0.

### 2.3.3 Platinum deposition solution

Platinum was deposited from HCPA solution. The solution was used as received.

### 2.3.4 Preparation of monoolein-Brij-56 mixture

Solutions of monoolein/ethanol wt/wt % (1:1) and Brij-56/ethanol wt/wt % (1:1) were prepared as described above in Section 2.3.1. Then mixtures with different wt % compositions of monoolein-ethanol/Brij-56-ethanol were prepared as shown in Table 2.1.

**Table 2.1** Composition of monoolein/Brij-56 mixtures used in this study

| Brij-56 % (w/w) | Monoolein % (w/w) |
|---|---|
| 3 | 97 |
| 5 | 95 |
| 7 | 93 |
| 10 | 90 |
| 15 | 85 |
| 20 | 80 |

### 2.3.5 Electrochemical preparation of mesoporous materials

Pre and post preparations as well as the experimental conditions used for preparation of mesoporous materials via electrodeposition process are described in the following sections.

### 2.3.5.1 Cleaning of platinum and gold wire electrodes

Prior to electrodeposition, the working wire electrodes (platinum or gold) were polished with sand paper and alumina in three grades (25, 1.0, and 0.3 μm). The polishing with alumina powder was performed on a polishing pad. The electrodes were polished until the surface appeared as a clean shiny mirror. After polishing, the electrodes were scanned 25-50 times by

cyclic voltammetry in 0.5 M $H_2SO_4$ at 200 mV/s between potential limits of +1.2 and -0.25 V vs. Ag/AgCl until hydrogen and oxygen adsorption peaks appear clearly.

### 2.3.5.2 Coating of working electrodes with surfactants

The working electrodes were coated with a film of surfactant (monoolein or/phytantriol) by dipping each electrode into the lipid ethanolic solution. The electrodes were then left to dry at room temperature for 30 min to allow the ethanol to evaporate leaving a film of the lipid at the electrode surface as shown in Figure 2.1. The film thickness was adjusted to be approximately 16 μm according to Akbar et al.[129]. This was estimated by dividing the volume of the ethanolic solution of the lipid with the electrode area which was covered by the lipid.

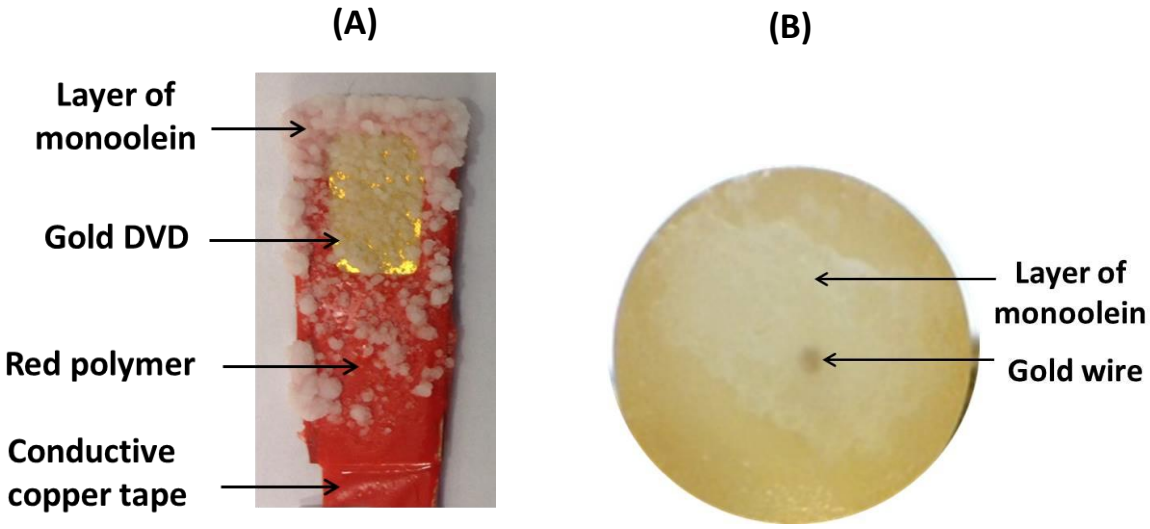


**Figure 2.1 Working electrodes coated with surfactant layers. A)** Gold DVD electrode and **B)** Gold wire electrode.

### 2.3.5.3 Soaking of working electrodes in metal solutions

Prior to electrodeposition, the lipid-coated working electrodes were soaked in metal electrolytes for 20 min. The soaking time showed potential effect on the formation of the liquid crystal phases at the electrode surface in the presence of excess metal solution[129].

### 2.3.5.4 Electrodeposition experiment

Electrodeposition of nanostructured metals was conducted using a potentiostatic controller at room temperature in excess of Ni deposition solution (for nickel deposition) or in excess of HCPA solution (for platinum deposition) using Ag/AgCl reference electrode, a platinum flag counter electrode and a working electrode. The working electrode (substrate) used in the deposition varied depending on the type of the targeted characterisation study. For cyclic voltammetry studies and electron microscopic analysis, nanostructured metal films were deposited on clean polished platinum/gold wire electrodes with an area of $1.96 \times 10^{-3}$ $cm^2$. For SAXS, XRD, SEM and TEM analysis, nanostructured metal films were deposited on different gold plate electrodes with large surface area (~1.0 - 1.3 $cm^2$) prepared from archival gold (24 karat) coated DVDs (purchased from Delkin Devices, UK). Electrodeposition was carried out at potentials of -0.95 V and -0.25 V vs. Ag/AgCl for nickel and platinum, respectively.

### 2.3.5.5 Post-treatment of working electrodes

Following the deposition, the working electrode was removed from the templating cell and immersed in ethanol (10-15 mL) for one hour in order to remove the lipid template. This process was repeated 1-2 times. Then the working electrode was washed by soaking in a mixture of ethanol and water (wt/wt ratio of 1:1) for 30 min followed by rinsing thoroughly with deionised distilled water. An electrodeposited metal layer on the working electrode was then analysed.

## 2.4 Techniques

### 2.4.1 Electrochemical techniques

Cyclic voltammetry and potential step are the electrochemical techniques used in this work. Details about the techniques as well as the experimental conditions used in this work are described below.

### Electrochemical cell

Electrochemical experiments take place in electrochemical cells. A typical electrochemical cell consists of a potentiostat which controls the electroanalytical process, a reference electrode (RE), a working electrode (WE), a counter electrode (CE), a glass cell, and an output device (computer) with analysis software (Figure 2.2).

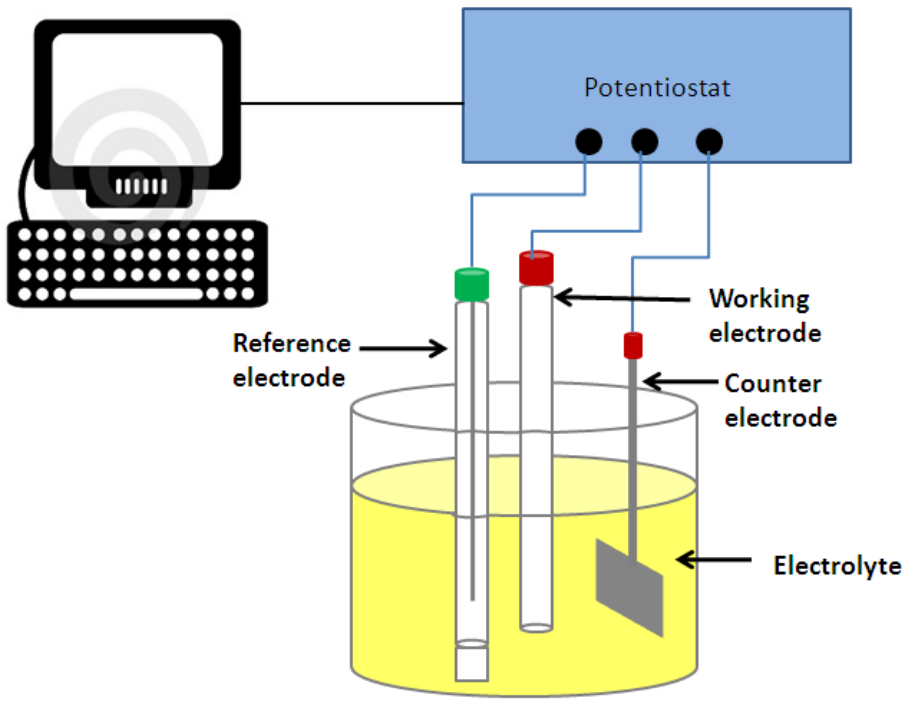


**Figure 2.2 A schematic illustration of a typical electrochemical cell.**

In our experiments, all electrochemical experiments were carried out at room temperature in a 20 mL glass cell. An Ag/AgCl electrode was used as the reference electrode (RE), a platinum flag with an area of ~ 1 $cm^2$ was used as the counter electrode (CE) and variable working electrodes (WE) were used depending on the purpose of the experiment. The glass tubing of the reference electrode is filled with 1 M KCl solution. The cell was controlled by an Autolab PGSTAT101 potentiostat. The cell was attached to a computer in order to process the data. Prior to each electrochemical experiment, the counter electrode was flamed 2-3 times followed by rinsing with distilled water, until a colourless flame was observed. The cell was cleaned with distilled water before each use. For cyclic voltammetry, the electrodes were immersed in either 0.5 M $H_2SO_4$ or 3 M KOH aqueous solutions. For electrodeposition, the three electrodes were immersed in the cell containing the metal electrolytes.

## Cyclic voltammetry

Cyclic voltammetry is the most common technique used to investigate electrochemical reaction mechanism. In this technique, the potential is scanned linearly between two values back and forth at a constant rate to measure the current with respect to the potential. The scan is repeated for many times. The output plot is called a voltammogram which shows the relation between the current and the potential.

In our work, cyclic voltammetry was initially used to clean the electrode surface (platinum or gold) before electrodeposition. The progressive formation and removal of oxide/hydride layers during cyclic voltammetry can clean all the impurities on the electrode surface. Platinum electrodes were cycled in 0.5 M $H_2SO_4$ aqueous solution at potentials scanned between +1.2 and -0.32 V vs. Ag/AgCl at room temperature (~ 20 °C) at various scan rates, while gold

electrodes were cycled in 0.5 M $H_2SO_4$ at potentials scanned between +1.6 and -0.2 V vs. Ag/AgCl at room temperature (~ 20 °C) at various scan rates.

Furthermore, cyclic voltammetry was used to characterise the electrodeposited platinum and nickel films. For characterisation of deposited nickel, nickel films were cycled in 3 M KOH for potentials scanned between +1.0 and -0.45 V vs. Ag/AgCl at 200 mV/s scan rate. A representative cyclic voltammogram of the deposited nickel is shown in Figure 2.3A. The voltammogram was used to identify the deposited nickel. According to Jabs et al.[130], cyclic voltammogram of nickel electrode shows the presence of characteristic anodic and cathodic peaks at a potential range from 0.3 to 0.5 V.

For characterisation of deposited platinum, platinum films were cycled in 0.5 $H_2SO_4$ at potentials scanned between +1.2 and -0.35 V vs. Ag/AgCl at 200 mV/s scan rate. A cyclic voltammogram of the deposited platinum is shown in Figure 2.3B. The voltammogram was then used for identification of platinum. Based on the literature, cyclic voltammogram of platinum electrode shows peaks at $H_c$, $H_a$, $O_a$, and $O_c$ which represent the formation of adsorbed hydrogen, the oxidation of adsorbed hydrogen, the formation of adsorbed oxygen or platinum oxide layer, and the reduction of the oxide layer, respectively[131]. Point A represents the start of bulk hydrogen evolution, while point B represents the start of the bulk oxygen evolution[131]. Cyclic voltammogram of platinum electrode also shows peaks at adsorbed hydrogen and adsorbed oxygen regions. The number, shape, and size of the peaks observed in the hydrogen region depend on the platinum crystal planes[132]. In general, the hydrogen region shows three peaks labelled 1, 2 and 3 in Figure 2.3B. These three peaks correspond to different platinum crystal planes (110), (100) and (111), respectively[131,133]. The hydrogen

region is known as hydrogen under potential (HUPD) region and is used to measure the electroactive surface area of the platinum electrodes as described below.

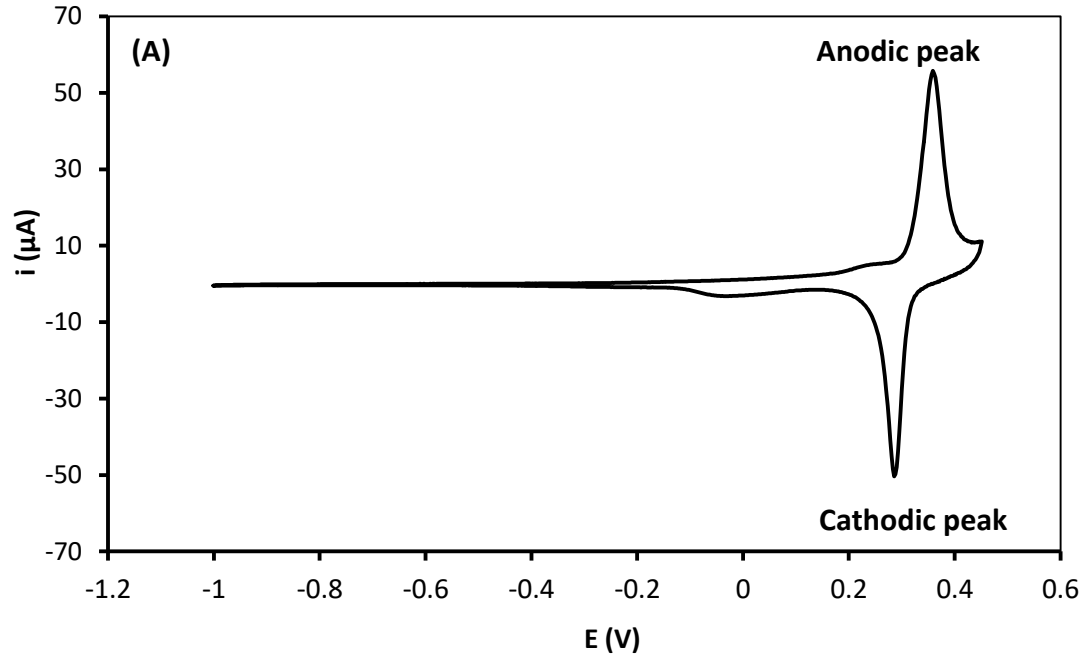


.

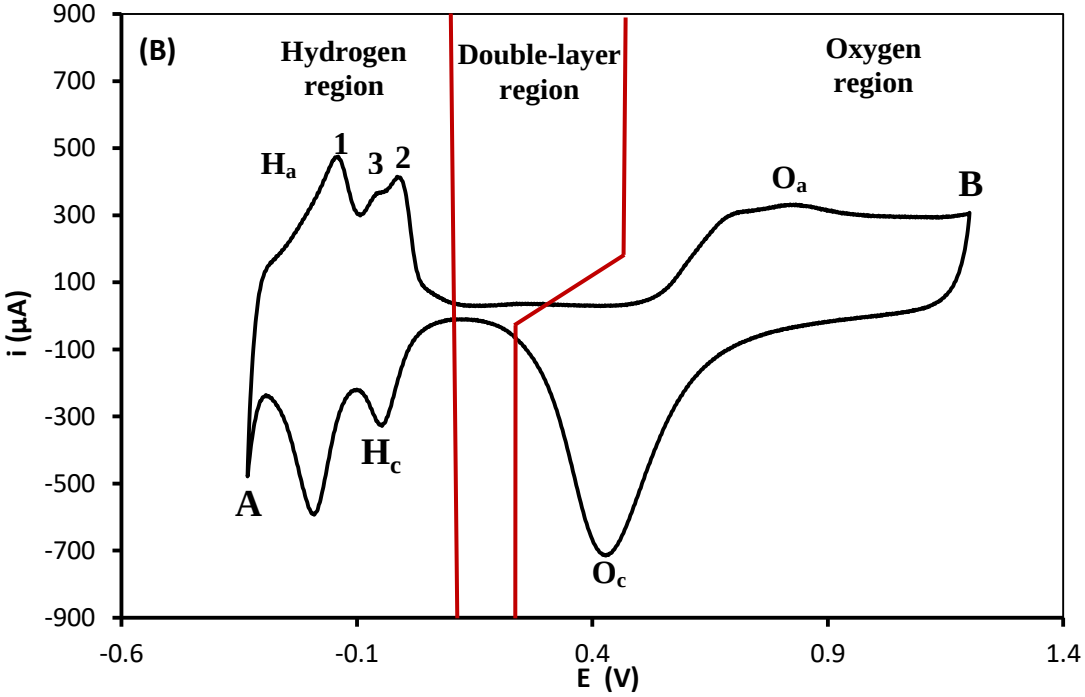


**Figure 2.3 Representative cyclic voltammograms for: A)** Nickel film, and **B)** Platinum film. Deposition were carried out at room temperature on gold wire electrode (area = 1.96 × $10^{-3}$ $cm^2$)**.** Cyclic voltammetry was recorded in 3M KOH at potentials scanned between +1.0 and -0.45 V vs. Ag/AgCl for nickel and in 0.5 M aqueous $H_2SO_4$ at potentials scanned between +1.2 V and -0.32 V vs. Ag/AgCl for platinum.

The electroactive surface area of nickel and platinum electrodes was calculated from the voltammograms by calculating the roughness factor (Rf). For deposited nickel and platinum films, the Rf values were from the formula in Equation 2.1:

$$\boldsymbol{Rf = \frac{S}{A}} \qquad \textbf{2.1}$$

Where A is geometrical surface area and S is the actual surface area. For nickel films S can be calculated from the following formula:

$$\boldsymbol{S = \frac{I}{0.000514 \times v}} \qquad \textbf{2.2}$$

Where I is value of the integration of the anodic region scan and ν is the value of the scan rate. The surface area was estimated assuming the charge density associated with the formation of one monolayer of α-$Ni(OH)_2$ is $q$$Ni(OH)_2$ = 0.000514 C $cm^{-2}$ as reported in the literature[134,135].

However the actual surface area (S) for platinum films can be calculated from the formula in Equation 2.3:

$$\boldsymbol{S = \frac{(I_1+I_2)/2}{0.00021 \times v}} \qquad \textbf{2.3}$$

Where $I_1$ and $I_2$ are the integrations for the hydrogen region (hydrogen under potential (HUPD) region) during forward scan and reverse scan and 'ν' is the san rate. The surface area was estimated assuming hydrogen adsorption charge density of 0.00021 C $cm^{-2}$ as reported by Brummer et al.[136].

Accordingly, the specific surface area ($\sigma_m$) for nickel and platinum was estimated using Equation 2.4 as follows:

$$\boldsymbol{\sigma_m = \frac{S}{m}} \qquad \mathbf{m^2\ g^{-1}} \qquad \mathbf{2.4}$$

Where, m is the mass of the metal, which was calculated using the same formula in Equation 2.5 as follows:

$$\boldsymbol{m = M \times MW} \qquad \mathbf{2.5}$$

Where MW is the molecular weight (MW = 58.7 g/mole for nickel and 195.08 g/mole for platinum) and M is number of moles of metal which can be calculated using the formula in Equation 2.6 as follows:

$$\boldsymbol{M = \frac{q}{N_A \times n \times e}} \qquad \mathbf{2.6}$$

Where q is the electrical charge, $N_A$ is Avogadro`s number ($6.022 \times 10^{23}$ $mol^{-1}$)**,** ***e*** is the electron charge ($1.6 \times 10^{-19}$ C), and n is number of electrons which makes 1 atom (n = 2 for nickel and 4 for platinum). The electric charge (q) can be calculated from the Equation 2.7 as follow:

$$\boldsymbol{q = \int i\, dt} \qquad \mathbf{2.7}$$

Where i = integral of current and dt = interval time.

## Potential step

In a typical potential step experiment, the applied potential (E) is changed suddenly from one value (E1) to another value (E2). The resulting current is then measured against time as shown in Figure 2.4

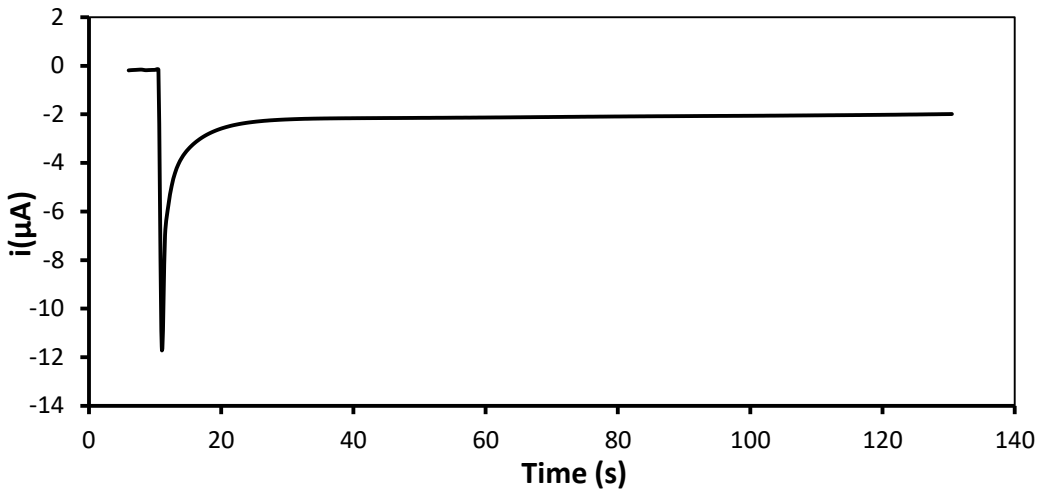


**Figure 2.4 A representative transient of nickel deposition on gold wire electrode (area = $1.96 \times 10^{-3}$ $cm^2$) at potential of -0.95V vs. Ag/AgCl.**

Potential step can be used for deposition of metals from metal electrolytes. This process is called electrodeposition. Platinum[129,137,57] , nickel[55] and other metals have been successfully deposited by this method. In our work, potential step was used for electrodeposition of Ni and Pt from their metal electrolytes. Details of electrodeposition experiments are described above in Section 2.3.5.

## 2.4.2 Electrodeposition process

Electrodeposition is commonly used to produce a thin layer of a desired material at a surface of an electrode (cathode). The substrate to be coated is immersed into a solution which contains the corresponding metal electrolyte. The three electrodes in the electrodeposition

cell are connected together to an external power supply (potentiostat). When an electric current passes through the electrolyte, the cations of the desired material will be reduced to its metallic form and deposited on the surface of the electrode[138,139]. The electrodeposition technique has many advantages including low cost as well as high deposition rates. Products of electrodeposition are widely used for many industries, such as electronics[140], jewellery[141], ship building, air space, machinery, and toy industries. In this work, thin films of mesoporous nickel and platinum were prepared using potential step deposition approach as reported previously by Ke et al.[142]. Sample preparations and experimental conditions used in the electrodeposition experiments are described above in Section 2.3.5.

### 2.4.3 X-ray diffraction (XRD)

This technique is primary used for phase identification of a crystalline material. The basic principle of this technique is based on the constructive interference of monochromatic X-rays and the crystalline sample. Diffraction patterns are generated upon interaction of the electromagnetic radiation with the sample when conditions satisfy Bragg's Law ($n\lambda = 2d \sin \theta$)[143] (Figure 2.5). The diffraction patterns are then detected and processed. The diffraction peaks can be then converted into d-spacings. The unknown materials can be then identified by comparing the d-spacings with patterns of a standard reference.

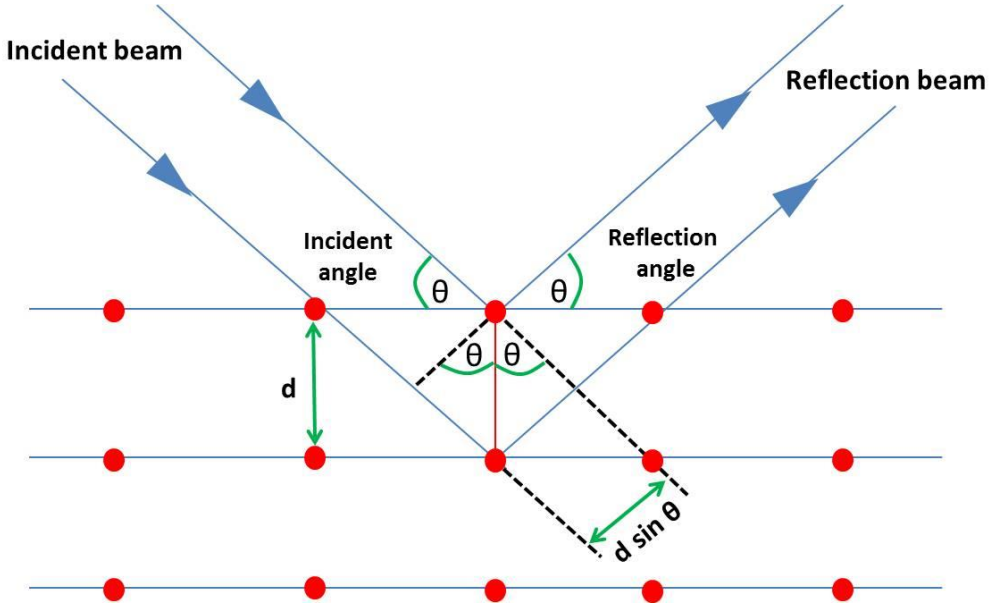


**Figure 2.5 A schematic illustration of Bragg's Law.**

In XRD measurements, a monochromatic beam of X-rays is focused on the sample. Most of the X-ray beam passes through the sample and some of beam is scattered at a specific diffraction angle depending upon the structural symmetry of the sample. The scattered X-rays form a scattering pattern which is then detected by 2-dimensional X-ray detector which generates 2-D patterns (Figure 2.6). The 2-dimensional X-ray patterns can be converted into 1-D patterns using a special software. The XRD patterns contain the information about the structure of the sample.

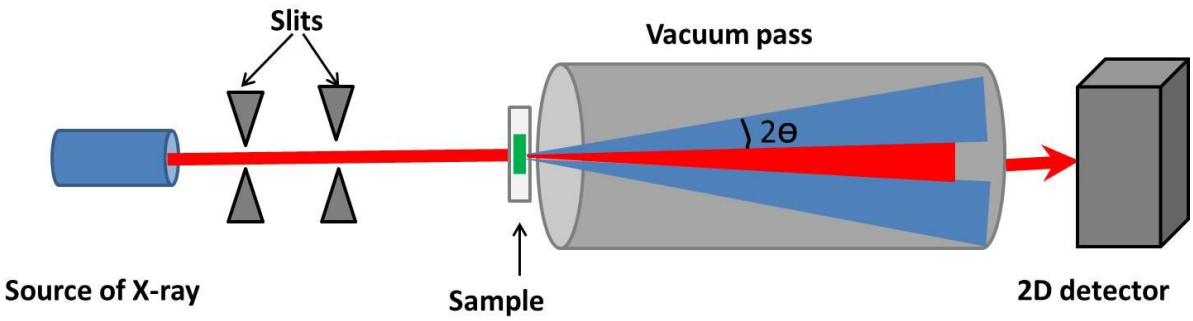


**Figure 2.6 A schematic illustration showing a typical setup of XRD instrument.**

### 2.4.4 Wide-angle powder diffraction (XRD)

X-ray powder diffraction (XRD) is used intensively for the identification of unknown crystalline materials. In our work, X-ray diffraction (XRD) was used to identify the deposited nickel materials. A thin layer of nickel was deposited on a gold DVD substrate (area = 1.0 $cm^2$). The substrate with the deposited nickel was analysed by X-ray diffraction (XRD) using D8 ADVANCE X-ray diffractometer (Bruker, Germany). The patterns of X-ray diffraction were run in normal 2 theta scan with Cu tube at wavelength of ($\lambda$ = 1.54 Å), voltage of 40 kV and current of 40 mA. As a control experiment, a blank gold DVD substrate (before deposition) was also analysed by XRD under the same conditions. The gold DVD substrate was fixed in the sample holder of the XRD machine by using blue-tack at the back of the substrate. The conductive side of the substrate was pushed by using two microscope glass substrates to make sure that the conductive side was flat with the edges of the sample holder.

### 2.4.5 Small angle X-ray scattering (SAXS)

#### 2.4.5.1 Technique overview, SAXS instrumentation and measurement

SAXS is one of X-ray scattering techniques which are mainly used to provide information about the nanostructure of materials[144]. It has been developed originally in the 1930s to study metal alloys[145]. Later, SAXS technique has been improved rapidly over the years and has become one of the most popular techniques used for structural characterisation of different materials, including polymers, biological macromolecules, colloids, liquid crystals and others. It has been used in broad range of applications including nanostructured metals, alloys, ceramics, and composite materials[146,147].

In this study, the small angle X-Ray Bruker Nanostar AXS (CAF lab, University of Reading, UK) was used to identify and confirm the phase behavior of liquid crystals (monoolein and phytantriol) under different conditions. The Bruker Nanostar AXS small-angle X-ray system was operated at 45 kV and 650 μA. Before use, the instrument was calibrated by silver behenate with d = 58.380 Å[148]. Sample to detector distances of 60 cm were used. Scattering patterns were obtained with the wavelength 1.54 Å[149]. The analysis was carried out under vacuum to minimize air scattering. The samples were equilibrated in SAXS instrument for 10 min before a 5-30 min SAXS exposure under vacuum. In order to study the phase transition of monoolein at different temperatures, monoolein samples were heated from 25-90 °C at a scan rate of 5 °C $min^{-1}$. In general, the SAXS data were displayed as 2D SAXS scattering patterns which were then converted into 1D patterns using Image J software with macros written in-house.

In addition, a synchrotron radiation facility (Beamline I07, Diamond Light Source, Oxford, UK) was used for structural characterisation for mesoporous nickel and platinum films. It was also used for studying the formation and stability of cubic phases of monoolein (Rylo) under excess of water. Measurements were conducted using a beam size of 300 μm × 500 μm with energy of 12.5 KeV. The wavelength of the X-rays was 0.99 Å. The data was collected using a Pilatus 100 K detector. In order to measure the sample to detector distance and beam center, silver behenate was used as a calibrant.

### 2.4.5.2 Sample preparation for SAXS

In this study, samples were prepared for SAXS analysis using different cells depending on the size of the sample, the purpose of the experiment as well as the type of the SAXS instrument used in the detection. Details about the cells used and the preparation process are shown in the following sections:

### Capillary cell

The capillary cells were used to prepare the samples used for identification of the phase behavior of the lipid crystalline templates (monoolein and phytantriol) in excess water or excess of metal solution. Also they were used to study the effect of temperature and Brij-56 on the phase behavior of monoolein (Rylo and Cithrol). Capillary cells were used for measurement with a Bruker Nanostar AXS system. The inside wall of the capillary tube (diameter 1.5 mm, thickness 10 µm) was coated with phytantriol or monoolein template with or without the additive (Brij-56) by pipetting phytantriol/ethanol mixture wt/wt % (1:1), monoolein/ethanol mixture wt/wt % (1:1) or monoolein/Brij mixture inside the tube. Then the tube was left to dry in air at room temperature for 10 min. A layer of the lipid was formed on the inside wall of the tube (~10-40 µm thick)[129]. The tube was then filled with water or metal solution. The glass capillary tube was then sealed on both sides to avoid liquid loss. The capillary tube was then placed on the capillary cell holder of the SAXS machine and used for the measurements (Figure 2.7).

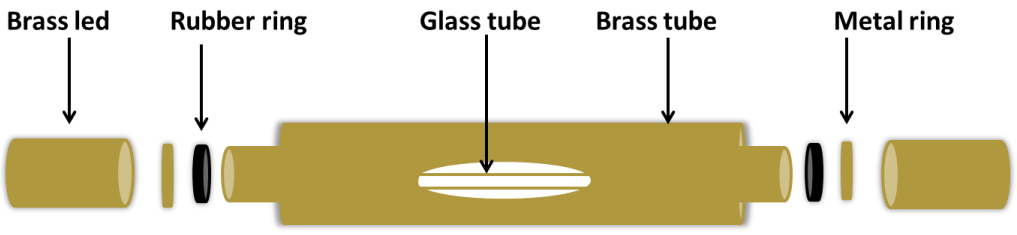


**Figure 2.7 A schematic illustration of the capillary cell used in SAXS measurements.**

## Sample preparation using gold DVD disk electrode

For structural characterisation by SAXS, mesoporous films of nickel or platinum were deposited on gold DVD disk working electrodes. In order to make these gold DVD electrodes, the two polycarbonate disks of the DVD were split apart by tweezers. Then the gold coated polycarbonate layer of the DVD was cut and used as electrodes. Conductive copper tape was attached to the DVD pieces. Then the back and the edges of the gold DVD pieces were coated with red polymer (Figure 2.8). The red polymer is used for many reasons:1) to mount the delicate gold layer firmly on the DVD pieces, 2) to cover the copper tape and thus to prevent the deposition of the metals on the copper tape, 3) to adjust the area of the electrode which is required for deposition. Electrodes of an area ranging from 1.0 to 1.3 $cm^2$ were made and used directly without polishing. High magnification SEM images of gold DVD electrodes showed that the electrode contains parallel grooves (Figure 2.8B). The DVD electrodes with the deposited metal films were exposed directly to SAXS for 1-10 min. This preparation was used for measurements with both Bruker Nanostar AXS instrument and synchrotron SAXS. DVD sample preparations were also used for XRD, SEM and TEM analysis.

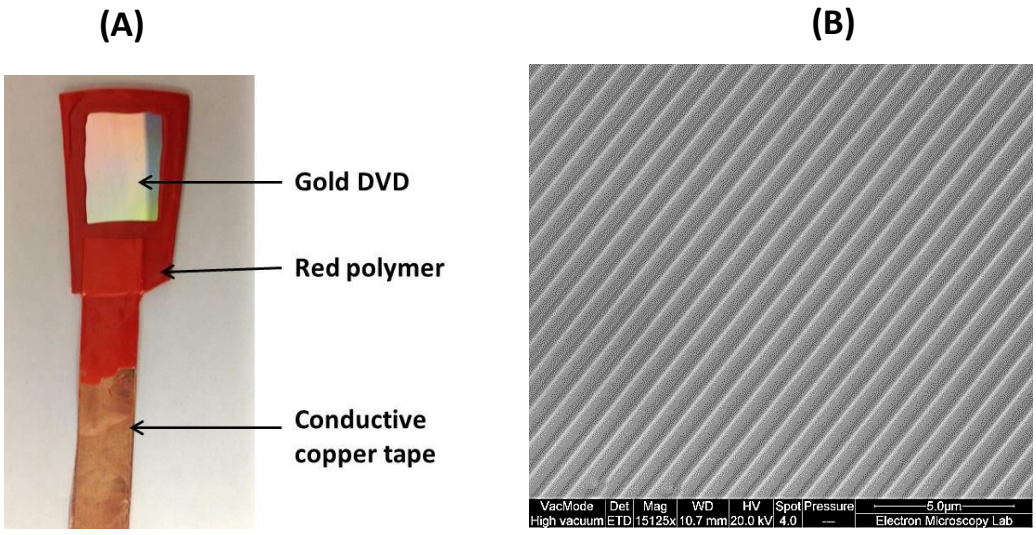


**Figure 2.8 Gold DVD working electrode: A)** An image of a blank gold DVD electrode and **B)** The corresponding high magnification SEM image**.**

## Nassar 14 cell

In order to assess the stability of cubic phase of the template after deposition, a Bruker Nanostar AXS instrument was used. However, to assess the cubic phase stability in the presence of a DVD gold substrate (area = 1 $cm^2$), the X-ray capillary tube (1.5 mm) was found to be too small for the substrate to be fitted in. To overcome this obstacle, we have designed a novel cell in which the substrate can be fitted inside and it is also suitable to be used under vacuum. This cell is named Nassar 14. The making steps of this cell are shown in Figure 2.9. After deposition and before dissolving the template with ethanol, the substrate was placed in the designed cell and characterised using a Bruker Nanostar AXS SAXS instrument.

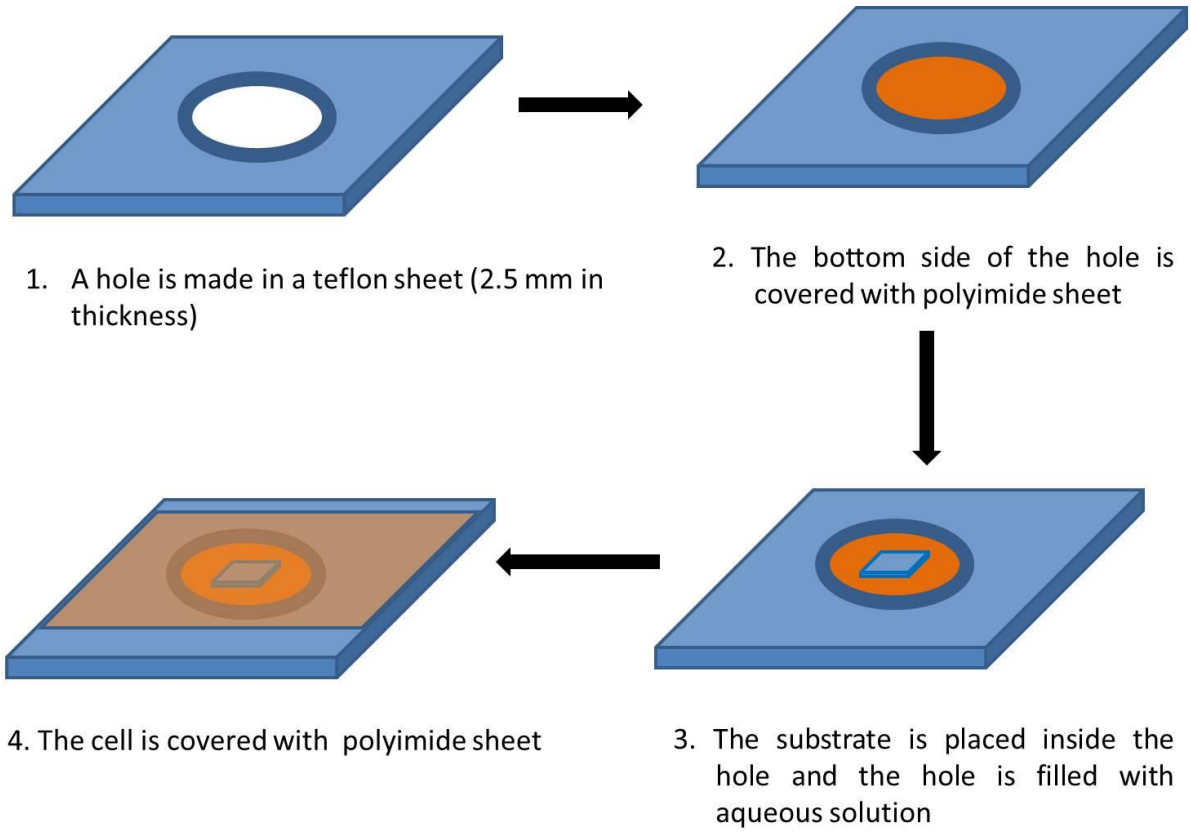


**Figure 2.9 Design steps of Nassar 14 cell used to study the stability of cubic phase after deposition on gold DVD substrate.**

## Acrylonitrile butadiene styrene (ABS)-polyimide water cell

This cell was used to study the effect of soaking time on the formation and stability of cubic phases of monoolein (Rylo) in excess of water. This cell was designed by Sam Richardson. The cell was printed from acrylonitrile butadiene styrene (ABS) by 3D printer (with dimension of 2 cm in width, 2 cm in highest and 0.5 cm in thickness) without the side walls. To make the cell side walls, two sheets of Kapton polyimide are mounted to the sides of the cell. The cell then is filled with water. A lipid coated-substrate is then soaked in the water inside the cell (Figure 2.10). The cell is placed in the x-ray chamber and x-ray beam passes through the Kapton Polyimide film. Synchrotron SAXS was used for the measurement.

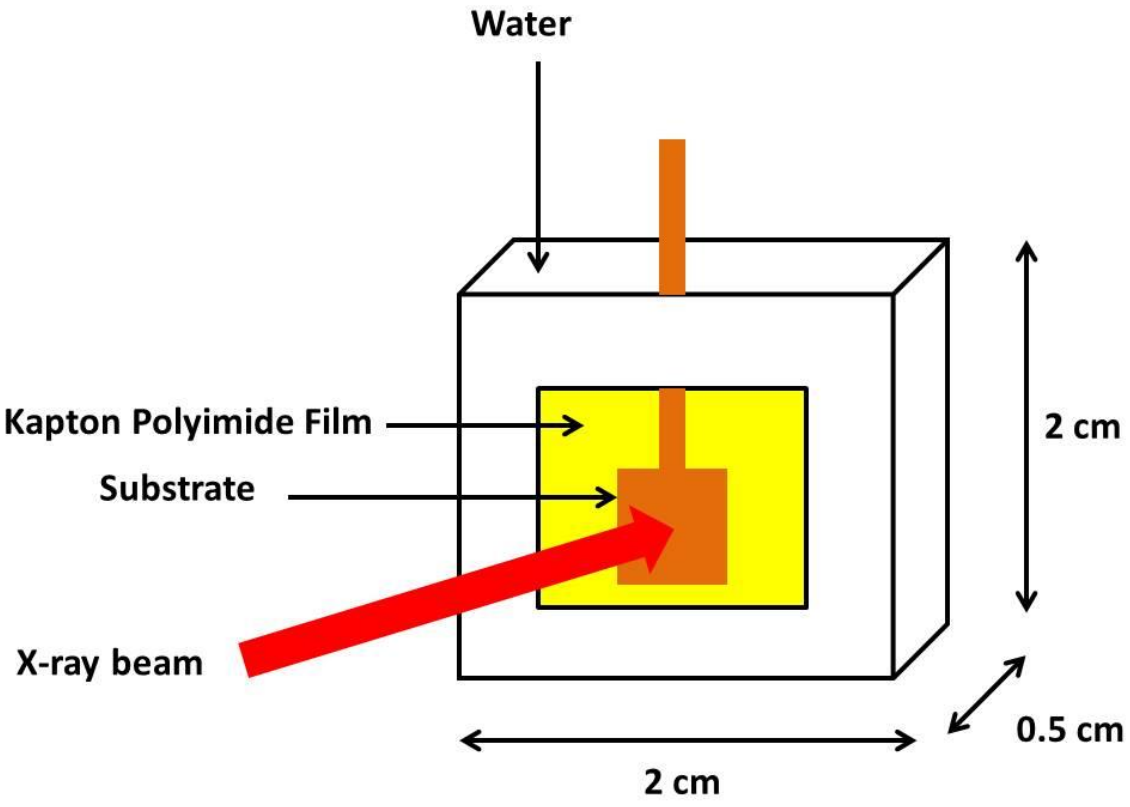


**Figure 2.10 A schematic illustration of the ABS-polyimide water cell used for SAXS measurements.**

### 2.4.5.3 Analysis of SAXS data

After SAXS measurements, the data were presented as 2D SAXS scattering patterns. Then these patterns could be converted into 1D patterns using Image J software with macros written in-house. The structure then could be identified using both the 2-D and 1-D patterns. In our work, the structure was identified by comparing the obtained 2-D SAXS patterns of the liquid phases with those reported previously for liquid crystals using SAXS analysis under the same conditions. The 1-D SAXS patterns show the ratios of Bragg reflection against each Bragg peak. For liquid crystal phases, each phase has characteristic ratio of Bragg peaks as shown in Table 2.2. Therefore, the structure symmetry can be identified from these ratios.

**Table 2.2** Ratios of Bragg reflections and their corresponding structure symmetry[150].

| **Ratio of Bragg reflections** | **Symmetry group** |
|---|---|
| √2:√3: √4:√6:√8:√9 | $Q_{II}^{D}$ with Pn3m symmetry |
| √3:√8 | $Q_{II}^{D}$ with Fd3m symmetry |
| √6:√8: √14:√16:√20 | $Q_{II}^{G}$ with Ia3d symmetry |
| √2:√4: √6 | $Q_{II}^{P}$ with Im3m symmetry |
| √1:√2 | $Q_{II}^{P}$ with Pm3m symmetry |
| √1:√3: √4 | $H_{II}$ or $H_{I}$ |
| 1:2:3 | $L\alpha$ |

## Lattice parameters of lyotropic phases

The best way for understanding and characterising the lipid phase behavior is through knowing the nano-structural parameters of the lipid phases, particularly with respect to temperature and water composition[4]. One of these nano-structural parameters is the lattice parameter. SAXS technique is usually used for determination of the lattice parameters of the

lipid mesophases. The calculations of the lattice parameter of different monoolein mesophases using SAXS technique [4] can be summarize in the following steps:

**1.** 2-D SAXS pattern is integrated into a 1-D scattering function I(q) where q ($Å^{-1}$) is the length of the scattering vector. It can be also expressed as a function of reciprocal spacing, s ($Å^{-1}$). The values of q and s can be calculated as follow:

$$q = \left(4\pi/\lambda\right)\sin\theta \qquad \textbf{2.8}$$

and

$$s = \left(2/\lambda\right)\sin\theta \qquad \textbf{2.9}$$

where 2ϴ is the scattering angle and λ is the wavelength of radiation

**2.** Then the lattice parameter of the mesophases (a) in units of Å can be calculated from the corresponding reciprocal spacings as follow:

A. For lamellar phase:

$$S_{lam} = \left(\frac{n}{a_{lam}}\right) \qquad \textbf{2.10}$$

where, $a_{lam}$ is the lattice parameter of the lamellar phase, and n is the order of reflection = 1, 2, 3…etc.

B. For cubic phases:

$$S_{cubic} = \left(\frac{1}{a_{cubic}}\right)\sqrt{h^2 + k^2 + l^2} \qquad \textbf{2.11}$$

where $a_{cubic}$ is the lattice parameter for cubic phase, the symbols *h, k, l* are Miller indices. The hkl values for the cubic diamond are [111] and [$11\bar{0}$] and for cubic gyroid are [202] and [$04\bar{0}$] [151].

C. For hexagonal phase:

$$\boldsymbol{S_{hex} = \left(\frac{2\sqrt{h^2 + k^2 + hk}}{a_{hex}\ \sqrt{3}}\right)} \qquad \textbf{2.12}$$

where $a_{hex}$ is the lattice parameter of hexagonal phase. As the lattice parameter for the hexagonal phase ($a_{hex}$) represents cylinder centre to cylinder centre distance therefore, it is related to the lowest order d-spacing by ($2/\sqrt{3}$), where h = 1, k = 0.

### 2.4.6 Scanning electron microscopy (SEM)

Scanning electron microscopy (SEM) is one of the electron microscopy techniques used for surface imaging which used to reveal the sample features at nanoscale level[152]. In this technique, electrons are used instead of light to produce images. A beam of electrons is focused on the sample. The beam interacts with the specimen and losses its energy. The lost energy is converted into some physical phenomena including emission of high-energy backscattered electrons, low-energy secondary electrons, Auger electrons and X-ray emission. All of these forms provide signals carrying information about the topology and composition of the specimen surface. The signals are collected by detectors and sent to a screen to display the image.

In our experiments, scanning electron microscopy was used to reveal the morphological features of the deposited nickel films. The analysis was performed using FEI Quanta FEG 600 Scanning Electron Microscope equipped with a Quorum PP2000T Cryo rotating stage at the at CfAM Electron Microscopy laboratory, University of Reading, UK. No pre-treatments were required for SEM. The edges of electrodes were painted with conductive colloidal graphite suspension in order to apply low conductance coating. Then the electrodes were placed in the sample holder inside the instrument. Imaging was carried out under vacuum at a working distance of 6-7 mm by FEI Quanta FEG 600 Scanning Electron Microscope operated at 20 kV accelerating voltages. A range of magnifications (250-15000x) was applied. The SEM data were analysed using INCA microanalysis software in order to identify the deposited material.

### 2.4.7 Transmission electron microscopy (TEM)

Transmission electron microscopy (TEM) is one of the powerful microscopic techniques used to reveal detailed structural information of the materials at the atomic level[153,154]. In TEM analysis, a beam generated from a specific source passes through the sample and is then focused to form an image which indicates the morphological features of the sample.

TEM instrument consists of an electron gun which generates the electron beams, objective and projector magnetic lenses to collect and magnify the electron beams, respectively and fluorescent viewing screen. The electron beam is accelerated towards an anode. Then it collected on the sample through an objective magnetic lens. The electron beam interacts with the sample and part of it is diffracted by the sample morphological features[155]. The transmitted beam is then magnified through a projector magnetic lens and viewed on a viewing fluorescent screen revealing a 2-D view of the material's density.

In our experiments, TEM was used to investigate the internal nanostructure of electrodeposited nickel films. The analysis was conducted using a Philips/FEI CM20 transmission electron microscope equipped with an Oxford Instruments INCA X-ray Analysis system. The analysis was carried out using the facilities at CfAM, University of Reading, UK. The electrodeposited nanostructured nickel films were scratched off from the electrodes with a scalpel and placed on a copper grid with a supporting carbon film (300 mesh). Imaging of the samples was carried out under vacuum with Philips/FEI CM20 microscope operated at 200 kV accelerating voltage.

### 2.4.8 Cross polarised light microscopy (CPLM)

Crossed polarised light microscopy (CPLM) has been widely used for identification of different liquid crystal phases[156,157]. It can provide means of identification of liquid crystal phases by CPLM based on observation of the characteristic birefringent textures or viscosity of the phase under CPLM. Lamellar and inverse hexagonal phases have anisotropic nature, therefore they exhibit characteristic birefringent texture when observed under CPLM, Lamellar phases may exhibit a Maltese cross[158], streaky or mosaic like texture[159] and hexagonal phases exhibit a flat fan like birefringent appearance[159]. On the other hand, no characteristic birefringent textures for either the bicontinuous cubic or the reverse micellar phases when they are seen under CPLM due to their isotropic nature. As a result, the whole sample appears dark under the CPLM in the case of these two phases[160]. Thus, cubic and the inverse micellar phases are differentiated by the structure of the phase boundary depending on its viscosity. Due to the low viscosity of the reverse micellar phase, the phase boundary appears as a straight line and contracted with excess water, while the highly viscous cubic phase exhibits an irregular shape boundary with excess water.

In our work, cross polarised light microscopy was used to study the phase behavior of monoolein at different temperatures. The analysis was conducted using Zeiss Axioskop 40 polarizing microscope (CAF lab based on chemistry department at University of Reading, Reading, UK) fitted with cross polarizing filters. The sample was placed on a glass slide and covered by a glass cover slip. The slide was then investigated under the microscope by heating and cooling cycles. The samples were heated from 25 - 90 °C at a scan rate of 2 °C $min^{-1}$ using Linkam PE 94 heating stage. The phase behavior of monoolein samples was observed at a magnification of 10X. Filming was carried out using a Cannon Digital Camera attached to the microscope.

## 2.4.9 Mass spectroscopy technique

Mass spectrometry (MS) is an analytical tool used to identify compounds based on the atomic composition of the molecules and their charge state[161]. Mass spectrometry is used for both industrial and research purposes. Some of the major applications of MS including, biotechnological application such as protein analysis and oligonucleotides; pharmaceutical applications such as drug discovery, pharmacokinetics, drug metabolism; clinical applications such as neonatal screening, drug testing; environmental applications such as water quality, food contamination and geological applications such as oil composition.

In general, the mass spectrometer consists of three main parts: an ionisation source, an analyser, and a detector as shown in Figure 2.11. The analyser, detector and the ionisation source are maintained under high vacuum in order to facilitate the movement of the ions from one end of the instrument to the other.

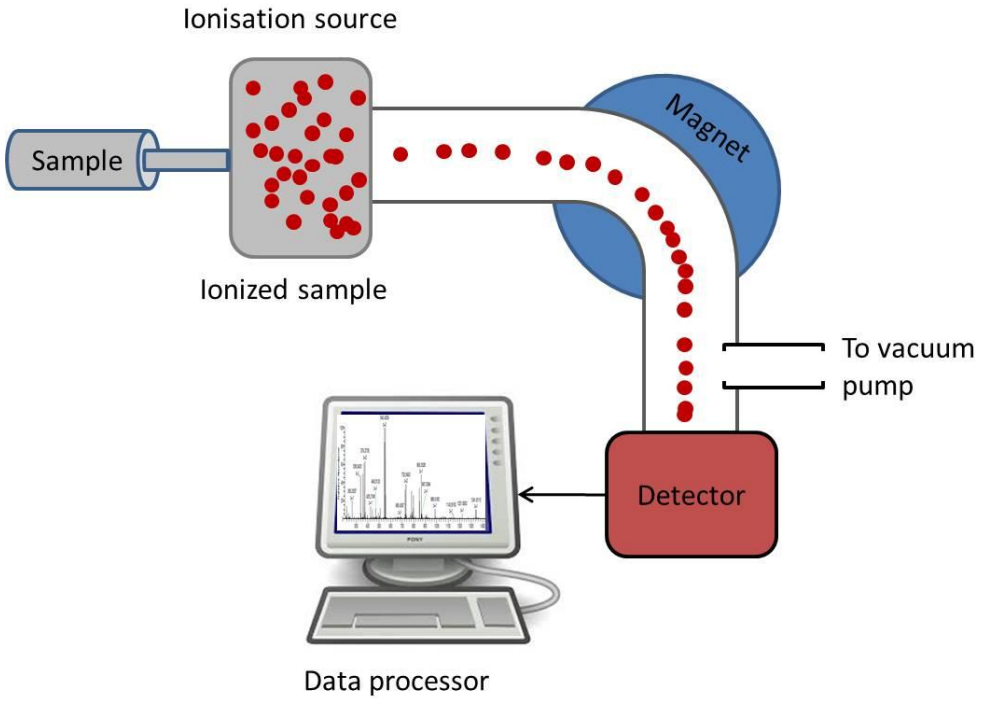


**Figure 2.11 A schematic diagram showing a simplified mass spectrometer instrument.**

In a typical MS experiment, the sample is initially subjected to ionisation into the ionisation source in the instrument, where the sample is ionised. Then the ions are extracted into the analyser region of the instrument where they are separated based on their mass (m) -to-charge (z) ratios (m/z). The ion signals then can be detected and sent to the data system. The m/z ratios of the sample are then plotted with respect to their relative abundance and presented as m/z spectrum. A typical m/z plot is shown in Figure 2.12.

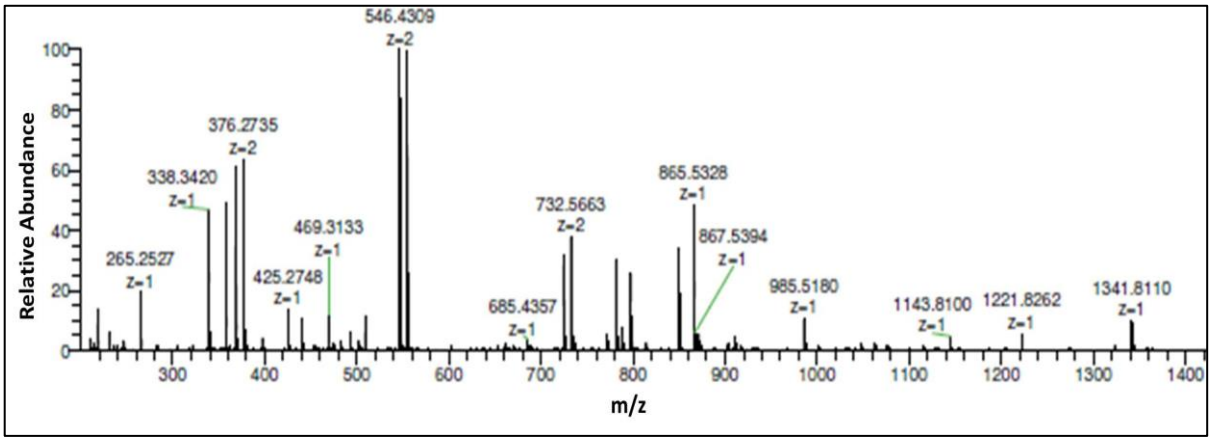


**Figure 2.12 A representative m/z spectra of monoolein (Rylo) investigated in this study.**

In our work, mass spectrometry is used to reveal the molecular mass of two monoolein products, namely Rylo and Cithrol. The analysis was conducted using the facility in CAF lab at Chemistry Department, Reading University. The samples were run on a Thermo Scientific LTQ-Orbitrap-XL Mass spectrometer via an Accela HPLC. Initially, HPLC was conducted for the samples using Accela HPLC. The samples were run on a C18 column (50 × 1 mm); 0.1% formic in $H_2O$ was used as buffer A and 0.1% formic acid in MeCN (acetonitrile) was used as buffer B. Then mass measurements were carried out using a Thermo Scientific LTQ-Orbitrap-XL Mass spectrometer. The mass data was then analysed using Thermo Xcalibur 2.1 software.

### 2.4.10 Differential scanning calorimetry (DSC) technique

DSC refers to the measurements of the difference in the rate of the heat flow of a sample and a reference while they are subjected to controlled temperature[162]. During the experiment, both the sample and reference are kept at nearly the same temperature. Basically, when the sample undergoes a physical transformation such as phase transitions, heat will need to flow to it and the reference to maintain both at the same temperature. The amount of heat need to flow to the sample depends on whether the process is exothermic or endothermic. The difference in heat flow between the sample and reference is monitored during the DSC measurement. Then the amount of heat absorbed or released during the transitions can be determined.

Generally, the DSC instrument consists of two chambers (cells) (sample cell and reference cell). The cells consist of small platforms mounted to thermocouples to measure the temperature changes. The DCS device is attached to a computer to monitor the temperature and heat flow (Figure 2.13). In a typical DSC experiment, the sample is placed in an aluminium pan. The sample pan and the reference pan are placed on the corresponding DSC chambers. The thermocouples sensors measure the heat changes during the transitions. Then the signals are sent to the computer for processing the data. The final output of a DSC experiment is a curve of heat flux with respect to temperature or with respect to time. This curve can be used to calculate enthalpies of the transitions.

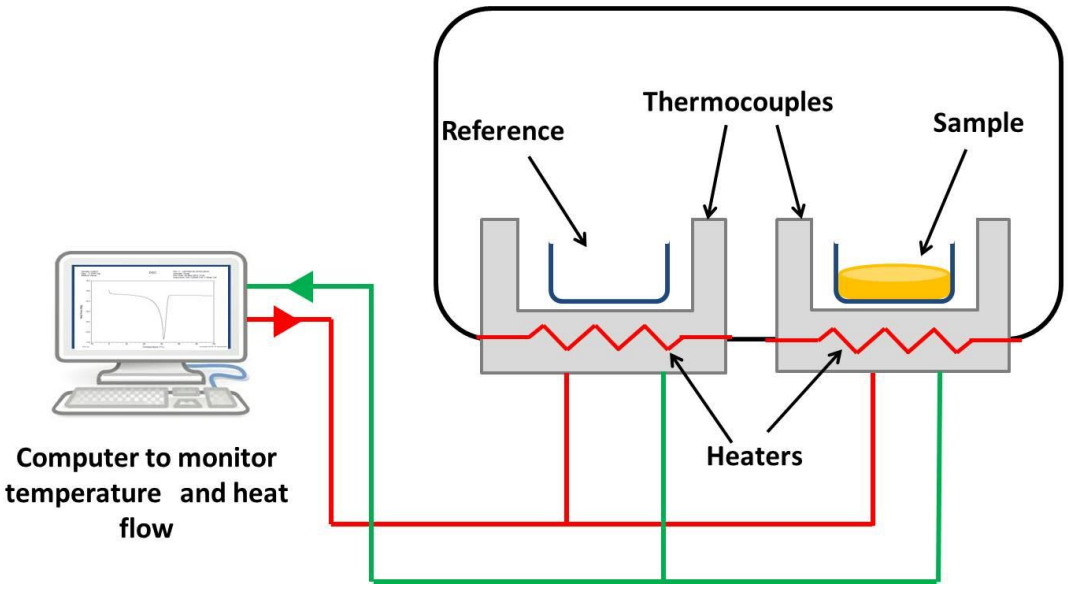


**Figure 2.13 A schematic illustration of the DSC instrument.**

DSC is a versatile thermal analysis technique which is used to measure many characteristic properties of materials including, melting, crystallization, resin curing, loss of solvents, glass transition and other processes. In our work, DSC was used to determine the melting point of monoolein materials, Rylo and Cithrol. The analysis was conducted using the TA Q2000 DSC instrument (UK) based on the CAF lab at University of Reading. Weights of 17.52 mg of Rylo and Cithrol, respectively were heated up from 0 to 60 $^{o}$C with a scan rate of 2 $^{o}$C /min. The data was then analysed using Universal Analysis 2000 version 4.5 A software.

# Chapter 3: Electrochemical fabrication of nanostructured nickel with single diamond morphology

## 3.1 Introduction

Nickel can be used in many electrochemical applications such as batteries, fuel cells[59,60] electrochemical hydrogenation of organic species[61] and in alkaline water electrolysis[62]. The use of nickel in electrochemical technology depends on its electrochemically active surface area, as all the reactions involved occur on the surface. Thus improvement in nickel surface area results in an improvement of the nickel electrode technology. Several attempts have been conducted to prepare high surface area nickel. However, all these previous attempts involved either a thermal treatment step or leaching with concentrated alkali solutions[69]. The materials obtained in all these attempts have non-uniform pore networks. This feature acts to delay or inhibit the movement of gas and liquid species through the pore network. In contrast, materials with a uniform, ordered pore network and high surface areas facilitate the movement of gas and liquid through the pore network and in turn exhibit superior performance in electrochemical systems which rely on gas or liquid diffusion within the electrode material. Therefore, research interest has increased towards producing nickel with high surface area and a uniform pore network. Recently, new approaches have been developed to prepare high surface area nickel using liquid crystal templates for electrochemical deposition[55]. The first synthesis of mesoporous nickel via the liquid crystal templating electrodeposition route was reported by Nelson et al[55] who used hexagonal ($H_1$) lyotropic liquid crystalline phases of polyoxyethylene (10) cetyl ether (Brij 56) and polyethylene glycol octadecyl ether (Brij 78) surfactant templates to form nanostructured nickel films. Recently, Zhao et al.[76,77] and Yamauchi et al.[72,74] have reported the fabrication

of $H_1$ mesoporous nickel using liquid crystal templating. All these studies were focused on the production of mesoporous nickel using electrochemical templating from hexagonal phases ( with 2-D symmetry). In contrast, the fabrication of nickel via electrochemical templating from cubic phases (with 3-D symmetry) has not been reported yet. This could be due to the difficulties associated with electrochemical templating from type 1 cubic phases via the true liquid crystal templating method. These includes: 1) only a small region of the composition-temperature phase diagram is occupied by the cubic phase and 2) The high vicosity of the bicontinuous cubic phases in comparision to the corresponding hexagonal phases[163]. However, recently, research has focused on the production of mesoporous materials with a bicontinuous cubic morphology[41]. The 3-D cubic symmetry provides high surface area as well as greater electronic and mechanical stability[164,165]. Also the 3-D symmetry overcomes the proplems associated with the use of the 2-D mesoporous materials such as poor diffusion[166] and pore blockage[167].

In this work, for the first time we report the production of nanostructured nickel with a 3-D bicontinuous cubic structure via the liquid crystal templating electrodeposition route. Solutions of nickel were used as aqueous phases in an attempt to prepare mesoporous nickel with high surface area at room temperature using direct electrochemical templating through the self-assembled diamond phase ($Q_{224}$) of monoolein (1-(cis-9-octadecenoyl)-rac-glycerol). Using monoolein as a template has two main advantages: 1) Monoolein is a cheap surfactant, 2) Monoolein forms bicontinuous cubic phases in excess water at room temperature, and therefore the fabricated nanostructured nickel is expected to have very high surface area. This work differs to that already reported by Akbar et al.[41] in two main ways: 1) Different metal was deposited here (Ni) and 2) Different surfactant was used (monoolein) as template.

## 3.2 Methodology

For the electrochemical fabrication of nanostructured nickel films, monoolein was dissolved in ethanol as described in chapter 2 and used as the template. A nickel mixture (135 g of $NiSO_4.6H_2O$ + 22.5 g $NiCl_2.6H_2O$ + 20 g of boric acid in 600 mL) was prepared and used as the aqueous electrolyte. The monoolein material, namely Rylo was used as a template for electrodeposition of nanostructured nickel. The stability of the monoolein (Rylo) cubic phases after and before deposition was characterised using small angle X-ray scattering (SAXS). Prior to electrodeposition, in order to find out the stability of the cubic phase under excess water, monoolein coated electrodes were placed in water inside a ABS-polyimide water cell, then SAXS scans were taken one every minute for 20 min. Details of the cell used are described in Chapter 2 (Section 2.4.5.2). Also stability of the phytantriol cubic phase was investigated using SAXS analysis. In order to optimise the deposition potential, the electrochemical fabrication of nanostructured nickel was conducted at different potentials ranging from -0.7 to -1.05 V vs Ag/AgCl in excess of nickel deposition solution. After electrodeposition, the deposited nickel films were washed as described in Chapter 2 and then characterised. Electrochemical deposition and characterization was carried at room temperature in a 20 mL glass cell. All electrochemical experiments were conducted using an Autolab PGSTAT101 potentiostatic controller with a three-electrode cell consisting of Ag/AgCl reference electrode, platinum counter electrode (area ~ 1 $cm^2$) and different working electrodes (gold coated-glass slide, gold wire, gold foil and gold DVD) of variable size. Electrochemical characterisation of the deposited films was carried out using cyclic voltammetry.

Structural characterisation of the deposited nickel films was carried out using small angle X-ray scattering (SAXS) and X-ray diffraction (XRD). Electron microscopy techniques were

used to investigate the morphological properties of the deposited nickel films as well as identify the deposited material. Details of the techniques and the instrumentation used in the structural and morphological characterisation are described in Chapter 2.

## 3.3 Results and discussion

### 3.3.1 Characterisation of monoolein based $Q_{II}^{D}$ phase template

In this work, the stability of monoolein (Rylo) under excess of water or excess of nickel solution was confirmed using small angle X-ray scattering (SAXS). The monoolein samples under excess of water or excess of nickel solution were prepared using X-ray glass capillary tubes as described in the methodology chapter. Then monoolein based cubic phases in excess of water and in excess of nickel solution were characterised using synchrotron SAXS (Beamline I07, Diamond, UK). The SAXS patterns of monoolein based cubic phases are shown in Figure 3.1.

In both cases, 2-D SAXS patterns showed typical series of reflection which are consistent with the bicontinuous cubic phases-*Pn3m* (diamond, $Q_{II}^{D}$) found in the binary phase diagram of monoolein-water[4]. This was confirmed by 1-D SAXS patterns of both cases which showed six strong Bragg peaks that follow the ratios √2: √3: √4: √6: √8: √9, which is in agreement with a cubic lattice of *Pn3m* crystallographic space group ($Q_{II}^{D}$)[168] and confirms the stability of the diamond bicontinuous cubic phase of the used monoolein/water system. Also 1-D SAXS patterns showed a small effect on the cubic phase behaviour of monoolein in the presence of nickel solution, showing the same six Bragg peaks observed in the absence of the nickel solution (Figure 3.1).

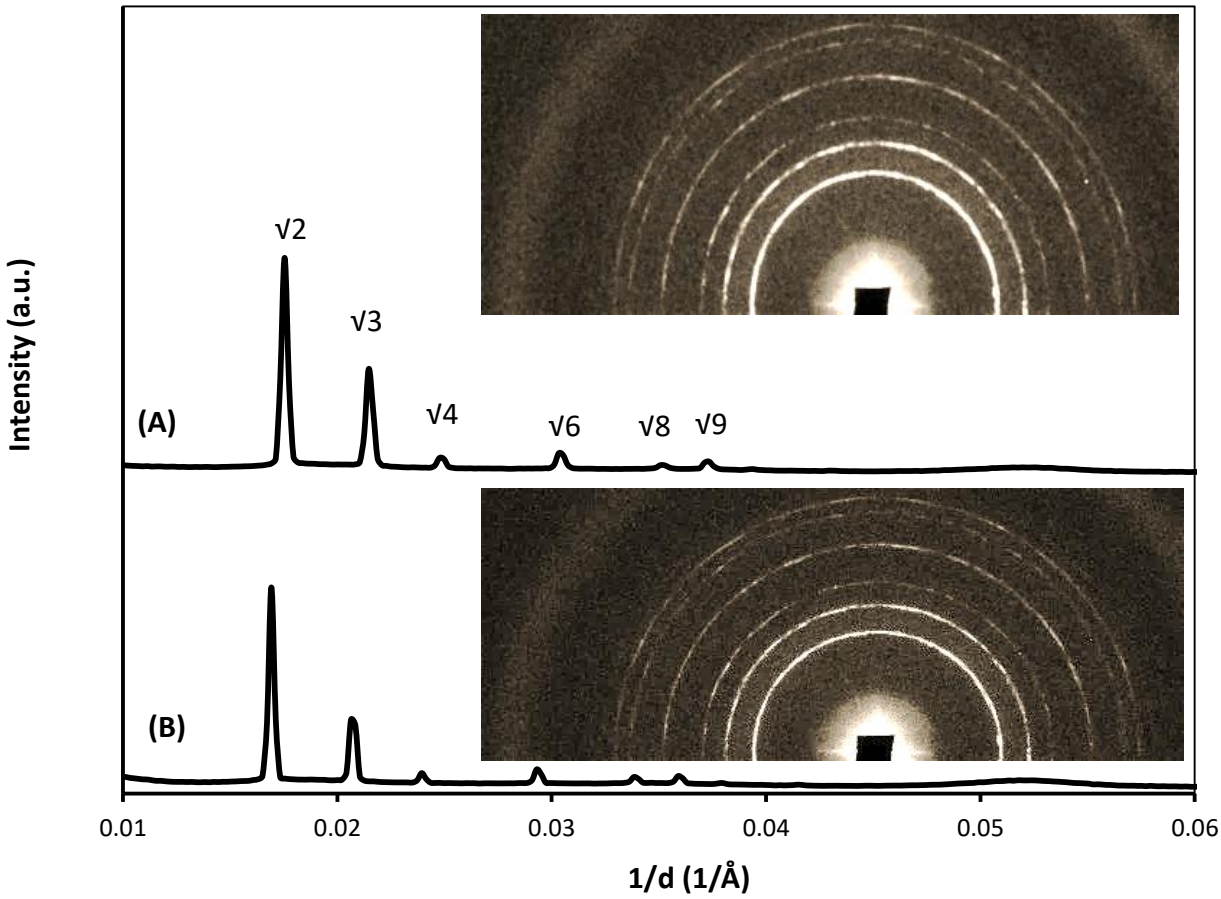


**Figure 3.1 1-D small angle X-ray scattering pattern for monoolein (Rylo) at room temperature. A)** in excess of nickel deposition solution, **B)** in excess of water. Insets are the 2-D SAXS patterns corresponding to each 1-D pattern.

The lattice parameter value was calculated to be 92.1 ± 0.3 Å with excess of water. This value is slightly smaller in comparison to that obtained with the pure monoolein at full hydration ($a$ =107 Å at 20 $^{o}$C)[169]. Most likely, this is due to the relatively low purity of Rylo (95 %). In the presence of nickel solution, there was a small decrease in the lattice parameter as compared to that obtained with Rylo, giving 87.0 ± 3.9 Å. This could be due to the presences of chloride and sulfate in the nickel solution. The chloride and sulfate were found to act as kosmotropes [170]. This leads to the 'dehydration' of the monoolein head groups at the interface, resulting in shrinking of the water channels, as indicated by a decrease in the lattice parameter[36,35]. However, there is no transformation of the cubic phase in the presence of

nickel solution as described above, indicating that the monoolein cubic phase is in equilibrium with this nickel mixture. And thus, this mixture could potentially be used to deposit nanostructured nickel at room temperature.

In comparison, SAXS was used to study the stability of the cubic phase of phytantriol under excess of water or excess of nickel solution. The samples were prepared for SAXS analysis using capillary tubes as described above. First, the inside walls of the capillary tube was coated with a layer of phytantriol. The tube was then filled with water and SAXS measurement was taken. Second, the water was removed from the tube and the tube filled with nickel deposition solution, followed by SAXS measurement. Last, the nickel deposition solution was removed from the tube and the tube was washed, filled with water and SAXS measurement was taken again. The SAXS patterns are shown in Figure 3.2. 2-D SAXS patterns confirmed the formation of diamond bicontinuous cubic phase of the phytantriol under excess of water. This was confirmed by the 1-D SAXS patterns which showed six strong Bragg peaks with ratios of √2: √3: √4: √6: √8: √9 (Figure 3.2A). This pattern is in agreement with the $Q_{II}^{D}$ of *Pn3m* symmetry ($Q_{224}$)[171]. The calculated lattice parameter was 66.5 Å under excess of water which is in agreement with the literature[5]. However, in the presence of nickel solution, there was a transformation in the cubic to inverse gyroid ($Q_{II}^{G}$) cubic phase. This was obvious from the 2-D SAXS showing a typical pattern for the gyroid phase. 1-D SAXS patterns of phytantriol under excess of nickel solution showed three Bragg peaks following the ratios: √6: √8: √14, which is in agreement with the $Q_{II}^{G}$ phase of *Ia3d* symmetry (crystallographic space group, $Q_{230}$)[171] (Figure 3.2B). The calculated lattice parameter for this phase was found to be 85.4 Å which is in good agreement with the lattice parameter values reported previously for the $Q_{II}^{G}$ phase of phytantriol at room temperature[5]. The phase transformation of phytantriol under excess of nickel deposition solution could be

due to the hydration effect of the chloride and sulfate existed in the nickel deposition solution as described above. The phase transformation of phytantriol from $Q_{II}^{D}$ to $Q_{II}^{G}$ was reported previously at lower water concentration[5,129]. When nickel deposition solution was removed from the tube and the phytantriol layer was washed and immersed with water, it was observed that the diamond cubic phase was formed again as indicated by the 2-D and 1-D SAXS patterns (Figure 3.2C). The calculated lattice parameter of the diamond cubic phase after refilling with water was found to be 63.9 Å, which is consistent with cubic lattice parameter reported for the cubic phase of the hydrated phytantriol at room temperature[5]. This finding confirms the hydration effect of the nickel deposition solution on phytantriol. Therefore, phytantriol could not be used as a template to deposit nanostructured nickel at room temperature using this nickel mixture.

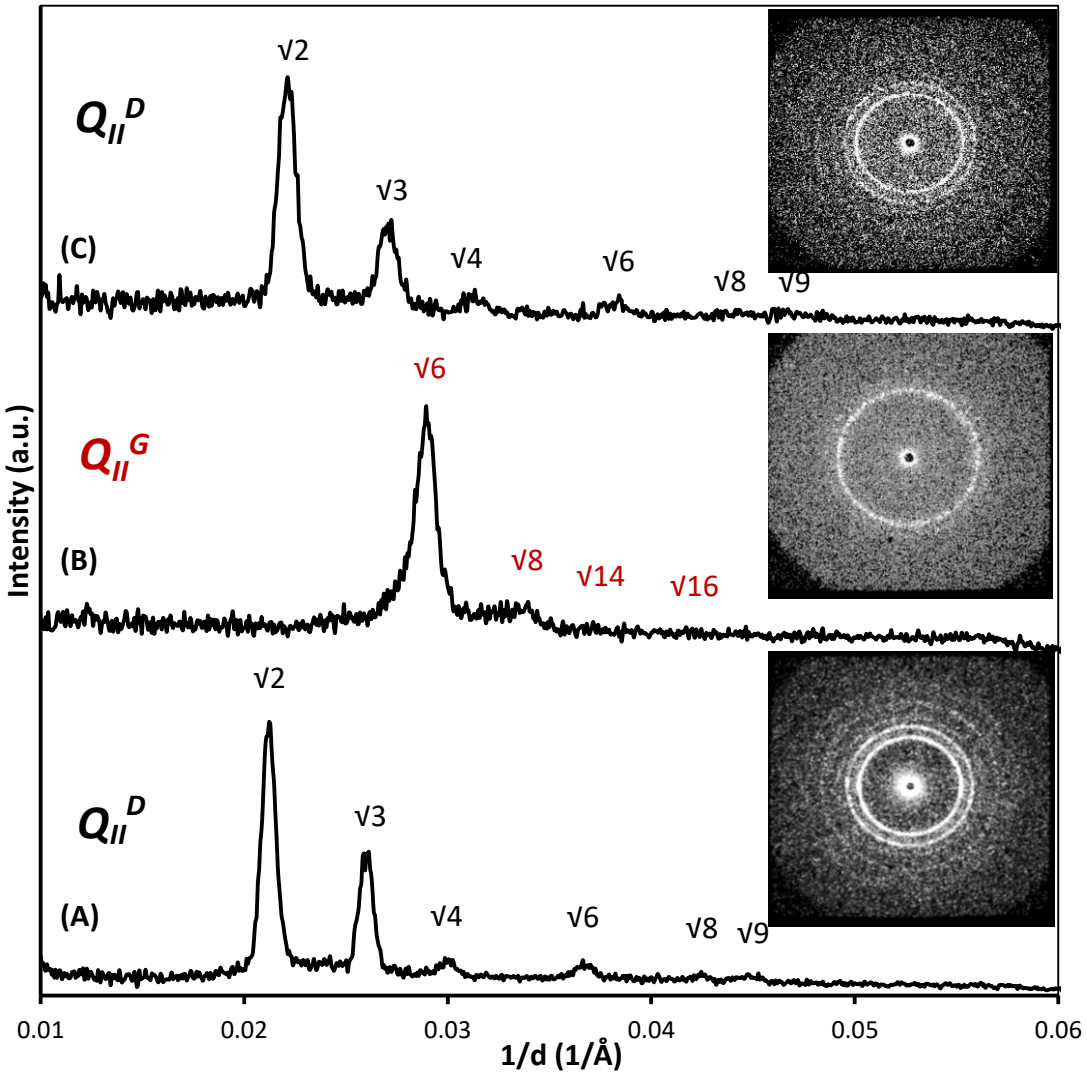


**Figure 3.2 1-D SAXS patterns for phytantriol at room temperature. A) in excess of water, B)** in excess of nickel deposition solution and **C)** in excess of water after washing the nickel deposition solution**.** Insets are the 2-D SAXS patterns corresponding to each 1-D pattern.

### 3.3.2 Optimisation of conditions used for electrochemical deposition of nickel through monoolein (Rylo)-based cubic phase

Preliminary experiments were carried out to find out the optimum conditions required for nickel electrodeposition including; the time dependency of cubic phase formation as well as the deposition potential. The details of these experiments are listed below.

#### 3.3.2.1 Time for cubic phase formation

The electrodeposition process involves soaking the monoolein coated electrodes in aqueous solution at room temperature. This allows the monoolein layer to spontaneously assemble into the cubic phase as described above. The stability of cubic phases at the electrode surface is dependent on soaking time in the aqueous solution as shown below.

Initially, gold DVD substrate (electrode) was dipped in monoolein ethanolic solution. Then the substrate was left in air for 30 min to dry and evaporate the ethanol. Then the monoolein-coated electrode was placed in water inside a ABS-polyimide water cell. Details of this cell are described in Section 2.4.5.2 in Chapter 2. The sample was analysed by synchrotron SAXS (I07 beamline). Scans were taken each minute. The results showed that the typical cubic phase of monoolein was successfully formed after soaking in water for a minimum of 10 min (Figure 3.3). This was indicated by the presence of the six Bragg peaks with the ratios of √2: √3: √4: √6: √8: √9, which are identical to the cubic lattice of *Pn*3*m* crystallographic space group ($Q_{II}^{D}$)[168] (Figure 3.1). The lattice parameter of this cubic phase was found to be 92.3 Å. At soaking times less than 10 min, the cubic phases were not completely assembled, this can be indicated by the big shift in the Bragg peaks at these times (Figure 3.3). Thus pre-coated monoolein electrode should be soaked in aqueous solution for at least 10 min prior to electrodeposition.

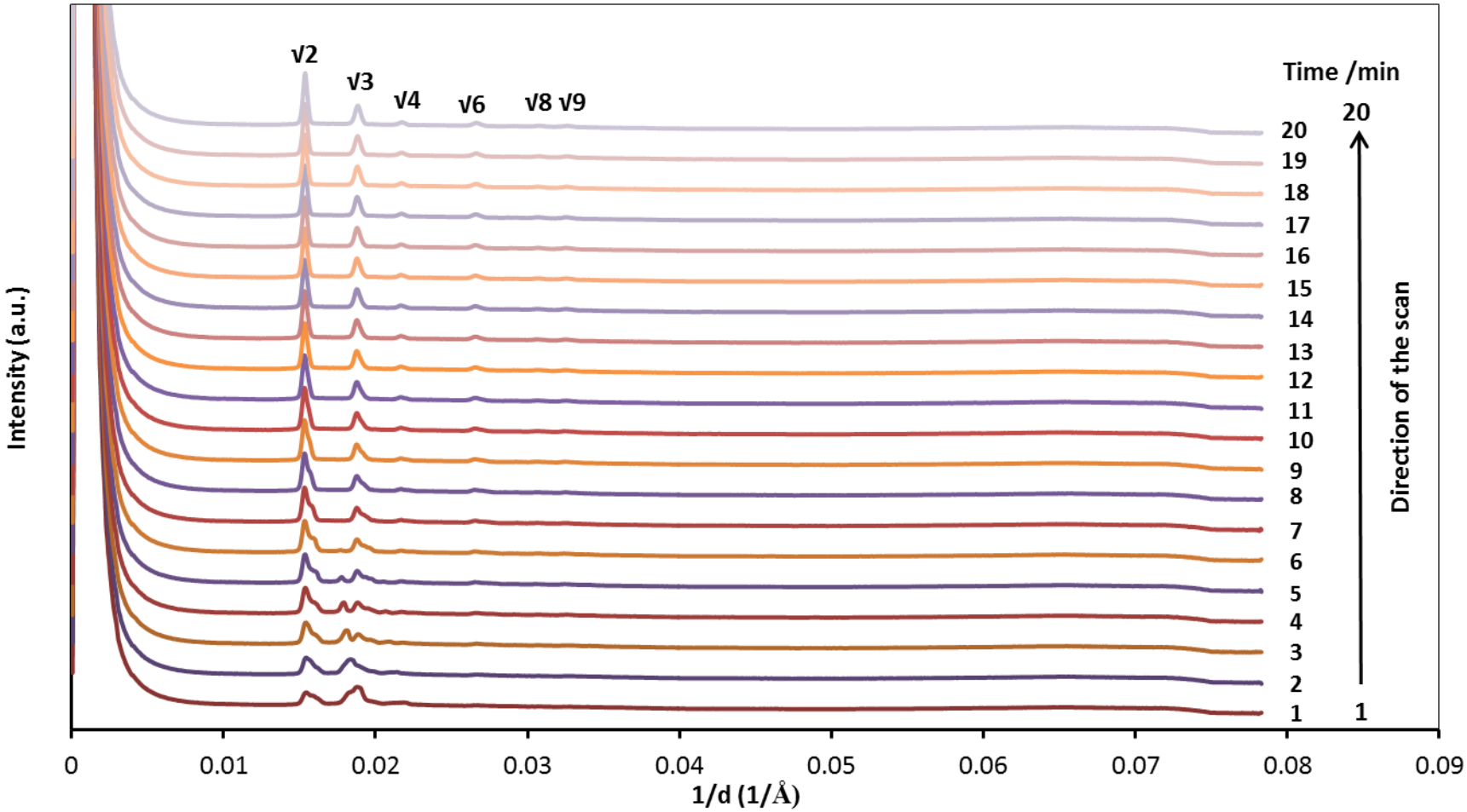


**Figure 3.3 Small angle X-ray scattering of monoolein in water before deposition.** 20 scans were taken (one every minute) for 20 min. The direction of the scan is indicated by an arrow.

### 3.3.2.2 Studying of the electro-reduction of nickel electrolyte

Cyclic voltammetry was used to study the electro-reduction of nickel solution at the surface of a gold electrode through the cubic phase. Initially, the gold electrode (area = $7.85 \times 10^{-3}$ $cm^2$) was soaked in nickel solution, then cyclic voltammetry was carried out at room temperature at potentials scanned between 0.4 V and -0.7 V vs. Ag/AgCl. The scan started at initial potential of -0.2 V vs Ag/AgCl. The recorded voltammogram showed the presence of one peak at -0.5 V in the cathodic region (Figure 3.4).

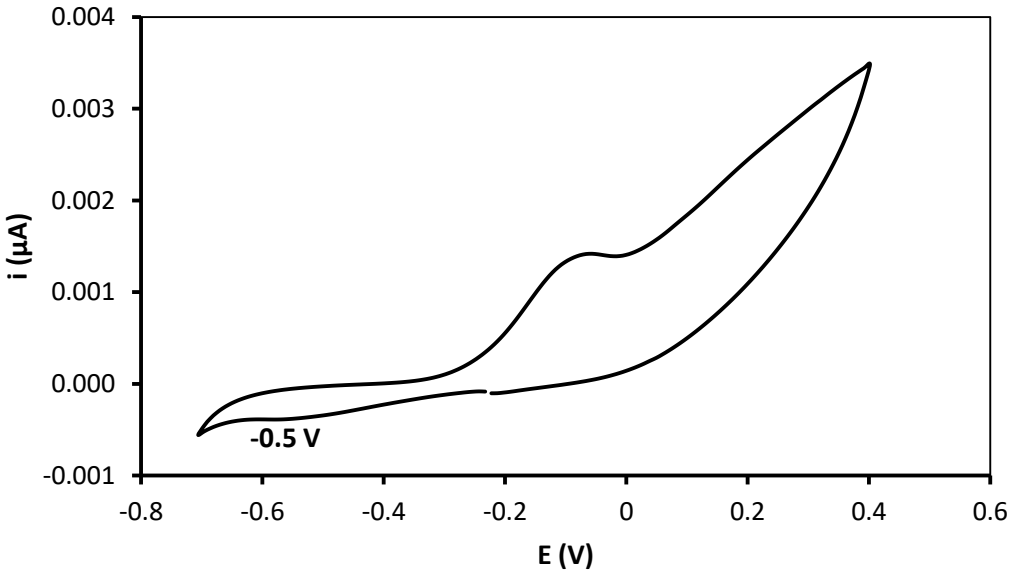


**Figure 3.4 Cyclic voltammogram of monoolein coated-gold electrode in nickel solution.** The cyclic voltammetry was carried out at potentials scanned between 0.4 V and -0.7 V vs. Ag/AgCl at room temperature.

Electrodeposition of nickel through the cubic phase of monoolein was carried out at -0.5 V vs. Ag/AgCl for different times (10, 60 and 120 min) on gold foil electrodes. The typical transients of the depositions are shown in Figure 3.5.

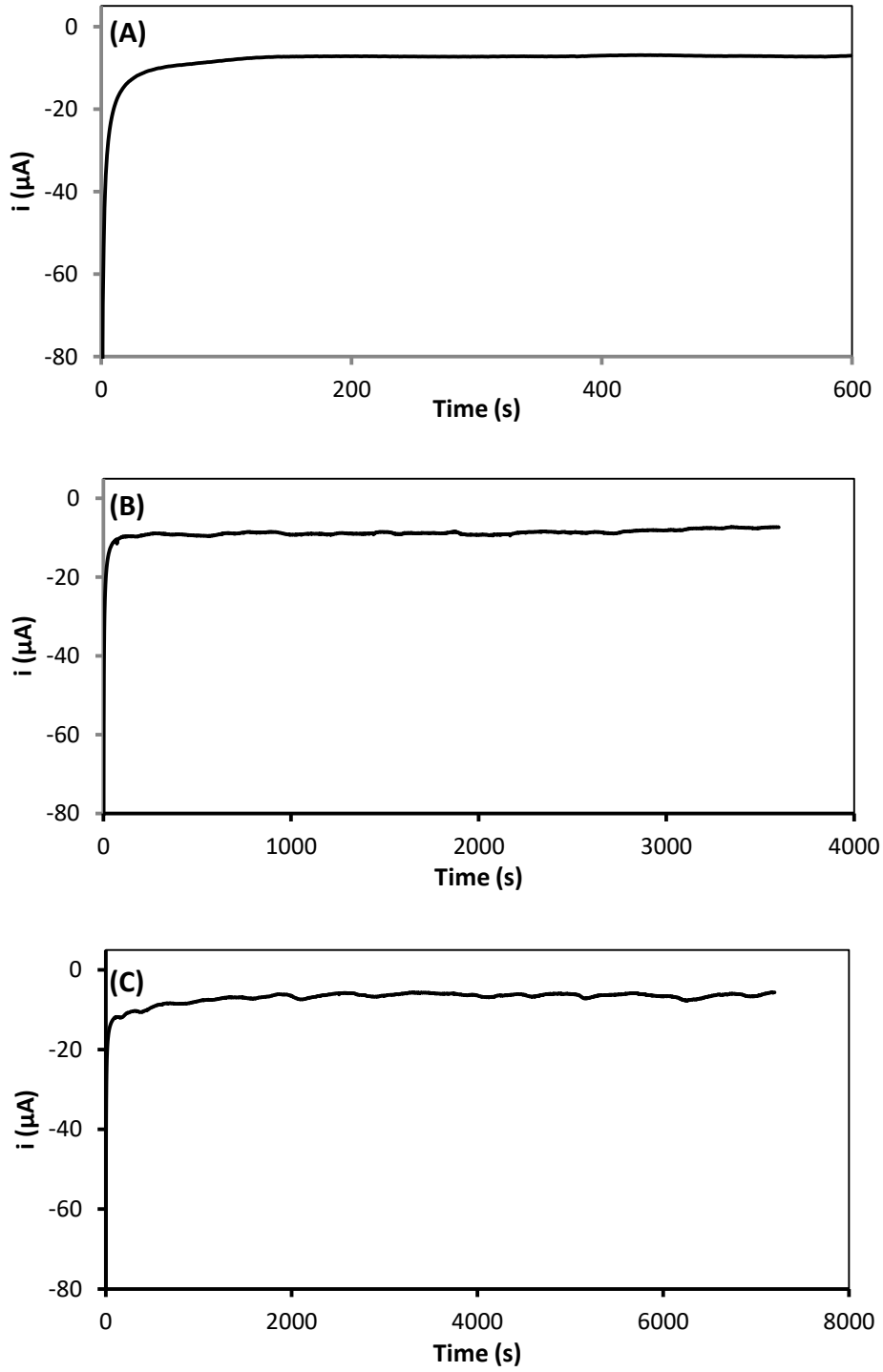


**Figure 3.5 Typical transients of nickel deposition at -0.5 V for different times: (A)** 10 min, **(B)** 60 min and **(C)** 120 min. Nickel deposition was carried out at room temperature on gold foil electrodes (area = 0.29 $cm^2$).

In order to confirm the deposition of nickel at -0.5 V, electrodeposition of nickel was carried out at -0.5 V at room temperature on a gold DVD electrode (area = 1.08 $cm^2$). Then XRD

analysis was conducted for the deposited nickel films. For composition, XRD analysis was conducted for the blank DVD electrode with the same area. The XRD patterns are shown in Figure 3.6. The patterns of the deposited nickel films at -0.5 V revealed the presence of three peaks at (2θ = 38 °, 44.9 ° and 52.3 °). The peak at (2θ = 38 °) is corresponding to Au as indicated from the XRD of the blank electrode. However the other two peaks corresponding to nickel[172]. The peaks at 2θ = 44.9 ° and 52.3 ° have been reported for nickel in many previous studies (Table 3.1). These results confirmed the deposition of nickel at potential of -0.5 V.

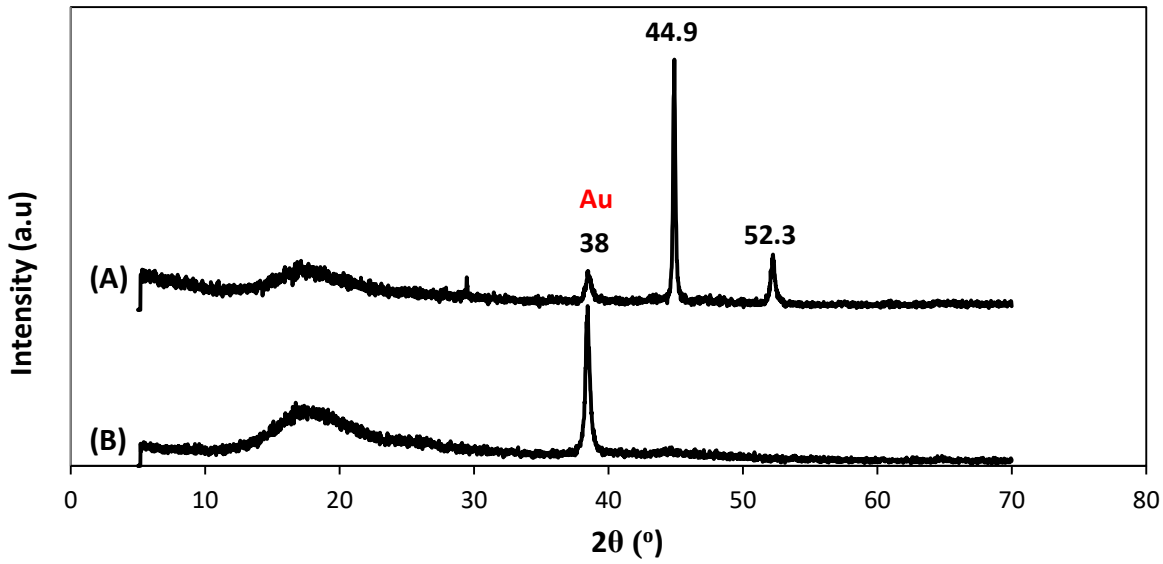


**Figure 3.6 XRD patterns recorded for: (A)** deposited nickel films at -0.5 V and **(B)** blank gold DVD electrode (area = 1.08 $cm^2$). Deposition of nickel was carried out at room temperature for 10 min**.** The positions of the peaks are indicated on the chart.

**Table 3.1** Theta values of x-ray diffraction of deposited nickel

| **Deposited nickel at 2θ (°)** | **References** |
|---|---|
| **44.9, 52.5** | This study |
| **45, 52.5** | Smirnov et al.[172] |
| **44, 51.5** | Sapkal et al.[173] |
| **44** | Xiangcheng Sun et al.[174] |

SAXS analysis was used to reveal the structure of the nickel films deposited at -0.5 V for different times. The SAXS patterns are shown in Figure 3.7.

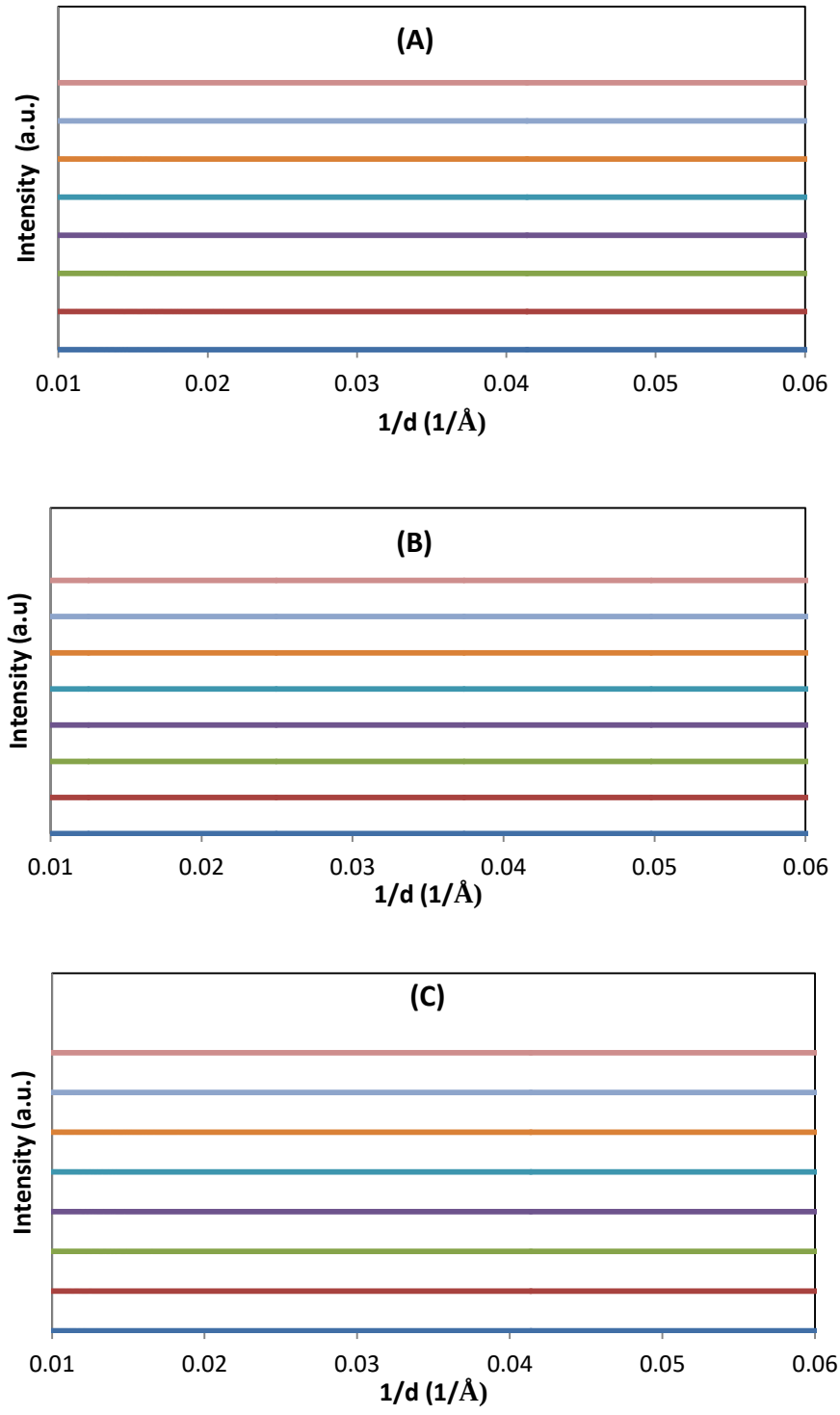


**Figure 3.7 SAXS patterns recorded for deposited nickel films at -0.5 V for different times: (A)** 10 min, Q = 0.01 C $cm^{-2}$, **(B)** 60 min, Q = 0.06 C $cm^{-2}$ and **(C)** 120 min, Q = 0.3 C $cm^{-2}$. Deposition was carried out at -0.5 V vs. Ag/AgCl at room temperature on gold DVD electrode (area = 1.08 $cm^2$). Measurements were conducted at 8 different positions of the deposited films.

The SAXS patterns of the deposited nickel films at -0.5 V did not show any structural peaks, confirming the absence of the nanostructure at this potential.

For further investigations, the electrodeposition of nickel through the cubic phase of monoolein was carried out at selected potentials ranging from -0.75 to -1.0 V vs. Ag/AgCl. The typical transients recorded for the deposited nickel films at different potentials are shown in Figure 3.8. The shape of the transients varied depending on the potential, indicating different nucleation and growth pattern. However, a massive increase in the current amplitude was recorded at potential of -1.0 V, possibly due to the presence of unwanted side reactions[175].

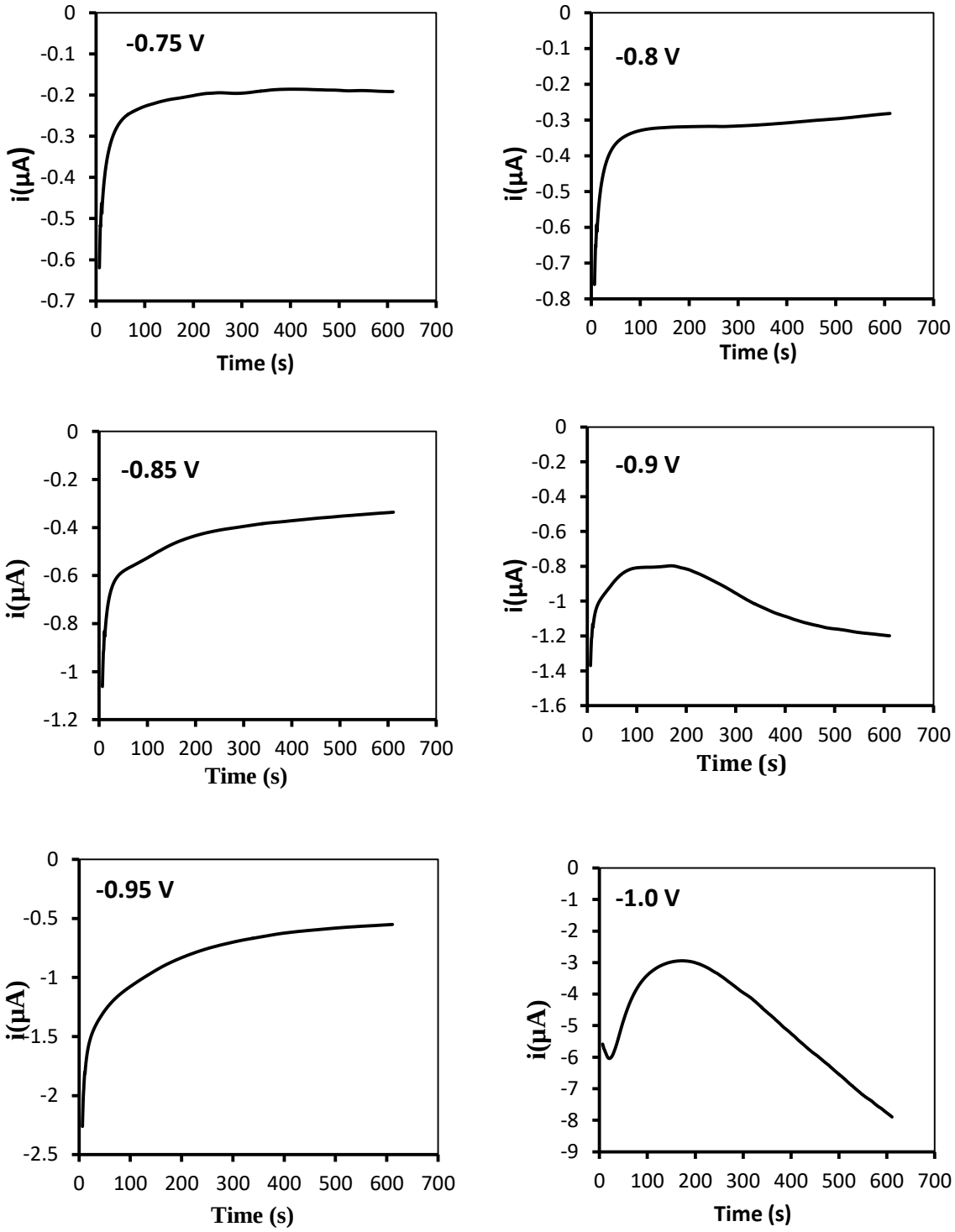


**Figure 3.8 Typical electrodeposition transients recorded at different potentials. (-0.75 to -1.0 V) vs. Ag/AgCl.** Nickel deposition was carried out at room temperature on gold wire electrodes (area = $1.96 \times 10^{-3}$ $cm^2$) for a constant time of 10 min for charge densities of Q = 0.06 $C/cm^2$ with -0.75 V, Q = 0.1 $C/cm^2$ with -0.8 V, Q = 0.13 $C/cm^2$ with -0.85 V, Q = 0.3 $C/cm^2$ with -0.9 V, Q = 0.25 $C/cm^2$ with -0.95 V and Q = 1.5 $C/cm^2$ with -1.0 V.

In order to calculate the roughness factor (Rf) and the specific surface area of the deposited nickel films at different potentials, cyclic voltammetry was conducted for each deposition. Cyclic voltammograms of the deposited nickel films at different potentials are shown in Figure 3.9.

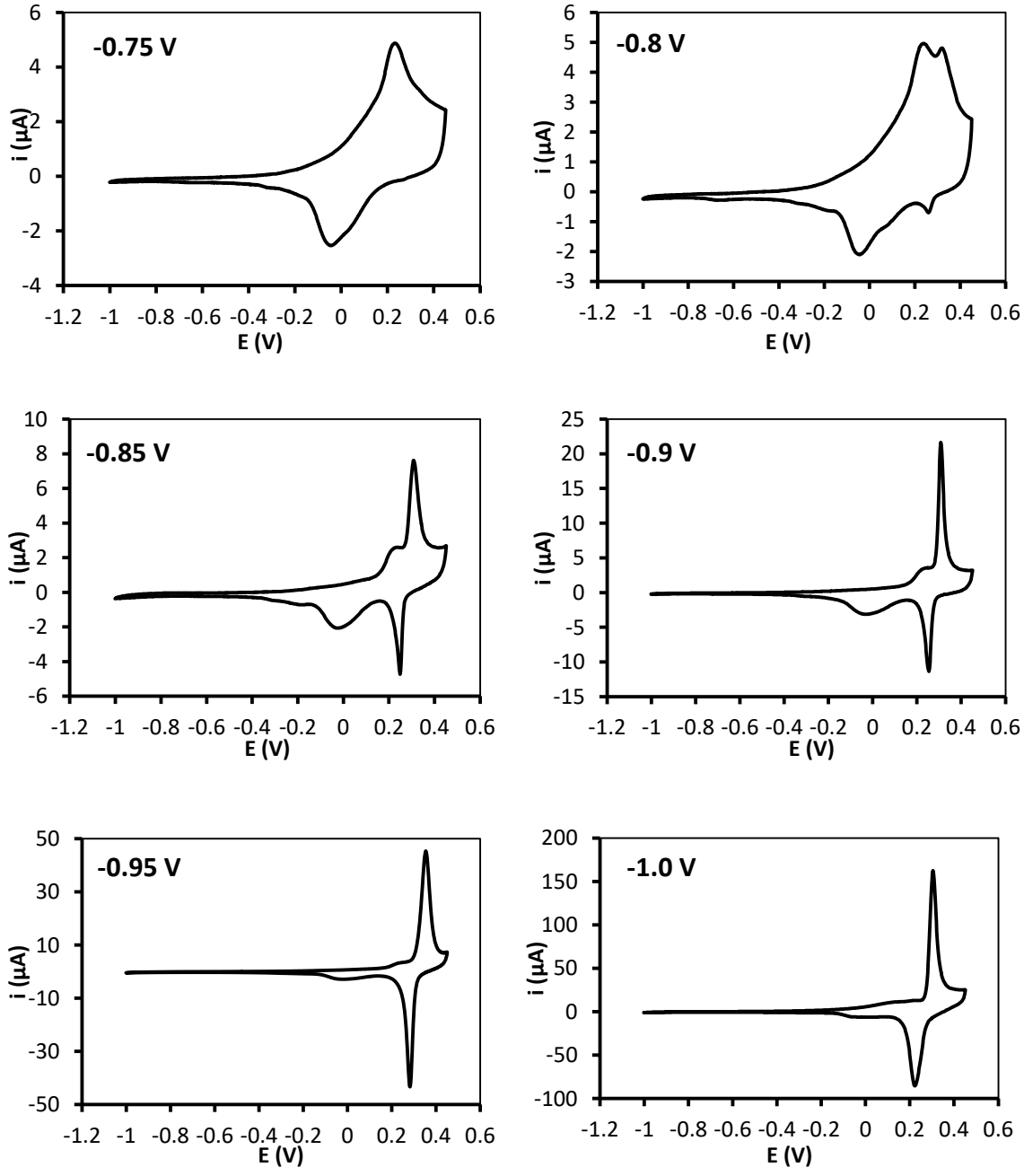


**Figure 3.9 Cyclic voltammograms of nickel films deposited at different potentials.** Deposition of nickel films were carried out at room temperature on gold wire electrodes ($1.96 \times 10^{-3}$ $cm^2$) for 10 min for variable deposition potentials from -0.75 V to -1.0 V.

The shape of the cyclic voltammograms varied with the deposition potential. This could be due to different growth of nickel at each potential. The cyclic voltammograms of the films deposited at potentials from -0.8 to -1.0 V showed anodic and cathodic peaks between 0.1 and 0.4 V vs Ag/AgCl which are attributed to the formation and subsequent reduction of a few monolayers of Ni(OOH)[176,55]. However, the films at -0.95 V and at -1.0 V showed large anodic peaks at 0.3 V and 0.35 V, respectively and large cathodic peaks at 0.28 V and 0.21 V, respectively.

In order to quantify the electroactive surface area of deposited nickel films, the roughness factor (Rf) of the electrode was calculated. The Rf was determined using the charge associated with the anodic peak divided by the electrode area[52] (details of the calculations are described in Chapter 2, Section 2.4.1). The values of Rf and the specific surface area of the electrode varied depending on the deposition potential. The variation of electrode surface area and Rf with respect to deposition potential is shown in Table 3.2.

**Table 3.2** Rf and specific surface area as functions of deposition potential

| **Deposition potential (V)** | **Charge density $C/cm^2$** | **Roughness factors (Rf)** | **Specific surface area ($m^2/g$)** |
|---|---|---|---|
| **-0.75** | 0.07 ± 0.01 (n=3) | 1.20 ± 0.20 (n=3) | 1.36 ± 0.22 (n=3) |
| **-0.8** | 0.11 ± 0.01 (n=3) | 2.25 ± 0.88 (n=3) | 3.15 ± 0.99 (n=3) |
| **-0.85** | 0.12 ± 0.02 (n=4) | 2.55 ± 0.36 (n=4) | 6.79 ± 0.37 (n=4) |
| **-0.9** | 0.3 ± 0.02 (n=3) | 7.57 ± 2.17 (n=3) | 8.29 ± 2.74 (n=3) |
| **-0.95** | 0.26 ± 0.02 (n=3) | 11.42 ± 2.02 (n=3) | 14.19 ± 2.84 (n=3) |
| **-1** | 3.06 ± 2.20 (n=3) | 30.68 ± 13.3 (n=3) | 4.19 ± 4.82 (n=3) |

n = number of replicates

The analysis showed an increase in the values of the roughness factor with the reduction in the deposition potential. This result is in agreement with the literature[175]. High values of roughness factor were obtained at potentials of -0.9, -0.95 and -1.0 V, however low values of roughness factor were obtained with the less negative potentials (Table 3.2).

The specific surface area of the electrode was calculated with each deposition using the electrochemical surface area of the electrode, divided by the weight of the deposited material (as described in Chapter 2, Section 2.4.1). High surface areas were recorded at potentials of -0.85, -0.9 and -0.95 V with the highest surface area at -0.95 V (Figure 3.10 and Table 3.2).

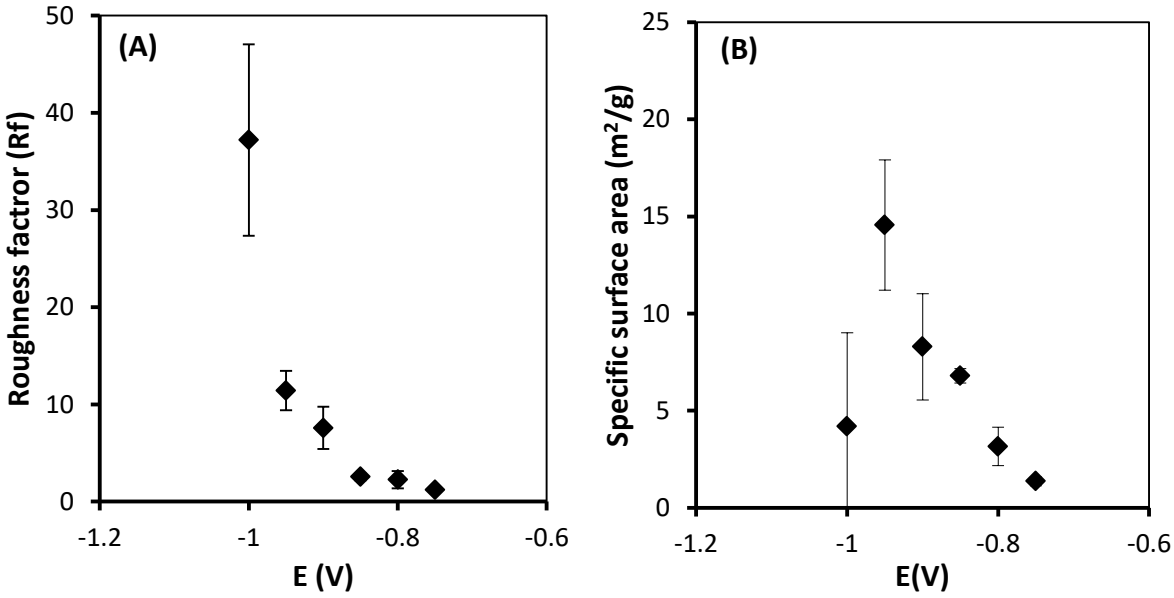


**Figure 3.10 Variation of roughness factor (A) and specific surface area (B) of electrodeposited Ni films as functions of deposition potential.** Deposition of Ni was conducted at room temperature on gold electrodes (area = $1.96 \times 10^{-3}$ $cm^2$) for 10 min. The values represent the mean +/- SD of 3-4 independent experiments.

For further investigations, SAXS analysis was used to reveal the structure differences for some of the nickel films deposited at different potentials. The SAXS patterns are shown in Figure 3.11. The SAXS patterns recorded for $Q_{II}^{D}$-*e*Ni films deposited at potentials of -0.9 V

and at -0.85 V showed the absence of any structural features. Also low Rf values were observed for the nickel films deposited at these potentials (Table 3.2), suggesting deposition of Ni with the absence of the nanostructure at these potentials. However, SAXS patterns recorded for $Q_{II}^{D}$-eNi films deposited at -0.95 V showed small Bragg peaks (Figure 3.11). A high Rf value was also observed for the films deposited at this potential, indicating the presence of a nanostructure. The SAXS patterns of the nanostructured nickel film deposited at -0.95 V is discussed in more detail in Section 3.3.5.1.

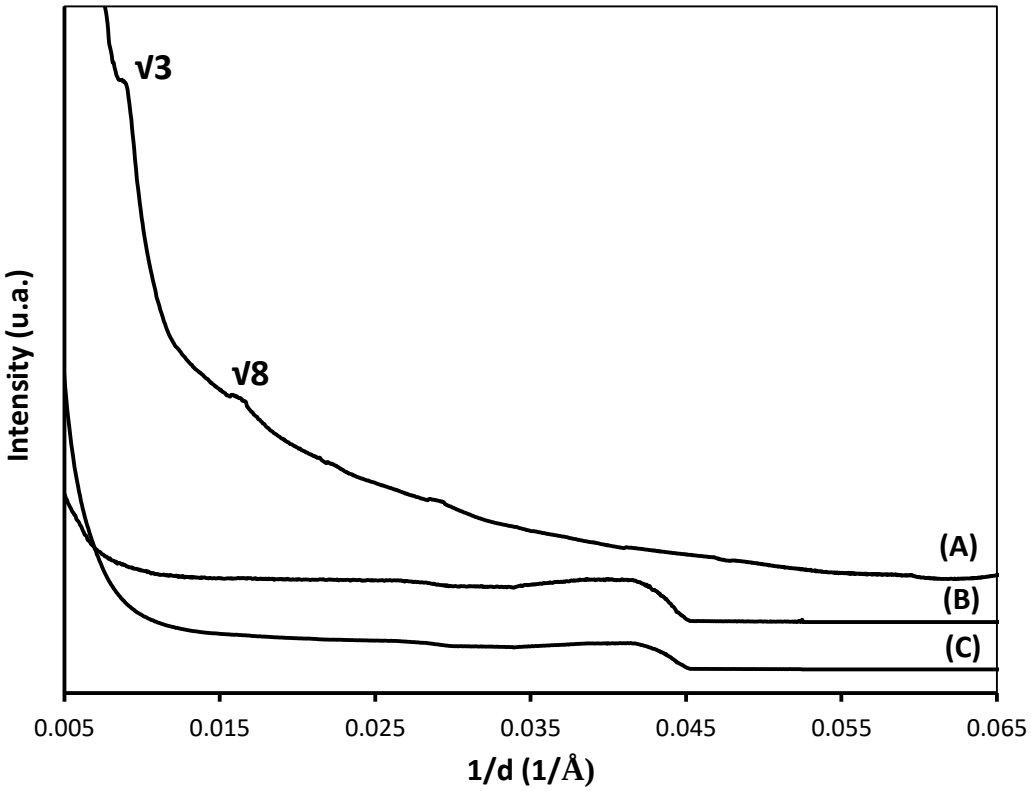


**Figure 3.11 SAXS patterns recorded for deposited $Q_{II}^{D}$-eNi films at different potentials. (A)** -0.95 V, Q = 0.24 cm$^{-2}$, **(B)** -0.9 V, Q = 6.7 C cm$^{-2}$ and **(C)** -0.85 V, Q = 6.4 C cm$^{-2}$, vs. Ag/AgCl at room temperature on gold glass substrates (area= ~ 0.24 cm$^{2}$).

From all the investigations above, it can be concluded that potential of -0.95 V was the best potential for fabrication of nanostructure nickel. Therefore, this potential was used for electrodeposition of nickel in all subsequent experiments.

### 3.3.3 Electrochemical deposition of nanostructured nickel at -0.95 V

As revealed from the above experiments, potential of -0.95 V vs. Ag/AgCl was the optimum potential for electrodeposition of nanostructured nickel (Section 3.3.2.2), while the best soaking time required for monoolein-coated electrodes in the aqueous solution prior to electrodeposition was found to be not less than 10 min (Section 3.3.2.1).

Potentiostatic controlled deposition of nickel through the cubic phase at gold electrodes was conducted at a deposition potential of -0.95 V vs Ag/AgCl. As a control experiment, the deposition was performed directly from nickel solution in the absence of the monoolein template. The typical transients of both depositions are shown in Figure 3.12.

The calculated charge density of the deposited nickel varied in each deposition, although the deposition time was kept constant in both depositions. In the absence of template, the charge density (15.73 C/cm$^2$) was higher than in the presence of the template (0.24 C/cm$^2$). This can be attributed to the rate of nickel deposition. In the presence of the template, the deposition takes place only through the aqueous channels of the cubic phase, while, in the absence of the cubic phase the whole electrode area is available. This leads to fast diffusion of the electrolyte which results in higher deposition rates of nickel.

A higher initial current was observed in the transient recorded for the deposition of nickel through the cubic phase. This can be due to the mass transport which controls the primary nucleation process on the electrode surface[177,178]. However, no characteristic features for primary nucleation was observed in the transient recorded for nickel deposition in the absence of the template.

In both depositions, there was an initial increase in the current, followed by almost stable current. This could be attributed to a secondary nucleation process of nickel[179] . However, the current flow was >50X higher for the nickel deposition through the cubic phase.

Furthermore, in both depositions, the color of the gold electrode surface was changed after the deposition process. In the presence of the template, the color of the electrode surface changed from golden to greyish-black, when removed from the electrochemical cell. However, in the absence of the template the electrode turned silver in color.

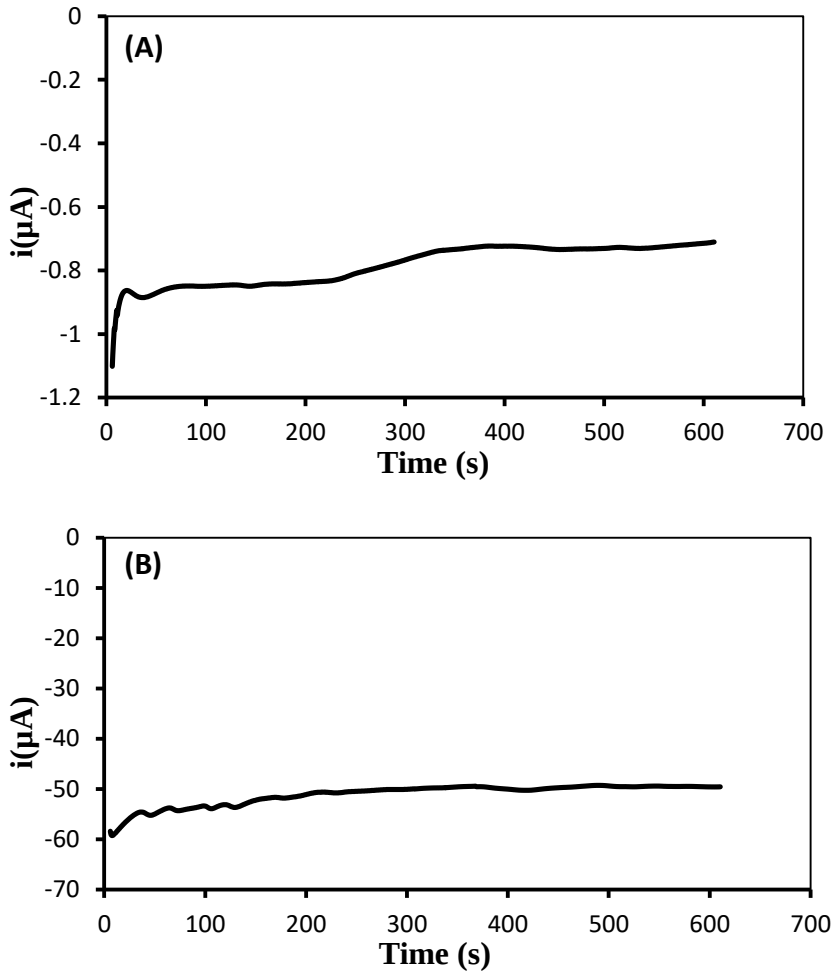


**Figure 3.12 Typical electrodeposition transients of deposited nickel from nickel mixture solution. (A**) with cubic phase template, and **(B)** without template. Deposition was performed at gold wire electrode (area = $1.96 \times 10^{-3}$ $cm^2$) at room temperature; deposition potential was -0.95 V vs. Ag/AgCl.

### 3.3.4 Stability of cubic phase after deposition

SAXS was used to assess the stability of cubic phase after deposition. Nickel films were deposited on a gold DVD substrate (area = 1 $cm^2$) coated with monoolein. SAXS analysis was conducted using a novel designed cell called Nassar 14. The fabrication steps of this cell are shown in Section 2.4.5.2 in Chapter 2. After deposition and before dissolving the template with ethanol, the substrate was placed in the designed cell and characterised using Bruker Nanostar AXS instrument. The SAXS pattern is shown in Figure 3.13.

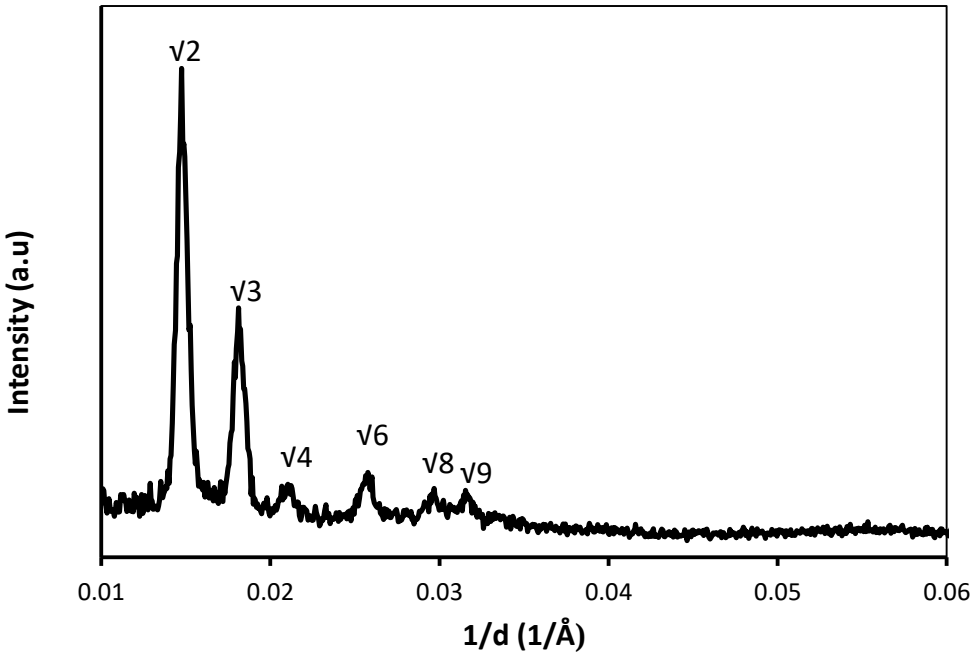


**Figure 3.13 Small angle X-ray scattering pattern for cubic phase of monoolein after deposition.** The analysis was performed under vacuum at room temperature.

The SAXS pattern of the cubic phase showed the presence of six strong Bragg peaks that follow the ratios √2: √3: √4: √6: √8: √9, which agrees with a diamond cubic lattice of *Pn*3*m* crystallographic space group ($Q_{II}^{D}$)[168] (Figure 3.13). The calculated lattice parameter of the phase was 95 Å. This pattern is the same as that obtained with monoolein before deposition (in the absence of the substrate) (Figure 3.1). These results confirm the stability of the diamond bicontinuous cubic phase of monoolein after electrodeposition.

### 3.3.5 Structural characterisation of nanostructured nickel

#### 3.3.5.1 Small angle X-ray scattering (SAXS)

Nickel was deposited from nickel solution on a glass gold substrate (area = 0.24 $cm^2$) through a monoolein cubic phase at a potential of -0.95 V vs. Ag/AgCl. The electrodeposition was carried out at room temperature using a potentiostatic controller. After deposition the electrode was washed in ethanol in order to dissolve the template. Then the structure of deposited nickel films was characterised using synchrotron SAXS as shown in Figure 3.14.

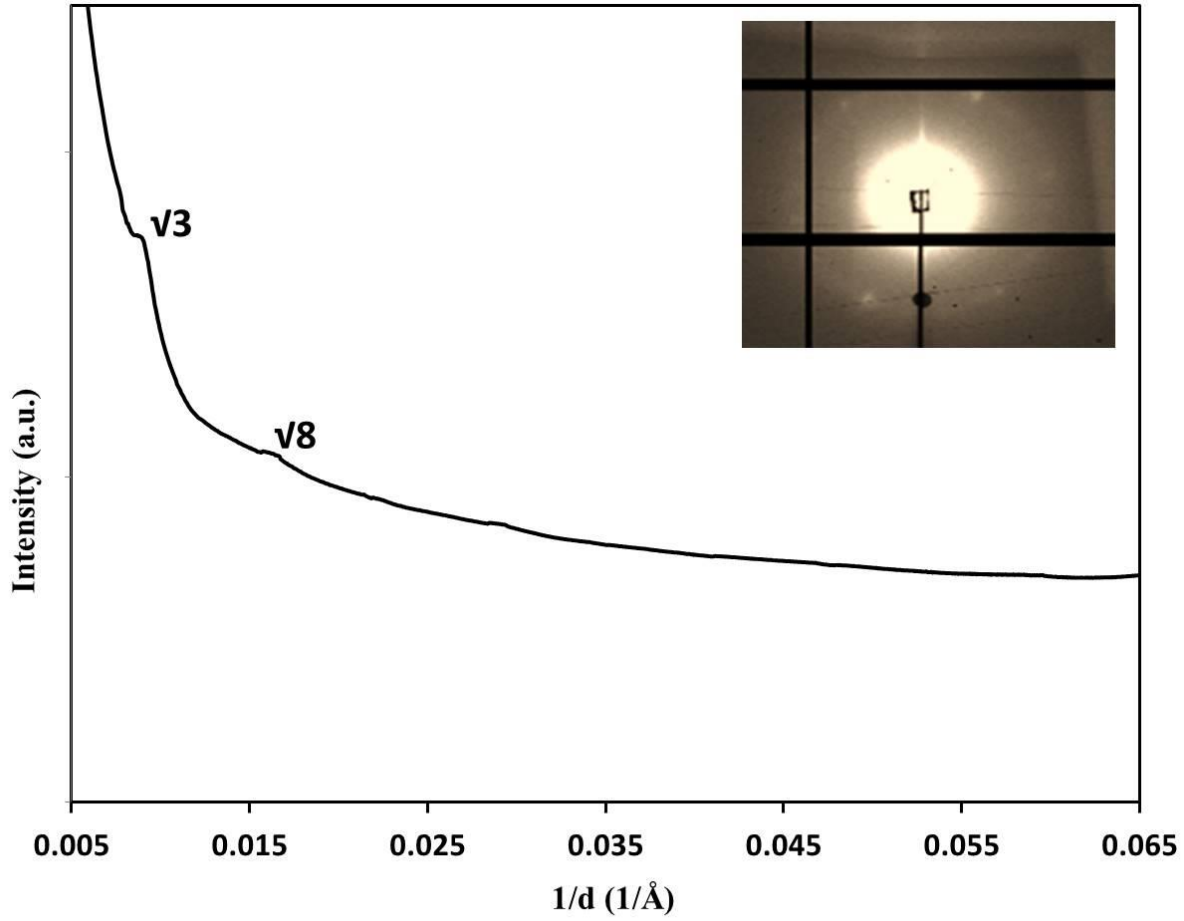


**Figure 3.14 1-D SAXS pattern for the $Q_{II}^{D}$-Ni film deposited on a glass gold electrode (area = 0.24 $cm^2$).** The deposition potential was -0.95 V vs. Ag/AgCl at room temperature. The electrode background was subtracted from the data. Inset is the 2-D SAXS pattern of $Q_{II}^{D}$-Ni film.

The 2-D SAXS pattern of the deposited nickel film showed a ring, indicating the presence of nanostructure nickel. The 1-D SAXS pattern of the nanostructured nickel showed two Bragg peaks with relative positions for 1/d in the ratio of √3:√8. These two peaks were not matching with the $Q_{224}$ space group, or with any of the other bicontinuous cubic structures formed by lyotropic liquid crystals. However, these two peaks match with the first two reflections of the structure (*Fd3m*) of $Q_{227}$ space group but with lattice parameter of 175 ± 2.5 Å[180]. This result suggests that a single diamond structure is produced with a lattice parameter twice as large as that of the expected double diamond structure (87.5 Å (175/2). In other words, it is likely that the symmetry of the double diamond structure is removed, resulting in unequal sides of the bilayer (or the two water channels). The possible explanation of this unexpected structure is due to asymmetric templating of the $Q_{224}$ phase, leading to electrodeposition of nickel in one of the two water channels, resulting in "single diamond" nickel nanostructure (Figure 3.15). This has been reported with bicontinuous cubic platinum nanowire networks templated from a phytantriol $Q_{II}^{D}$ phase[41]. Our novel structure is named "$Q_{II}^{D}$ e-Ni".

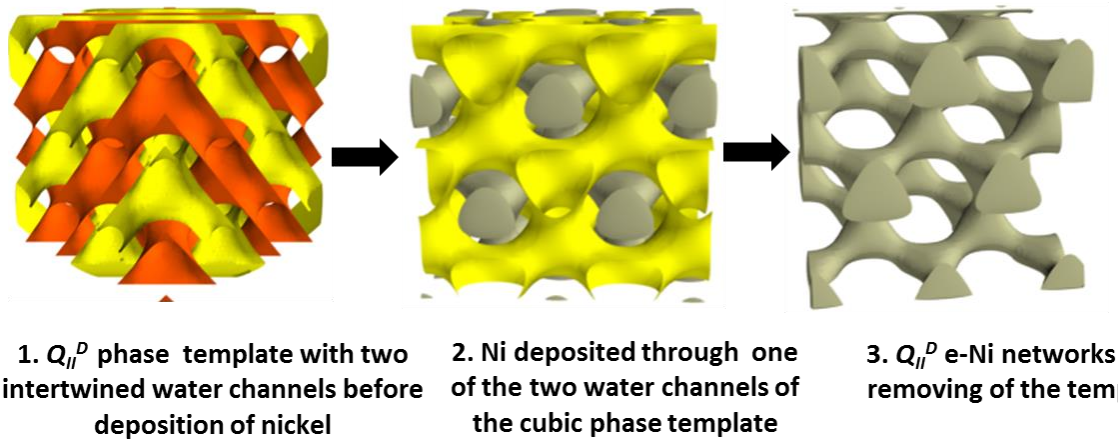


**Figure 3.15 A schematic illustration showing the mechanism of Ni deposition through monoolein $Q_{II}^{D}$ phase.** The figures were designed using Enthought Canopy Python software.

### 3.3.5.2 X-ray diffraction analysis of the deposited nickel films

Powder XRD was carried out in order to confirm the presence of nickel in the deposited films. Nickel deposition was carried out at room temperature on the surface of gold DVD electrode (area = 1.3 $cm^2$) through the monoolein cubic phase. After deposition, the electrode was washed thoroughly with ethanol in order to remove the monoolein template. For comparison nickel was also deposited on gold DVD electrode (area = 1.3 $cm^2$) in the absence of the cubic phase. XRD analysis was conducted for the deposited nickel films. As a negative control, XRD has been conducted for a blank gold DVD electrode (area = 1.3 $cm^2$). The XRD analysis was performed using D8 ADVANCE X-ray diffractometer (Bruker, Germany). XRD analysis confirmed that the deposited material in both depositions is metallic nickel. XRD pattern of the blank DVD electrode showed the presence of only one peak at ($2\theta = 38.44^{o}$), which is corresponding to Au (Figure 3.16). However, beside the Au peak at ($2\theta = 38.44^{o}$), two strong peaks at ($2\theta = 44.9^{o}$, $52.3^{o}$) were observed with the deposited nickel films (Figure 3.16). These peaks are attributed to nickel as indicated above in Section 3.3.2.2.

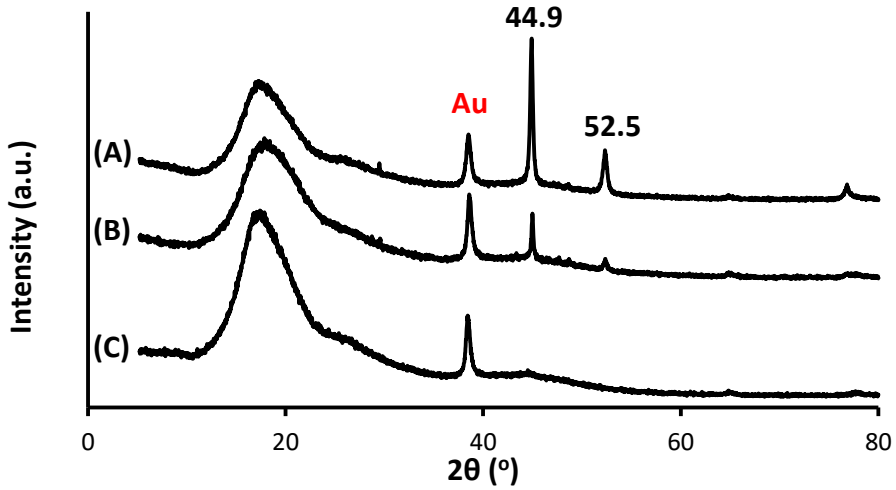


**Figure 3.16 XRD analysis of the deposited nickel films. A)** on gold DVD substrate in the absence of cubic phase **(B)** on gold DVD substrate in the presence of cubic phase and (**C)** blank gold DVD substrate. The deposition was carried out on gold DVD substrate (area = 1.3 $cm^2$) for 10 min at room temperature; deposition potential was adjusted at -0.95 V vs. Ag/AgCl.

## 3.3.6 Electrochemical characterisation of nanostructured nickel films

### 3.3.6.1 Voltammetric behaviour of nickel film in KOH

In order to investigate the electrochemical behaviour of nanostructured nickel, nickel was deposited on the surface of a gold wire electrode (area = $1.96 \times 10^{-3}$ $cm^2$) at room temperature through the monoolein cubic phase. Then the deposited films were washed thoroughly with ethanol and water to remove the monoolein template. For comparison, nickel was deposited at room temperature on gold wire electrode of the same area ($1.96 \times 10^{-3}$ $cm^2$) in the absence of the monoolein cubic phase template. The electrodes with both depositions were then analysed by cyclic voltammetry in 3 M KOH aqueous solution. Cyclic voltammetry was also conducted for the blank gold electrode as negative control.

Besides using cyclic voltammetry to determine the electroactive surface area, it can be also used to clean the electrode surface. During the cyclic voltammetry, the progressive formation and removal of oxide/hydride layers can clean any impurities on the electrode surface. Therefore, extensive cleaning of the electrode surface is not required prior to cyclic voltammetry. A few cycles of cyclic voltammetry recorded for deposited nickel in KOH are presented in Figure 3.17.

The cyclic voltammograms of both nickel depositions showed the presence of anodic and cathodic peaks between -0.28 and 0.4 V vs Ag/AgCl (Figure 3.17B). These findings are typical of those found in the literature and attributed to nickel[130,176,55]. The peaks obtained with the deposited nickel films are also different from those obtained with a gold electrode before deposition (Figure 3.17A). This is indicates the depositition of nickel on the gold electrodes.

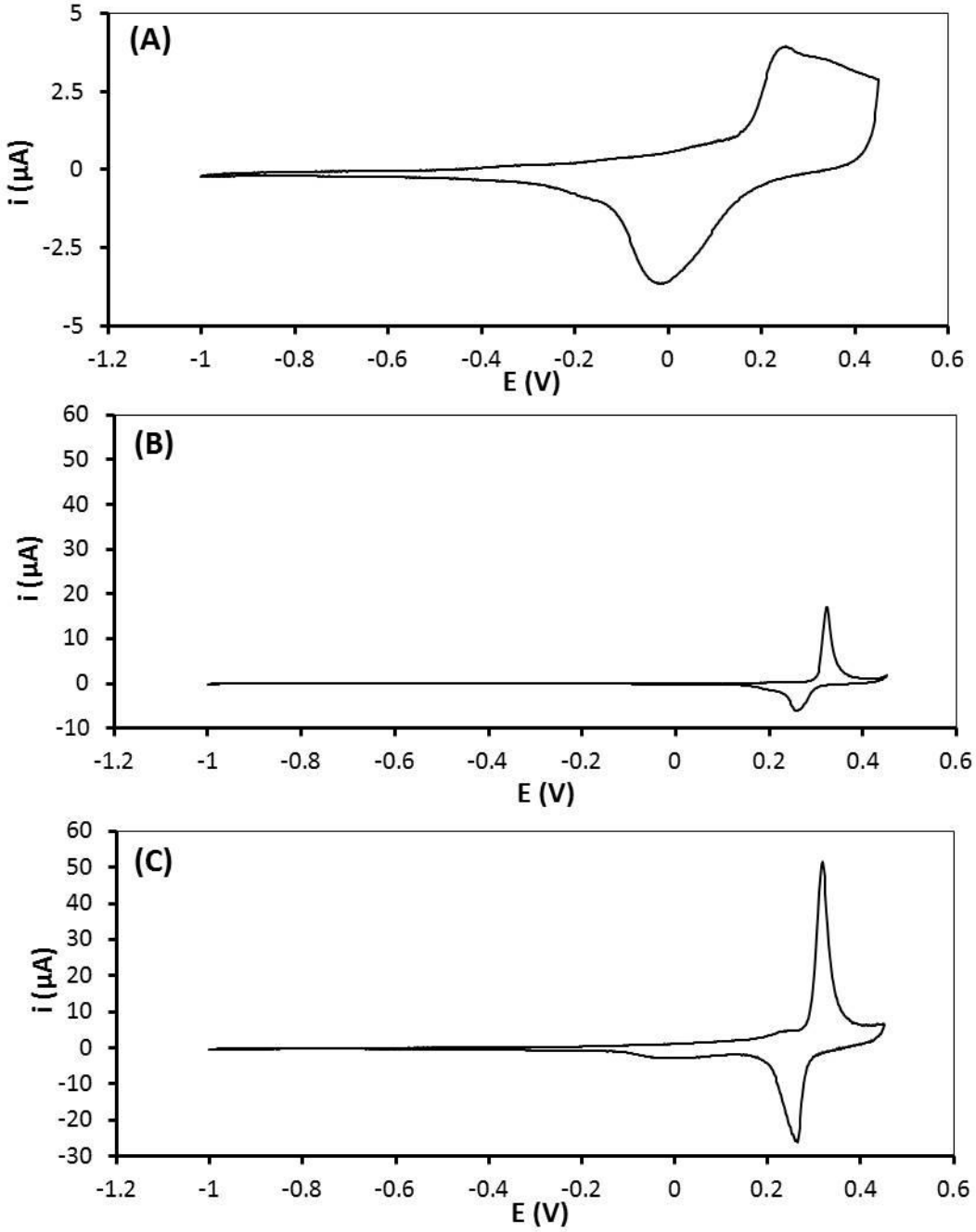


**Figure 3.17 Cyclic voltammetry in 3 M KOH of (A)** gold wire electrode before deposition of nickel (**B)** Ni film in the absence of the monoolein template, Q = 15.73 C/m$^2$ and **(C)** nanostructured Ni film, Q = 0.25 C/m$^2$. Depositions were carried out on gold wire electrodes ($1.96 \times 10^{-3}$ cm$^2$) at room temperature for 10 min. The deposition potential was -0.95 V vs. Ag/AgCl.

However, there was a big different in the charge density associated with each deposition. The charge density was higher in the absence of template (15.73 C/cm$^2$) than that in the presence

of template (0.25 C/cm$^2$). Also, the cyclic voltammogram of the nickel film deposited in the presence of the template showed a very large anodic peak at 0.3 V compared to that observed with the film deposited in the absence of the template.

Interestingly, it was found that the electrochemical surface area of the nickel film deposited in the presence of the template was ~266 fold higher than that deposited in the absence of the template, giving areas of $2.06 \times 10^{-2}$ cm$^2$ and, $4.86 \times 10^{-3}$ cm$^2$, respectively. These results indicate the deposition of nanostructured nickel with a high surface area.

### 3.3.6.2 Scan rate dependence of deposited nickel film in diluted aqueous KOH

Figure 3.18 shows cyclic voltammograms for deposited Ni film recorded at different scan rates ranging from 0.1 to 1.0 V/s. All the recorded voltammograms exhibited the same shape. But it is apparent that the anodic and cathodic peaks increased with increasing scan rate. The intensity of oxidation peaks (inset A Figure 3.18) and reduction peaks (inset B Figure 3.18) increased almost linearly with the scan rate, indicating a surface controlled reaction[181].

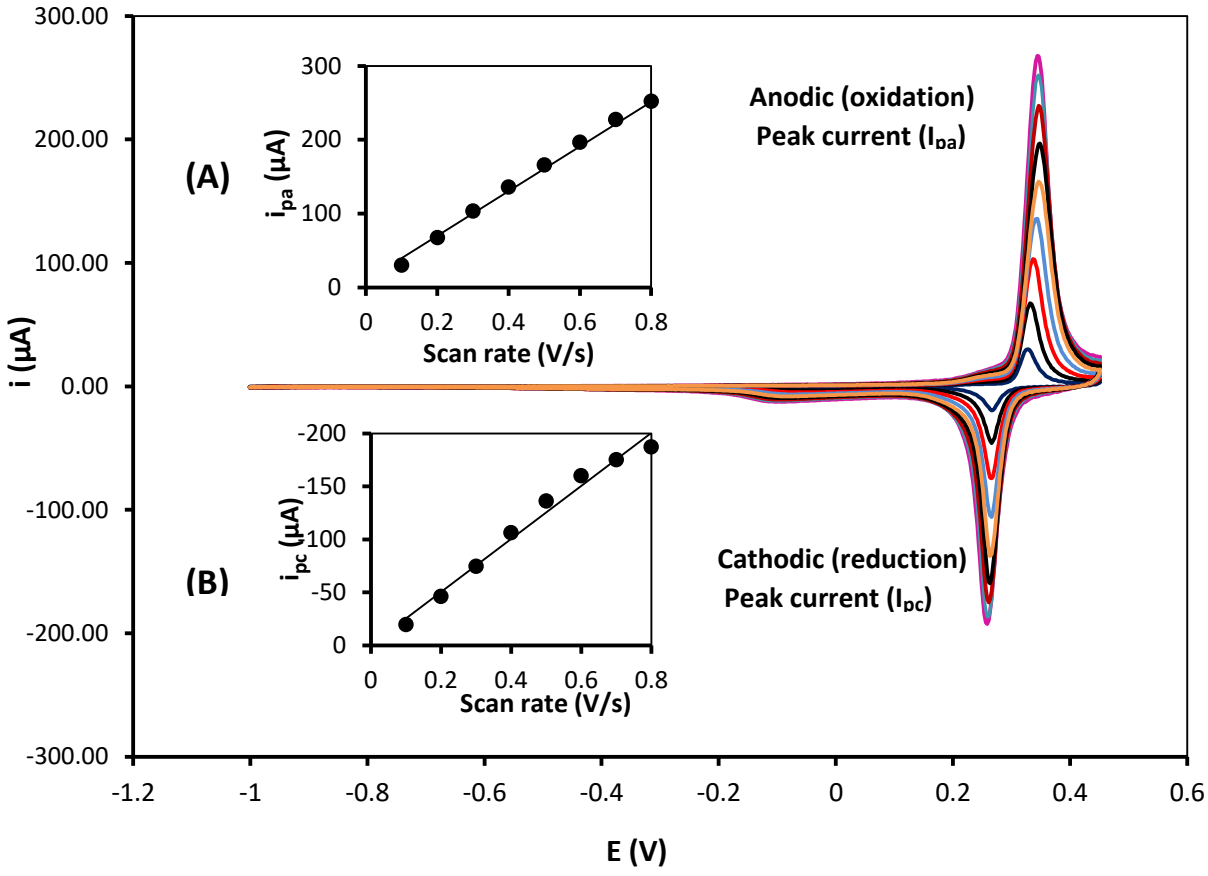


**Figure 3.18 Cyclic voltammogram of Ni film coated Au electrode recorded in 3M aqueous KOH at different scan rates.** Inner to outer: 0.1, 0.2, 0.3, 0.4, 0.5, 0.6, 0.7 and 0.8 V/s. Deposition charge density 0.25 C/cm$^2$ and the deposition was carried out by potential step from 0.45 to -1.0 V vs. Ag/AgCl at room temperature. Platinum flag was used as counter electrode. Inset A and B show plots of the current of oxidation and reduction peaks respectively, versus scan rate.

### 3.3.6.3 Determination of electroactive surface area of nickel films

The roughness factor (Rf) of the electrode was calculated and used to determine the electroactive surface area of the cubic phase. The Rf was calculated as described in Chapter 2, Section 2.4.1. Then the Rf values were plotted against the calculated charge density (Q) as represented in Figure 3.19A.

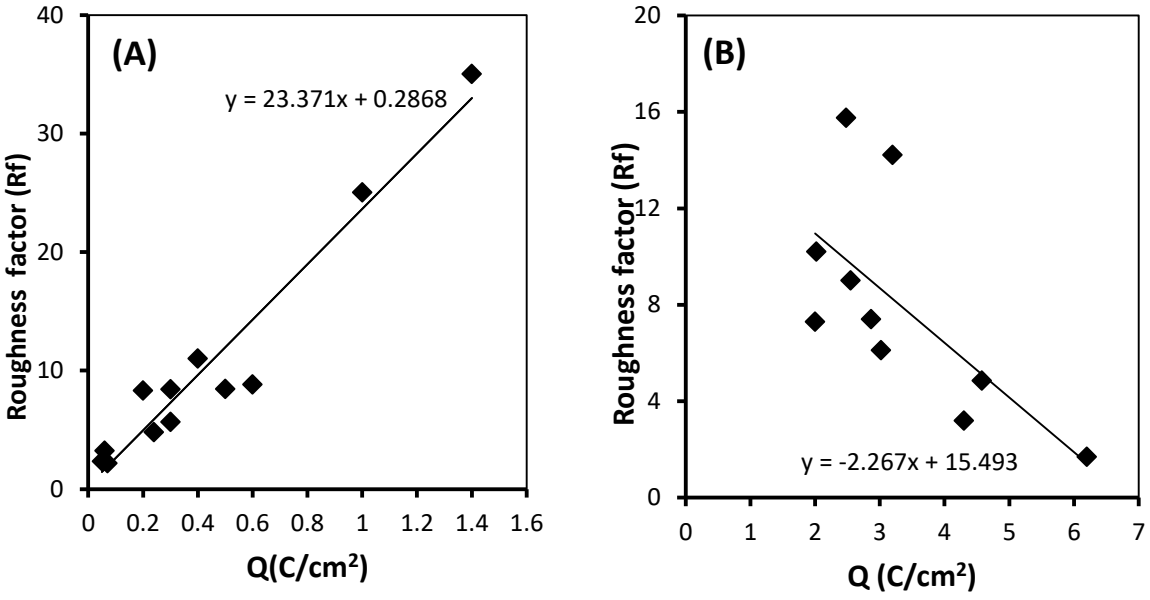


**Figure 3.19 Relation between roughness factor (Rf) and deposition charge density (Q).** Nickel deposition was conducted at room temperature on gold electrode (area = $1.96 \times 10^{-3}$ $cm^2$) in the presence of the monoolein cubic phase template **(A)** and in the absence of the template **(B)** at a deposition potential of -0.95 V vs. Ag/AgCl. Rf was calculated by cycling in 3 M KOH at room temperature.

The analysis of the roughness factor (Rf) showed that there is a linear relationship between Rf and the calculated charge density, even with high values of charge density (1.2 and 1.4 C $cm^{-2}$). The charge density is proportional to the amount of the metal, and thus to the thickness of the deposited nanostructured film. Thus, increasing the thickness of the deposited film increases the effective surface area. This proves the deposition of high surface area nickel.

This result demonstrates that the high surface area is due to a uniformly accessible internal 3-D nanostructure. The specific surface area of the deposited nickel films in the presence of the template was calculated to be ~13 $m^2/g$.

In order to compare the electrochemical behavior of nickel films in the absence of the cubic phase with that in the presence of the cubic phase, the electrochemical deposition were conducted directly on gold electrode without the cubic phase. Then the roughness factor (Rf) of the electrode was calculated as described above. Then the Rf values were plotted verses the deposition charge density (Q) as shown in Figure 3.19B. The data analysis demonstrates that the roughness factor decreases with increasing the charge density, however the scattering of the data is high.

### 3.3.6.4 Electrochemical stability of $Q_{II}^{D}$-eNi film

In order to assess the electrochemical stability of the deposited $Q_{II}^{D}$-eNi film, The $Q_{II}^{D}$-eNi film was deposited through monoolein cubic phase on gold electrode ($1.96 \times 10^{-3}$ $cm^2$) at potential of -0.95 V vs. Ag/AgCl with a deposition charge density of 1.44 C $cm^{-2}$. The deposited nickel film was then cycled repeatedly in 3 M KOH at room temperature. The roughness factor and the specific surface area of the deposited film were then calculated after every 20 cycles (Table 3.3). The values of the roughness factor and the specific surface area were plotted against the number of CV cycles (Figure 3.20 A and B, respectively). Surprisingly, the value of roughness factor and the specific surface area was found to increase with increasing the number of cycles up to 440 cycles. This finding was reproducible when the experiment was repeated with another $Q_{II}^{D}$-eNi film. These results suggested the electrochemical stability of the deposited $Q_{II}^{D}$-eNi film up to 440 cycles. Therefore the deposited $Q_{II}^{D}$-eNi film is promising as a catalytic material.

**Table 3.3** Variation of roughness factor and specific surface area of $Q_{II}^{D}$-eNi film with respect to the number of Cv cycles

| No of Cv cycles | Roughness factor (Rf) | Specific surface area ($m^2/g$) |
|---|---|---|
| **20** | 35 | 8.1 |
| **40** | 41 | 9.3 |
| **60** | 45 | 10.3 |
| **80** | 48 | 10.9 |
| **100** | 53 | 12.1 |
| **120** | 57 | 12.9 |
| **140** | 61 | 13.9 |
| **160** | 64 | 14.6 |
| **180** | 67 | 15.4 |
| **200** | 69 | 15.8 |
| **220** | 72 | 16.4 |
| **240** | 74 | 16.9 |
| **260** | 75 | 17.1 |
| **280** | 77 | 17.6 |
| **300** | 79 | 18.1 |
| **320** | 81 | 18.4 |
| **340** | 82 | 18.6 |
| **360** | 83 | 18.9 |
| **380** | 85 | 19.3 |
| **400** | 85 | 19.4 |
| **420** | 86 | 19.7 |
| **440** | 87 | 19.9 |

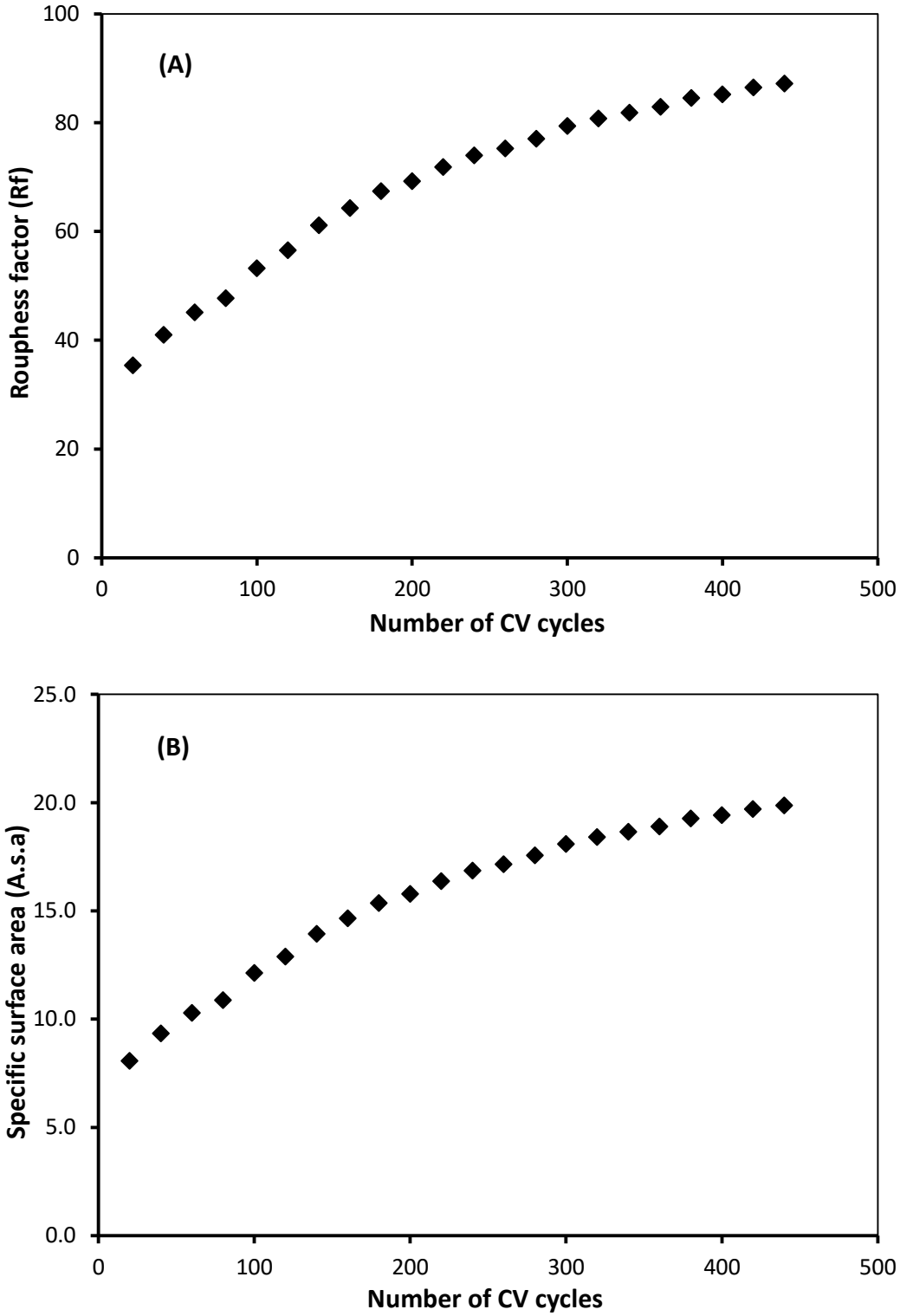


**Figure 3.20 Changes in A) Roughness factor and B) Specific surface area of the deposited $Q_{II}^{D}$-eNi film with respect the number of CV cycles.** $Q_{II}^{D}$-eNi film was deposited through monoolein template on gold wire electrode (area = $1.96 \times 10^{-3}$ $cm^2$) at room temperature at potential of -0.95 V vs. Ag/AgCl. The charge density of the deposited film was 1.44 C $cm^{-2}$.

### 3.3.7 Morphological characterisation of the deposited nickel films

SEM and TEM techniques were used to investigate the surface morphology and the porosity of the deposited nanostructured nickel films. SEM was also used to identify the composition of the deposited nickel film. For SEM analysis, nickel was deposited on gold DVD electrodes either in the absence or presence of the monoolein cubic phase template. Then SEM analysis was conducted using a FEI Quanta FEG 600 Scanning Electron Microscope equipped with a Quorum PP2000T Cryo rotating stage. Imaging was carried out at a 20 kV accelerating voltage. SEM images were taken at different magnifications (250-15000x). Elemental analysis of the corresponding magnifications was carried out using INCA microanalysis software. As a negative control, SEM images were taken for a blank gold DVD electrode (no deposition) (Figure 3.21).

High magnification SEM images demonstrate the grooved nature of the DVD electrodes. The images showed the presence of parallel grooves with equal distance between them (Figure 3.21). Au was identified at low and high magnifications, where observed predominant peaks recorded are corresponding to Au (Figure 3.21 and Table 3.4).

SEM images for the non-templated nickel showed some morphological features. These structures were absent in the blank DVD electrode. The elemental analysis confirmed that these structures are nickel (Figure 3.22, Table 3.4). The trace of carbon could be the conductive colloidal graphite used to apply low conductance coating to the electrode during the analysis. High magnification SEM image showed that nickel film (uneven morphology) extensively covered all the electrode area with a non-uniform pattern.

However, it was observed that the $Q_{II}^{D}$-eNi film showed different morphological structures from that shown by the non-templated nickel film. A low magnification image showed that $Q_{II}^{D}$-eNi film covered the electrode surface in certain pattern. However at high magnification, SEM image of the nanostructured nickel film shows some morphological features (Figure 3.23). The spectrum confirms that the morphological features observed with $Q_{II}^{D}$-eNi film belong to metallic nickel as indicated by the elemental analysis (Table 3.4). At low and high magnifications, the analysis showed that the predominant peaks in the electrode with the deposited film correspond to metallic nickel. The nickel peaks are absent in the blank electrode (no deposition) (Table 3.4). Further details about the porosity of the $Q_{II}^{D}$-eNi film were revealed in TEM images (Figure 3.24).

**Blank**

**(A)** **(B)**

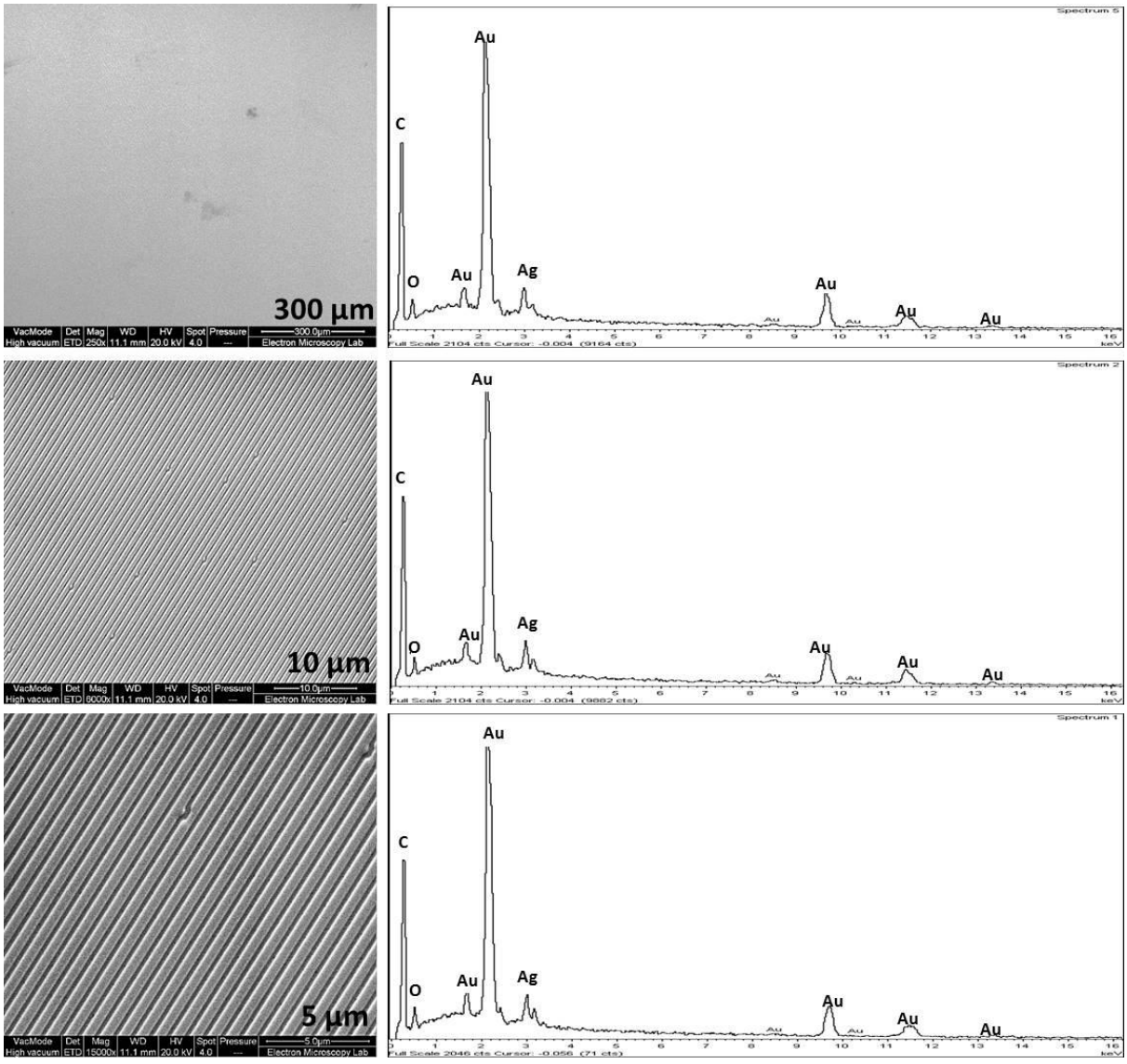


**Figure 3.21 SEM images of blank gold DVD electrode.** Images at different magnifications showing blank gold DVD electrode (area = 1.3 $cm^2$) **(A)** and the corresponding elemental analysis **(B).**

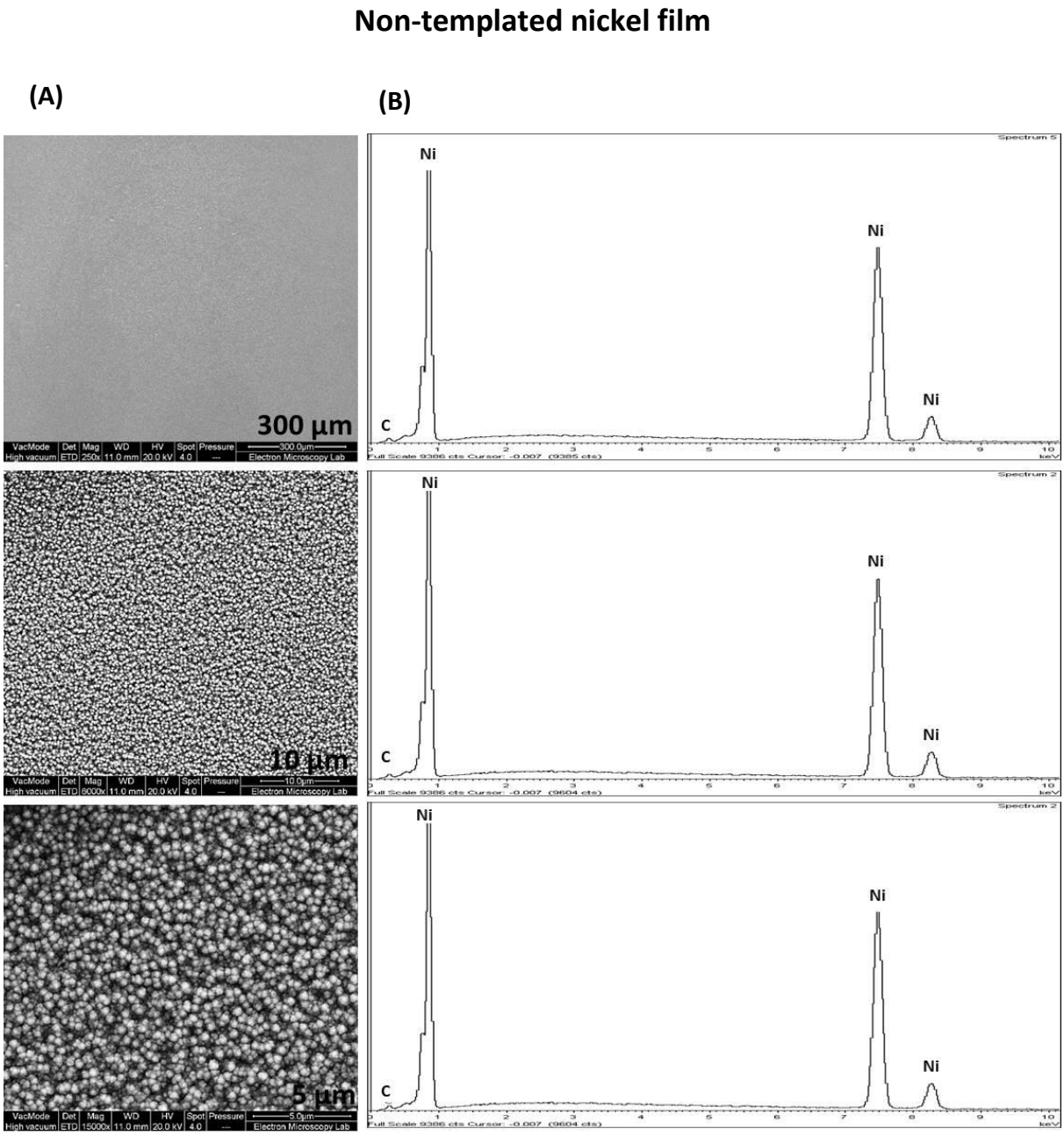


**Figure 3.22 SEM images of the non-templated nickel film.** Images show gold DVD electrode with non-templated nickel film at different magnifications **(A)** and the corresponding elemental analysis **(B).** The deposition of nickel was carried out at room temperature on gold DVD electrode (area = 1.3 $cm^2$) at a deposition potential of -0.95 V vs. Ag/AgCl with the deposition charge density of 15.3 C $cm^{-2}$

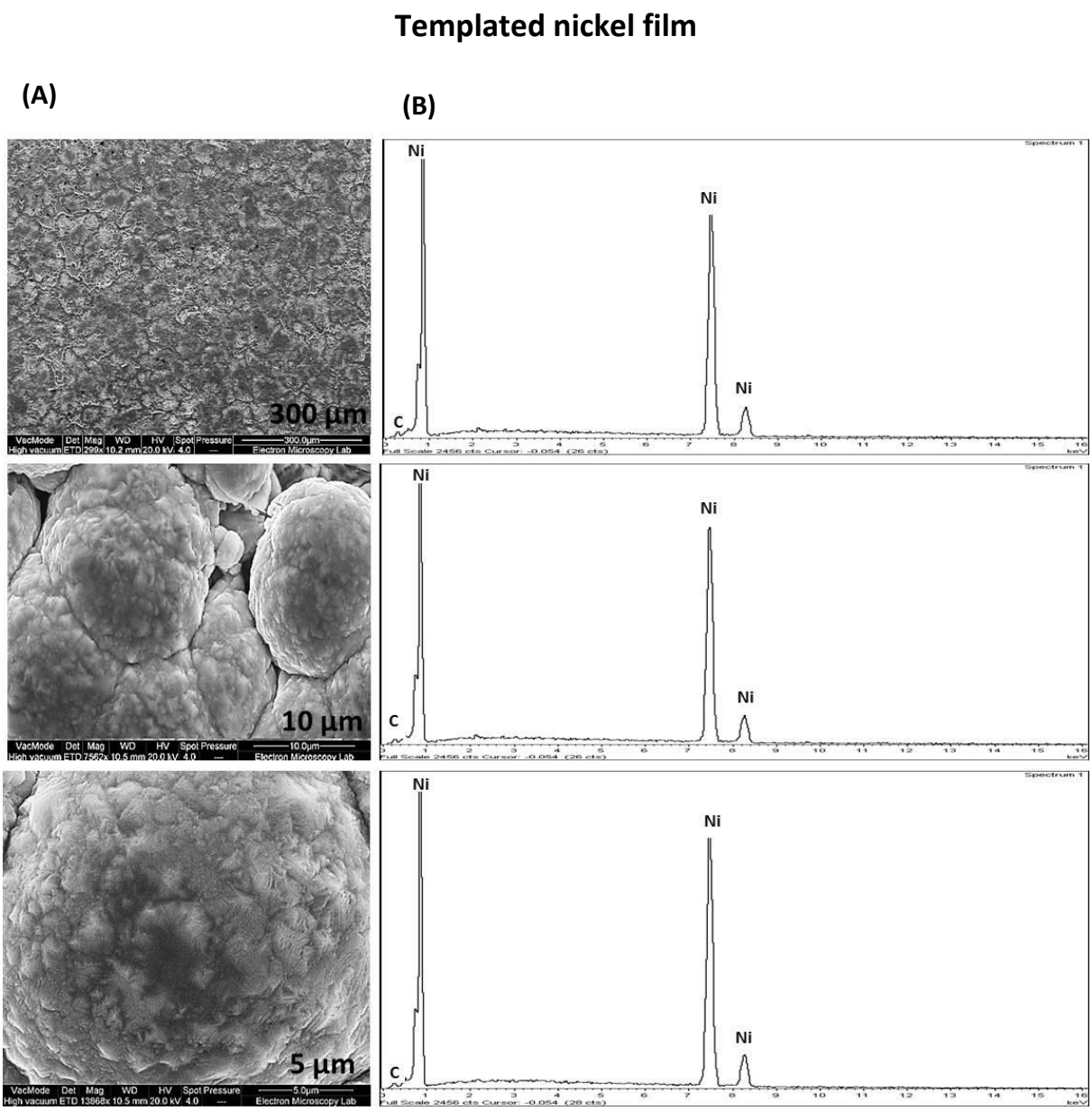


**Figure 3.23 SEM images of the liquid crystal templated nickel film.** Images show gold DVD electrode with $Q_{II}^{D}$-eNi film at different magnifications **(A)** and the corresponding elemental analysis **(B).** The deposition of nickel was carried out at room temperature on a gold DVD electrode (area = 1.3 $cm^2$) at a deposition potential of -0.95 V vs. Ag/AgCl with a deposition charge density of ~0.24 C $cm^{-2}$.

**Table 3.4** Composition of the deposited nickel films deposited on gold DVD electrode.

| **Magnification** | **Blank Au electrode** | | **Au electrode with non- templated Ni film** | | **Au electrode with templated Ni film** | |
|---|---|---|---|---|---|---|
| | **Element** | **Weight** | **Element** | **Weight%** | **Element** | **Weight%** |
| **250x(300 nm)** | C K | 43.65 | C K | 3.04 | C K | 5.06 |
| | O K | 6.45 | Ni K | 96.96 | Ni K | 94.94 |
| | Ag L | 5.85 | - | - | - | - |
| | Au M | 44.05 | - | - | - | - |
| | **Total** | **100.00** | **Total** | **100.00** | **Total** | **100.00** |
| **6000x(10 µm)** | C K | 42.95 | C K | 3.04 | C K | 5.07 |
| | O K | 6.61 | Ni K | 96.96 | Ni K | 94.93 |
| | Ag L | 6.38 | - | - | - | - |
| | Au M | 45.07 | - | - | - | - |
| | **Total** | **100.00** | **Total** | **100.00** | **Total** | **100.00** |
| **15000x(5 µm)** | C K | 41.91 | C K | 3.23 | C K | 3.15 |
| | O K | 6.88 | Ni K | 96.77 | Ni K | 96.85 |
| | Ag L | 5.75 | - | - | - | - |
| | Au M | 45.46 | - | - | - | - |
| | **Total** | **100.00** | **Total** | **100.00** | **Total** | **100.00** |

Details about the porosity of the liquid crystal templated nickel were revealed by TEM analysis (Figure 3.24). TEM analysis was conducted by a Philips/FEI CM20 transmission electron microscope equipped with an Oxford Instruments INCA X-ray defractor. Imaging was carried out under vacuum using a Philips/FEI CM20 microscope operated at an accelerating voltage of 200 kV. TEM analysis showed that the $Q_{II}^{D}$-eNi films were composed of 3-D network of interconnected nickel nanowires (Figure 3.24A). However, TEM technique cannot be used to provide more details about the structure and orientation of the deposited nickel networks. This was due to the difficulty of imaging deposited nickel by TEM under high voltage. It was observed that most of the tested nickel films were damaged when subjected to TEM with high accelerating voltage. This damage possibly was due to the incoming high energy electron beams[182]. The pore size of our nanostructure was estimated to be 17 nm (Figure 3.24B).

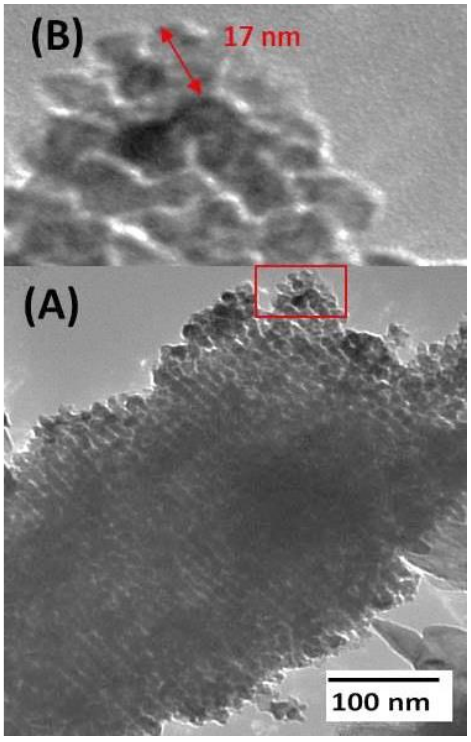


**Figure 3.24 (A) TEM image of $Q_{II}^{D}$-eNi film, (B) enlarged TEM image from the highlighted area shown in image (A).** Deposition of nickel was carried out at room temperature for 10 min on a gold glass electrode (area = 0.24 $cm^2$) through monoolein cubic phase. Deposition potential was adjusted at -0.95 V vs. Ag/AgCl. Charge density was ~0.24 C $cm^{-2}$.

## 3.4 Conclusion

3-D mesoporous nickel with single diamond morphology has been successfully fabricated using an inexpensive cubic phase liquid crystal of monoolein (Rylo) as a template. In the presence of the template, the electrochemically accessible surface area has been estimated to be ~266 fold higher than samples fabricated in the absence of the template. The 3-D nanoarchitecture of the deposited nickel films was confirmed by SAXS, TEM and electrochemical analysis. This attempt is promising since the improvement in nickel surface area has great potential in the improvement of the nickel electrode technology.

# Chapter 4: Electrochemical deposition of mesoporous platinum using monoolein (Cithrol) based bicontinuous cubic phase as a template

## 4.1 Introduction

Platinum and platinum based materials are characterised by high electrocatalytic activity[183] as well as high chemical, and mechanical stability. Therefore, these materials are used in many applications such as electronics, biomedical science and optics [184,185,186,187]. Recently, the demand has increased towards the fabrication of mesoporous platinum with high surface area, high mechanical stability, and enhanced electronic properties which have the potential to be used in energy sector. Such materials can be used to produce high efficiency and low emission energy storage devices and energy conversion devices such as catalysts and membrane components for fuel cells, solar cells and cathodes for batteries. In this century, fuel cells [184, 188] and solar cells[189,188] are considered the most promising renewable energy. Such devices could be used to maintain the increased demand of energy as well as to replace the natural energy sources which in turn will help to decrease the environmental pollution problem associated with the natural sources of energy. Moreover, it has been reported that nanostructured platinum materials exhibit magnetic properties depending on their morphology[190] and temperature[95]. This makes these materials interesting for magnetic storage devices.

The electrocatalytic efficiency of the nanostructured materials is greatly affected by the particle size of the materials. 3-D nanowire networks have many advantages over other different nanostructures. With the 3-D structural symmetry, some problems associated with

the 1-D and 2-D structures can be avoided. Such problems include pore blockage[167] and poor diffusion[191] of the electrolyte. For these reasons, there is a high demand to produce 3-D nanowire networks. Several attempts have been reported to prepare 3-D platinum using different methods. For examples, 3-D platinum nanowires were prepared using nanostructured silica material as a template[102]. Also 3-D platinum nanowires were prepared at room temperature on carbon nanospheres support by Sun et al.[100] using a simple chemical route. Recently, 3-D platinum with a helical structure was produced using a tricontinuous mesoporous silica IBN-9 as a template. The deposited platinum material had an ordered mesostructure consisting of highly oriented nanocrystals[192]. 3-D platinum nanowires were fabricated via an electrodeposition route using phytantriol bicontinuous phase as a template[41]. More recently, Cao et al.[105] have reported the fabrication of 3-D Pt nanocubes with uniform shapes and sizes using a novel meso-crystal self-assembly mechanism. The fabricated Pt nanocubes exhibited high electrocatalytic ability for methanol and formic acid oxidation. Mesoporous gyroid platinum was fabricated by electroless plating using a block copolymer, polystyrene-b-poly(L-lactide) (PS-PLLA) as a template[107]. Kibsgaard[108] reported the fabrication of high surface area mesoporous Pt/Ni alloy thin film with double gyroid morphology using co-electrodeposition of Pt and Ni into mesoporous silica as a template. The fabricated film showed high activity and stability for the oxygen reduction reaction.

In this work, we report for the first time the fabrication of nanostructured platinum with 3-D morphology via electrodeposition through monoolein bicontinuous cubic phase template. Preliminary investigations were carried out including an examination of: 1) soaking time and 2) deposition potential. This was followed by more detailed investigations of Rf and 3-D nanostructure.

## 4.2 Methodology

Initially, an ethanolic solution of monoolein (Cithrol) wt/wt % (1:1) was prepared as described in Chapter 2. The stability of Cithrol either in excess of water or in excess HCPA solution was investigated using the small angle X-ray scattering (SAXS) technique. The analysis was carried out using a Bruker Nanostar AXS small angle X-ray scattering instrument. In order to confirm the stability of Cithrol in excess of HCPA solution over time, Cithrol coated SAXS capillary tube (1.5 mm in diameter) was immersed with HCPA for 20 min, then the sample was analysed by SAXS. The sample was scanned every 5 min for 4 hours.

In order to find the optimum deposition potential, a number of preliminary electrodeposition experiments were carried out at different deposition potentials ranging from -0.15 to -0.38 V vs. Ag/AgCl in excess of HCPA solution. Also to find out the minimum soaking time limit, a number of soaking time experiments were performed by dipping the working electrode in HPCA solutions for different times (10-50 min) prior to electrodeposition. The electrodeposited platinum films were prepared and washed as described in Chapter 2. The deposited films were then characterised using cyclic voltammetry. After determining the best conditions required for electrodeposition of platinum through Cithrol template, platinum films were electrodeposited on different substrates and then characterised. After electrodeposition, electrochemical characterisation of the deposited platinum films was carried out using cyclic voltammetry. The electroactive surface of the platinum films deposited using Cithrol template was determined by calculating the Rf values using cyclic voltammetry. Initially, a number of electrodeposition experiments were conducted through Cithrol cubic phase on gold or platinum electrodes ($1.96 \times 10^{-3}$ $cm^2$). The electrodes were then washed with ethanol in order to remove the template. Cyclic voltammetry was then

carried out for the deposited films. The Rf values of the deposited films were then calculated from the cyclic voltammograms. For comparison, platinum films were electrodeposited through phytantriol template on gold electrodes ($1.96 \times 10^{-3}$ $cm^2$) and then the electroactive surface of these platinum films were determined using cyclic voltammetry as described above. All the electrochemical experiments were conducted using an Autolab PGSTAT101 potentiostat with a three-electrode cell consisting of Ag/AgCl as reference electrode, platinum flag (area ~ 1 $cm^2$) as counter electrode and gold and platinum as working electrodes. Electrochemical synthesis and characterization was carried out in a 20 mL glass cell at room temperature. Structural characterisation of the deposited platinum films through Cithrol template was carried out using synchrotron SAXS analysis (Beamline I07, Diamond, UK). Details of the synchrotron SAXS are described in Chapter 2.

## 4.3 Results and discussion

### 4.3.1 Stability of monoolein (Cithrol) based cubic phases

In this chapter, we had to change the monoolein material Rylo used in chapter 3 to another monoolein material called Cithrol because the supplier (DANISCO, UK) stopped producing Rylo. Initially, the stability of monoolein (Cithrol) under excess of water or excess of HCPA was investigated by SAXS analysis. The inside wall of an X-ray capillary tube (diameter = 1.5 mm) was coated with a thin film of ethanolic monoolein solution and left for 30 min in order to evaporate the ethanol. The tube was then filled with either water or HCPA and left for 20 min to allow the formation of the monoolein cubic phase (as recommended in the previous chapter). The monoolein cubic phases in both cases were then characterised by SAXS analysis. The SAXS patterns are shown in Figure 4.1.

The 2-D SAXS patterns of monoolein under excess of water and excess of HCPA solution showed typical SAXS patterns corresponding to the inverse bicontinuous cubic diamond ($Q_{II}^{D}$) phase. This was indicated from the 1-D SAXS patterns corresponding to both cases. Six strong Bragg peaks which follow the ratios √2:√3:√4:√6:√8:√9 was observed in the 1-D SAXS patterns of both cases. These ratios are consistent with the cubic lattice of *Pn3m* crystallography space group ($Q_{II}^{D}$)[193]. In the presence of HCPA, a small effect on the cubic phase behaviour was observed as shown in 1-D SAXS pattern. The calculated lattice parameters of the obtained monoolein cubic phases were 90.6 ± 1.7 Å and 92.9 ± 0.74 Å in excess of water and excess of HCPA solution, respectively. These values are slightly lower than the lattice parameters reported for pure monoolein based cubic phases under excess of water at room temperature ($a$ = 107 Å, at 20 $^{o}$C)[169]. This could be due to presences of some impurities in Cithrol which might decrease the lattice parameter. However, no phase transformation was observed with Cithrol under excess of HCPA confirming, the formation and stability of monoolein cubic phase in the presence of HCPA solution.

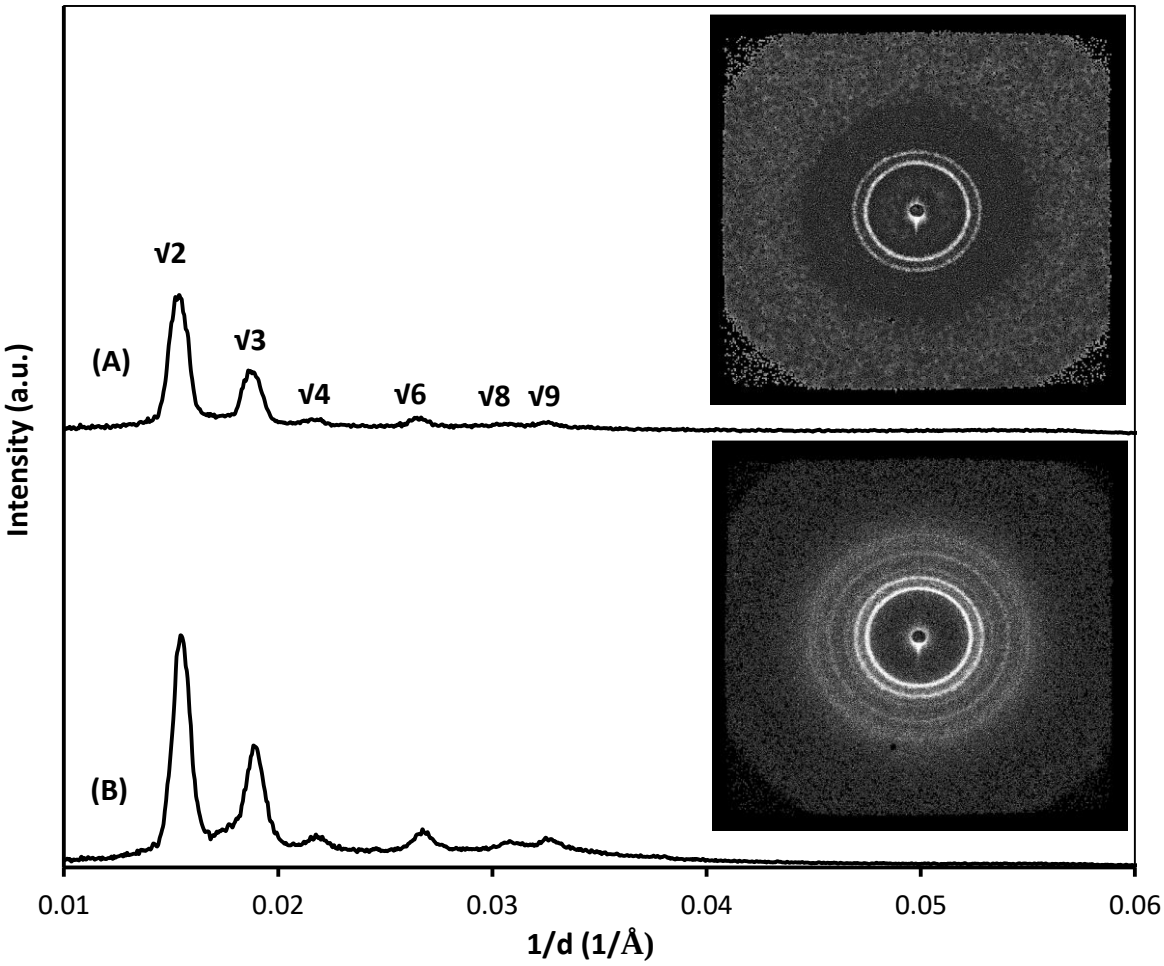


**Figure 4.1 1-D SAXS patterns for monoolein (Cithrol) at room temperature: A)** in excess of HCPA solution (calculated lattice parameter of the cubic phase = 92.9 ± 0.74 **Å**) and **B)** in excess of water (calculated lattice parameter of the cubic phase = 90.6 ± 1.7 Å). Insets are the 2-D SAXS patterns corresponding to each 1-D pattern.

Further investigations were carried out to study the stability of Cithrol in excess of HCPA solution with time at room temperature. The inside wall of the X-ray capillary tube (diameter = 1.5 mm) was coated with a thin film of ethanolic solution of Cithrol as described above. In order to dry and evaporate the ethanol, the tube was left in air for 30 min. Then the tube was filled with HCPA and left for 20 min to allow the formation of the Cithrol based cubic phase. After which the sample was analysed by SAXS. Scans were taken every 5 min for 4 h as shown in Figure 4.2. As control experiment, SAXS was conducted for Cithrol in excess of

water as described above and the corresponding SAXS patterns are shown in Figure 4.2. The results confirmed the formation of the cubic phase in excess of water and in excess of HCPA after 20 min as described above. This was indicated from the 2-D SAXS patterns showing typical pattern for the cubic phase. The corresponding 1-D showed six Bragg peaks with the ratio√2:√3:√4:√6:√8:√9 which are characteristic for the cubic lattice of *Pn3m* crystallographic space group ($Q_{II}^{D}$)[193] (Figure 4.2). Also the results revealed that the cubic phase of Cithrol in excess of HCPA was stable up to 60 min, showing typical 2-D and 1-D patterns which corresponding to the $Q_{II}^{D}$ phase. The calculated lattice parameter of this cubic phase was found to be 96.6 ± 1.4 Å. However, after 60 min, HCPA solution was found to have an effect on the phase behavior of Cithrol, causing a transition in the phase. There was a gradual change in the lattice parameter of the cubic phase. This was indicated by the 1-D SAXS patterns which showed a steady shift in the peaks corresponding to the cubic phases (Figure 4.2). This could be due to acid catalysed hydrolysis of monoolein.

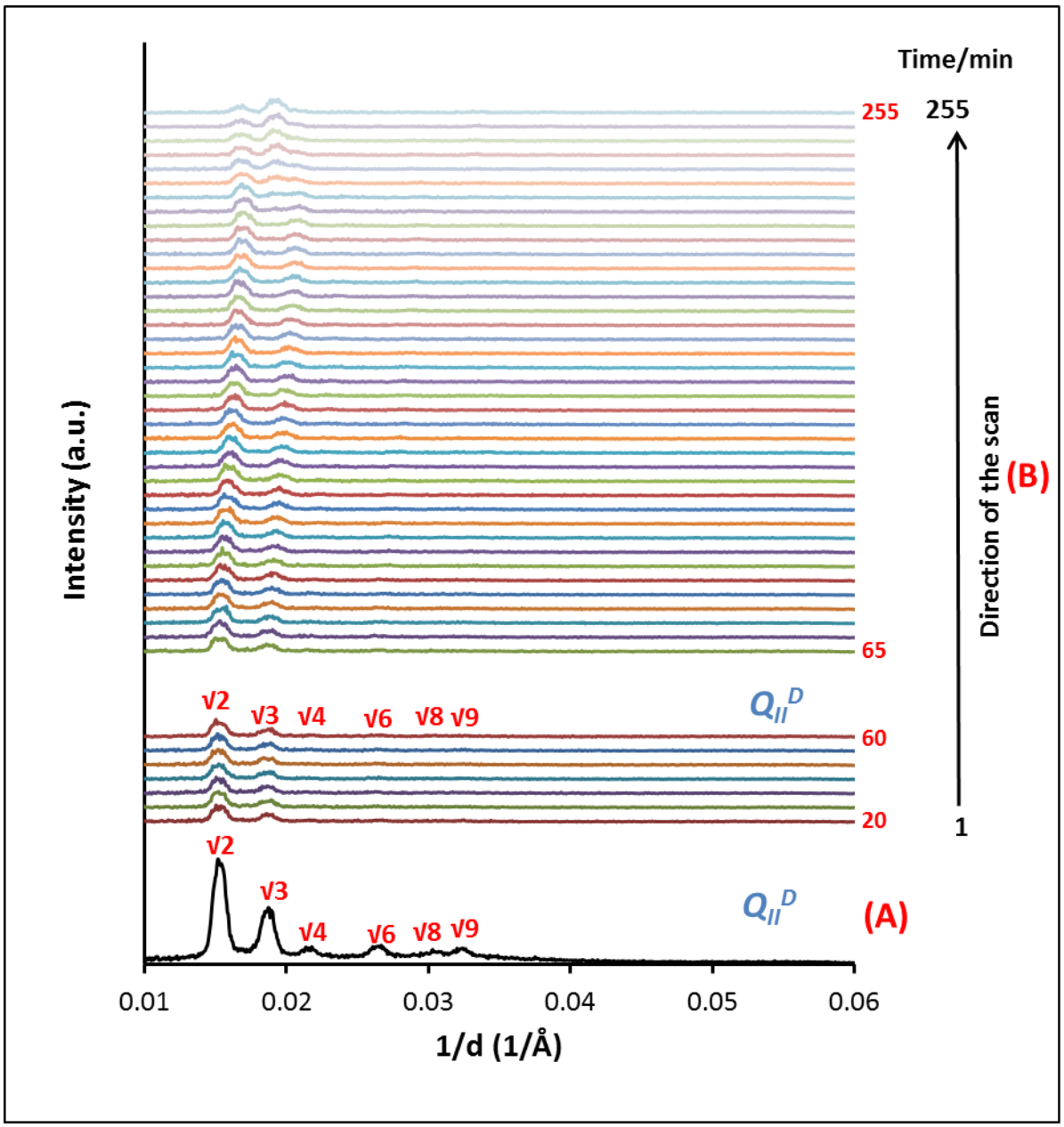


**Figure 4.2 1-D SAXS patterns for Cithrol in excess of HCPA at room temperature. A)** Cithrol in excess of water (lattice parameter = 95.6 Å) and **B)** Cithrol sample in excess of HCPA solution (lattice parameter = 96.6 ± 1.4 Å); the sample was scanned every 5 min for ~ 4h. The arrow shows the direction of the scan.

### 4.3.2 Experimental conditions required for electrochemical deposition of platinum through monoolein-based cubic phases

A number of preliminary experiments were carried out to find out the optimum conditions required for electrodeposition of platinum through the monoolein-based cubic phase. Such conditions include deposition potential and soaking time limit in HPCA solution. The results of these experiments are shown below.

#### 4.3.2.1 Deposition potential

The electro-reduction of HCPA at the electrode surface through the cubic phase of monoolein was investigated by cyclic voltammetry. The electro-reduction was carried out at a gold electrode with an area of $1.96 \times 10^{-3}$ $cm^2$. Initially, the electrode was coated with a thin layer of monoolein. Then the monoolein-coated electrode was soaked in HCPA solution for 20 min. The electro-reduction of the HCPA-soaked electrode was tested by cyclic voltammetry. The cyclic voltammetry was carried out at room temperature between the limits +0.1 and -0.4 V vs. Ag/AgCl at a scan rate of 10 mV $s^{-1}$. The cyclic voltammogram is shown in Figure 4.3. The cyclic voltammograms recorded for HCPA solution showed a predominant peak at -0.25 V vs. Ag/AgCl during the cathodic scans. Based on the literature, the electro-reduction of a platinum salt is a complex process[194]. Therefore, the electro-reduction of HCPA may involve a number of redox couples giving more than one peak in the current-voltage curve[195,129].

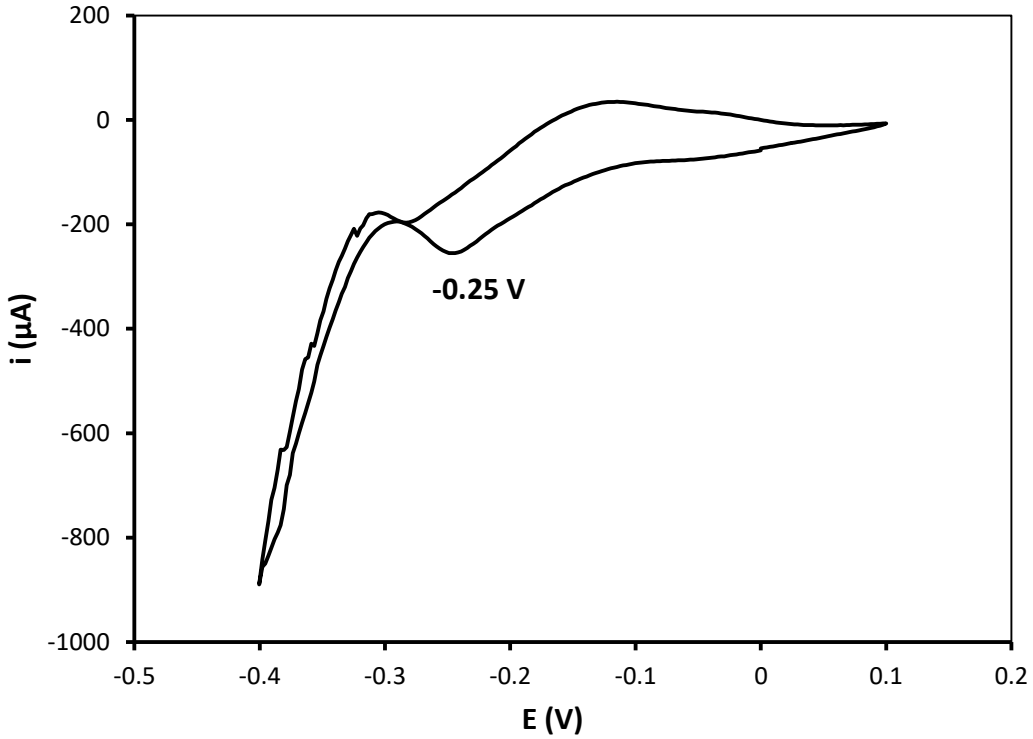


**Figure 4.3 The electro-reduction of platinum at a gold electrode (pre-coated with a thin film of monoolein).** Cyclic voltammetry from HCPA solution at 10 mV/ $s^{-1}$ at potentials scanned between +0.1 and -0.4 V vs. Ag/AgCl. Potential was measured against Ag/AgCl reference electrode. The area of the gold electrode was $1.96 \times 10^{-3}$ $cm^2$.

For further investigations, the electrodeposition of platinum through the cubic phase of monoolein was carried out at selected potentials ranging from -0.15 to -0.38 V vs. Ag/AgCl. Gold electrodes were coated with thin layer of monoolein and soaked in HPCA solution for 20 min. Then electrodeposition of platinum was carried out though the monoolein-coated gold electrodes at the selected potentials. Electrochemical experiments were performed using an Autolab PGSTAT101 potentiostat. The charge density was constant in all depositions (~ 4 C $cm^{-2}$). The data showed that the magnitude of the current, and therefore the deposition time, varied depending on the deposition potentials. The values are shown in Table 4.1.

**Table 4.1** Variation of deposition time with respect to deposition potential

| **Deposition potential (V)** | **Deposition time (sec)** | **Charge density (C $cm^{-2}$)** |
|---|---|---|
| **-0.15** | 199 ± 16 (n = 2) | 3.8 ± 0.3 |
| **-0.2** | 195 ± 7.01 (n = 2) | 3.53 ± 0.7 |
| **-0.23** | 131 ± 4.2 (n = 2) | 4 ± 0.7 |
| **-0.25** | 119 ± 17 (n = 3) | 3.6 ± 1.33 |
| **-0.3** | 104 ± 7.07 (n = 2) | 3.95 ± 0.08 |
| **-0.35** | 62 ± 7.1 (n = 2) | 3.96 ± 0.06 |
| **-0.38** | 56 ± 10 (n = 2) | 4.1 ± 0.12 |

n = number of measurements, values represent the mean ± SD of two independent experiments

The data showed that depositions at less negative potentials required longer times. This could be due to slow reaction kinetics at these potentials. Representative deposition transients recorded for the deposited platinum films deposited at different potentials are shown in Figure 4.4.

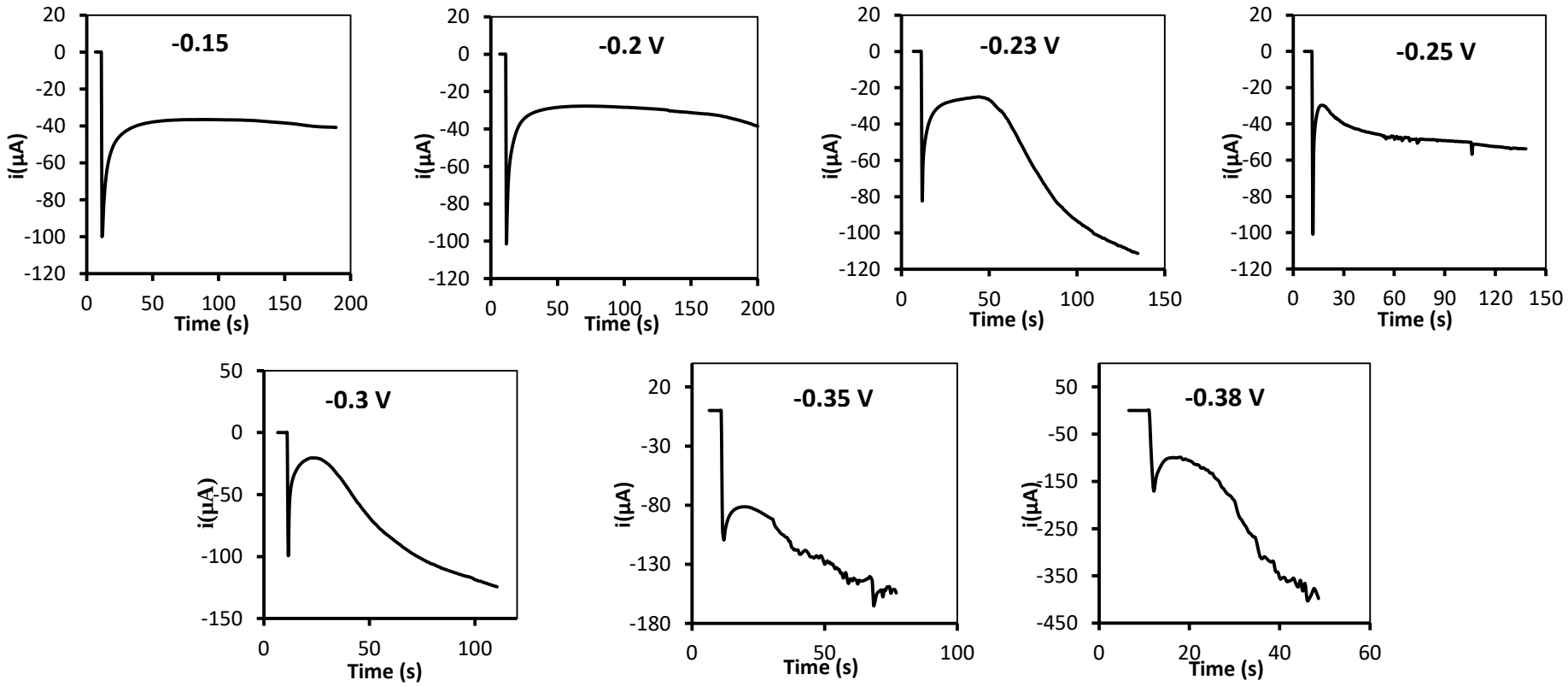


**Figure 4.4 Representative examples of electrodeposition transients recorded at different potentials.** Deposition of platinum was carried out at room temperature on gold wire electrodes (area = $1.96 \times 10^{-3}$ $cm^2$) at potentials of -0.15, -0.2, -0.23, -0.25, -0.3, -0.35 and -0.38V vs. Ag/AgCl at room temperature. The charge density was constant with all depositions (~ 4 C $cm^{-2}$).

In all transients, there was an initial decrease in the current, followed by increase in the negative current. When the electrodeposition of platinum was carried out at the potentials of -0.15 and -0.2 V, a very small amount of current was observed. While, at a deposition potential of -0.25 V, the current was higher. However, a massive increase in the current amplitude was observed at potentials of -0.23, -0.3, -0.35 and -0.38 V. This may be attributed to the presence of unwanted side reactions[52].

Following the electrodepositions, the electrodes were washed with ethanol in order to remove the monoolein template. Then the platinum films were analyzed electrochemically in 0.5 M aqueous $H_2SO_4$ between the limits -0.28 to +1.2 V vs. Ag/AgCl. The cyclic voltammograms of the platinum films deposited at different potentials are shown in Figure 4.5. The shape of the voltammograms varied with the deposition potential, depending on the growth of the deposited platinum. The cyclic voltammogram of platinum film deposited at -0.25 V showed typical adsorption/desorption features in the hydrogen under potential region (-0.35 to 0.1 V) vs. Ag/AgCl which are attributed to different platinum facets[131,133].

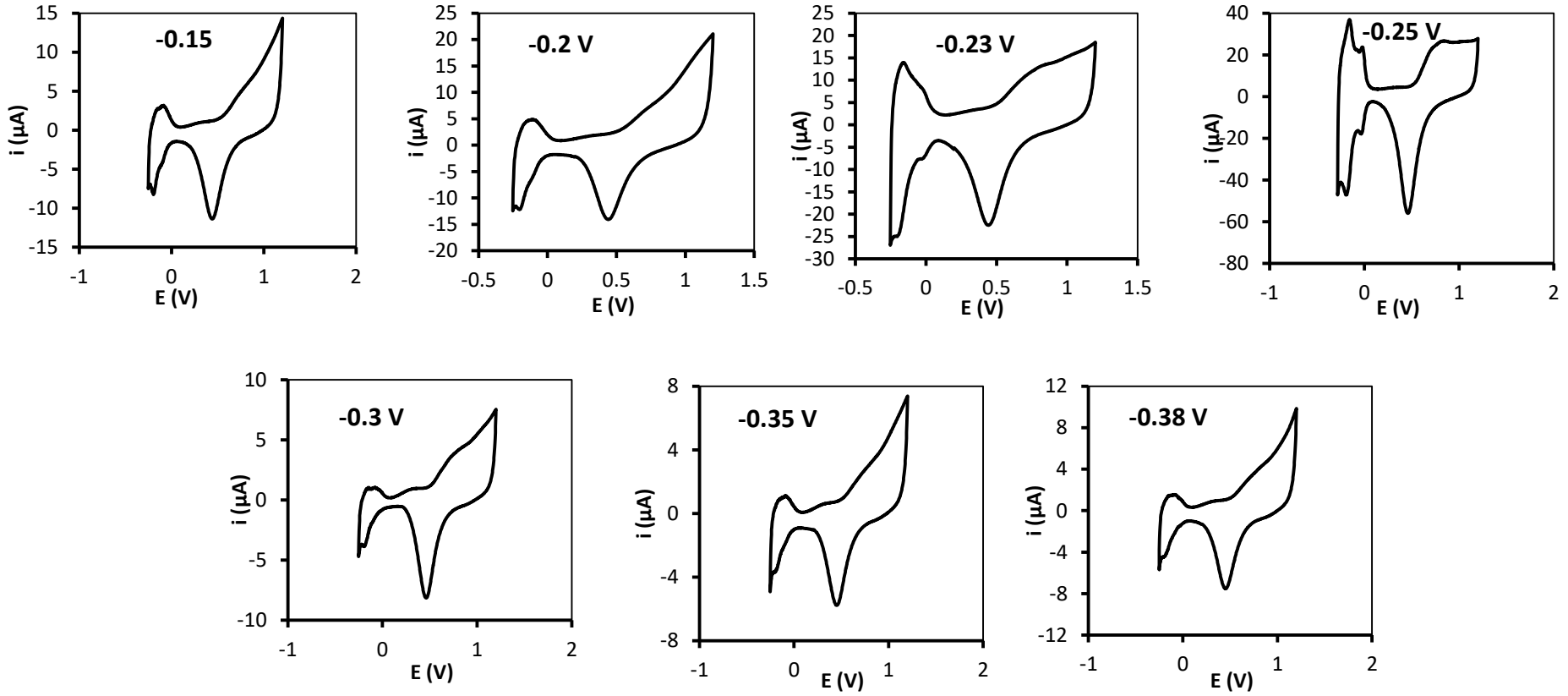


**Figure 4.5 Cyclic voltammograms of platinum films deposited at different potentials.** Deposition of platinum films were carried out at room temperature on gold wire electrodes ($1.96 \times 10^{-3}$ $cm^2$) for variable deposition potentials from -0.15 V to -0.38 V vs. Ag/AgCl and constant charge density of ~ 4 $C/cm^2$.

The Rf value of the electrodeposited Pt film at each potential was calculated according to a method described by Elliott et al.[52]. The Rf value was calculated by dividing the charge associated with the hydrogen under-deposition potentials by the electrode area. The details of the calculations are shown in Section 2.4.1. Then the values of the Rf were plotted against the deposition potential as shown in Figure 4.6.

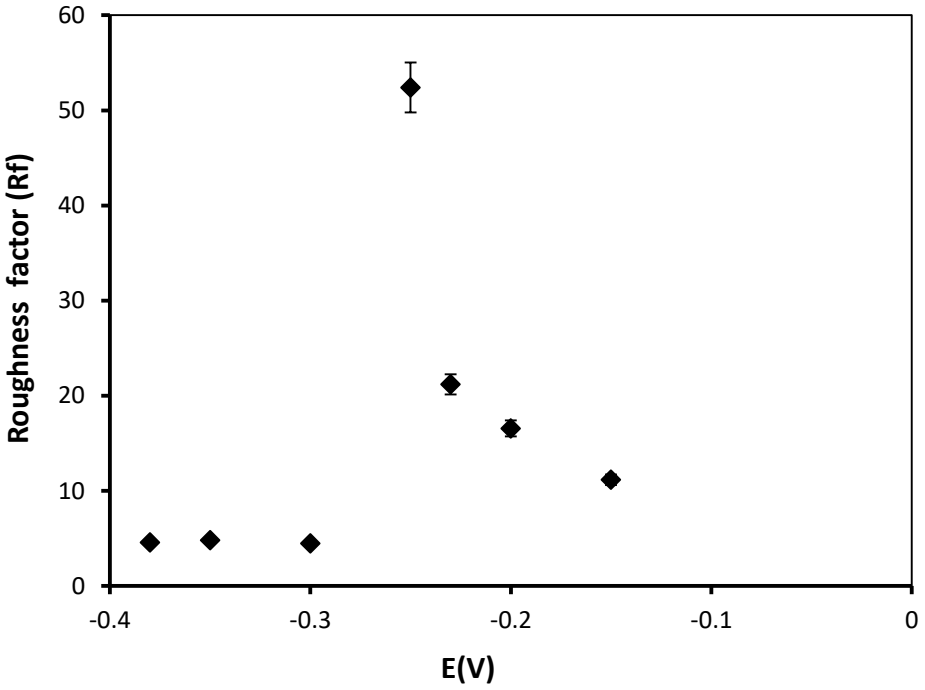


**Figure 4.6 Variation of Rf with respect to deposition potential for the electrodeposited Pt films.** Gold wire electrodes (area = $1.96 \times 10^{-3}$ $cm^2$) were coated with a thin layer of monoolein. Electrodeposition carried out at room temperature at different potentials from -0.15 to -038 V vs. Ag/AgCl and charge density of approximately (~ 4 $C/cm^2$). The values represent the mean ± SD of two independent experiments.

The analysis showed that the Rf values increased with decreasing deposition potential until it reached a maximum value at a potential of -0.25 V. Then the Rf value decreased with further decrease in potential (Figure 4.6). The highest values of Rf were recorded at potentials of -0.2, -0.23 and -0.25 V. This result is consistent with Akbar et al.[129] who reported the highest values of roughness factor of electrodeposited $Q_{II}^{D}$-ePt films deposited through phytantriol at

potentials of -0.2 and -0.25 V using HPCA solution. Also this agrees with the main peak observed during the electro-reduction of platinum shown in Figure 4.3.

It can be suggested from our data that the deposition potential of -0.25 V is the most suitable potential for the electrodeposition of Pt films through the cubic phase of monoolein. Therefore, a potential of -0.25 V was used for electrodeposition of platinum films in all the subsequent experiments.

### 4.3.2.2 Soaking time

A series of experiments were carried out to find out the effect of soaking time on the deposition of platinum through monoolein cubic phase. Initially, the electrodes were coated with a thin layer of monoolein. Then they were soaked in HCPA solution for different periods of time prior to the electrodeposition. The electrodeposition was conducted at room temperature at deposition potential of -0.25 V vs. Ag/AgCl. The electrodeposition was carried out with reasonably constant charge density (~ 4 $C/cm^2$). Following electrodeposition, the electrodes were washed and analyzed electrochemically to measure the Rf values. The calculated Rf values are shown in Figure 4.7. The maximum Rf value (60) was obtained after 20 min, then the Rf values decreased with further increase in the soaking time. Therefore, the soaking time of 20 min in the HCPA solution was identified as suitable for electrodeposition of platinum through monoolein cubic phase. This was in agreement with the time required for the formation of monoolein (Rylo) based cubic phase under excess of water described in Chapter 3 (Section 3.3.2.1).

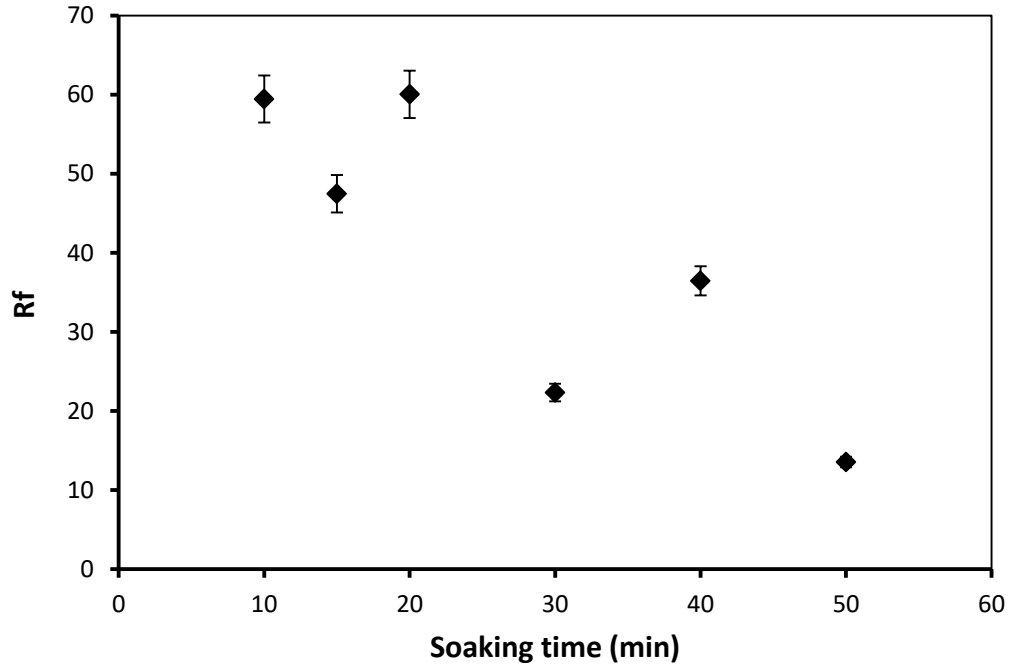


**Figure 4.7 Variation of Rf with respect to soaking time for the electrodeposited Pt films deposited through a thin layer of monoolein.** Electrodeposition carried out at room temperature on gold electrode (area = $1.96 \times 10^{-3}$ $cm^2$) at -0.25 V vs. Ag/AgCl and charge density of approximately (~ 4 $C/cm^2$). The values are mean ± SD of two independent experiments. Error bars represent SD.

### 4.3.3 Detailed investigation of electrochemical deposition of platinum at potential of - 0.25 V vs. Ag/AgCl

Gold electrodes (area = $1.96 \times 10^{-3}$ $cm^2$) were coated with thin film of monoolein. Then the monoolein-coated electrodes were then soaked in HPCA solution for 20 min as described above in Section 4.3.2.2. Electrodeposition of platinum was then carried out at room temperature using a Autolab PGSTAT101 potentiostat. The deposition potential was adjusted at -0.25 V vs. Ag/AgCl as suggested above in Section 4.3.2.1. As a control experiment, the electrodeposition of platinum was carried out directly from HCPA solution in the absence of the monoolein template. The typical transients of both depositions are shown in Figure 4.8.

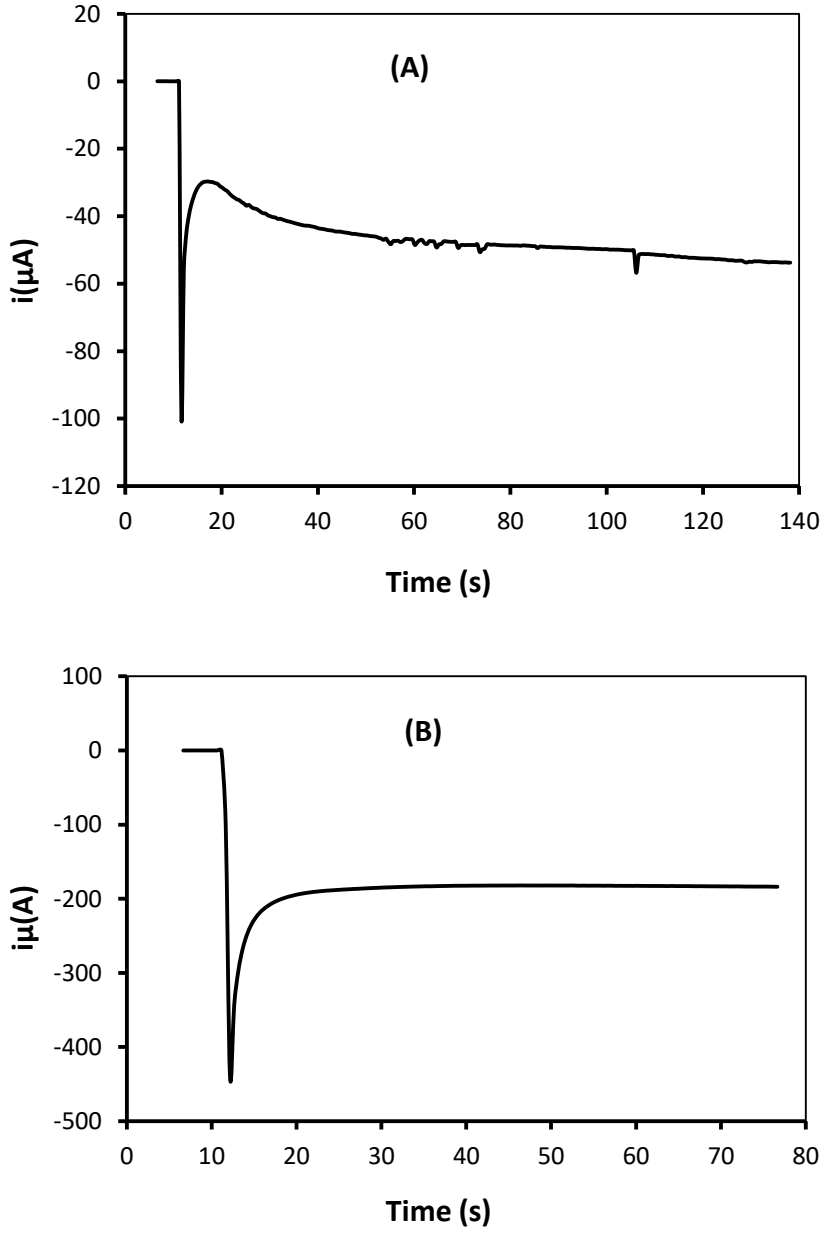


**Figure 4.8 Typical electrodeposition transients recorded for platinum deposition: A)** in the presence of monoolein template (Q = ~3 C/cm$^2$) and **B)** in the absence of the template (Q = 6.31 C/cm$^2$). Depositions were carried out at room temperature on gold wire electrodes (area=1.96 × 10$^{-3}$) at potential of -0.25 V vs. Ag/AgCl.

The non-templated deposition shows a higher current than in the templated one. Therefore the calculated charge density of the non-templated platinum is higher than that of the templated

platinum. In order to achieve the same charge density, deposition had to be carried out for less time.

A high initial current was observed in transients recorded for the deposition through the cubic template at gold electrode. This could be due to a mass transport controlled primary nucleation process on the surface of the electrode[177].

In both cases, there was an initial decrease in the current, followed by almost stable current. This could be attributed to secondary nucleation process of platinum[137]. However, the current flow was >4X lower for the platinum deposition in the absence of the cubic phase. Furthermore, there was no characteristic features of the primary nucleation was observed in the transient recorded in the absence of the template. This could be due to high rate of platinum deposition, at which the secondary nucleation processes can hide the primary nucleation processes[137].

In addition, there was a notable change in the surface of the gold electrode when the electrodes were removed from the electrochemical cell after deposition. In the presence of the template, the color of the electrode surface changed from golden to black. The deposited platinum films obtained at high charge density were slightly darker in comparison to those obtained at low charge density. While, in the absence of the template the electrode became silver in color. Images were taken for the gold electrode before and after deposition of platinum using Zeiss Axioskop 40 light microscope. Images are shown in Figure 4.9.

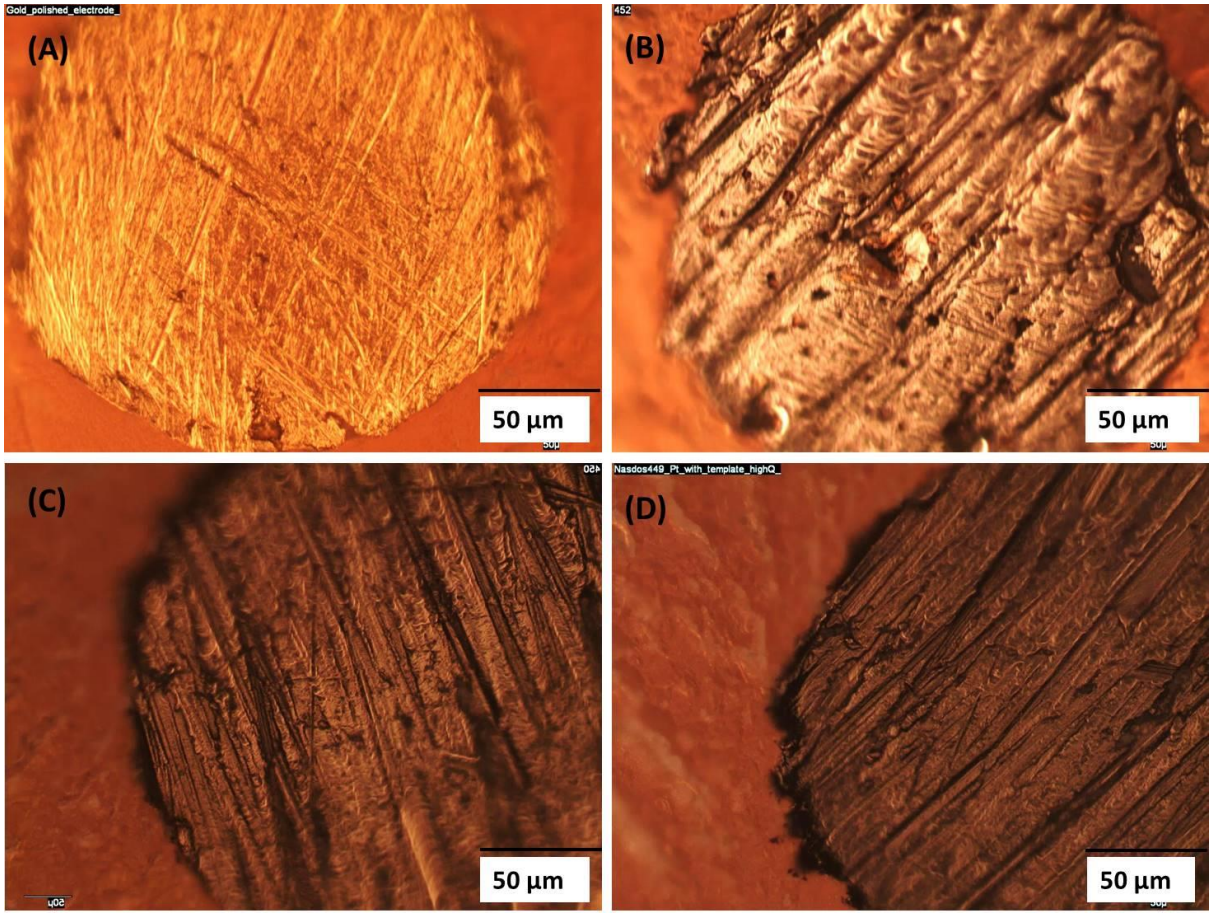


**Figure 4.9 Light microscope images of deposited platinum films on gold wire electrode (area = 1.96 × $10^{-3}$ $cm^2$): A)** before deposition (blank gold electrode), **B)** deposited platinum without template, **C)** deposited platinum through the template with low charge density and **D)** deposited Pt film through template with high charge density. Scale bars are indicated on the images.

### 4.3.4 Electrochemical characterisation of deposited platinum films

#### 4.3.4.1 Voltammetric behaviour of the deposited platinum films in $H_2SO_4$

The electrochemical behaviour of the $Q_{II}^{D}$-ePt films was investigated using cyclic voltammetry. Platinum were deposited on platinum and gold disc electrodes (area = $1.96 \times 10^{-3}$ $cm^2$). Then the films were washed thoroughly with ethanol and water in order to remove the monoolein template. The electrodes were analyzed by cyclic voltammetry in dilute $H_2SO_4$. As controls, the platinum and gold electrodes were analysed by cyclic voltammetry before electrodeposition. The cyclic voltammograms recorded for the electrodes before and after deposition are shown in Figure 4.10.

The voltammograms recorded for the deposited platinum on both electrodes showed increased current confirming the formation of a platinum electrode. Also the voltammetric features for the gold surface were completely masked in the film deposited on the gold electrode (Figure 4.10B). This could be due to the large difference in current amplitude. The voltammograms of the deposited platinum films on both electrodes exhibited typical adsorption/desorption features of different platinum facets which appeared in the hydrogen-under potential region (-0.35 to 0.1 V) vs. Ag/AgCl (Figure 4.10B, D). This suggested the presence of Pt (111), Pt (110), and Pt (100) crystal facets in the deposited films[131,133]. However, the surface area of the deposited platnuim films is relatively low. Thus further optimisations were required to improve the surface area of the deposited material.

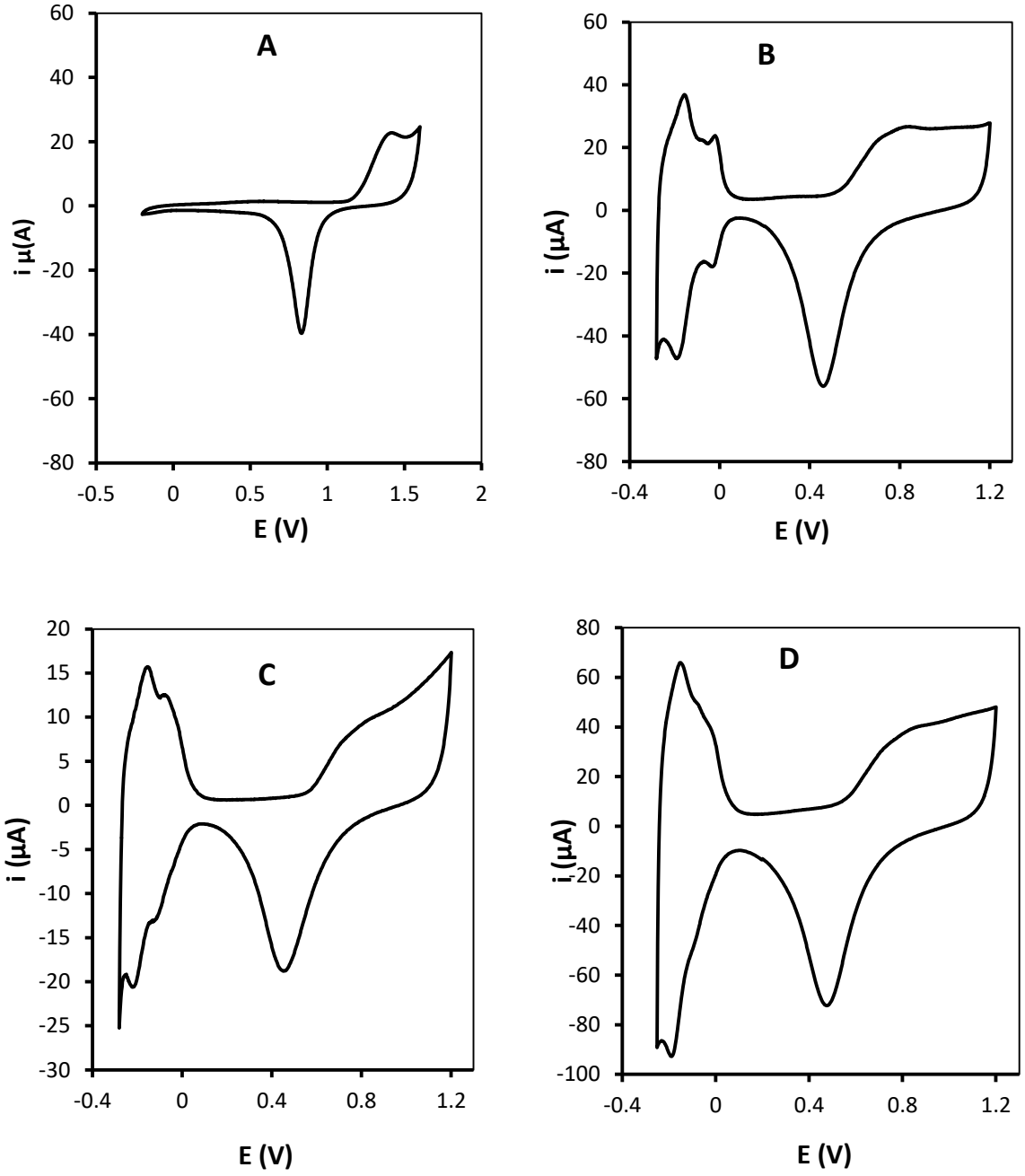


**Figure 4.10 Cyclic voltammetry in diluted $H_2SO_4$ for : A)** Gold electrode of area $1.96\times10^{-3}$ $cm^2$ **B)** platinum film deposited on gold electrode (Q = 3 C/$cm^2$, Rf = 93), **C)** polished platinum electrode of area $1.96 \times 10^{-3}$ $cm^2$ and **D)** platinum film deposited on platinum electrode (Q = 12.6 C/$cm^2$, Rf =175).

### 4.3.4.2 Determination of electroactive surface area of platinum films

In order to determine the electroactive surface area of the deposited platinum films, a number of electrodeposition experiments were carried out through the cubic phase of monoolein at -0.25 V and different charge densities (0.53 to 20.9 C/cm$^2$). Depositions were carried out on both gold and platinum electrodes ($1.96 \times 10^{-3}$ cm$^2$). The Rf values for the deposited platinum films were calculated according to Elliott et al.[52] as described in Section 2.4.1, Chapter 2. Values of the Rf were then plotted against the deposition charge density as shown in Figure 4.11.

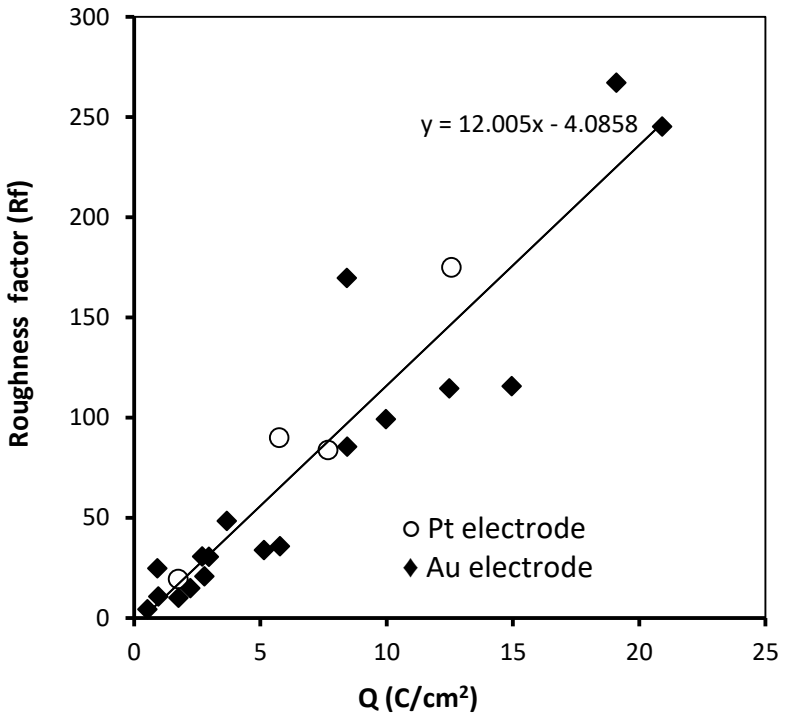


**Figure 4.11 Relation between roughness factor and deposition charge density for deposited platinum through monoolein template**. Deposition was carried out at platinum electrodes and gold electrodes of area $1.96 \times 10^{-3}$ cm$^2$ at a deposition potential of -0.25 V vs. Ag/AgCl at room temperature. (Pt ○ Au ♦).

The analysis of the Rf showed that the Rf values increased linearly with the deposition charge density. The results are not affected by whether the electrode is made of Pt or Au as shown in Figure 4.11. These results confirm uniform accessibility of pores throughout the film

thickness. The specific surface area of the platinum films deposited through monoolein (Cithrol) was estimated to be (~ 2.2 $m^2/g$) which is 6X lower that estimated for the nickel films deposited through monoolein (Rylo). For comparison, platinum films with different charge densities (2 to 20.4 $C/cm^2$) were deposited through phytantriol at -0.25 V as reported by Akbar et al.[41]. The Rf values were calculated for the deposited platinum films as described above. The Rf values were plotted against the charge density (Figure 4.12). Similar results were obtained when electrodeposition experiments were performed through a cubic phase of phytantriol (Figure 4.12). However, the values of Rf were much higher with the phytantriol template than with monoolein template (Figure 4.11). For the same charge density the surface area of the phytantriol templated platinum was found to be > 10X greater than the monoolein templated one. The possible explanation of this could be due to a greater surface area relative to volume because the lattice parameter is smaller for phytantriol. However, further investigations are needed to clarify this point.

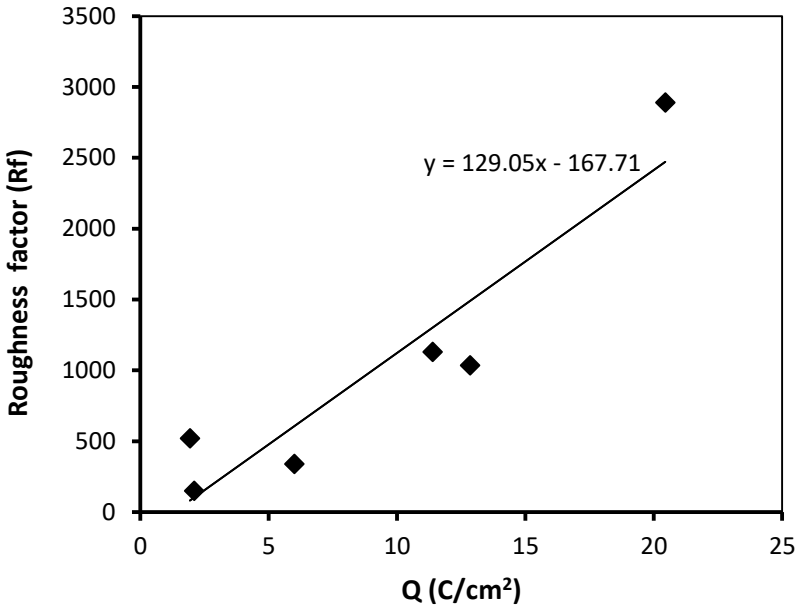


**Figure 4.12 Variation in roughness factor with respect to deposition charge density for deposited platinum through phytantriol template.** Deposition of platinum was carried out at room temperature on gold electrodes (area = $1.96 \times 10^{-3}$ $cm^2$) through cubic phases of phytantriol at a deposition potential of -0.25 V vs. Ag/AgCl.

### 4.3.5 Structural characterisation of nanostructured platinum film

SAXS analysis was used to reveal the structure of the electrodeposited platinum films. Initially, electrodeposition of platinum metal through the cubic phase of monoolein was carried out on a gold-coated glass slide (area = 0.24 $cm^2$) using a Autolab PGSTAT101 potentiostat. Then the film was washed in ethanol to remove the monoolein template. The structural characterisation of the deposited platinum film was conducted using synchrotron SAXS (Beamline I07, Diamond, UK). SAXS patterns of the deposited film are shown in Figure 4.13.

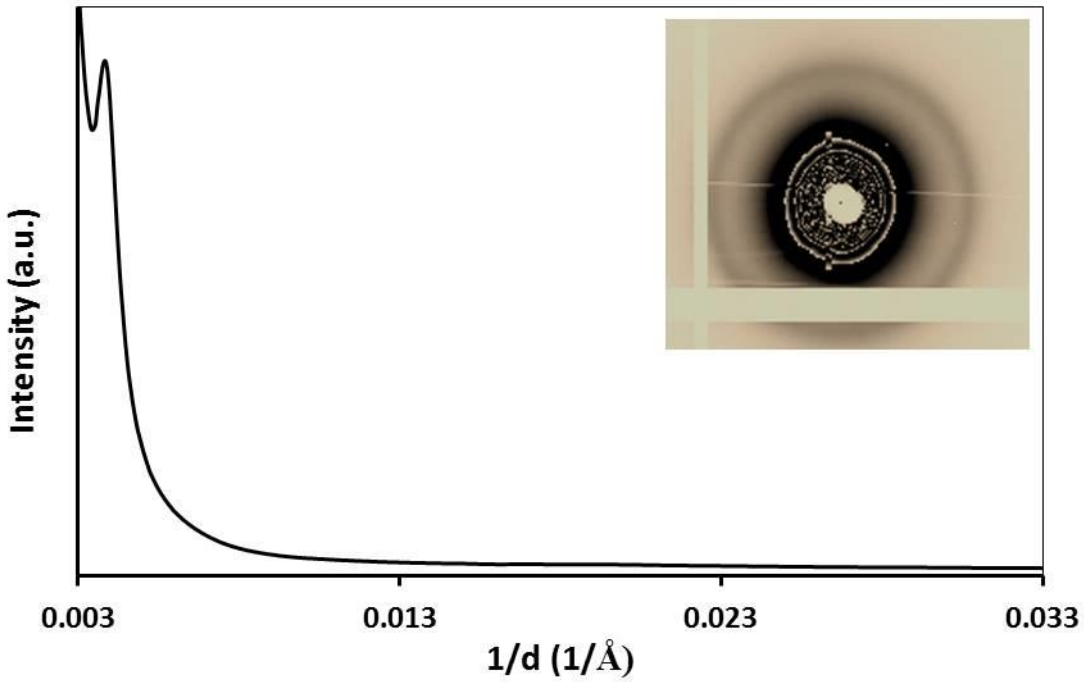


**Figure 4.13 SAXS patterns for nanostructured platinum film.** Platinum deposition was carried out at room temperature on gold glass electrode (area = 0.24 $cm^2$) at potential of -0.25 V vs Ag/AgCl. Charge density of the deposited film was calculated to be 2 $C/cm^2$.

2-D SAXS patterns of the deposited platinum film showed a ring indicating the presence of nanostructure of the deposited platinum film. 1-D SAXS patterns of the deposited platinum film showed the presence of one predominant peak at 1/d = 0.0038 $Å^{-1}$. The calculated lattice parameter for this peak is 456 Å. Based on the data in Figure 4.1, this lattice parameter is not consistent with the lattice parameters of the double ($a$ = ~ 93 Å) or single diamond ($a$ = ~186 Å) cubic phases of monoolein obtained with excess of HPCA solution. Therefore it is difficult to identify the structural symmetry of the deposited platinum film. However the 2-D pattern of the deposited films showed a ring which indicates the presence of nanostructure (Figure 4.13, inset). The possible explanation of this is that the obtained nanostructure of the platinum wire has very high lattice parameter which makes the peak shifted to $d$-spacing of 1/0.0038 Å. This also possibly decreased the accessible surface area.

## 4.4 Conclusion

3-D nanostructured platinum materials have been successfully fabricated using direct templating through the cubic phase of monoolein (Cithrol). The fabricated films were characterised using cyclic voltammetry and SAXS analysis. The deposition of the nanostructured platinum films was confirmed by SAXS and electrochemical analysis. However, the structure of the deposited film could not be identified from the SAXS analysis. Thus further analysis is required to find out the structure and stability of the deposited platinum materials. This work is the first attempt to use monoolein as a template for fabrication of 3-D nanostructured platinum.

# Chapter 5: Electrodeposition of nickel and platinum on 3-D metal porous scaffolds

## 5.1 Introduction

Currently, carbon-supported Pt nanoparticles systems are used for oxygen reduction reactions in energy conversion devices and storage devices such as fuel cells[196] and batteries[197]. However, besides the high cost and the limited resource of pure Pt[198], the high-surface-area carbon supports are subject to aggregation and corrosion during the oxygen reduction reaction inside the fuel cells[88]. For these reasons, research interest has increased towards replacing the conventional carbon-supported platinum nanoparticles systems with systems of mesoporous platinum only or mesoporous Pt-alloys. In 2012, it was reported that mesoporous platinum was found to show high stability compared to Pt nanoparticles[103]. Interestingly, the catalytic activity of pure platinum was found to increase by alloying platinum with transition metals (e.g. Ni, Co, Fe, Cu, etc)[199]. Transition metals were found to change the electronic structure of the surface Pt atoms in the Pt alloys leading to beneficial interaction with oxygenated intermediates during oxygen reduction reactions[199].

The ability to design a 3-D porous network with a high surface area to act as a current collector, is highly desirable in order to increase the mass loading of active materials and facilitate the transport of ions and electrons[56]. Recently a Pt/Ni thin film with double gyroid morphology was fabricated using co-electrodeposition of Pt and Ni into mesoporous silica. The fabricated film exhibited high activity and stability for the oxygen reduction reaction[108].

Herein, we report for the first time the fabrication of Pt/Ni and Ni/Pt composite by electrodeposition of Pt and Ni through 3-D Ni and Pt porous metal scaffolds, respectively. In the previous chapters in this thesis, we reported a versatile approach for the fabrication of novel 3-D Ni and Pt porous nanostructures via electrodeposition through a thin film of monoolein. Herein, 3-D Ni porous networks were fabricated again using the same approach and under the same conditions used in the previous chapters. The 3-D Ni porous networks were fabricated by electrodeposition through cubic phases of monoolein at room temperature at -0.95 V vs. Ag/AgCl. The 3-D porous Pt films were fabricated by electrodeposition through cubic phases of phytantriol[41] at room temperature at potential of -0.25 V vs. Ag/AgCl. The fabricated 3-D Ni and Pt[41] films are expected to have single diamond morphology structure. Also they are expected to have high electrochemical surface area. The fabricated 3-D Ni and 3-D Pt porous films were then used as scaffolds to provide high surface area for loading platinum and nickel to form Pt/Ni and Ni/Pt composite, respectively. The fabricated composites are expected to have high surface area.

The possible hypotheses by which the Pt and Ni (referred to as second metal) deposited through the porous metal scaffolds (referred to as first metal) are illustrated in Figure 5.1. In these hypotheses, the structure of the first metal (the porous Ni or Pt film) is assumed to be 3-D structure with single diamond morphology.

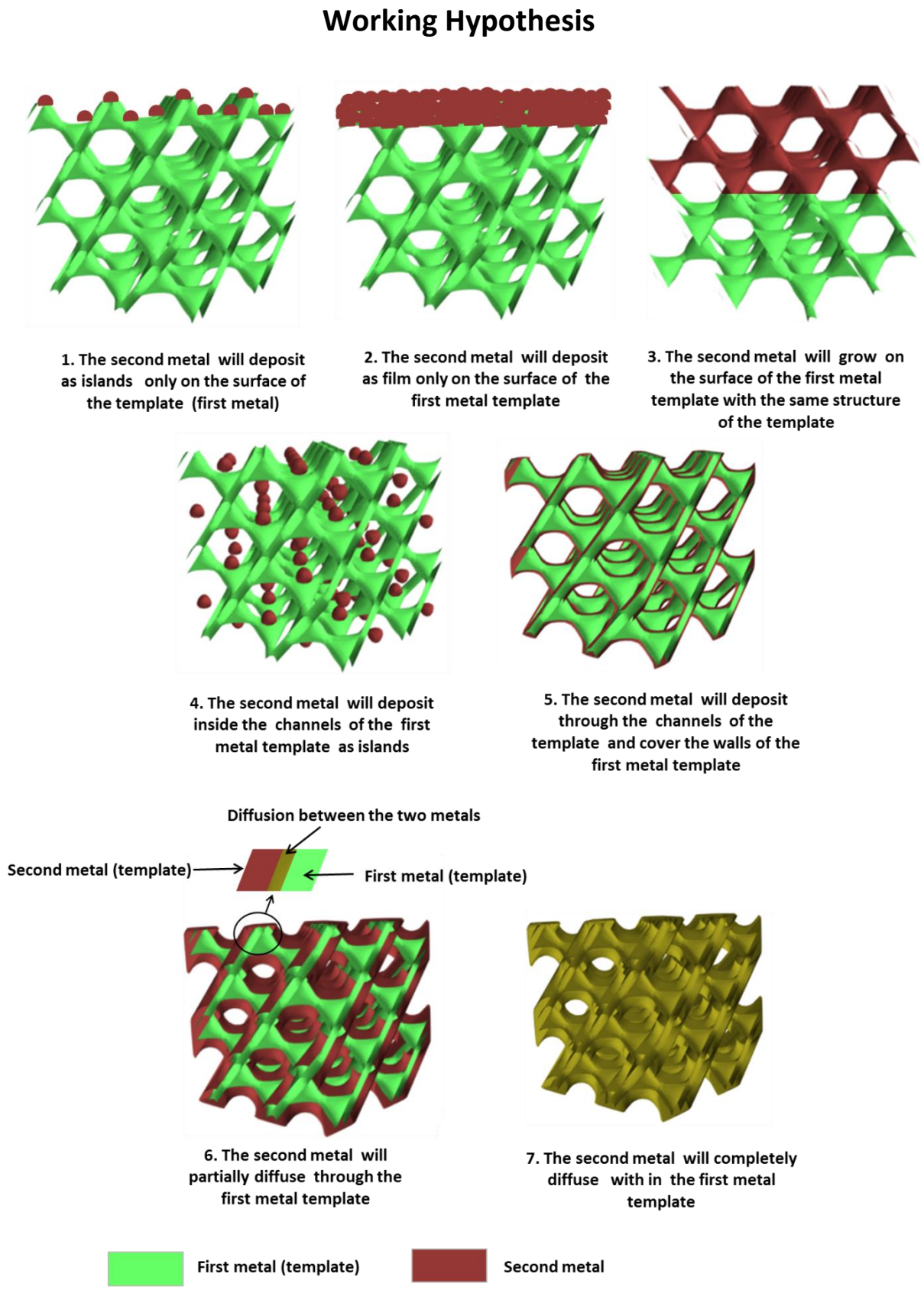


**Figure 5.1 The possible hypothesis of the deposition mechanism of the second metal (Ni or Pt) on the porous metal scaffolds (first metal).** The figures were designed using Enthought Canopy Python software

## 5.2 Methodology

Initially, mesoporous nickel and platinum films were prepared by direct templating through the cubic phases of monoolein (Cithrol) and phytantriol, respectively via electrodeposition. The electrodeposition was carried out on gold wire electrodes (area = $1.96 \times 10^{-3}$ $cm^2$) at room temperature. Electrodeposition of nickel films through monoolein (Cithrol) was conducted under the conditions used for electrodeposition of nickel at potential of -0.95 V through monoolein (Rylo) in Chapter 3. However, electrodeposition of platinum through phytantriol was conducted according to Akbar et al.[41,129], who previously reported the fabrication of 3-D platinum nanowires through cubic phases of phytantriol at potentials of -0.2 V and -0.25 V. The fabricated nickel and platinum films were then used as hard templates for the electrodeposition of platinum and nickel, respectively. The fabricated Ni, Pt, Ni/Pt and Pt/Ni films were characterised by cyclic voltammetry. All electrodeposition and characterisation experiments were carried out using an Autolab PGSTAT101 potentiostat.

## 5.3 Results and discussion

### 5.3.1 Fabrication of Pt/Ni mesoporous composite

#### 5.3.1.1 Electrodeposition of 3-D porous nickel film

Initially, four nickel films were electrodeposited from Ni deposition solution at room temperature with different charge densities. Electrodeposition was carried out on gold electrodes (area = $1.96 \times 10^{-3}$ $cm^2$) as described in Chapter 3. A deposition potential of -0.95 V was used. Prior to electrodeposition, the monoolein-coated electrodes were soaked in Ni deposition solution for 20 min as recommend in Chapter 3. Typical transients for nickel depositions are shown in Figure 5.2.

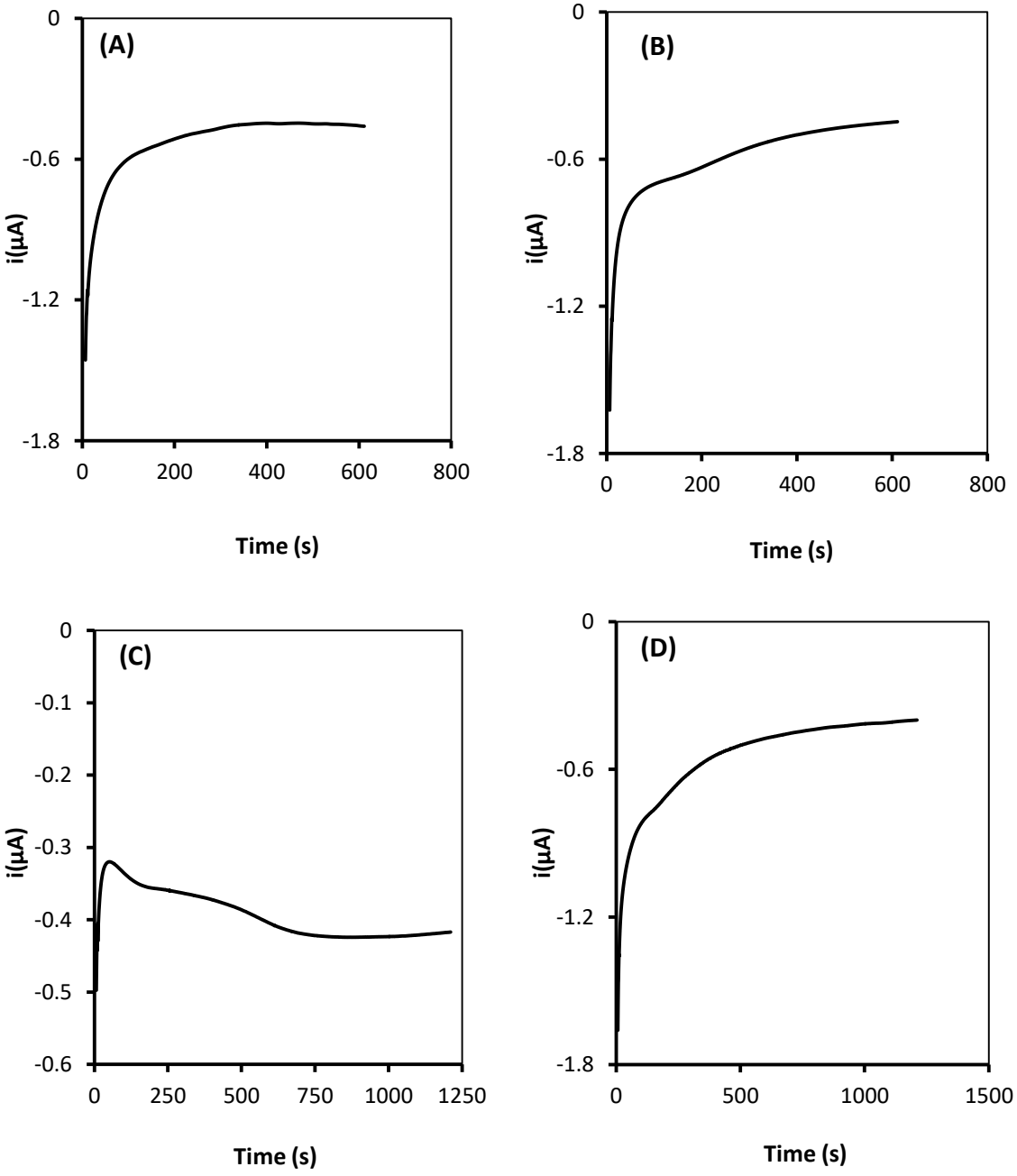


**Figure 5.2 Typical transients for nickel deposition on gold electrodes.** Electrodepositions were carried out on gold electrodes at room temperature through monoolein cubic phases at a deposition potential of -0.95 V with different charge densities **A)** 0.16 C/cm$^2$, **B)** 0.18 C/cm$^2$, **C)** 0.22 C/cm$^2$ and **D)** 0.33 C/cm$^2$.

### 5.3.1.2 Voltammetric behavior of the deposited Ni films in KOH

The deposited nickel films were characterised by cyclic voltammetry. Typical voltammograms of the deposited nickel films are shown in Figure 5.3. The differences in shapes of the voltammograms are due to different amount of the deposited nickel (as the films have different charge densities). The voltammograms of all deposited films showed large characteristic anodic peaks and large cathodic peaks at 0.3 and -0.28 V vs Ag/AgCl, respectively which correspond to nickel[130,55,176]. These results confirm the successful deposition of nickel through the cubic phases of monoolein (Cithrol).

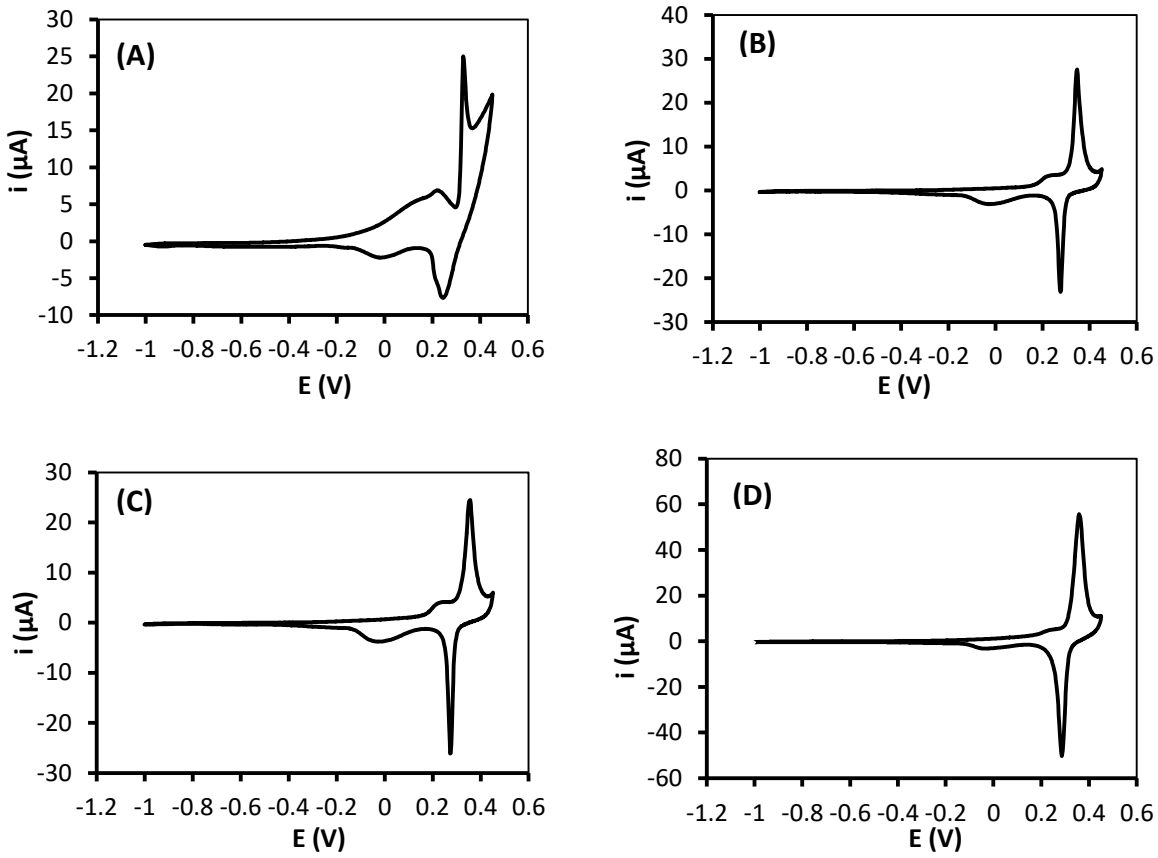


**Figure 5.3 Typical cyclic voltammograms of the deposited Ni films in 3 M KOH.** Cylic voltammetry was carried out at potentials between + 0.45 and -1.0 V vs Ag/AgCl at a scan rate of 200 mV/s. Charge densities of the nickel films were 0.16 C/cm$^2$ **(A)** 0.18 C/cm$^2$ **(B)** 0.22 C/cm$^2$ **(C)** and 0.33 C/cm$^2$ **(D).**

For further analysis, the voltammograms of the deposited nickel films through monoolein (Cithrol) were used to calculate the electrochemical surface area, specific surface area and the Rf for each deposition. The calculations were carried out as described in the methodology chapter, Section 2.4.1. The calculated values of Rf, electrochemical surface area and the specific surface area are shown below in Table 5.1. The calculated values of surface area of the deposited Ni films were relatively high, giving values of 18.49, 13.40, 10.02 and 16.21 $m^2/g$ for Ni films with charge density of 0.16, 0.18 0.22 and 0.33 $C/cm^2$, respectively.

The values of the Rf for the deposited nickel films were plotted against their charge density (Figure 5.4). The roughness factor was found to increase with increasing the charge density. These results confirm the deposition of nickel through monoolein (Cithrol) with 3-D nanostructure and in turn with high surface area. These results also confirmed the results obtained in Chapter 3 with electrodeposition of nickel through monoolein (Rylo) template.

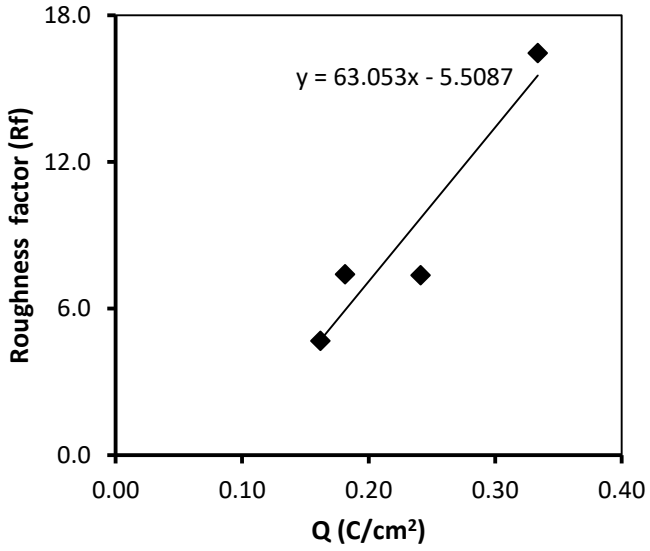


**Figure 5.4 Changes in the Rf value with respect to charge density of the Ni films deposited through monoolein (Cithrol).** Nickel was deposited through monoolein (Cithrol) on gold electrodes (area = $1.96 \times 10^{-3}$ $cm^2$) at room temperature at potential of -0.95 V vs. Ag/AgCl). Rf values were calculated after cycling deposited nickel films in 3 M KOH at 200 mV/s scan rate.

### 5.3.1.3 Electrodeposition of platinum through porous nickel scaffold

The deposited nickel films prepared in Section 5.3.1.1 were used as templates for preparation of Pt/Ni mesoporous composite by electrodeposition. Platinum was electrodeposited from HCPA solution through the porous nickel scaffolds at a potential of -0.25 V vs. Ag/AgCl (as recommended in Chapter 4 in this work). Based on the charge density of the deposited nickel films, from the lowest to the highest ($Q_{Ni}$ = 0.16, 0.18, 0.24 and 0.33 C/cm$^2$), the deposited Pt/Ni composite were named Pt/Ni-eD1, Pt/Ni-eD2, Pt/Ni-eD3 and Pt/Ni-eD4, respectively. The typical transients for the Pt deposition through the porous nickel scaffolds are shown in Figure 5.5.

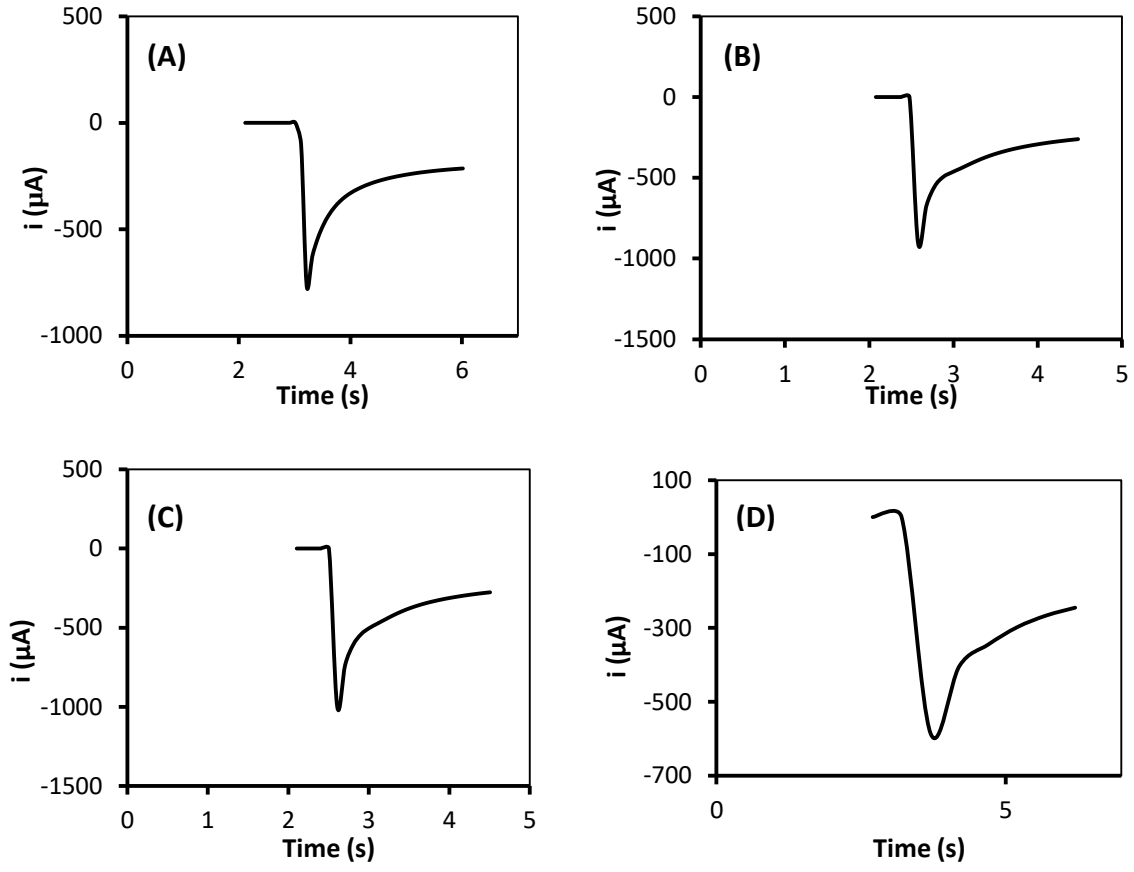


**Figure 5.5 Typical transients of platinum deposition through porous Ni scaffold.** Electrodeposition of platinum was carried out at room temperature at potential of -0.25 V through porous nickel films with different charge densities ($Q_{Ni}$ = 0.16 **(A)**, 0.18 **(B)**, 0.24 **(C)** and 0.33 **(D)**. The charge density of the corresponding platinum films ($Q_{Pt}$ = 0.45 C/cm$^2$ **(A)**, 0.39 C/cm$^2$ **(B)**, 0.42 C/cm$^2$ **(C)**, and 0.48 C/cm$^2$ **(D)**.

### 5.3.1.3.1 Voltammetric behavior of Pt/Ni films

After electrodeposition, the Pt/Ni films were analyzed electrochemically in 0.5 M aqueous $H_2SO_4$ between the limits of 1.2 to -0.28 V vs. Ag/AgCl. The typical cyclic voltammograms of the Pt/Ni films are shown in Figure 5.6. All the cyclic voltammograms demonstrated the successful deposition of Pt, showing typical adsorption/desorption features in the hydrogen under potential region (-0.35 to 0.1 V vs. Ag/AgCl) which correspond to different platinum facets[131,133]. These results indicate the deposition of platinum on the porous nickel films.

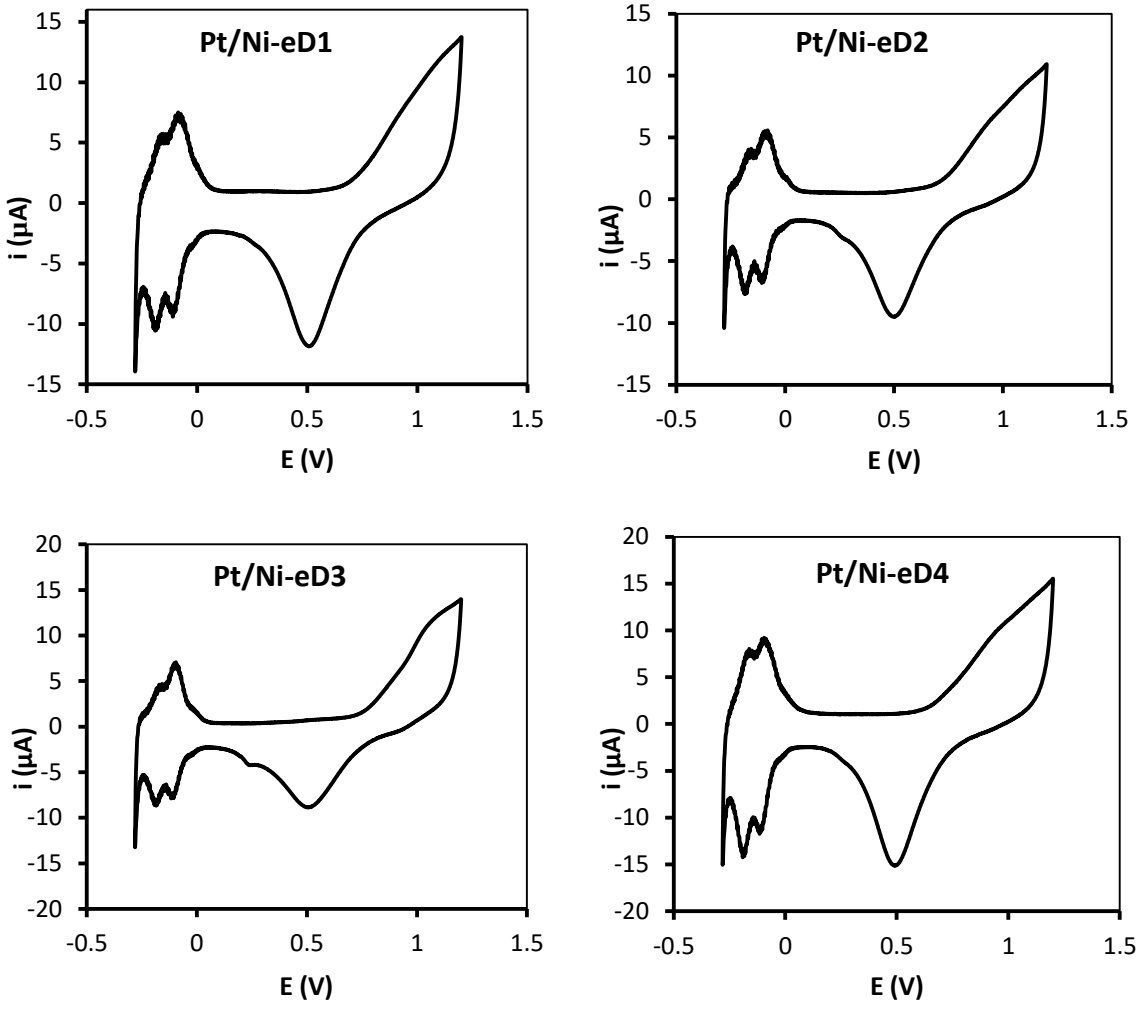


**Figure 5.6 Typical cyclic voltammograms of deposited Pt/Ni film in 0.5 M $H_2SO_4$.** Pt/Ni electrodes were cycled in 0.5 M $H_2SO_4$ at room temperature between the limits of +1.2 to -0.28 V vs Ag/AgCl at 200 mV/s scan rate.

For further analysis, the Rf values, electrochemical surface area as well as the specific surface area of the deposited platinum films were calculated from the voltammograms of each deposition. The calculations were carried out as described in the methodology chapter, Section 2.4.1. The values of Rf and specific surface area of the deposited Pt films through nickel are shown below in Table 5.1.

Changes in roughness factor with respect to charge density of the deposited platinum on the nickel scaffolds are shown in Figure 5.7. The value of roughness factor was found to increase with the charge density. These results confirm the deposition of platinum through nickel with a 3-D nanostructure.

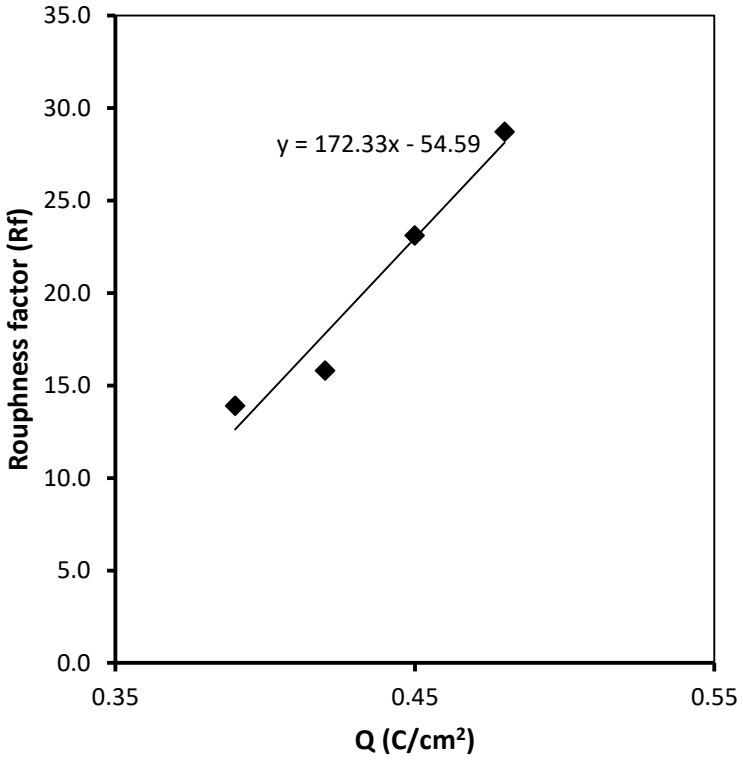


**Figure 5.7 Relation of the roughness factor and charge density of platinum films deposited through Ni scaffold.** Platinum was deposited through nickel template at room temperature at deposition potential of -0.25 V vs. Ag/AgCl). Rf values were calculated by cycling in in 0.5 M $H_2SO_4$ at 200 mV/s scan rate.

In order to confirm the presence of nickel in the deposited Pt/Ni composite, the four fabricated Pt/Ni composites were cycled also in 3 M KOH. The corresponding voltammograms are shown in Figure 5.8. The voltammograms of all Pt/Ni composites showed the presence of small anodic and small cathodic peaks at 0.3 V and at -0.28 V instead of the large ones which appear in the cyclic voltammogram of pure nickel (shown in Section 2.4.1, Chapter 2). The voltammograms of Pt/Ni also showed some other features which correspond to platinum. These results indicate the deposition of Pt through the porous nickel scaffolds (first metal), however the nickel films are not fully covered with platinum (second metal).

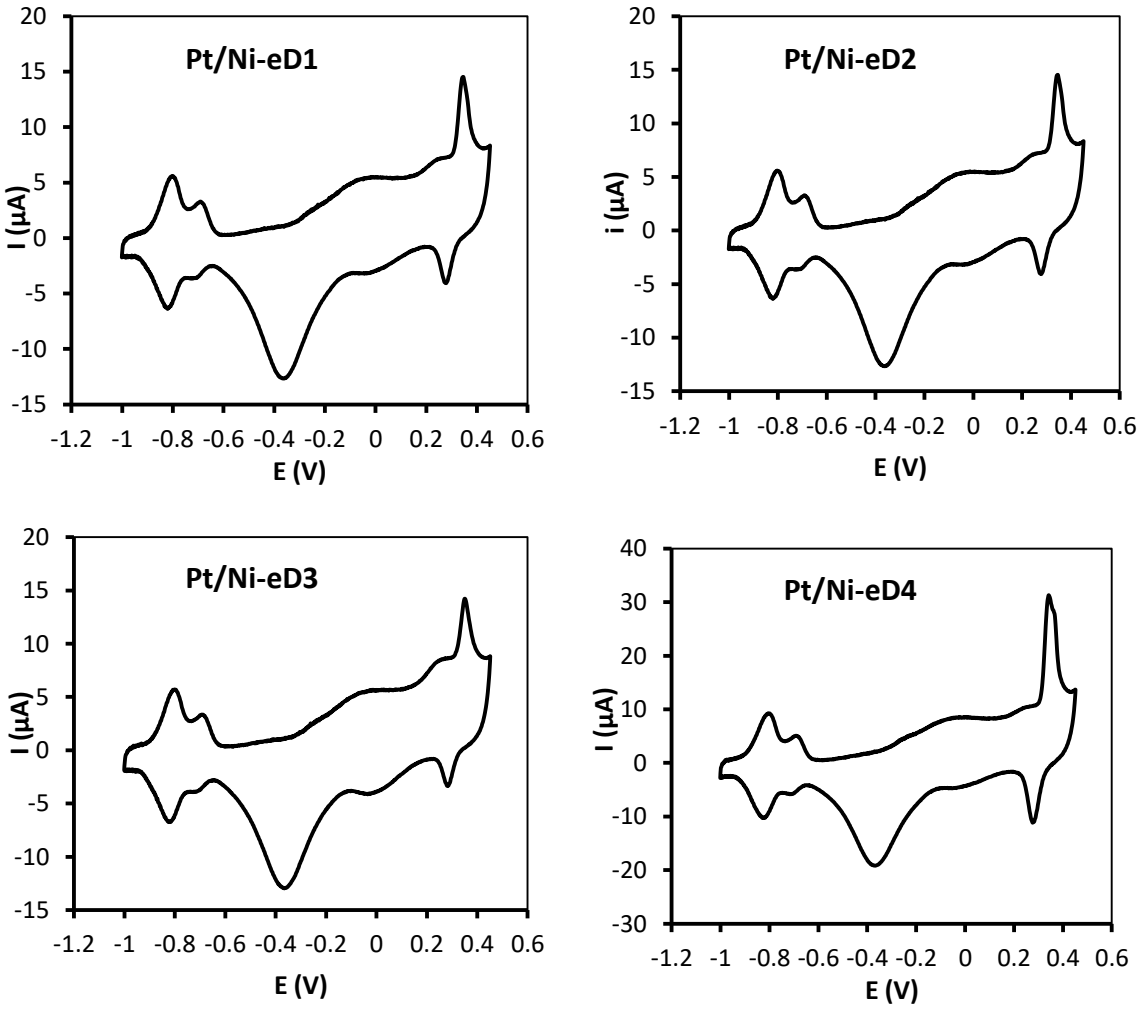


**Figure 5.8 Typical cyclic voltammograms of deposited Pt/Ni films KOH.** Cyclic voltammetry of Pt/Ni films was conducted in 3 M KOH solution at room temperature by potentials between +0.45 and -1.0 V vs Ag/AgCl and a scan rate of 200 mV/s.

The Rf and electrochemical surface area of the deposited nickel films after deposition of platinum were calculated from the voltammograms obtained when Pt/Ni films were cycled in KOH (Table 5.1). The values of roughness ratio (RR) were then calculated by dividing the values of the electroactive chemical surface area (ESA) of the second metal by that of the first metal. The analysis revealed that the values of the electrochemical surface area of nickel films (templates) were almost equal before and after deposition of platinum (Table 5.1).

**Table 5.1** Calculated electrochemical parameters for Pt/Ni composite

| **Electrochemical parameters** | | **Pt/Ni-eD1** | **Pt/Ni-eD2** | **Pt/Ni-eD2** | **Pt/Ni-eD4** |
|---|---|---|---|---|---|
| **Charge Density Q (C/cm$^2$)** | $Q_{Ni}$[a] | 0.16 | 0.18 | 0.24 | 0.34 |
| | $Q_{Pt}$ | 0.45 | 0.39 | 0.42 | 0.48 |
| **Rf** | $Rf_{Ni}$[a] | 4.1 | 7.4 | 7.4 | 16.5 |
| | $Rf_{Pt}$ | 23.1 | 13.9 | 15.8 | 28.7 |
| | $Rf_{Ni}$[b] | 6.0 | 6.7 | 7.0 | 13.0 |
| **Electrochemical s.a. (cm$^2$)** | $ESA_{Ni}$[a] | 0.016 | 0.015 | 0.014 | 0.032 |
| | $ESA_{Pt}$ | 0.045 | 0.027 | 0.031 | 0.056 |
| | $ESA_{Ni}$[b] | 0.012 | 0.013 | 0.014 | 0.026 |
| **RR($ESA_{Pt}/ESA_{Ni}$[a])** | $RR_{Pt}$ | 2.8 | 1.9 | 2.2 | 1.74 |
| **Specific s.a. (m$^2$/g)** | $ASA_{Ni}$[a] | 16.20 | 13.4 | 10.02 | 16.21 |
| | $ASA_{Pt}$ | 10.14 | 7.0 | 7.38 | 11.74 |
| | $ASA_{Ni}$[b] | 12.12 | 12.1 | 9.54 | 12.81 |

a = first metal before deposition of second metal, b = first metal after deposition of the second metal

### 5.3.2 Fabrication of high surface area Ni/Pt mesoporous composite via electrodeposition

Following the successful fabrication of high surface area Pt/Ni mesoporous composite demonstrated in the above sections, high surface area Ni/Pt mesoporous composites were fabricated using the same technique. The fabrication and the characterisation steps of Ni/Pt composite are discussed in the following sections.

#### 5.3.2.1 Electrodeposition of mesoporous platinum film

Based on the results reported in Chapter 4 in this thesis, the electrodeposition of mesoporous platinum from HCPA through monoolein (Cithrol) was found to produce 3-D platinum films with a relatively low surface area. However, in order to produce Ni/Pt composite with high surface area, 3-D porous platinum with a high surface area is required to act as an accessible surface area for nickel films. Therefore, platinum films were electrodeposited from HCPA solution through cubic phases of phytantriol which was expected to produce platinum nanowires with high surface according to Akbar et al.[41]. However, a deposition potential of -0.25 V was used as recommended in Chapter 4 in this thesis instead of potential of -0.2 V reported by Akbar et al.[41]. Four platinum films were deposited with different charge densities. Typical transients of platinum electrodeposition through phytantriol are shown in Figure 5.9.

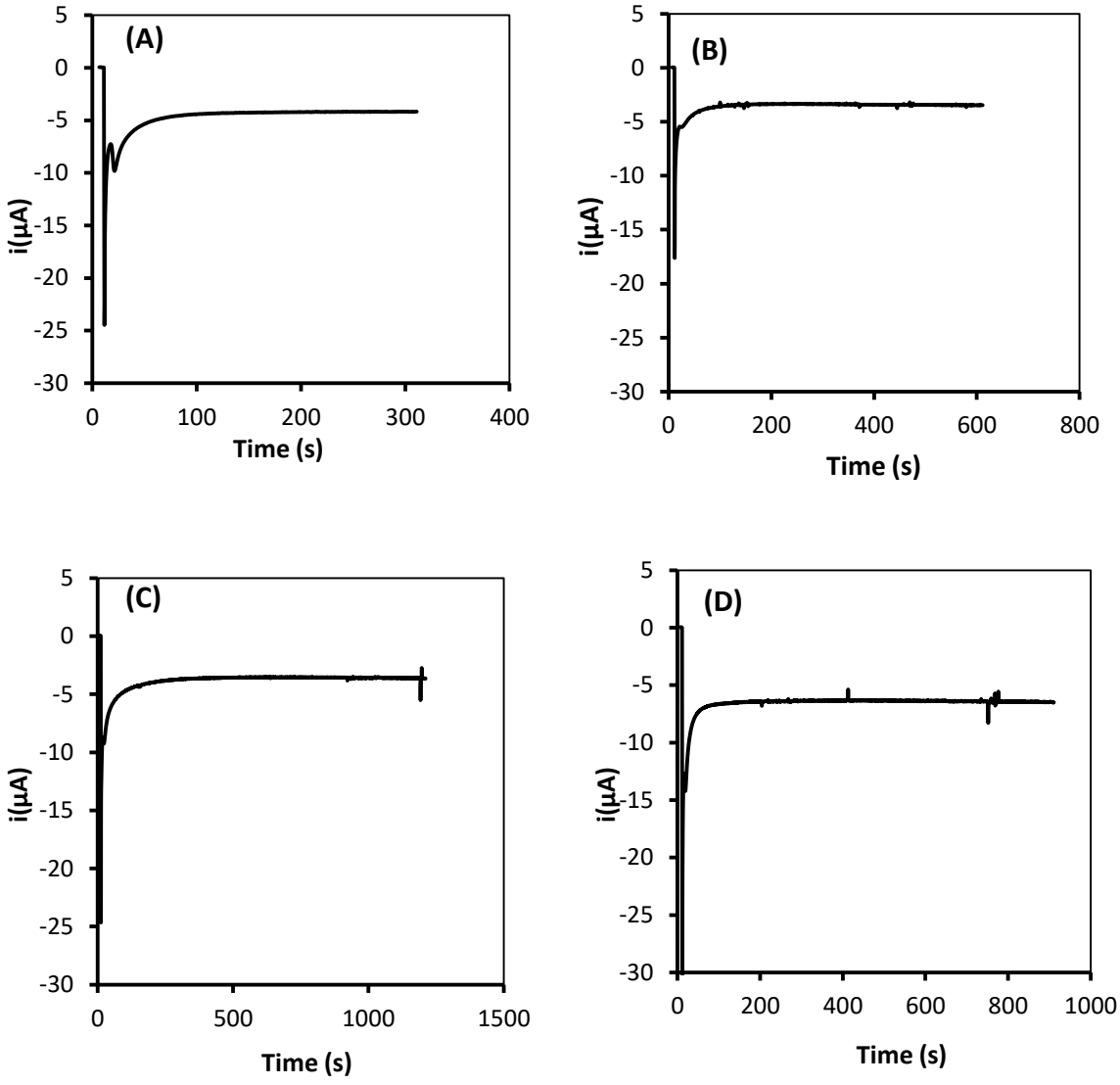


**Figure 5.9 Typical transients for platinum deposition on the gold electrodes.** Deposition of platinum was conducted though cubic phases of phytantriol at room temperature on gold electrodes with area of (area = $1.96 \times 10^{-3}$ $cm^2$) at a potential of -0.25 V vs. Ag/Ag/Cl with different charge densities $Q_{Pt}$ = 0.72 C/$cm^2$ **(A)**, 1.1 C/$cm^2$ **(B)**, 2.4 C/$cm^2$ **(C)** and 3.02 C/$cm^2$ **(D).**

### 5.3.2.2 Voltammetric behavior of deposited platinum films in $H_2SO_4$

After electrodeposition of platinum, the phytantriol template was removed from the films using ethanol. The deposited platinum films were then characterized electrochemically by cycling in 0.5 M aqueous $H_2SO_4$ between the limits of +1.2 to -0.28 V vs. Ag/AgCl. Figure

5.10 shows the typical cyclic voltammograms of the deposited platinum films. The voltammograms of all the deposited films showed typical platinum features in the region (-0.35 to 0.1 V) vs. Ag/AgCl[131,133]. These results indicate the successful deposition of platinum through the cubic phases of phytantriol.

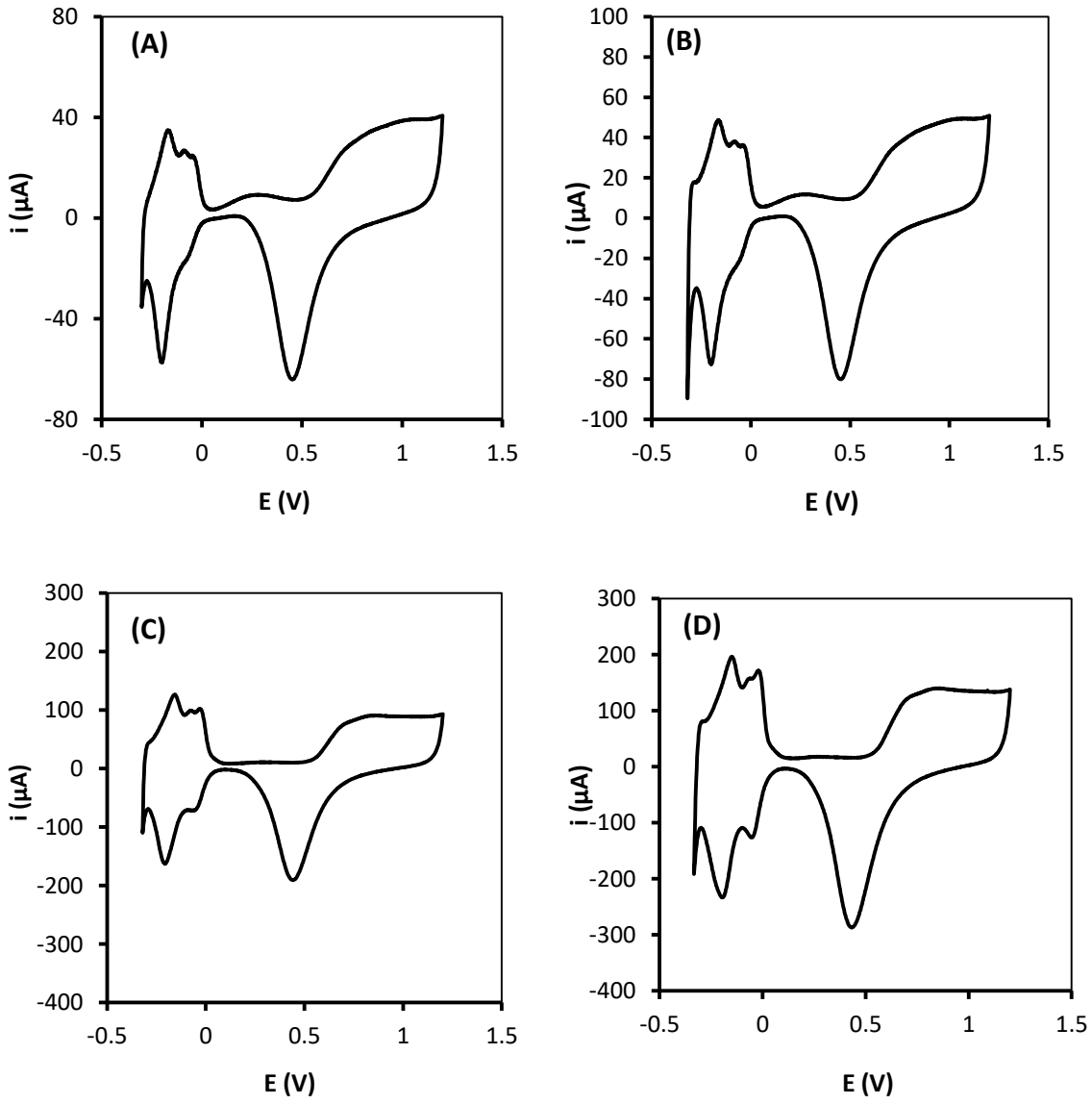


**Figure 5.10 Typical cyclic voltammograms of deposited platinum films in $H_2SO_4$.** Platinum electrodeposition was carried out though cubic phases of phytantriol at room temperature on gold electrodes with area of (area = $1.96 \times 10^{-3}$ $cm^2$) at potential of -0.25 V with different charge densities. Charge densities of the films ($Q_{Pt}$ = 0.72 $C/cm^2$ **(A)**, 1.1 $C/cm^2$ **(B)**, 2.4 $C/cm^2$ **(C)** and 3.02 $C/cm^2$ **(D)**. Cyclic voltammetry of the deposited platinum films was carried out at room temperature in 0.5 M $H_2SO_4$ at potentials between +1.2 and -0.28 V vs. Ag/AgCl at a scan rate of 200 mV/s.

The Rf values and the specific surface area of the deposited platinum were calculated from the voltammograms as described above. The values of Rf and specific surface are shown in Table 5.2. The Rf values were plotted against the charge density of the deposited films (Figure 5.11). A linear relation was found between the roughness factor and the charge density of the deposited platinum through phytantriol. These results confirm the 3- D symmetry of the deposited platinum films. The results also indicate the high surface area of the deposited films, giving specific surface area of the values of 23.1, 25.8, 28.5 and 39.4 $m^2/g$ for platinum films deposited with charge densities of 0.72, 1.1, 2.4 and 3.02 $C/cm^2$, respectively (Table 5.2). These results are in agreement with the results obtained with platinum films deposited through phytantriol at -0.2 V vs. Ag/AgCl by Akbar et al.[41]. Also they are consistent with the results obtained with the platinum films deposited through phytantriol at -0.25 V vs. Ag/AgCl performed in Chapter 4 in this thesis (Section 4.3.4.2).

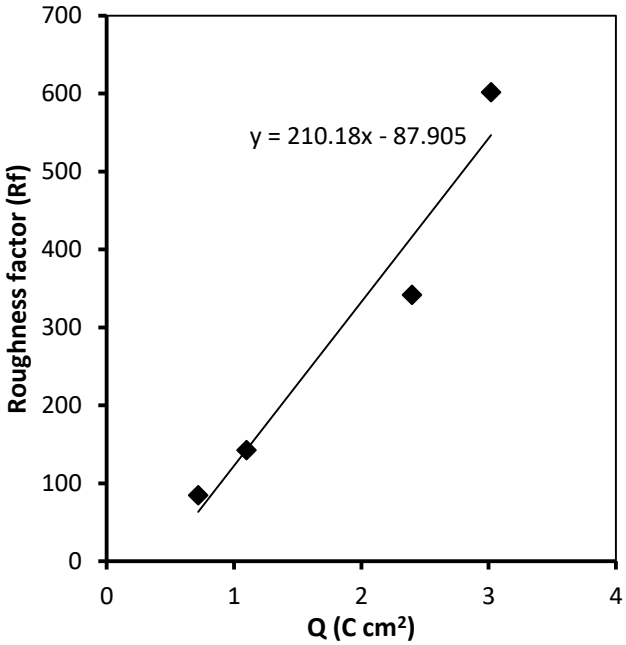


**Figure 5.11 Relationship between roughness factor and charge density for the deposited platinum on gold electrode.** Platinum deposited on gold electrodes (area = $1.96 \times 10^{-3}$ $cm^2$) at room temperature through cubic phase of phytantriol at potential of -0.25 V vs Ag/AgCl, Rf values were calculated after cycling the films in 0.5 $H_2SO_4$ at 200 mV/s scan rate.

### 5.3.2.3 Electrodeposition of nickel through porous platinum scaffold

The four platinum films prepared in Section 5.3.2.1 were used as templates for preparation of Ni/Pt composite. Nickel was electrodeposited at room temperature from Ni deposition solution through the porous platinum scaffolds at a potential of -0.95 V for almost constant time (~ 6 sec). The deposited Ni/Pt composites were named based on the charge density of the platinum templates: (Ni/Pt-eD1, Ni/Pt-eD2, Ni/Pt-eD3 and Ni/Pt-eD2), deposited through platinum films with charge densities of ($Q_{Pt}$ = 0.72, 1.1, 2.4 and 3.02 C/cm$^2$), respectively. Figure 5.12 shows the typical transients of nickel deposition through porous platinum scaffolds.

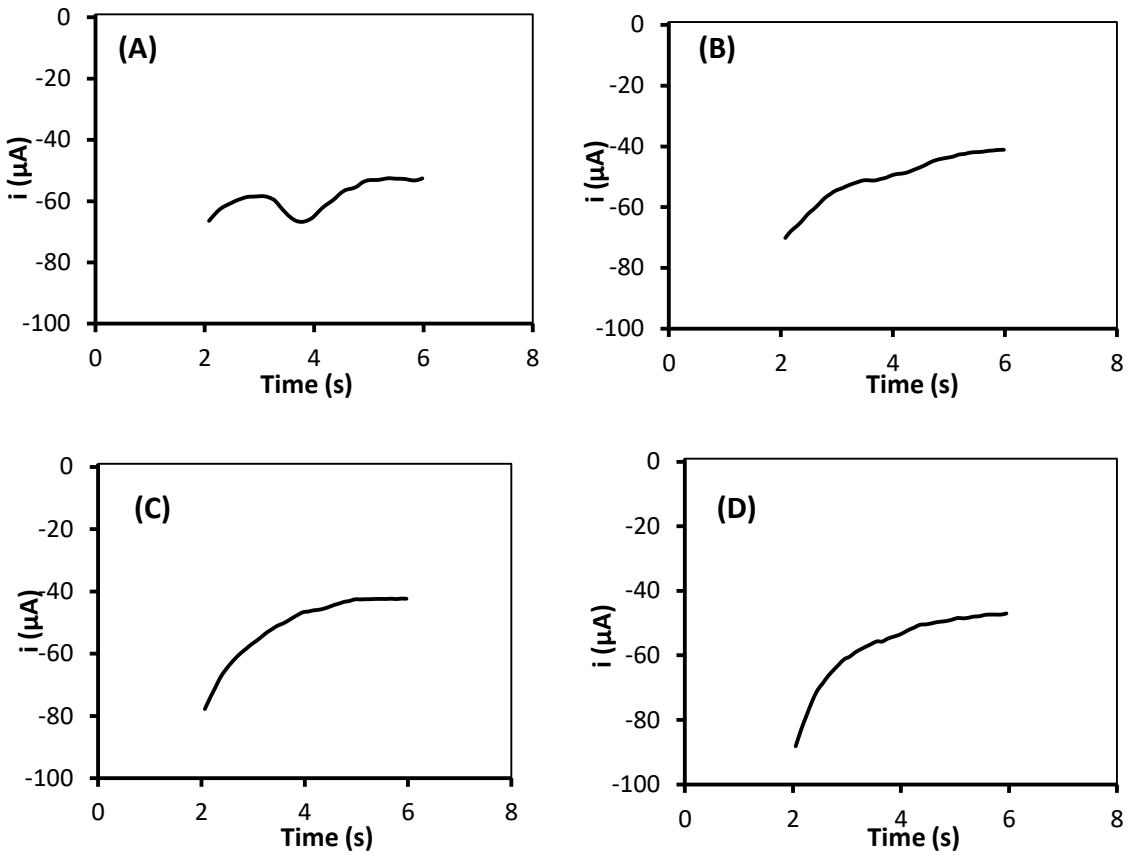


**Figure 5.12 Typical transients of nickel deposition through platinum scaffold.** Deposition of nickel was carried out through platinum films with different charge densities. Charge density of platinum films ($Q_{Pt}$ = 0.72 C/cm$^2$ **(A),** 1.1 C/cm$^2$ **(B)**, 2.4 C/cm$^2$ **(C)** and 3.02 C/cm$^2$ **(D).** The charge density of the corresponding nickel films ($Q_{Ni}$ **= 0.12** C/cm$^2$ **(A)**, 0.1 C/cm$^2$ **(B)** 0.1 C/cm$^2$ **(C)**, and 0.11 C/cm$^2$ **(D)**.

### 5.3.2.4 Voltammetric behavior of Ni/Pt films

The analysis was carried out by cyclic voltammetry in 3 KOH. Figure 5.13 show the typical voltammograms of the four fabricated Ni/Pt composite. The voltammograms of all four films indicted the presence of anodic large peaks at 0.3 V and large cathodic peaks at -0.28 V. These anodic and cathodic peaks are consistent with the reported peaks for nickel. However, the voltammograms showed other features appeared in region (-0.35 to 0.1 V) vs. Ag/AgCl which are most likely attributed to platinum. These results confirm the deposition of nickel on the porous platinum template, however the platinum templates were not covered completely with nickel. This was confirmed by the cyclic voltammetry of the composite in 0.5 M $H_2SO_4$, which revealed the typical features of platinum (Figure 5.14).

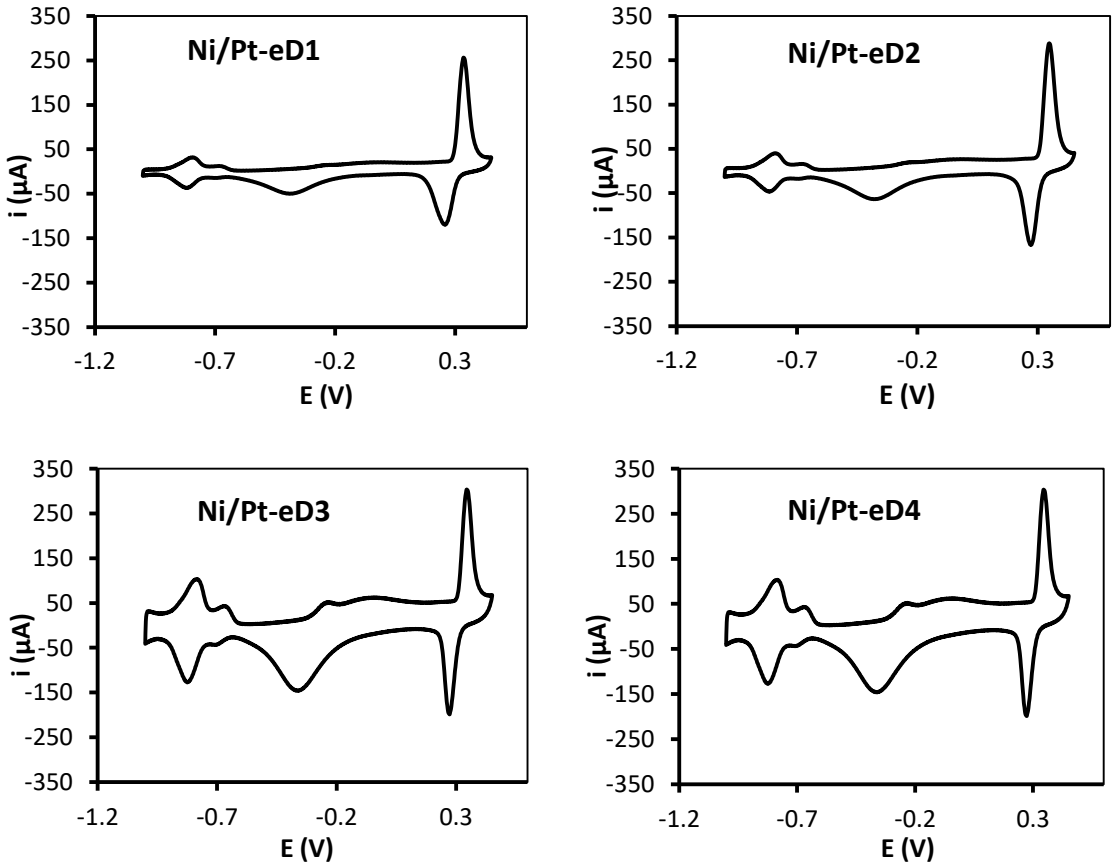


**Figure 5.13 Typical cyclic voltammograms of Ni/Pt films in KOH.** Ni/Pt films were cycled in 3 M KOH 200 mV/s scan rate at room temperature at potentials between + 0.45 and -1.0 V vs Ag/AgCl.

In order to reveal the surface area of the deposited nickel in the Ni/Pt composite, the values of the roughness factor and electrochemical surface area and the specific surface area were calculated for the deposited nickel films from the voltammograms corresponding to nickel deposition as described above. The calculated values of Rf and the electrochemical surface area are shown in Table 5.2. With all the fabricated Ni/Pt films, the values of the Rf and the associated specific surface area of the nickel films deposited through platinum were extremely high compared to these of the nickel films deposited through cubic phases of monoolein (Rylo and Cithrol).

For further analysis, the four fabricated Ni/Pt composite were cycled in 0.5 M $H_2SO_4$. Figure 5.14 show the typical voltammograms of Ni/Pt composite in $H_2SO_4$. With all four Ni/Pt composites, the voltammograms demonstrated the presence of platinum characteristic peaks at (-0.35 - 0.1 V) region vs. Ag/AgCl[131,133]. These results indicate the deposition of Ni through the porous platinum (first metal), however the platinum films are not fully covered with nickel (second metal).

The voltammograms obtained when Ni/Pt composite were cycled in $H_2SO_4$ were used to calculate the Rf and specific surface area of the deposited platinum films after deposition of nickel (Table 5.2). The results showed a slight decrease in the surface area of the deposited platinum films (scaffolds) after deposition of nickel compared to that before deposition of nickel (Table 5.2).

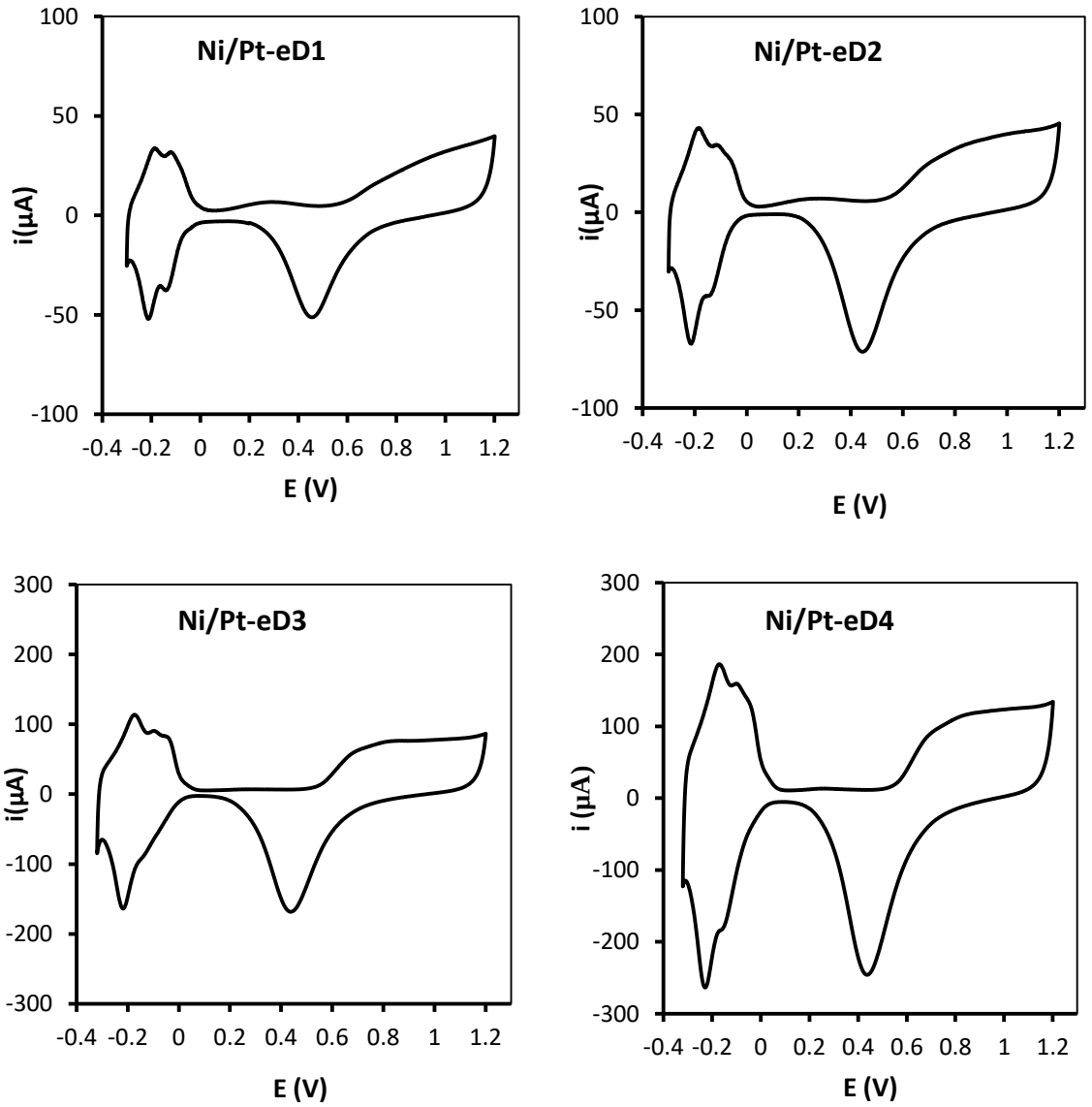


**Figure 5.14 Typical cyclic voltammograms of Ni/Pt films in $H_2SO_4$.** Ni/Pt films were cycled in 0.5 M $H_2SO_4$ at room temperature at potentials between +1.2 and -0.28 V vs. Ag/AgCl at 200 mV/s scan rate.

**Table 5.2** Calculated electrochemical parameters of the fabricated Ni/Pt composites

| **Electrochemical parameters** | | **Ni/Pt-eD1** | **Ni/Pt-eD2** | **Ni/Pt-eD3** | **Ni/Pt-eD4** |
|---|---|---|---|---|---|
| **Charge Density Q (C/cm2)** | $Q_{Pt}$[a] | 0.72 | 1.1 | 2.37 | 3.02 |
| | $Q_{Ni}$ | 0.12 | 0.1 | 0.1 | 0.11 |
| **Rf** | $Rf_{Pt}$[a] | 84.4 | 142.4 | 341.5 | 601.8 |
| | $Rf_{Ni}$ | 78.1 | 100.3 | 98.1 | 243.8 |
| | $Rf_{Pt}$[b] | 83.7 | 108.5 | 315.4 | 537.3 |
| **Electrochemical s.a. ($cm^2$)** | $ESA_{Pt}$[a] | 0.166 | 0.279 | 0.670 | 1.181 |
| | $ESA_{Ni}$ | 0.153 | 0.197 | 0.192 | 0.478 |
| | $ESA_{Pt}$[b] | 0.164 | 0.213 | 0.619 | 1.054 |
| **RR($ESA_{Ni}/ESA_{Pt}$[a])** | $RR_{Ni}$ | 0.93 | 0.70 | 0.29 | 0.41 |
| **Specific s.a. ($m^2/g$)** | $ASA_{Pt}$[a] | 23.09 | 25.84 | 28.55 | 39.43 |
| | $ASA_{Ni}$ | 219.36 | 327.39 | 317.33 | 708.1 |
| | $ASA_{Pt}$[b] | 22.91 | 19.69 | 26.36 | 35.2 |

a = first metal before deposition of second metal, b = first metal after deposition of the second metal

### 5.3.3 Proposed mechanism of the deposition of Ni and Pt through the porous metal scaffolds

Based on the electrochemical analysis of the fabricated Pt/Ni composites, it was found that the values of the specific surface area of the films of the second metal (Pt) were lower than these of the films of the first metal (Ni). Besides, the values of the electrochemical surface area of the films of the first metal (Ni) were approximately equal before and after deposition of the second metal (Table 5.1). These results suggested that the second metal (Pt) could be deposited only on the surface of the first metal (Ni) as islands (mechanism number 1, Figure 5.1). However, in case of Ni/Pt composites, the electrochemical analysis revealed that the values of the specific surface area of the second metal (Ni) were much higher than that of the first metal (Pt) (Table 5.2). In addition, the values of the electrochemical surface area of the films of the first metal (Pt) were slightly higher before deposition of the second metal (Ni) than for these films after deposition of the second metal (Table 5.2). These results suggested that the second metal deposited inside the channels of the first metal as islands as illustrated in Figure 5.1 (mechanism number 4). This is different from the deposition mechanism of the second metal in case of Pt/Ni composites. This could be related to the type of liquid crystalline template used in the fabrication of the films of the first metal (templates). Phytantriol has a smaller lattice parameter than monoolein therefore, the Pt films (first metal) fabricated through the phytantriol template has a smaller lattice parameter compared to the Ni films fabricated through cubic phases of monoolein. This helped the second metal (Ni), in case of Ni/Pt composites to deposit inside the channels of the first metal (Pt) as islands, giving films with very high surface area. The proposed mechanism of the deposition of Ni and Pt through the fabricated porous metal scaffolds is illustrated in Figure 5.15.

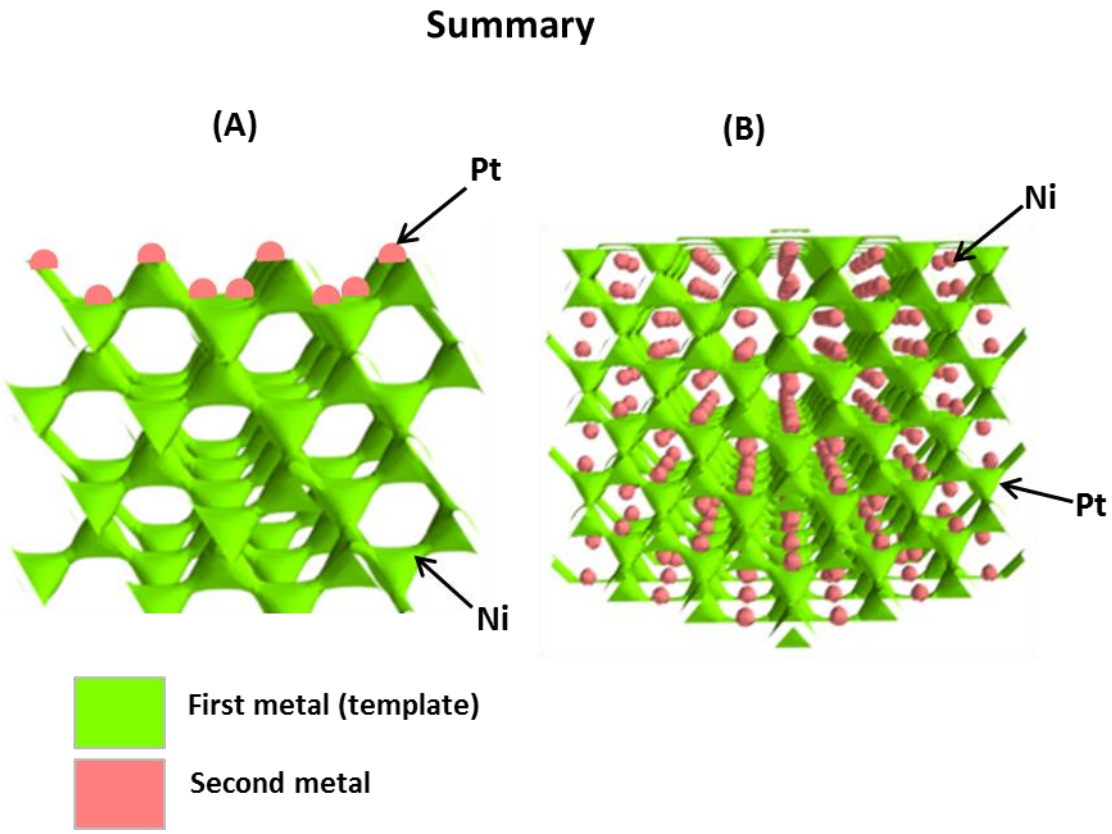


**Figure 5.15 Schematic illustration of the proposed mechanism for the deposition of the second metal on the first metal in the fabricated composites. (A)** Pt/Ni, the first metal (Ni) was fabricated by electrodeposition through monoolein and **(B)** Ni/Pt, the first metal (Pt) was fabricated by electrodeposition through phytantriol. Both figures were constructed using Enthought Canopy Python software.

## 5.4 Conclusion

In this chapter, we reported for the first time the fabrication of mesoporous Pt/Ni and Ni/Pt composites with high surface area using 3-D Ni and Pt porous scaffolds, respectively. The electrochemical analysis confirmed the 3-D symmetry of all the deposited metal films. Based on the electrochemical analysis, the proposed mechanism of the deposition of the second metal on the porous metal scaffold (first metal) for Pt/Ni composite varied from that for Ni/Pt composites. In case of Pt/Ni composites, it was suggested that platinum may be deposited only on the surface of the porous Ni films. However, in case of Ni/Pt composites, it was suggested that Ni may be deposited inside the channels of Pt porous films, producing films with very high surface area. Due to the high surface area of the Pt/Ni and Ni/Pt electrodes, they are expected to exhibit high electrocatalytic activity, Therefore they could be promising electrode materials for batteries and fuel cells. Further investigations are required to reveal the structural and the morphological features of the deposited (Pt/Ni) and (Ni/Pt) electrodes as well as to assess their electrocatalytic activities.

# Chapter 6: Physico-chemical characterisation of monoolein and control of its lattice parameters

## 6.1 Introduction

In the presence of water, monoolein assembles into a number of phases including lamellar, hexagonal, bicontinuous cubic and fluid isotropic (inverse micellar) phases[4]. The type of phase formed for monoolein-water mainly depends on temperature and/or water content. However, there are many different factors that can modulate the behavior of the monoolein-water system[4]. These include environmental factors such as temperature[6,4] pressure[25], magnetic fields[26] and electric fields[27]. Furthermore, addition of chemical compounds such as solvents or other additives could modulate the lyotropic behavior of monoolein-water system[200,4,29]. For example, addition of certain concentrations of lipids such as phosphatidylcholine (PC), cholesterol and others as additives to the monoolein-water system resulted in different phase transitions[29]. Other lipids were found to modify the phase behavior of monoolein-water system such as dioleoyl-phosphatidylglycerol (DOPG)[30], dioleoylphosphatidic acid (DOPA)[201], distearoylphosphatidylglycerol (DSPG)[31]. Furthermore, it was reported that addition of certain additives at certain concentrations can cause an increase in the lattice parameter and hence swelling of the aqueous channels of the monoolein cubic phases[202]. Further addition of these additives results in the transition to a 'sponge phase' made of a disordered bicontinuous film[4]. Examples of theses additives are polyethylene glycol (PEG) 400, potassium thiocyanate, Brij-58 and Brij-700[203]. In this work, the surfactant polyoxyethylene (10) cetyl ether (Brij-56) was used as a swelling agent. The choice of Brij-56 was based on its nature as a non-ionic surfactant which was found to alter the surface curvature of some liquid crystals[204,129]. Therefore, addition of such material to

monoolein/water system is expected to modulate the surface curvature of this system causing a swelling of the cubic phase of monoolein. In addition Brij-56 is chemically stable and it was used previously used for electrochemical templating of nanostructured metals[55]. Phytantriol/Brij-56/water was also used for fabrication of nanostructured platinum[129].

In this chapter, we have investigated some of the physicochemical properties of two monoolein products, namely Rylo (DANISCO, UK) and Cithrol (CRODA, UK) as used in the previous chapters as templates to fabricate of mesoporous nickel and platinum, respectively. The work in this chapter was carried out using different analytical techniques such as mass spectrometry, cross polarised light microscopy, and SAXS. Also the effect of Brij-56 as a swelling agent on the phase behavior of the monoolein-water system was investigated.

## 6.2 Methodology

In this chapter, the physical properties of monoolein products, namely Rylo and Cithrol were investigated using different analytical techniques. Initially the solidification of the two monoolein products was monitored using photography. Mass spectrometry was then used to assess the purity of the two materials. The mass analysis was carried out using a Thermo Scientific LTQ-Orbitrap-XL mass spectrometer connected to an Accela HPLC. The melting point of both materials was determined using differential scanning calorimeter (DSC). A Q2000 DSC instrument (UK) was used in the analysis. In order to study the phase behavior of Rylo and Cithrol at different temperatures, cross polarised light microscopy was used. The analysis was conducted using Zeiss Axioskop 40 polarizing microscope fitted with cross polarizing filters. During the analysis, monoolein samples were heated from 20 - 90 °C at a scan rate of 2 °C $min^{-1}$ using Linkam PE 94 heating stage. For further analysis, the effect of

temperature on the phase behavior of Rylo and Cithrol was also studied using SAXS analysis. The analysis was conducted using a Bruker Nanostar AXS small angle X-ray scattering instrument. The samples were scanned at different temperatures (25-90 °C). Initially, the samples were equilibrated for 20 min at each temperature followed by SAXS exposure for 10 min. Subsequently, the effect of the addition of Brij-56 on the phase behavior of the two monoolein products was studied. Initially, an ethanolic solution of monoolein, ethanolic solution of Brij-56 and monoolein/Brij-56 mixtures (containing 3-25 % Brij-56 (w/w) were prepared as described in Chapter 2, Section 2.3.4 The samples of monoolein/water in the absence or presence of different concentrations of Brij-56 were prepared for SAXS analysis using capillary cell preparation as described in Chapter 2, Section 2.4.5.2. The phase behavior of these samples was then characterised using a Bruker Nanostar AXS small angle X-ray scattering system operated at 45 kV and 650 µA.

## 6.3 Results and discussion

### 6.3.1 Comparison of purity of monoolein

Mass spectroscopy was used to investigate the purity of Rylo and Cithrol. The analysis of the mass spectra was performed using a Thermo Xcalibur 2.1 software. In general, mass spectrometry provides accurate information on the relative masses of the isotopes and their proportions (relative abundance). The mass spectra revealed that Rylo and Cithrol are relatively impure monoolein. The analysis showed that the relative abundance of the isotopes in both materials is essentially the same. The only obvious difference between the two materials is the peak at approx. 6.1 mins which is higher in Rylo (Figure 6.1A) than Cithrol (Figure 6.1B). The main component of this peak may potentially be $C_{22}H_{43}NO$ (mass =

338.34174) which is Erucyl amide; Cis-13-Docosenoamide, reportedly used as a solvent for waxes. This indicates the presence of fewer impurities in Cithrol than in Rylo.

The analysis of the relative masses of the isotopes in Rylo and Cithrol revealed the presence of many peaks in the region (300 -1342 m/Z), indicating the presence of some impurities (Figure 6.2A, 6.3A). The analysis also confirmed the presence of monoolein in both Rylo (Figure 6.2) and Cithrol (Figure 6.3). This was indicated by the presence of a peak with a mass of 357.3002 m/Z in the mass spectra corresponding to both products (Figure 6.2B, and 6.3B). This peak is potentially corresponding to the first isotope of monoolein. The molecular formula of this component is calculated to be $C_{21}H_{41}O_4$. This means the mass is 1 g/mol higher than the empirical molar mass of monoolein (356.55 g/mol) for the formula of $(C_{21}H_{40}O_4)^4$. The detected extra hydrogen mass unite could be a contaminant from the buffer used in the analysis. The analysis also showed the presence of a second peak with a mass of 358.3035 m/Z which is most likely corresponding to the second isotope of monoolein.

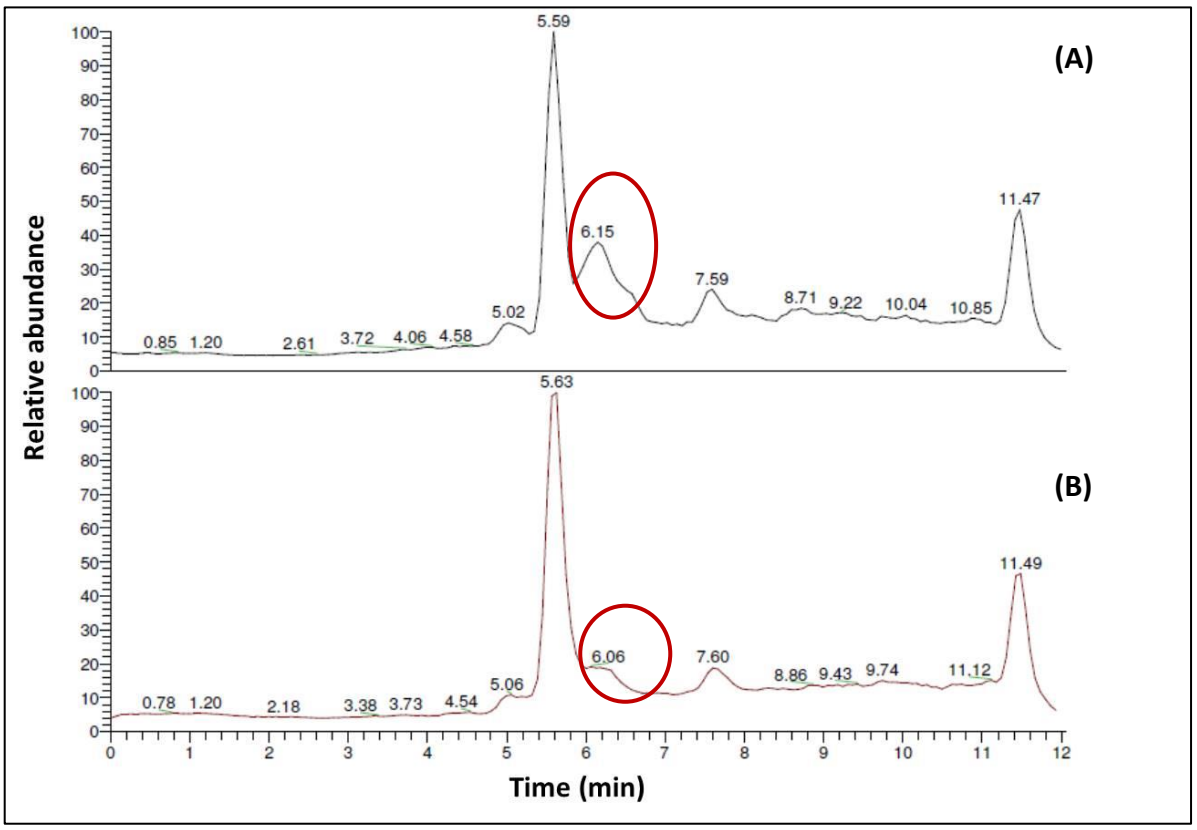


**Figure 6.1 Relative abundance of A) Rylo and B) Cithrol with time.** Red circles represent peaks observed after ~ 6.01 min in both spectra which are corresponding to Erucyl amide.

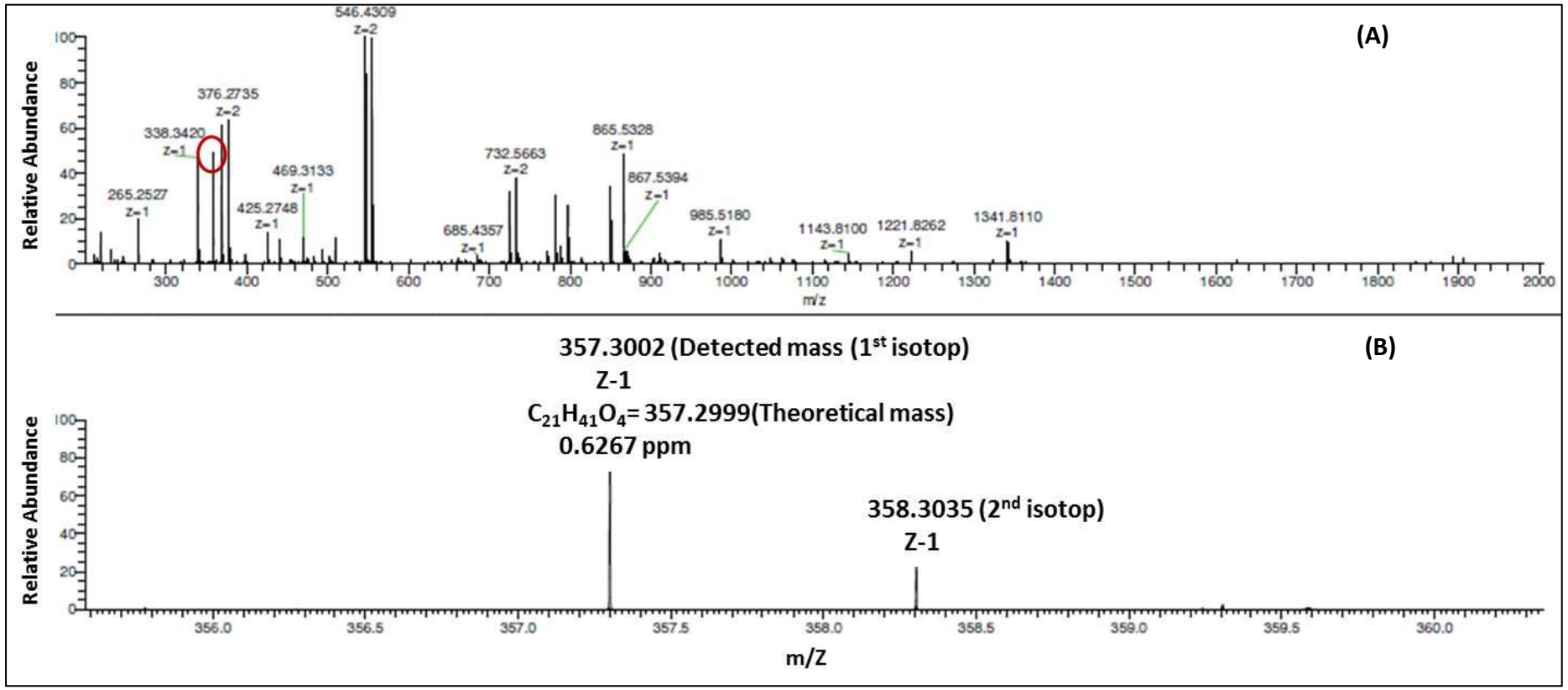


**Figure 6.2 Mass spectra of Rylo.** Red circle represents isotopic mass of Rylo: **(A)** Raw data and **(B)** Identification of the peaks corresponding to monoolein using a Thermo Xcalibur 2.1 software.

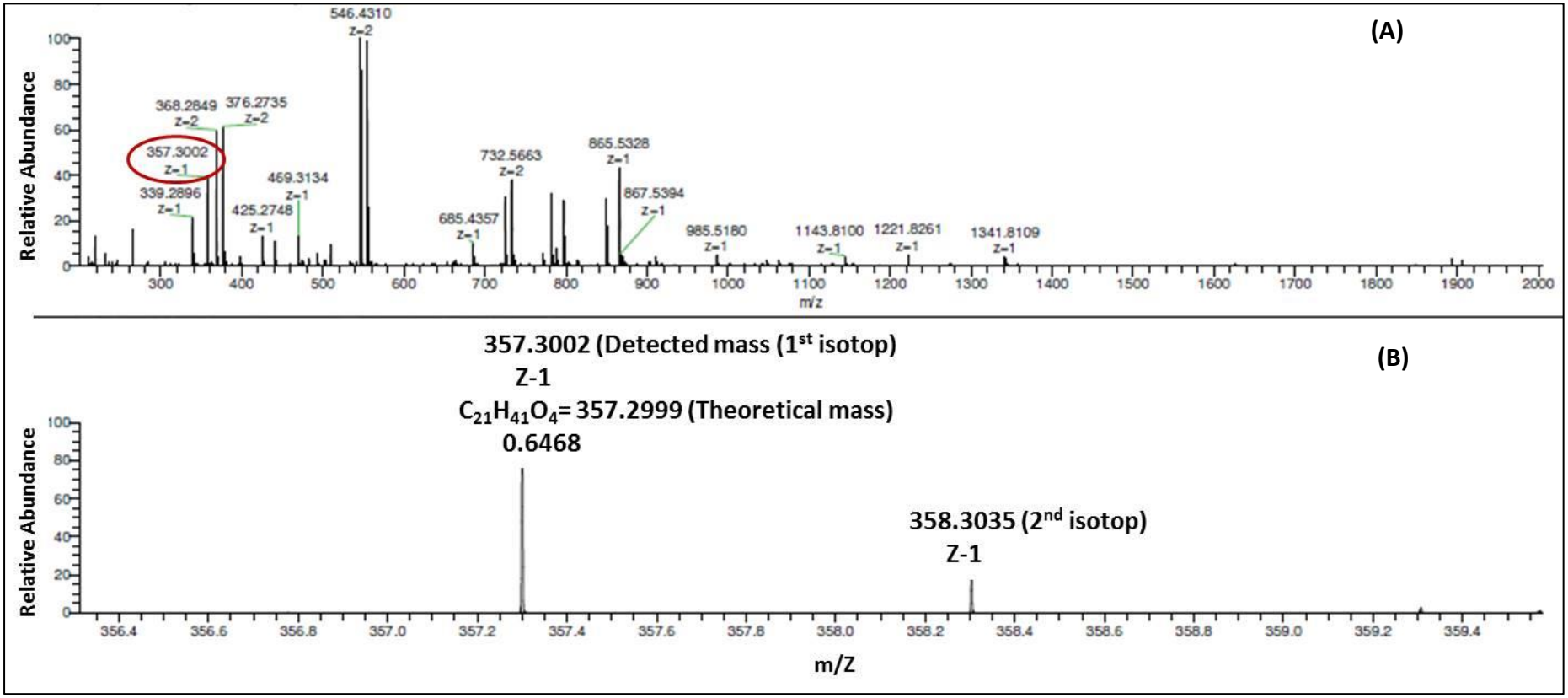


**Figure 6.3 Mass spectra of Cithrol.** Red circle points to the isotopic mass of Cithrol. **(A)** Raw data and **(B)** Identification of the peaks corresponding to monoolein using a Thermo Xcalibur 2.1 software.

### 6.3.2 Solidification of monoolein at room temperature

During experiments using monoolein samples of Rylo and Cithrol, it was observed that the two materials had different solidification behavior at room temperature. In order to study the solidification behavior of the two monoolein materials at room temperature, equal amounts of Rylo and Cithrol were melted at 40 $^{o}$C and then left at room temperature for more than 24 hours. It was observed that after melting Rylo at 40 $^{o}$C, it stays liquid at room temperature for approximately 30 min, and then it starts to solidify again (Figure 6.4). However, after melting Cithrol at 40 $^{o}$C, it can stay liquid at room temperature for more than 3 days and a nucleation event is required to start solidification (Figure 6.4). Photographs of monoolein solidification at room temperature are shown in Figure 6.4.

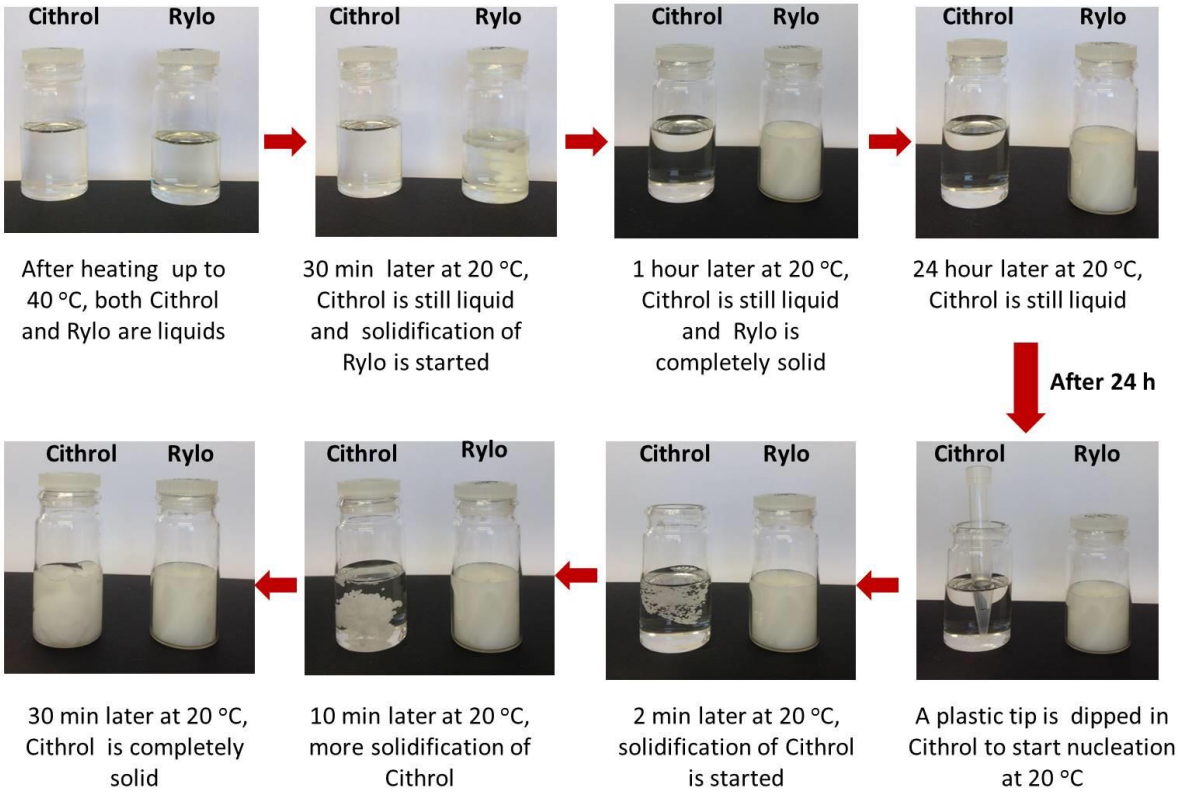


**Figure 6.4 Photographs of the solidification behavior of monoolein.**

### 6.3.3 Differential scanning calorimetry analysis (DSC)

In order to detect the melting point of Rylo and Cithol, DSC analysis was used. The analysis was conduct using a Q2000 DSC instrument (UK). The results are shown in Figure 6.5. Generally, the melting temperature is measured at the onset point of the melting curve. From the melting curves of Rylo and Cithrol shown in Figure 6.5, the melting points of Rylo and Cithrol were found quite close, giving values of 28 and 28.5 $^{o}$C, respectively.

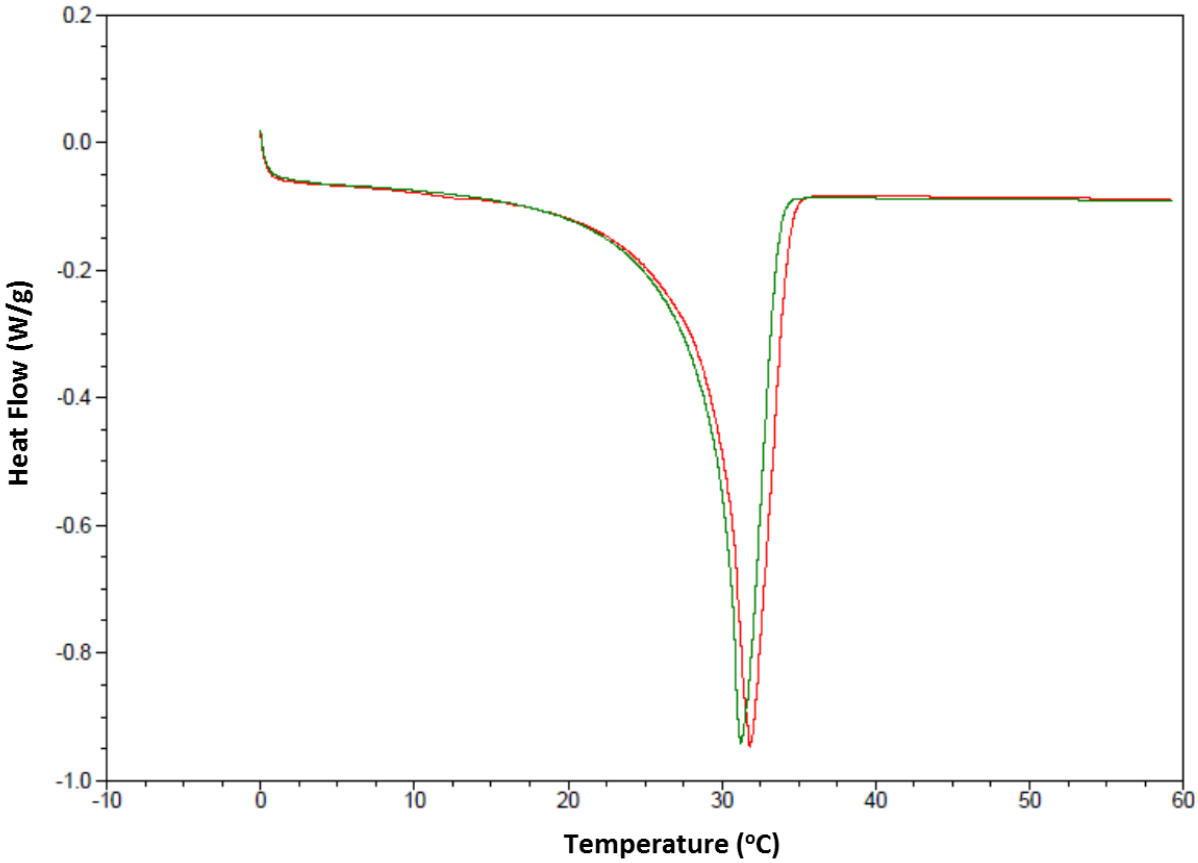


**Figure 6.5 DSC thermograms for Rylo (in red) and Cithrol (in green).**

### 6.3.4 The phase behavior of monoolein

Cross polarised light microscopy (CPLM) and SAXS analysis were used to compare the phase behavior of Rylo and Cithrol monoolein samples. The CPLM analysis was conducted at different temperatures (25-90 °C). The analysis revealed that both monoolein materials exhibited a $Q_{II}$ phase in contact with excess water at room temperature. This was indicated by conversion of the optically birefringent phase (dry material at 25 °C) to distinct optically isotropic cubic phase with a structured phase boundary (with a more irregular shape) when water was added to small droplets of both materials under CPLM at room temperature (Figure 6.6 and 6.7). By increasing the temperature, the isotropic texture of monoolein/water interface of the $Q_{II}$ phase was converted to hexagonal $H_{II}$ phase, which is characterized by a birefringent flat fan like appearance[159]. This was expected, as the increase in temperature makes the surface curvature more negative and therefore enhances the formation of more curved phases. For Rylo, the phase transition started at 65 °C and the hexagonal phase ($H_{II}$) was observed between (65-90°C) (Figure 6.6). However, for Cithrol, the phase transition started at 52.3 °C and $H_{II}$ phase was observed between (52.3-90 °C) (Figure 6.7). By cooling from 90 to 25 °C, the phase transition moved into the opposite direction ($H_{II} \rightarrow Q_{II}$) with both materials. The lower cubic-hexagonal transition temperature in Cithrol is possibly due to the presence of some impurities such as free glycerol

diglycerides, triglycerides and sodium phosphate which could be possible found in Cithrol as residues from the manufacturing process[205]. Both glycerol[38] and sodium phosphate[36] were found to increase the transition of monoolein from bicontinuous cubic phase to more curved phases with a reduction in the lattice parameter.

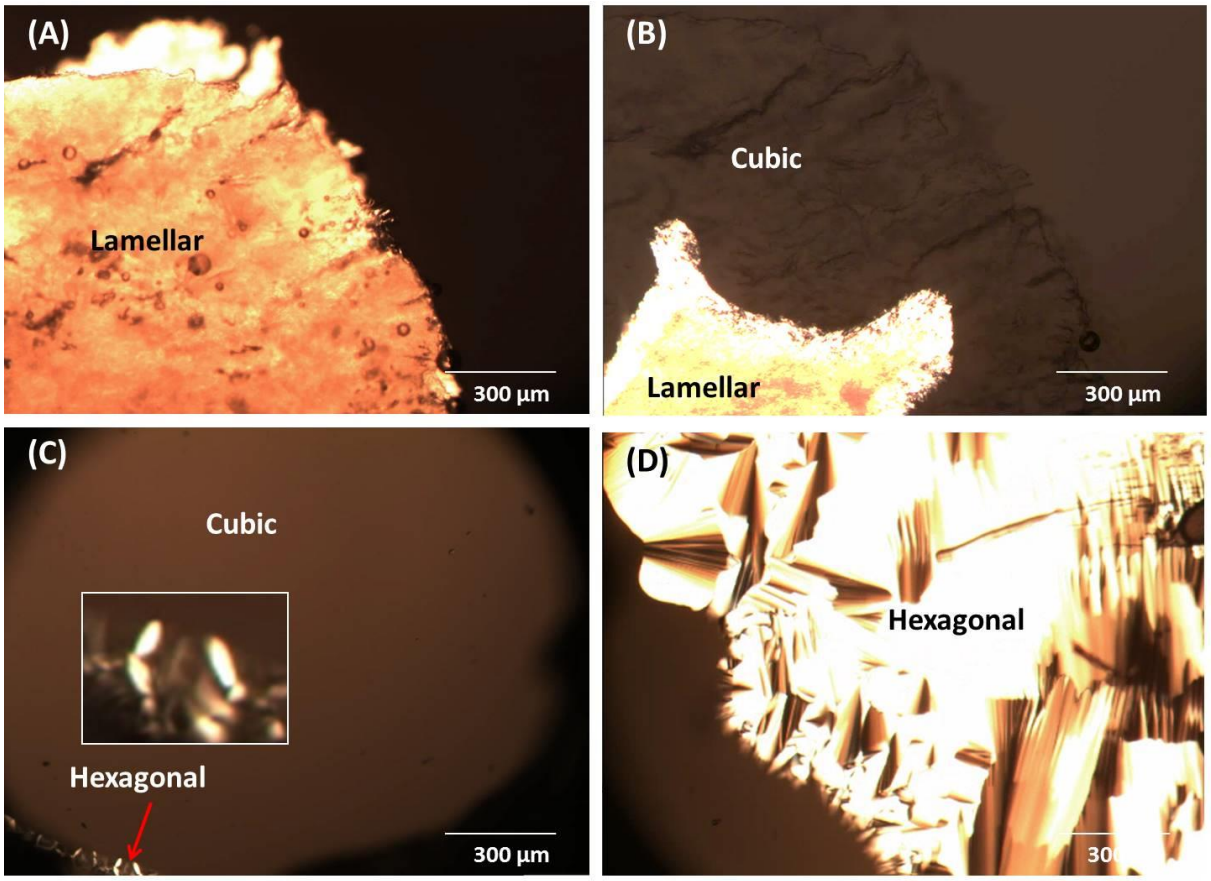


**Figure 6.6 Cross polarized light micrographs of Rylo at different temperatures. A)** Dry Rylo, **B)** Rylo in the presence of water at 25 $^{o}$C, **C)** Rylo in the presence of water at 65 $^{o}$C, inset shows enlarged fan like texture and **D)** Rylo in excess water at 90 $^{o}$C. Scale bar on the images = 300 µm.

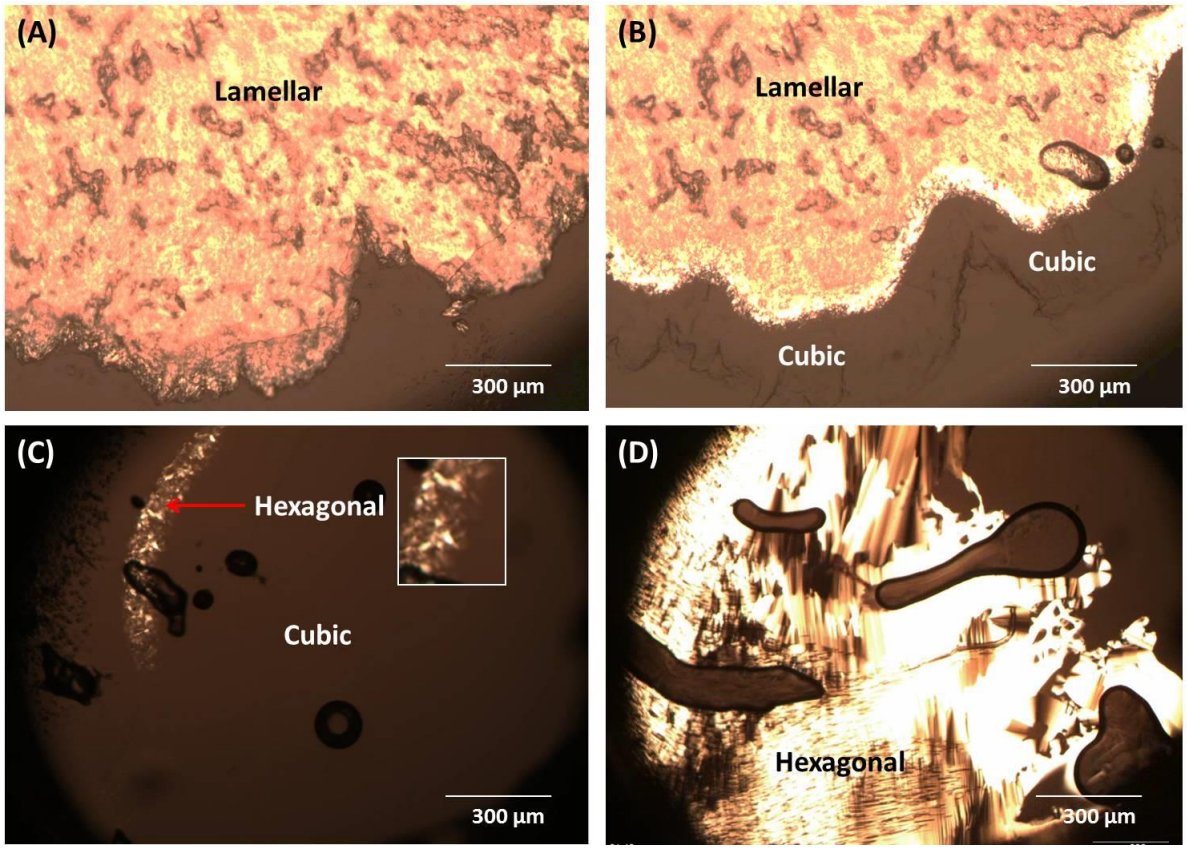


**Figure 6.7 Cross polarized light micrographs of Cithrol at different temperatures. A)** Dry Cithrol, **B)** Cithrol in the presence of water at 25 $^{o}$C, **C)** Cithrol in the presence of water at 52.3 $^{o}$C, inset represents magnified fan-like texture and **D)** Cithrol in the presence of water at 90 $^{o}$C. Scale bar on the images = 300 µm.

The effect of temperature on the phase behavior of both Rylo and Cithrol in excess water was confirmed using SAXS analysis. The samples were scanned at different temperatures (25-90 °C). The SAXS data obtained for Rylo and Cithrol are consistent with CPLM data for both materials. The SAXS patterns showed that the phase behavior of Rylo and Cithrol in excess of water is affected by temperature changes. SAXS patterns showed two phases with the structures $Q_{II}^{D}$ and $H_{II}$ observed when Rylo and Cithrol were heated from 25 to 90 °C. 2-D patterns which are consistent with $Q_{II}^{D}$ phase only were observed at temperatures from 25-60 °C and from 25-50 °C with Rylo (Figure 6.8) and Cithrol (Figure 6.9), respectively. The phase transition from $Q_{II}^{D}$ to $H_{II}$ started at 65 °C in the case of Rylo (Figure 6.8), while with

Cithrol, the phase transition was started at lower temperature (at 55 °C) (Figure 6.9). The phase transition at these temperatures with Rylo and Cithrol was indicated by the presences of 2-D patterns which are related to mixed $Q_{II}^{D}$ and $H_{II}$ phases (Figure 6.8 and Figure 6.9, respectively). 2-D patterns corresponding to $H_{II}$ phase only were observed at temperatures from 75-90 °C and from 60-90 °C for Rylo and Cithrol, respectively.

1-D SAXS patterns confirmed the changes in the phase behavior of hydrated Rylo and Cithrol at different temperatures (Figure 6.10). The 1-D SAXS patterns indicated the presences of six Bragg peaks in the ratio of √2: √3: √4: √6: √8: √9, which are typical for the $Q_{II}^{D}$ phase at temperatures from 25-60 °C for Rylo and from 25-50 °C for Cithrol. Peaks corresponding to both $Q_{II}^{D}$ and $H_{II}$ phases were observed at 65-70 °C for Rylo and at 55 °C for Cithrol, confirmation the phase transition towards the hexagonal phase (Figure 6.10). Three Bragg peaks in the ratio of √1: √3: √4 which are typical for $H_{II}$ phase[4] were observed at temperatures from 75-90 °C for Rylo and from 60-90 °C for Cithrol (Figure 6.10). The calculated lattice parameters for the Rylo and Cithrol at different temperatures are shown in Table 6.1. With both cases, the lattice parameter decreased with increasing the temperature (Figure 6.11), confirming the modulation of the phase behavior of hydrated monoolein with temperature.

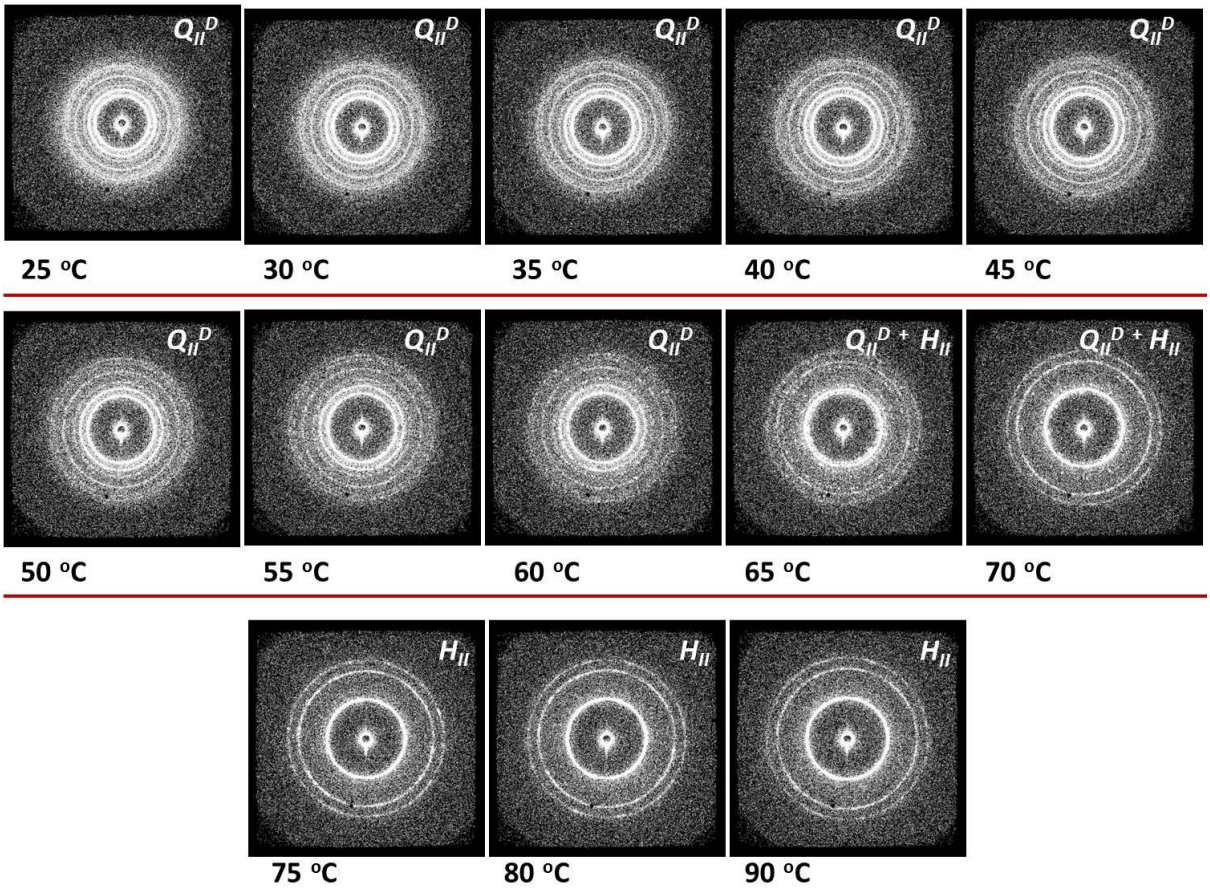


**Figure 6.8 2-D SAXS patterns of hydrated Rylo at different temperatures.**

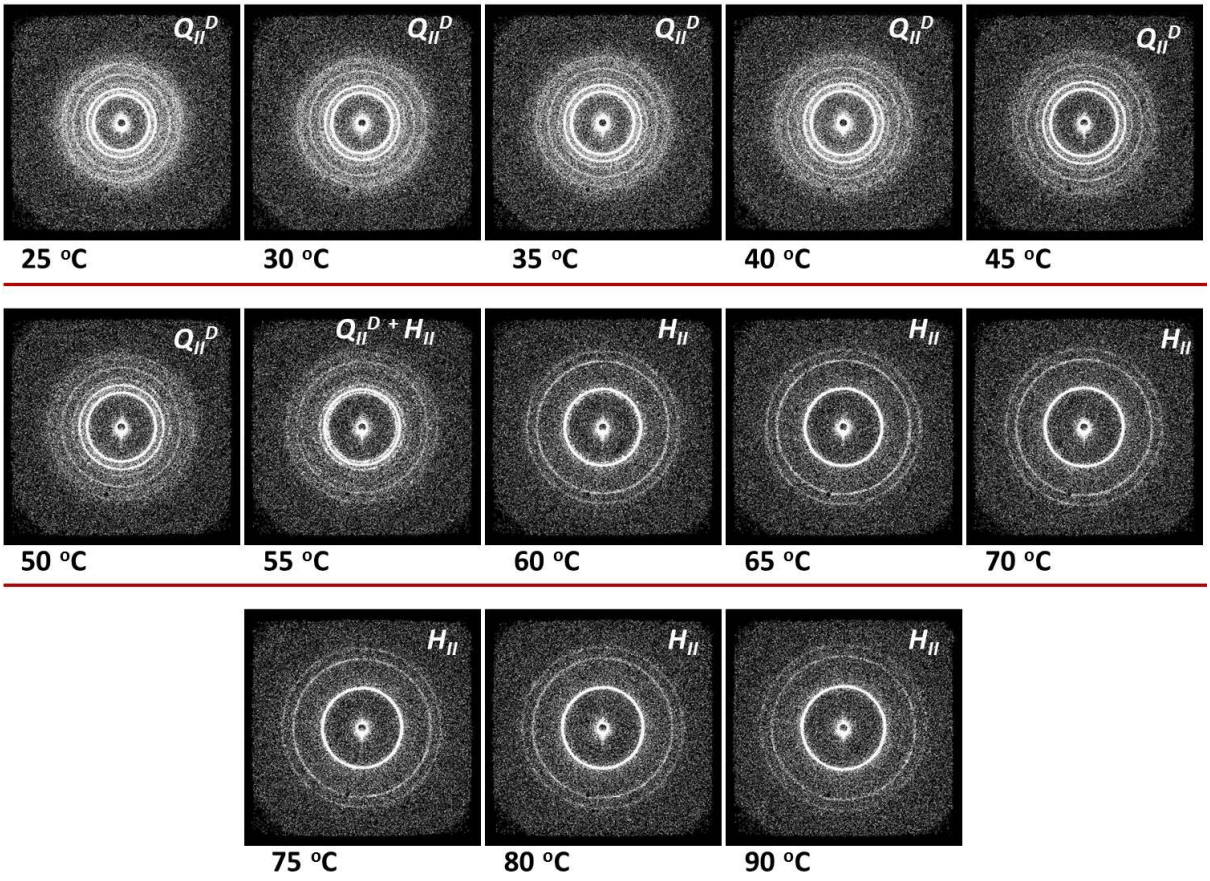


**Figure 6.9 2-D SAXS patterns of hydrated Cithrol at different temperatures.**

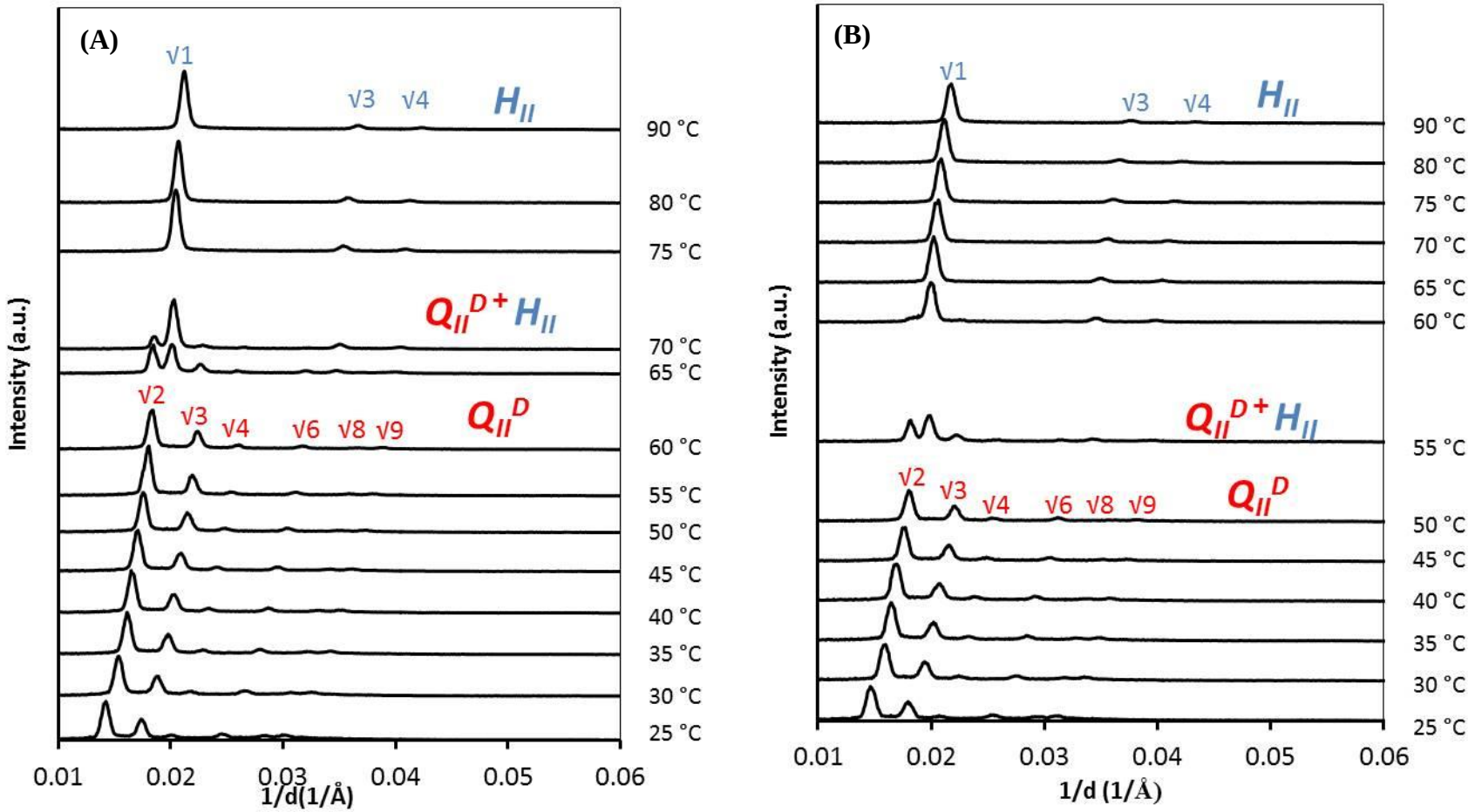


**Figure 6.10 SAXS patterns recorded for (A) Rylo and (B) Cithrol in excess water at different temperature.** Samples were heated from 20 to 90 °C.

**Table 6.1** Variation in the lattice parameter for the $Q_{II}^{D}$ phase of monoolein at different temperatures

| Tem ($^{o}$C) | Lattice parameter ($a$)/Å | |
|---|---|---|
| | **Rylo** | **Cithrol** |
| 25 | 102.0 | 100.9 |
| 30 | 94.0 | 92.9 |
| 35 | 89.8 | 89.5 |
| 40 | 87.7 | 87.1 |
| 45 | 84.9 | 82.3 |
| 50 | 82.3 | 80.5 |
| 55 | 80.3 | -- |
| 60 | 78.2 | 51.8 |
| 65 | -- | 51.1 |
| 70 | -- | 50.1 |
| 75 | 49.8 | 49.3 |
| 80 | 48.8 | 48.5 |
| 90 | 47.7 | 47.0 |

Shaded numbers are the lattice parameters for the hexagonal phases

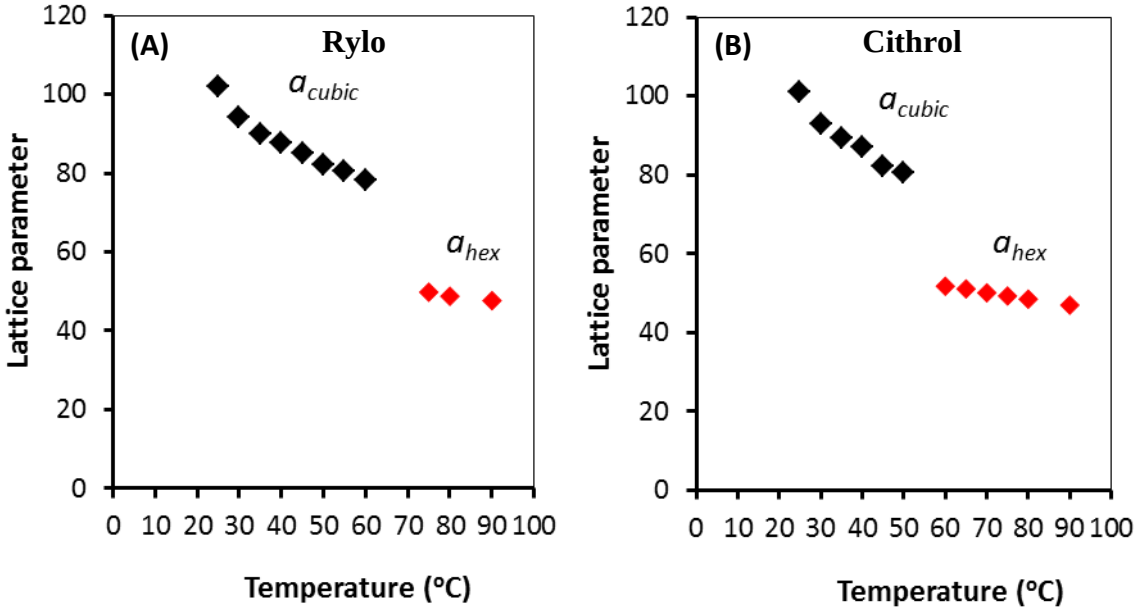


**Figure 6.11 Variation of the lattice parameter of the $Q_{II}^{D}$ phase ($a_{cubic}$) of hydrated A) Rylo and B) Cithrol with different temperatures (25-90 $^{o}$C).** ($a_{cubic}$) is the lattice parameter of the cubic phase and ($a_{hex}$) is the lattice parameter of the hexagonal phase.

### 6.3.5 Effect of Brij-56 on the phase behavior of monoolein/water system

The effect of Brij-56 on the phase behavior of Rylo and Cithrol was studied under excess of water using SAXS. The SAXS analysis were carried out for Rylo and Cithrol containing concentrations of Brij-56 ranging from 0 to 25 % (w/w) of the binary mixture under excess water. The data showed that the phase behavior of Rylo/Brij-56 was similar to that of Cithrol/Brij-56 with each concentration of Brij-56. Cubic phases of Rylo and Cithrol were formed with concentrations of Brij-56 from 0 to 20%. However, increasing the concentration of Brij-56 to 25% led to the transformation of the phase from cubic to lamellar. This was indicated from the 2-D SAXS patterns of both Rylo and Cithrol containing 0-20 % of Brij-56 (Figure 6.13 and 6.14, respectively) which showed typical SAXS patterns consistent with the bicontinuous cubic phases-*Pn3m* ($Q_{II}^{D}$) found in monoolein/water phase diagram[4]. However, a 2-D SAXS pattern of lamellar phase was observed for both Rylo and Cithrol containing 25% of Brij-56 (Figure 6.12 and 6.13, respectively). The formation of the cubic phases of Rylo or Cithrol containing 0-20% of Brij-56 was confirmed by the 1-D SAXS patterns showing six Bragg peaks in the ratios of √2:√3:√4:√6:√8:√9, which matches the cubic lattice of *Pn3m c*rystallographic space group ($Q_{II}^{D}$)[4,193] (Figure 6.14). However the 1-D SAXS patterns of either Rylo or Cithrol containing 25% of Brij-56 showed a single Bragg peak which is characteristic to the lamellar phase (Lα)[4] (Figure 6.14).

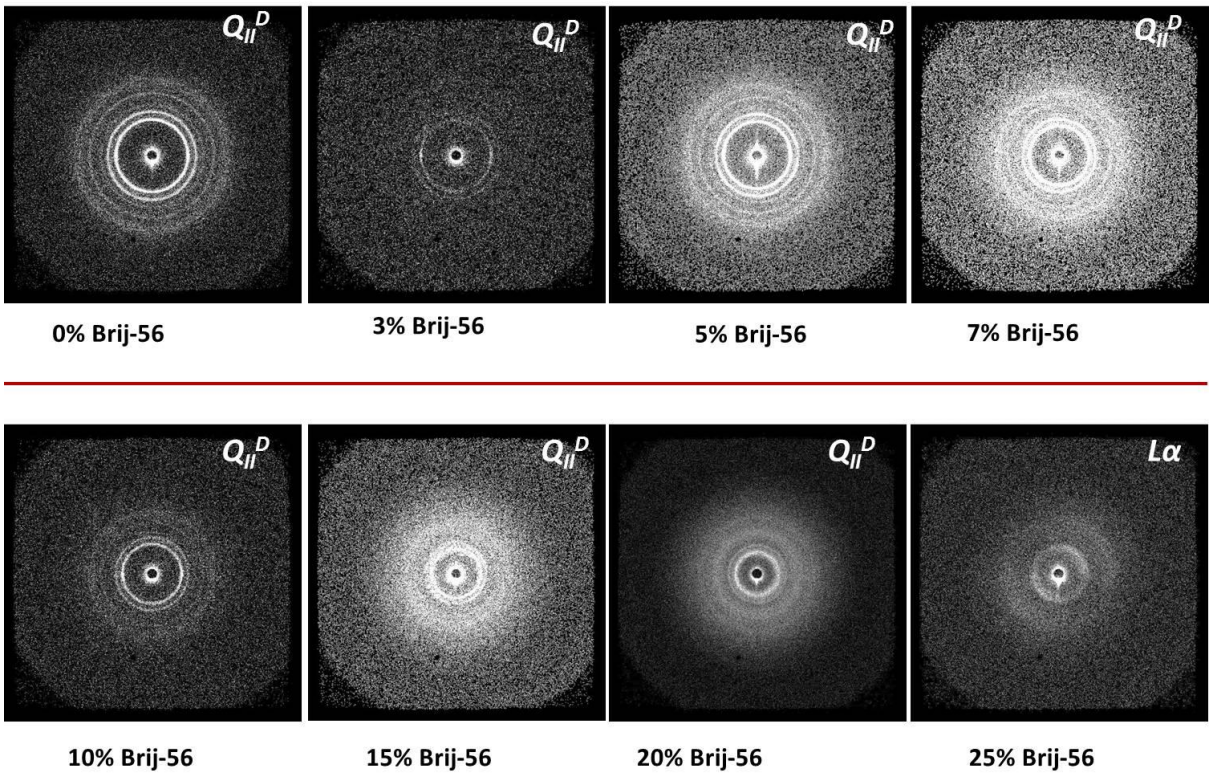


**Figure 6.12 2-D SAXS patterns Rylo with different concentrations Brij-56.**

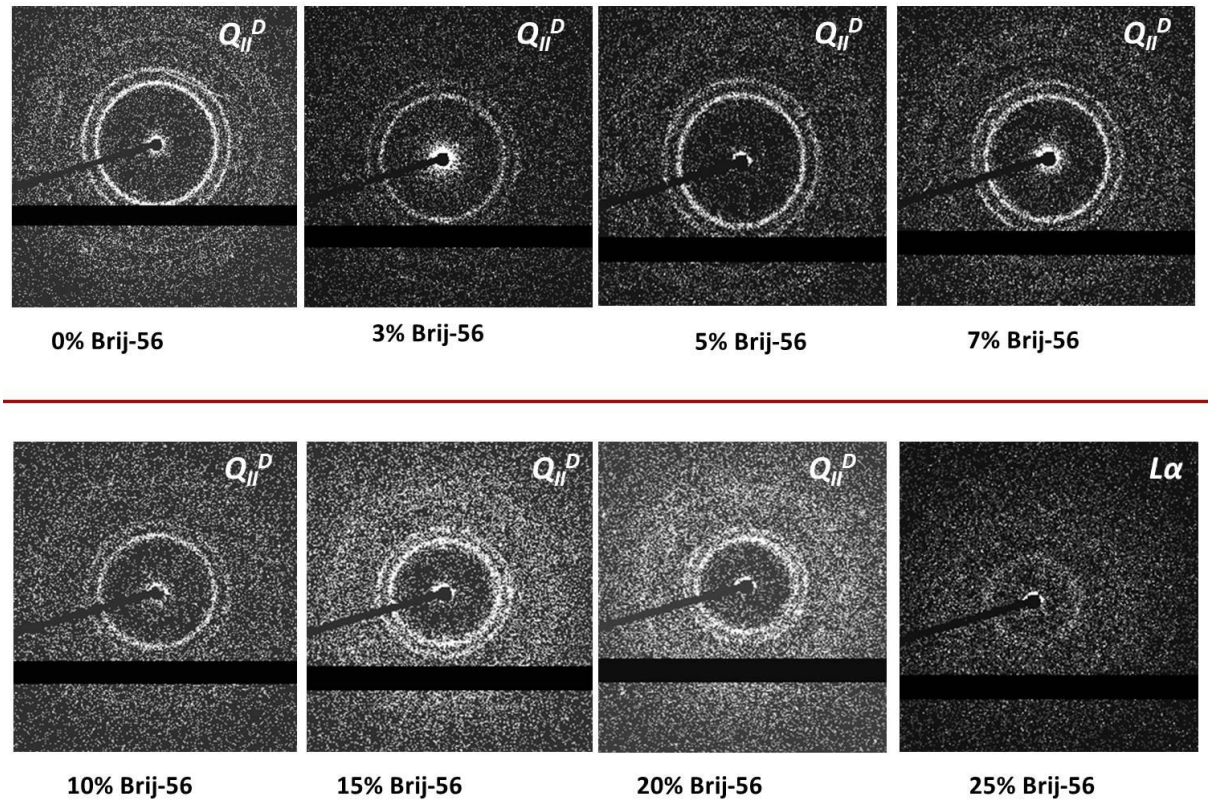


**Figure 6.13 2-D SAXS patterns Cithol with different concentrations Brij-56.**

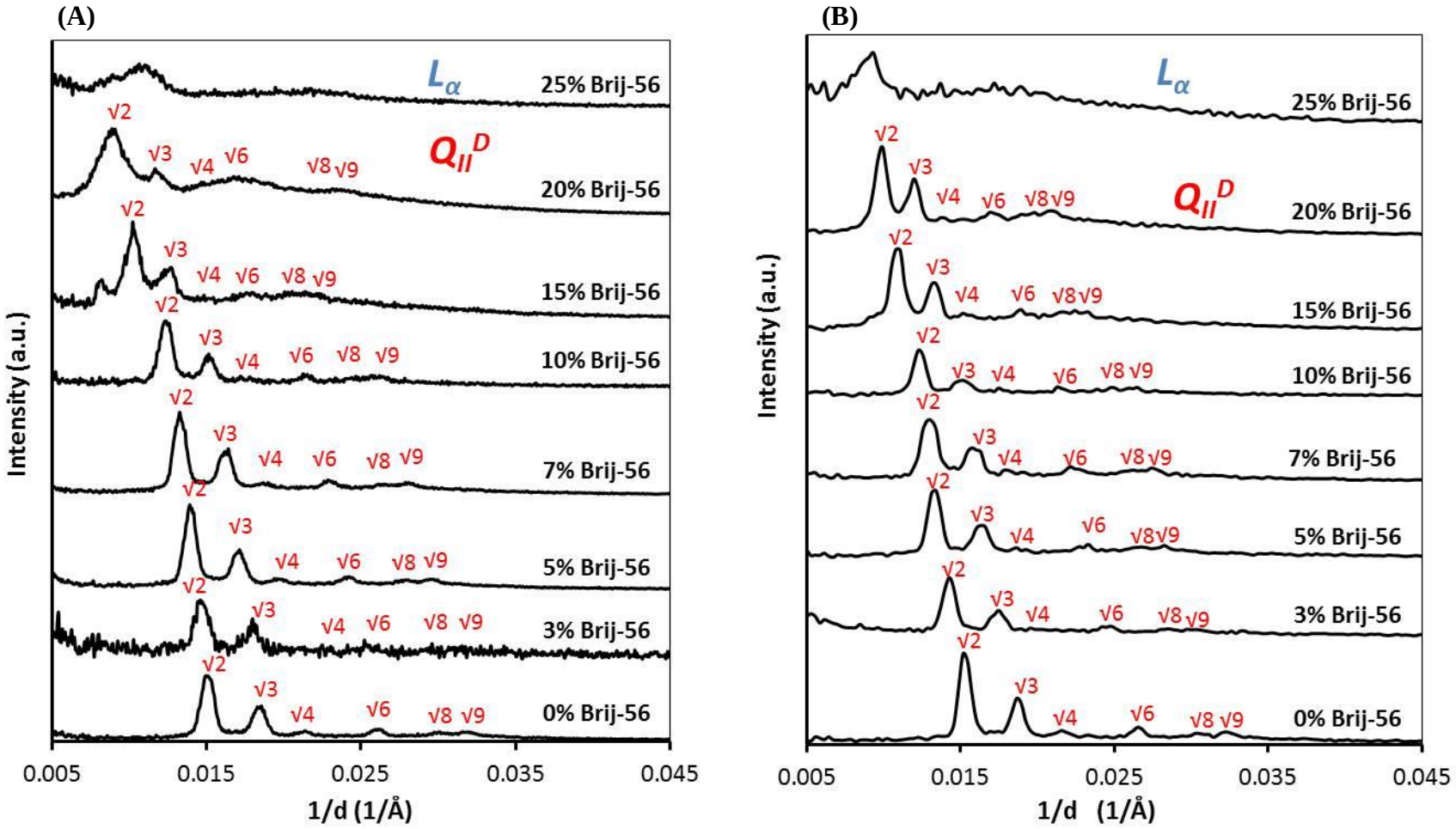


**igure 6.14 SAXS patterns for: (A) Rylo and (B) Cithrol with different concentrations of Brij-56 % (w/w) in excess water at room temperature.**

The calculated lattice parameters of Rylo and Cithrol in the absence and presence of Brij-56 are shown in Table 6.2. The data analysis showed that the lattice parameters of Rylo and Cithrol in the absence of Brij-56 were 95 Å and 93 Å respectively, which are slightly smaller as compared to those obtained with pure monoolein at full hydration ($a$ =107 Å at 20 $^{o}$C)[169]. The reduction in the lattice parameter could be related to the relatively low purity of these monoolein products. While, in the presences of Brij-56, it was found that the lattice parameters of the cubic phases of both Rylo and Cithrol increased with increasing concentration of Brij-56 (Figure 6.15). With both materials, a slight increase in the lattice parameters of the cubic phases was observed upon addition of 3 % (w/w) of Brij-56, however, a massive increase in lattice parameters was observed when concentration of 20 % of Brij-56 was added (Table 6.2, Figure 6.15). No big difference between the lattice parameter of the cubic phase of both materials was observed when the same concentration of Brij-56 was added (Table 6.2, Figure 6.15).

**Table 6.2** Change in the lattice parameter for the $Q_{II}^{D}$ phase of monoolein containing different concentrations of Brij-56

| **Brij-56** | **Lattice parameter (*a*)/Å** | |
|---|---|---|
| **% (w/w)** | **Rylo** | **Cithrol** |
| 0 | 95 | 93 |
| 3 | 96.6 | 99 |
| 5 | 101.3 | 105 |
| 7 | 110.7 | 110 |
| 10 | 118.3 | 115 |
| 15 | 138.8 | 140 |
| 20 | 159.1 | 151 |

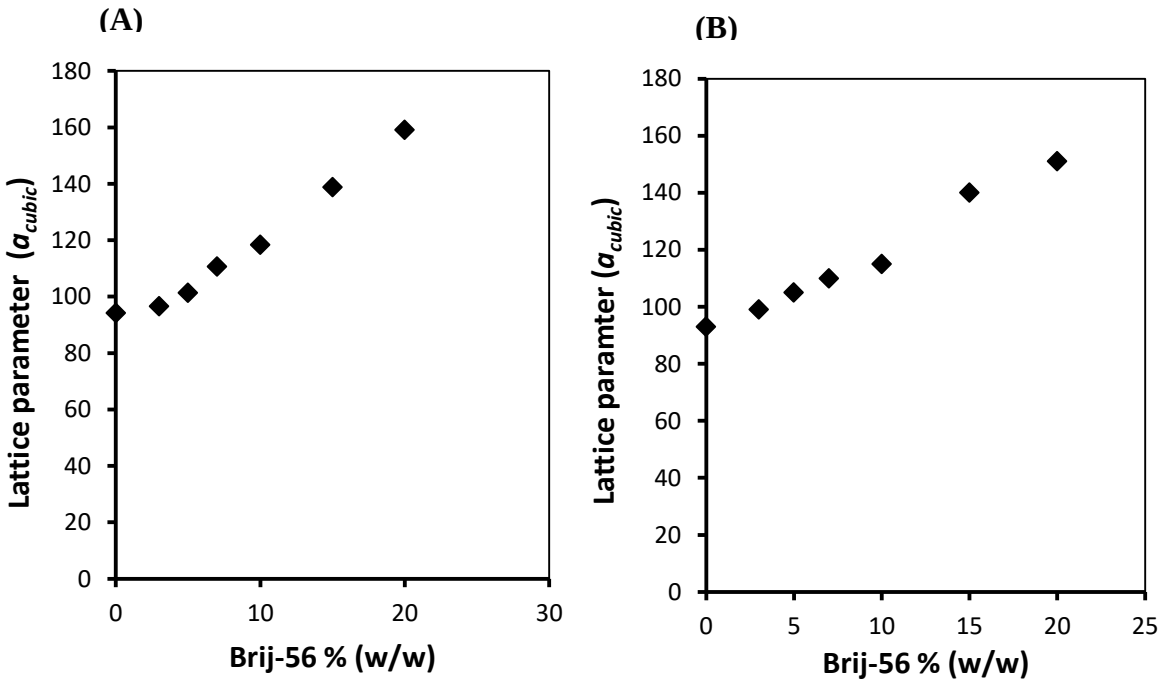


**Figure 6.15 Variation in the lattice parameter of the $Q_{II}^{D}$ phase ($a_{cubic}$) of monoolein in excess of water at room temperature upon addition of different concentrations of Brij-56**: **A)** Rylo and **B)** Cithrol.

Increasing the lattice parameter of monoolein upon addition of Briji-56 is most likely due to the swelling of the aqueous channels in the diamond-type cubic phase, which known as cubic phase swelling[202]. This effect was expected from Brij-56 as it is a non-ionic surfactant. It has been reported previously that the swelling of the diamond-type bicontinuous cubic phase can be induced by additives[202]. Cubic phase swelling has been reported with self-assembled mixtures of monoolein with cationic[206] and nonionic surfactants[169] and charged lipid-like peptides[207]. Angelova et al.[202] reported that the possible explanation of the cubic phase swelling phenomenon is related to a decrease in the lipid membrane curvature due to the accumulation of the additive molecules. Therefore, here we can assume that when Brij-56 was added to monoolein, the Brij-56 molecules penetrated to the monoolein bilayer resulting in a reduction in the bilayer curvature, increasing hydration and widening of the water

channels in the $Q_{II}^{D}$ phase. The possible mechanism of the effect of brij-56 on swelling of the aqueous channels in monoolein is shown below in Figure 6.16.

It was also reported previously that the bicontinuous *Pn3m* cubic phase tolerate high concentrations of non-ionic detergents before being transformed to a lamellar phase at higher surfactant concentration[202]. In our experiment, upon addition of concentrations ranging from 3 to 20% of Brij-56 to monoolein, the cubic phases of monoolein was stable, however a lamellar phase (L$\alpha$) occurred with addition of 25% of Brij-56. Beyond a certain concentration of the additives, the swelling of the cubic phase proceeds through a phase transition to form a sponge phase[208]. This phase is characterised by large non-ordered aqueous channels which are three times larger than the nanochannels in the normal bicontinuous cubic phase[4].

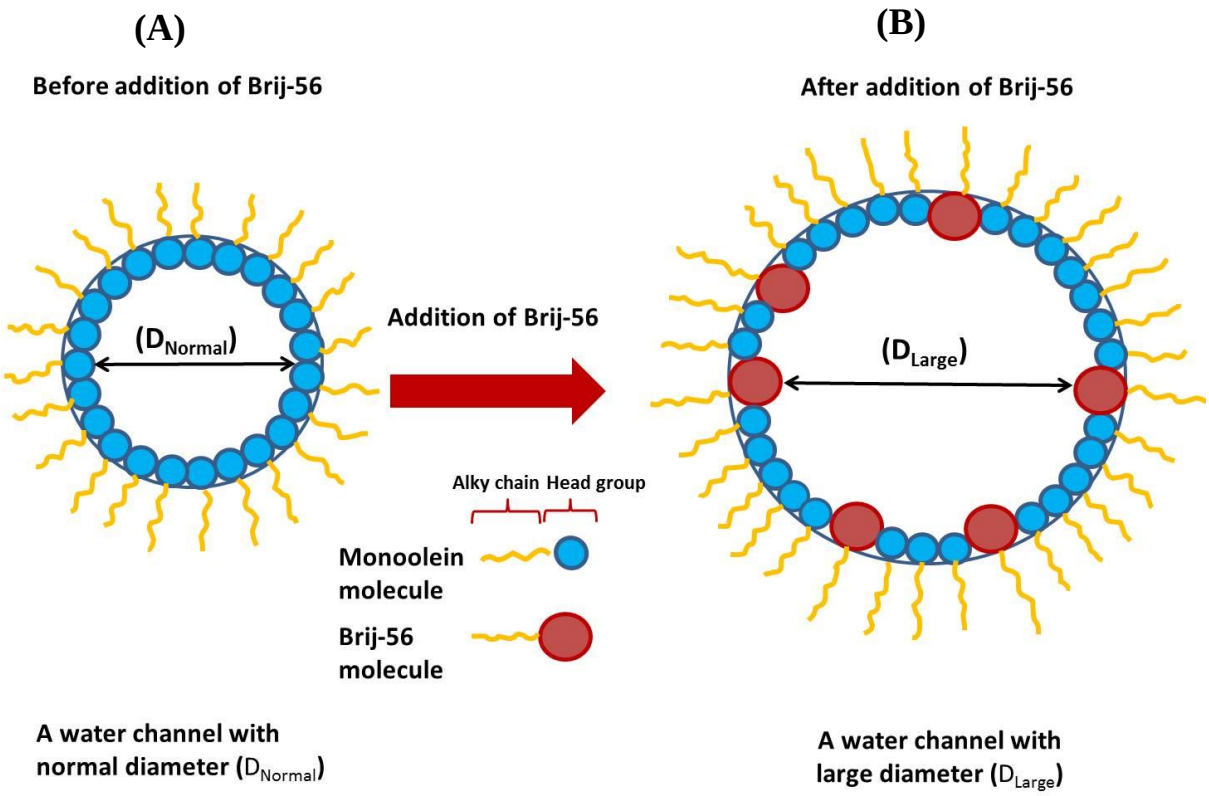


**Figure 6.16 A Schematic illustration showing a cross section in a water channel in monoolein based cubic phase: A)** before addition of Bri-56 and **B)** after addition of Brij-56.

## 6.4 Conclusion

Different analytical methods have been used to investigate the physical properties of two commercial products of monoolein, namely Rylo and Cithrol. Mass spectrometry revealed that both Rylo and Cithrol are relatively impure monoolein. Cithrol was found to be less impure than Rylo. Both products were found to have similar melting points, 28 $^{o}$C for Rylo and 28.5 $^{o}$C for Cithrol. Consistently, CPLM and SAXS data confirmed the formation of $Q_{II}^{D}$ phase with Rylo and Cithrol at full hydration at room temperature. The phase transition from $Q_{II}^{D}$ to $H_{II}$ was observed at ~65 $^{o}$C for Rylo and at ~52 $^{o}$C for Cithrol. Monoolein /Brij-56 systems were found to form stable cubic phases with higher lattice parameters (up to an addition of 20 % (wt/wt) of Brij-56). Therefore, the addition of Brij-56 as a swelling agent to monoolein-water system could be potentially used for tuning the structural parameters which has great practical importance for many applications such as electrodeposition templating of nanostructured materials, membrane protein crystallization and drug delivery. For future work, monoolein/Brij-56/water ternary system containing 3-20% wt of Brij-56 can be used for fabrication of 3-D networks of nanostructured nickel and platinum with different structural parameters depending upon the concentrations of Brij-56.

# Chapter 7: Conclusions and future directions

## 7.1 General discussions and conclusions

Liquid crystal templating is considered a facile and versatile method for fabrication of mesoporous materials with different structures[51,41,53]. This work aimed to fabricate novel nanostructured materials with 3-D structure. First, a direct, soft templating approach was used in this work to fabricate mesoporous Ni and Pt films via the electrodeposition route. Nickel and platinum were electrodeposited at room temperature through bicontinuous phases of monoolein products, namely Rylo and Cithrol, respectively. Then the electrodeposited films were characterised using different analytical methods including, cyclic voltammetry, SAXS and electron microscopy. Subsequently, Pt/Ni and Ni/Pt composite were fabricated by electrodeposition of Pt and Ni on to 3-D Ni and Pt porous templates. The fabricated composites were then analysed by cyclic voltammetry. Finally, it was necessary to study the physicochemical properties of Rylo and Cithrol templates. This was achieved using different methods such as mass spectrometry, differential scanning calorimetry, cross polarised light microscopy (CPLM) and SAXS. The effect of additives such as Brij-56 on the phase behavior of Rylo and Cithrol was also investigated using SAXS. The main findings of this work are summarised in the following list:

1. Electrochemically stable 3-D mesoporous nickel with single diamond morphology (lattice parameter = 175 ± 2.5 Å) was successfully fabricated for the first time by electrodeposition of nickel from a Ni electrolyte at room temperature through a bicontinuous phase of monoolein (Rylo) at -0.95 V vs. Ag/AgCl electrode. The specific surface area of the fabricated films was estimated to be (~13 $m^2/g$). The electrochemically accessible surface area of the templated nickel film has been

estimated to be ~266 fold higher than that of the non-templated nickel film. TEM images for the templated nickel films showed that the nickel was deposited in a 3-D network of interconnected nanowires.

**2.** Mesoporous platinum was successfully electrodeposited for the first time from HCPA solution at room temperature through bicontinuous phase of monoolein (Cithrol) at -0.25 V vs. Ag/AgCl. Probably the structure of the fabricated platinum is not a single diamond giving a lattice parameter of (456 Å). The specific surface area of the fabricated platinum films was estimated to be (~ 2.2 $m^2/g$).

**3.** Mesoporous Pt/Ni and Ni/Pt composites with high surface area were fabricated for the first time via the electrodeposition route using 3-D Ni and Pt porous scaffolds. The fabricated Pt/Ni and Ni/Pt composites are expected to exhibit high electrocatalytic activity. Therefore, they could be promising to be used as electrode materials for batteries and fuel cells.

**4.** Two commercial monoolein products, Rylo and Cithrol were found to form diamond cubic phases ($Q_{II}^{D}$) at room temperature in excess water with lattice parameters of (102 Å and 100.9 Å, respectively). However a phase transition from $Q_{II}$ to $H_{II}$ was found to occur at ~ 65 $^{o}$C for Rylo and at ~ 52 $^{o}$C for Cithrol.

**5.** The lattice parameters of the cubic phases of both monoolein types (Rylo and Cithrol) increased by increasing the concentration of Brij-56 up to 20% (wt/wt), which increased the lattice parameter from 95 Å to 159 Å (Rylo) and 93 Å to 151 Å (Cithrol), indicating a swelling of monoolein cubic phases.

## 7.2 Future work

Mesoporous nickel was successfully fabricated and well characterised. The next step is to test the fabricated mesoporous nickel as a supercapacitor electrode material. In addition, in this work, nanostructured platinum was successfully electrodeposited. However, further characterisation is required in order to reveal the precise structure of the deposited platinum film. This can be performed repeating the SAXS analysis. Morphological characterisation is also required for the deposited films. This can be performed using SEM and TEM microscopy. Furthermore, the deposited platinum can be tested as electrode material for batteries, fuel cells, sensors and others. The catalytic performance of the electrode is affected by the electrochemical stability of the electrode; therefore it is necessarily to test the electrochemical stability of the fabricated platinum electrode. This can be conducted initially using cyclic voltammetry by cycling repeatedly in diluted $H_2SO_4$.

Pt/Ni and Ni/Pt composites were successfully fabricated using electrodeposition route. The deposited films were characterised using electrochemical analysis. However, further investigations are required for structural and morphological characterisation of the fabricated composites. This can be performed using SAXS, XRD and electron microscopy.

In this study, it was found that addition of 3-20 % of Brij-56 to monoolein/water system produced stable cubic phases with higher lattice parameters. Therefore, this system can be used for fabrication of metal nanowires via electrodeposition. Electrodeposition of metals such as nickel and platinum can be carried out under the conditions mentioned in this thesis using a monoolien-Brij-56-water tertiary template containing different concentrations of Brij-56 (3-20%)(wt/wt) instead of a monoolein-water system only. This is expected to produce metal nanowires with controlled structural parameters.

## 7.3 Final comments

In this thesis we have demonstrated the production of nickel and platinum films with a unique 3D nanoarchitecture and high surface area. This was achieved using direct templating through bicontinuous cubic phases of monoolein via the electrodeposition route. This approach is a one step process and environmentally safe reagents.

This study is the first study to validate the use of monoolein cubic phases for fabrication of 3-D mesoporous materials. This provides a developed method for fabrication of 3-D mesoporous materials. In addition, the successful fabrication of mesoporous nickel and platinum in this study using a cheap surfactant such as monoolein as a template instated of the relatively expensive surfactants such as Brij-56[55], octaethylene glycol monohexadecyl ether[51,52] and tetraethylene glycol monododecyl ether[91] which have been used previously for fabrication of mesoporous materials, is considered a big achievement and makes monoolein a promising template for metal deposition application.

In addition, this study reports for the first time the fabrication of Pt/Ni and Ni/Pt composites by electrodeposition of platinum and nickel through porous 3-D Ni and Pt scaffolds, respectively. This attempt is the first ever to validate the electrodeposition of Ni/Pt materials through porous metal templates. The fabricated composites with high electrochemically active surface area are expected to be used for designing catalytic materials and therefore required further investigations. Pt/Ni and Ni/Pt films which have been fabricated in this work could be promising to be used as electrodes materials in batteries and fuel cells which might replace the carbon Pt nanoparticle and overcome the problems associated with using these materials. This may lead to the development of clean energy sources to replace the fossil fuel which in turn might help to reduce the environmental pollution caused by fossil fuels.

This study is the only detailed study to investigate the effect of Brij-56 as a swelling agent on the phase behavior of monoolein. This provides additional understanding concerning the phase behavior of monoolein in the presence of such additive and enables the tuning of the structure parameters of monoolein which is of great importance for many applications.

# References


(1) Reinitzer, F. *Monatsh. Chem* **1888**, *9*, 421.
(2) Kekicheff, P.; Cabane, B. *Acta Crystallographica Section B: Structural Science* **1988**, *44 (4)*, 395.
(3) Ekwall, P.; Mandell, L.; Fontell, K. *Molecular Crystals* **1969**, *8 (1)*, 157.
(4) Kulkarni, C. V.; Wachter, W.; Iglesias-Salto, G.; Engelskirchen, S.; Ahualliac, S. *Phys. Chem. Chem. Phys* **2011**, *13*, 3004.
(5) Barauskas, J.; Landh, T. *Langmuir* **2003**, *19*, 9562.
(6) Briggs, J.; Chung, H.; Caffrey, M. *J. Phys II* **1996**, *6*, 723.
(7) Qiu, H.; Caffrey, M. *Biomaterials* **2000**, *21(3)*, 223.
(8) Krister, H. *J. Colloid and Interface Science* **2004**, *274(2)*, 355.
(9) Ganem-Quintanar, A.; Quintanar-Guerrero, D.; Buri, P. *Drug Dev. Ind. Pharm* **2000**, *26*, 809.
(10) Food and Nutrition Board National Academy of Sciences *Food Chemicals Codex, 4th Ed. , National Academy Press, Washington, DC* **1996**.
(11) Spicer, P. T.; Hayden, K. L.; Lynch, M. L.; Ofori-Boateng, A.; Burns, J. L. *Langmuir* **2001**, *17*, 5748.
(12) Hyde, S.; Andersson, S.; Ericsson, B.; Larsson, K. *Z. Kristallogr* **1984**, *168*, 213.
(13) Lutton, E. S. *J. Am. Oil Chem. Soc* **1965**, *42*, 1068.
(14) Qiu, H.; Caffrey, M. *Chem Phys Lipids* **1999**, *100*, 55.
(15) Drummond, C. J.; Fong, C. *Curr. Opin. Colloid Interface Sci* **1999**, *4*, 449.
(16) Wagner, E. *Parfuem. Kosmet* **1994**, *75*, 260.
(17) Landau, E. M.; Rummel, G.; Rosenbusch, J. P.; Cowan-Jacob, S. W. *J Phys Chem B* **1997**, *101*, 1935.
(18) Caffrey, M. *J Struct Biol* **2003**, *142*, 108.
(19) Cherezov, V.; Clogston, J.; Papiz, M. Z.; Caffrey, M. *J. Mol. Biol* **2006**, *357*, 1605.
(20) Caboi, F.; Nylander, T.; Razumas, V.; Talaikyte, Z.; Monduzzi, M. *Langmuir* **1997**, *13*, 5476.
(21) Drummond, C.; Fong, C. *Curr Opin Colloid Interface Sci* **2000**, *4*, 449.
(22) Caboi, F.; Murgia, S.; Monduzzi, M.; Lazzari, P. *Langmuir* **2002**, *18*, 7916.
(23) Cruise, N.; Jansson, K.; Holmberg, K. *J. Colloid and Interface Science* **2001**, *241(2)*, 527.
(24) Friedel, G. *Annales de Physique* **1922**, *18*, 273.
(25) Winter, R.; Pilgrim, W. C. *Berichte Der Bunsen-Gesellschaft-Physical Chemistry Chemical Physics* **1989**, *93*, 708.
(26) Katsaras, J.; Donaberger, R. L.; Swainson, I. P.; Tennant, D. C.; Tun, Z.; Vold, R. R.; Prosser, R. S. *Phys. Rev. Lett* **1997**, *78*, 899.
(27) Small, D. M. *Handbook of lipid research: The physical chemistry of lipids From alkanes to phospholipids, Plenum, New YorK* **1986**.
(28) Wang, Z. N.; Zheng, L. Q.; Lin, G. Z. *Acta Chim Sinica* **2005**, *63*, 274.
(29) Cherezov, V.; Clogston, J.; Misquitta, Y.; Abdel-Gawad, W.; Caffrey, M. *Biophys. J* **2002**, *83 (6)*, 3393.
(30) Yaghmur, A.; Laggner, P.; Sartori, B.; Rappolt, M. *PLoS One* **2008**, *3*, e2072.
(31) Razumas, V.; Talaikyte, Z.; Barauskasa, J.; Larsson, K.; Miezis, Y.; Nylander, T. *Chem. Phys. Lipids* **1996**, *84 (2)*, 123.
(32) Liu, W.; Caffrey, M. *J. Struct. Biol* **2005**, *150*, 23.
(33) Persson, G.; Edlund, H.; Lindblom, G. *Eur. J. Biochem* **2002**, *270*, 56.

(34) Sennoga, C.; Heron, A.; Seddon, J. M.; Templer, R. H.; Hankamer, B. *Acta Crystallogr., Sect. D: Biol. Crystallogr* **2003**, *59*, 239.
(35) Takahashi, H.; Matsuo, A.; Hatta, I. *Mol. Cryst. Liq. Cryst* **2000**, *347*, 231.
(36) Vargas, R.; Mateu, L.; Romero, A. *Chem. Phys. Lipids* **2004**, *127*, 103.
(37) Wang, Z.; Zheng, L.; Inoue, T. *J. Colloid Interface Sci* **2005**, *288*, 638.
(38) Abe, S.; Takahashi, H. *J. Appl. Crystallogr* **2003**, *36*, 515.
(39) Nguyen, T. H.; Hanley, T.; Porter, C. J.; Larson, I.; Boyd, B. J. *J Pharm Pharmacol* **2010**, *62 (7)*, 844.
(40) Qin, L.; Mei, L.; Shan, Z.; Huang, Y.; Pan, X.; Li, G.; Gu, Y.; Wu, C. *Drug Dev Ind Pharm* **2016**, *42(2)*, 307.
(41) Akbar, S.; Elliott, J. M.; Rittman, M.; Squires, A. M. *Adv. Mater* **2013**, *25 (8)*, 1160.
(42) Wadsten-Hindrichsen, P.; Bender, J.; Unga, J.; Engström, S. *J. Colloid Interface Sci* **2007**, *315*, 701.
(43) Rouquerol, J.; Avnir, D.; Fairbridge, C. W.; Everett, D. H.; Haynes, J. M.; Pernicone, N.; Ramsay, J. D. F.; Sing, K. S. W.; Unger, K. K. *Pure and Applied Chemistry* **1994**, *66 (8)*, 1739.
(44) Sanchez, C.; Boissière, C.; Grosso, D.; Laberty, C.; Nicole, L. *Chem. Mater* **2008**, *20*, 682.
(45) Alothman, Z. A. *Materials* **2012**, *5*, 2874.
(46) Attard, G. S.; Glyde, J. C.; Goltner, C. G. *Nature* **1995**, *378*, 366.
(47) Kresge, C. T.; Leonowicz, M. E.; Roth, W. J.; Vartuli, J. C.; Beck, J. S. J. S. *Nature* **1992**, *359*, 710.
(48) Yang, P.; Zhao, D.; Margolese, D. I.; Chmelka, B. F.; Stucky, G. D. *Nature* **1998**, *396*, 152.
(49) Tanev, P. T.; Pinnavaia, T. J. J. *Science* **1995**, *267*, 865.
(50) Bagshaw, S. A.; Prouzet, E.; Pinnavaia, T. J. *Science* **1995**, *269*, 1242.
(51) Attard, G. S.; Bartlett, P. N.; Coleman, N. R. B.; Elliott, J. M.; Owen, J. R.; Wang, J. H. *Science* **1997**, *278*, 838.
(52) Elliott, J. M.; Attard, G. S.; Bartlett, P. N.; Coleman, N. R. B.; Merckel, D. A. S.; Owen, J. R. *Chem. Mater* **1999**, *11*, 3602.
(53) Asghar, K. A.; Elliott, J. M.; Squires, A. M. *J. Mater. Chem* **2012**, *22*, 13311.
(54) Whitehead, A. H.; Elliott, J. M.; Owen, J. R. *J. Power Sources* **1999**, *81-82*, 33.
(55) Nelson, P. A.; Elliott, J. M.; Attard, G. S.; Owen, J. R. *Chem. Mater* **2002**, *14*, 524.
(56) Xiao, J.; Yang, S.; Wan, L.; Xiao, F.; Wang, S. *Journal of Power Sources* **2014**, *245 (1)*, 1027.
(57) Islam, M. d. A.; Islam, M. S. *Engineering International* **2013**, *1(2)*.
(58) Ganesh, V.; Lakshminarayanan, V.; Pitchumani, S. *Electrochemical and Solid-State Letters* **2005**, *8 (6)* A308.
(59) Al-Saleh, M. A.; Sleem-Ur-Rahman; Kareemuddin, S. M. M. J.; Al-Zakri, A. S. *J. Power Sources* **1998**, *72(2)*, 159.
(60) Kiros, Y.; Schwartz, S. *J. Power Sources* **2000**, *87(1-2)*, 101.
(61) Anantharaman, V.; Pintauro, P. N. *J. Electrochem. Soc* **1994**, *141 (10)*, 2729.
(62) Sealey, S. *Royal Society of Chemistry: Cambridge* **1998**, 7.
(63) Wang, L.; Lu, Z.; Cheng, Q.; Liu, L. *Analytical Letters* **2015**, *48*, 1854.
(64) Song, Y.-Y.; Zhang, D.; Gao, W.; Xia, X.-H. *Chemistry - A European Journal* **2005**, *11(7)*, 2177.
(65) Park, S.; Chung, T. D.; Kim, H. C. *Analytical Chemistry* **2003**, *75(13)*, 3046.
(66) Li, Y.; Song, Y.-Y.; Yang, C.; Xia, X.-H. *Electrochemistry Communications* **2007**, *9(5)*, 981.

(67) Erlebacher, J.; Aziz, M. J.; Karma, A.; Dimitrov, N.; Sieradzki, K. *Nature* **2001**, *410(6827)*, 450.
(68) Lu, W.; Qin, X.; Asiri, A. M.; Al-Youbi, A. O.; Sun, X. *The Analyst* **2013**, *138(2)*, 417.
(69) Brown, I. J.; Sotiropoulos, S. S. *J. Appl. Electrochem* **2000**, *30*, 107.
(70) Brown, I. J.; Sotiropoulos, S. *Electrochim. Acta* **2001**, *46*, 2711.
(71) Ganesh, V.; Lakshminarayanan, V. *Electrochimica Acta* **2004**, *49*, 3561.
(72) Yamauchi, Y.; Yokoshima, T.; Momma, T.; Osaka, T.; Kuroda, K. *J. Mater. Chem* **2004**, *14*, 2935.
(73) Xing, W.; Li, F.; Yan, Z. F.; Lu, G. Q. *J. Power Sources* **2004**, *134*, 324.
(74) Yamauchi, Y.; Momma, T.; Yokoshima, T.; Kuroda, K.; Osaka, T. *J.Mater.Chem* **2005**, *15*, 1987.
(75) Wang, Y. G.; Xia, Y. Y. *Electrochim. Acta* **2006**, *51*, 3223.
(76) Zhao, D.-D.; Bao, S.-J.; Zhou, W.-J.; Li, H. L. *Electrochem. Commun* **2007**, *9 (5)*, 869.
(77) Zhao, D.-D.; Xu, M. W.; Zhou, W.-J.; Zhang, J.; Li, H. L. *Electrochim. Acta* **2008**, *53*, 2699.
(78) Deki, S.; Hosokawa, A.; Béléké, A. B.; Mizuhata, M. *Thin Solid Films* **2009**, *517*, 1546.
(79) Hsueh, H.-Y.; Huang, Y.-C.; Ho, R.-M.; Lai, C.-H.; Makida, T.; Hasegawa, H. *Advanced Materials* **2011**, *23(27)*, 3041.
(80) Bartlett, P. N.; Pletcher, D.; Esterle, T. F.; Low, C. T. J. *Journal of Electroanalytical Chemistry* **2013**, *688*, 232.
(81) Chen, W.; Xia, C.; Alshareef, H. N. *ACS Nano* **2014**, *8*, 9531.
(82) Li, Y.; Xiao, X.; Zhao, R.; Yu, K.; Hou, C.; Liang, J. *Synthesis and Reactivity in Inorganic, Metal-Organic, and Nano-Metal Chemistry* **2016**, *46*, 286.
(83) Evans, S. A. G.; Elliott, J. M.; Andrews, L. M.; Bartlett, P. N.; Doyle, P. J.; Denuault, G. *Analytical Chemistry* **2002**, *74*, *(6)*, 1322.
(84) Han, J. H.; Choi, H. N.; Park, S.; Chung, T. D.; Lee, W. Y. *Anal Sci* **2010**, *26(9)*, 995.
(85) Tong, D. H.; Tran, P. D.; Pham, X. T. T.; Pham, V. B.; Le, T. T. T. *Adv. Nat. Sci.: Nanosci. Nanotechnol* **2010**, *1*, 015011.
(86) Qu, F.; Yang, M.; Shen, G.; Yu, R. *Biosens. Bioelectron* **2007**, *22*, 1749.
(87) Liang, H. W.; Cao, X.; Zhou, F.; Cui, C. H.; Zhang, W. J.; Yu, S. H. *Adv. Mater* **2011**, *23*, 1467.
(88) Yu, X.; Ye, S. *Journal of Power Sources* **2007**, *172*, 133.
(89) Xu, H.; Ding, L. X.; Liang, C. L.; Tong, Y. X.; Li, G. R. *NPG Asia Materials* **2013**, *5*, 69.
(90) Ma, L.; Wang, C.; Gong, M.; Liao, L.; Long, R.; Wang, J.; Wu, D.; Zhong, W.; Kim, M. J.; Chen, Y.; Xie, Y.; Xiong, Y. *ACS Nano* **2012**, *11*, 9797.
(91) Zhao, J.; Chen, X.; Jiao, L.; Chai, Y.; Wang, L. *Scripta Materialia* **2004**, *51*, 593.
(92) Qu, L.; Dai, L.; Osawa, E. *J. Am. Chem. Soc* **2006**, *128*, 5523.
(93) Kundu, S.; Huitink, D.; Liang, H. *J. Phys. Chem. C* **2010**, *114*, 7700.
(94) Song, Y.; Garcia, R. M.; Dorin, R. M.; Wang, H.; Qiu, Y.; Coker, E. N.; Miller, J. E.; Shelnutt, J. A. *Nano Lett* **2007**, *7*, 3650.
(95) Teng, X.; Han, W.-Q.; Ku, W.; Hücker, M. *Angew. Chem* **2008**, *120*, 2085.
(96) Napolskii, K. S.; Barczuk, P. J.; Vassiliev, S. Y. V.; eresov, A. G.; Tsirlina, G. A.; Kulesza, P. J. *Electrochim. Acta* **2007**, *52*, 7910.
(97) Muench, F.; Kaserer, S.; Kunz, U.; Svoboda, I.; Brotz, J.; Lauterbach, S.; Kleebe, H.-J.; Rotha, C.; Ensinger, W. *J. Mater. Chem* **2011**, *21*, 6286.
(98) Jiang, J.; Kucernak, A. *Electrochem. Commun* **2009**, *11*, 623.

(99) Lin, Z.-H.; Lin, M.-H.; Chang, H.-T. *Chem.-Eur. J* **2009**, *15*, 4656.
(100) Sun, S. H.; Yang, D. Q.; Villers, D.; Zhang, G. X.; Sacher, E. *Adv. Mater* **2008**, *20*, 571.
(101) Rajalakshmi, N.; Dhathathreyan, K. S. *international journal of hydrogen energy* **2008**, *33*, 5672.
(102) Shin, H. J.; Ko, C. H.; Ryoo, R. *J. Mater. Chem* **2001**, *11*, 260.
(103) Kibsgaard, J.; Gorlin, Y.; Chen, Z.; Jaramillo, T. F. *J. Am. Chem. Soc* **2012**, *134*, 7758.
(104) Doi, Y.; Takai, A.; Sakamoto, Y.; Terasaki, O.; Yamauchi, Y.; Kuroda, K. *Chem. Commun* **2010**, *46*, 6365.
(105) Cao, Y.; Yang, Y.; Shan, Y.; Chaoli Fu; Long, N. V.; Huang, Z.; Guoa, X.; Nogamic, M. *Nanoscale* **2015**, *7*, 19461.
(106) Li, Y.; Bastakoti, B. P.; Malgras, V.; Li, C.; Tang, J.; Kim, J. H.; Yamauchi, Y. *Angew. Chem. Int. Ed* **2015**, *54*, 11073.
(107) Cheng, C.-F.; Hsueh, H.-Y.; Lai, C.-H.; Pan, C.-J.; Hwang, B.-J.; Hu, C.-C.; Ho, R.-M. *NPG Asia Materials* **2015**, *7*, e170.
(108) Kibsgaard, K.; Jackson, A.; Jaramillo, T. F. *Nano Energy* **2016**, *In press*, DOI: http://dx.doi.org/10.1016/j.nanoen.2016.05.005.
(109) Kim, H.; Cho, J. *J. Mater. Chem.* **2008**, *18*, 771.
(110) Liu, Z.; Sakamoto, Y.; Ohsuna, T.; Hiraga, K.; Terasaki, O.; Ko, C. H.; Shin, H. J.; Ryoo, R. *Angew. Chem* **2000**, *112*, 3237.
(111) Jaya Sarkar, J.; Khan, G. G.; Basumallick, A. *Bulletin of Materials Science* **2007**, *30 (3)*, 271.
(112) Sulka, G. D.; Brzózka, A.; Liu, L. *Electrochimica Acta* **2011**, *56 (14)*, 4972.
(113) Ying, J. Y.; Mehnert, C. P.; Wong, M. S. *Angew. Chem., Int. Ed* **1999**, *38*, 56.
(114) Lu, Y.; Fan, H.; Stump, A.; Ward, T. L.; Rieker, T.; Brinker, C. J. *Nature* **1999**, *398*, 223.
(115) Imhof, A.; Pine, D. J. *Nature* **1997**, *389*, 948.
(116) Schmidt-Winkel, P.; Lukens, W. W.; Yang, P.; Margolese, D. I.; Lettow, J. S.; Ying, J. Y.; Stucky, G. D. *Chem. Mater* **2000**, *12*, 686.
(117) Jatupaiboon, N.; Wang, Y.; Wu, H.; Song, X.; Song, Y.; Zhang, J.; Ma, X.; Tan, M. *J. Mater. Chem. B* **2015**, *3*, 3130.
(118) Velev, O. D.; Jede, T. A.; Lobo, R. F.; Lenhoff, A. M. *Nature* **1997**, *389*, 447.
(119) Holland, B. T.; Blanford, C. F.; Stein, A. *Science* **1998**, *281*, 538.
(120) Ryoo, R.; Joo, S. H.; Jun, S. *J. Phys. Chem. B* **1999**, *103*, 7743.
(121) Takai, A.; Ataee-Esfahani, H.; Doi, Y.; Fuziwara, M.; Yamauchi, Y.; Kuroda, K. *Chem. Commun* **2011**, *47*, 7701.
(122) Kawamura, G.; Muto, H.; Matsuda, A. *Front Chem* **2014**, *2*, 104.
(123) Byrne, F.; Prina-Mello, A.; Whelan, A.; Mohamed, B. M.; Davies, A.; Gunko, Y. K. *J. Magn.Magn.Mater* **2009**, *321*, 1341.
(124) Thongmee, S.; Pang, H. L.; Ding, J.; Yi, J. B.; Lin, J. Y. *J. Magnetism and Magnetic Materials* **2009**, *321(18)*, 2712.
(125) Proenca, M. P.; Sousa, C. T.; Escrig, J.; Ventura, J.; Vazquez, M.; Araujo, J. P. *J. Appl.Phys* **2013**, *113 (9)*, 093907.
(126) Suib, S. L. *New and Future Developments in Catalysis: Solar Photocatalysis, Newnes, Technology & Engineering* **2013**, 492.
(127) Yamauchi, Y.; Sawada, M.; Komatsu, M.; Sugiyama, A.; Osaka, T.; Hirota, N.; Sakka, Y.; Kuroda, K. *Chem Asian J* **2007**, *2(12)*, 1505.
(128) Yamauchi, Y.; Kuroda, K. *Chem Asian J* **2008**, *3*, 664.

(129) Akbar, S.; Elliott, J. M.; Rittman, M.; Squires, A. M. *PhD Thesis, University of Reading* **2012**.
(130) Jabs, T.; Borthen, P.; Strehblow, H. H. *J. Electrochem. Soc* **1997**, *144(4)*, 1231.
(131) Bard, A. J.; Faulkner, L. R. *Electrochemical methods : fundamentals and applications; Wiley: New York* **1980**.
(132) Ross, P. N.; Jr *J. Electrochem. Soc* **1979**, *126* 67.
(133) Will, F. G. *J. Electrochem. Soc* **1965**, *112*, 451
(134) Grden, M.; Alsabet, M.; Jerkiewicz, G. *ACS Appl Mater Interfaces* **2012**, *4(6)*, 3012.
(135) Machado, S. A. S.; Avaca, L. A. *Electrochim. Acta* **1994**, *39*, 1385.
(136) Brummer, S. B.; Ford, J. I.; Turner, M. J. *J. Phys. Chem* **1965**, *69*, 3424.
(137) Plyasova, L. M.; Molina, I. Y.; Gavrilov, A. N.; Cherepanova, S. V.; Cherstiouk, O. V.; Rudina, N. A.; Savinova, E. R.; Tsirlina, G. A. *Electrochim Acta* **2006**, *51*, 51.
(138) Lei, Y.; Zhang, L.; Fan, J. *Chemical Physics Letters* **2001**, *338*, 231.
(139) Liu, S. H.; Sol, K. *Energy Mater* **2004**, *85*, 125.
(140) Clark, D.; Wood, D.; Erb, U. *Nanostructured Materials* **1997**, *9*, 755.
(141) Mordechay Schlesinger, M. P. *Handbook* **2000**, 115.
(142) Ke, J.; Su, W.; Howdle, S. M.; George, M. W.; Cock, D.; Perdjon-Abel, M.; Bartlett, P. N.; Zhang, W.; Cheng, F.; Levason, W.; Reid, G.; Hyde, J.; Wilson, J.; Smith, D. C.; Mallik, K.; Sazio, P. *Natl. Acad. Sci* **2009**, *106*, 14768.
(143) Bragg, W. H.; Bragg, W. L. *Proc. R. Soc. London, Ser. A* **1913**, *88*, 428.
(144) Blanchet, C. E.; Svergun, D. I. *Annu. Rev. Phys. Chem* **2013**, *64*, 37.
(145) Guinier, A. *Ann. Phys. (Paris)* **1939**, *12*, 161.
(146) Luzzati, V.; Husson, F. *J. Cell Biol* **1962**, *12*, 207.
(147) Fratzl, P. *J. Appl. Crystallogr* **2003**, *36*, 397.
(148) Lee, B.; Lo, C.-T.; Seifert, S.; Winans, R. E. *Journal of Applied Crystallography* **2006**, *39*, 749.
(149) Huang, T. C.; Toraya, H.; Blanton, T. N.; Wu, Y. *J. Appl. Crystallogr* **1993**, *26*, 180.
(150) Chan, K. K.; Pershan, P. S.; Sorensen, L. B.; Hardouin, F. *Physical Review Letters* **1985**, *54*, 1694.
(151) Oka, T. *Langmuir* **2015**, *31 (41)*, 11353.
(152) Muller, D. A. *Nat Mater* **2009**, *8*, 263.
(153) Bozzola, J. *J. Electron Microscopy; John Wiley & Sons, Ltd* **2001**.
(154) Williams, D. B.; Carter, C. B.; Williams, D. B.; Carter, C. B. *Springer US* **2009**, 3.
(155) Reimer, L. *Transmission Electron Microscopy: Physics of Image Formation and Microanalysis. Springer - Science* **2013**, 521.
(156) Nguyen, T. H.; Hanley, T.; Porter, C. J.; Larson, I.; Boyd, B. J. *J Pharm Pharmacol* **2010**, *62(7)*, 844.
(157) Laughlin, R. G. *Advances in Colloid and Interface Science* **1992**, *41*, 57.
(158) Rosevear, F. B. *Journal of the Society of Cosmetic Chemists* **1968**, *19*, 581.
(159) Hyde, S. *Identification of lyotropic liquid crystalline mesophases, ed. Chichester, UK John Wiley & Sons* **2002**.
(160) Collings, P. J.; Hird, M. *Introduction to Liquid Crystals: Chemistry and Physics (the liquid crystal book series)* **1998**.
(161) De Hoffmann, E.; Stroobant, V. *Mass Spectrometry: Principles and Applications, 3rd ed.; Wiley and Sons* **2007**.
(162) Höhne, G.; Hemminger, W. F.; Flammersheim, H.-J. *Differential Scanning Calorimetry. Springer Science & Business Media* **2013**, 298
(163) Montalvo, G.; Valiente, M.; Rodenas, E. *Langmuir* **1996**, *12*, 5202.
(164) Shi, Y. F.; Meng, Y.; Chen, D. H.; Cheng, S. J.; Chen, P.; Yang, T. F.; Wan, Y.; Zhao, D. Y. *Adv. Funct. Mater* **2006**, *16*, 561.

(165) Rauber, M.; Alber, I.; Müller, S.; Neumann, R.; Picht, O.; Roth, C.; Schökel, A.; Toimil-Molares, M. E.; Ensinger, W. *Nano Lett* **2011**, *11*, 2304.
(166) Wei, T.-C.; Hillhouse, H. W. *Langmuir* **2007**, *23*, 5689.
(167) Landry, C. C.; Tolbert, S. H.; Gallis, K. W.; Monnier, A.; Stucky, G. D.; Norby, P.; Hanson, J. C. *Chem. Mater* **2001**, *13*, 1600.
(168) Chung, H.; Caffrey, M. *Biophys J* **1994**, *66*, 377.
(169) Angelov, B.; Angelova, A.; Ollivon, M.; Bourgaux, C.; Campitelli, A. *J. Am. Chem. Soc* **2003**, *125*, 7188.
(170) Marcus, Y. *Ion Solvation, Wiley, Chichester* **1985**.
(171) Seddon, J. M.; Templer, R. H. *Philos. Trans. R. Soc. London, Ser. A* **1993**, *344*, 377.
(172) Smirnov, A.; Hausner, D.; Laffers, R.; Strongin, R. D.; Schoonen, M. A. A. *Geochemical Transactions* **2008**, *91*, 335.
(173) Sapkal;, S. B.; Shelke;, K. F.; Shingate;, B. B.; Shingare., M. S. *Tetrahedron Letters* **2009**, *50*, 1754.
(174) Xiangcheng Sun; A. Gutierrez; M. Jose Yacaman; Xinglong Dong; Shouri Jin *Materials Science and Engineering: A* **2000**, *286*, 157.
(175) Schwarz, U. S.; Gompper, G. *Phys. Rev. Lett* **2000**, *85*, 1472.
(176) Amjad, M.; Pletcher, D.; Smith, C. *J. Electrochem. Soc* **1977**, 203.
(177) Scharifker, B.; Hills, G. *Electrochim. Acta* **1983**, *28*, 879.
(178) Feltham, A. M.; Spiro, M. *Chem. Rev* **1971**, *71*, 177.
(179) Plyasova, L. M.; Molina, I. Y.; Gavrilov, A. N.; Cherepanova, S. V.; Cherstiouk, O. V. *Electrochim. Acta* **2006**, *51*, 4477.
(180) Seddon, J. M. *Biochem* **1990**, *29*, 7997.
(181) Fisher, A. C. *Oxford University Press: Oxford; New York,* **1996**.
(182) Ginsberg, D. M. *Physical properties of high temperature superconductors II. World Scientific, Singapore* **1990**, 700.
(183) Tang, H.; Chen, J. H.; Huang, Z. P.; Wang, D. Z.; Ren, Z. F. *Carbon* **2004**, *42*, 191.
(184) Arico, A. S.; Bruce, P.; Scrosati, B.; Tarascon, J.-M.; Walter, V. S. *Nat. Mater* **2005**, *4*, 366.
(185) Goldberg, M.; Langer, R.; Jia, X. J. *Biomater. Sci., Polym. Ed* **2007**, *18(3)*, 241.
(186) Liu, C.; Li, F.; Ma, L.-P.; Cheng, H.-M. *Adv. Mater* **2010**, *22*, E28.
(187) Koenigsmann, C.; Wong, S. S. *Energy Environ. Sci* **2011**, *4*, 1161.
(188) Serrano, E.; Rus, G.; García-Martínez, J. *Renewable and Sustainable Energy Rev* **2009**, *13*, 2373.
(189) Oelhafen, P.; Schuler, A. *Sol. Energy* **2005**, *79*, 110.
(190) Zhang, H.-T.; Ding, J.; Chow, G.-M. *Langmuir* **2007**, *24*, 375.
(191) Omer, L.; Ruthstein, S.; Goldfarb, D.; Talmon, Y. *J. Am. Chem. Soc* **2009**, *131*, 12466.
(192) Zhao, Y.; Zhang, D.; Zhao, L.; Wang, G.; Zhu, Y. *Chem. Mater* **2011**, *23 (16)*, 3775.
(193) Chung, H.; Caffrey, M. *Biophys J.* **1994**, *66(2 Pt 1)*, 377.
(194) Goldberg, R. N.; Hepler, L. G. *Chem. Rev* **1968**, *68*, 229.
(195) Burgers, W. G. *Physica* **1934**, *1*, 561.
(196) Gasteiger, H. A.; Kocha, S. S.; Sompalli, B.; Wagner, F. T. *Appl. Catal., B* **2005**, *56*, 9.
(197) Lewis, N. S.; Nocera, D. G. *Proc. Natl. Acad. Sci. U. S. A* **2006**, *103*, 15729.
(198) Stamenkovic, V. R.; Fowler, B.; Mun, B. S.; Wang, G.; Ross, P. N.; Lucas, C. A.; Marković, N. M. *Science* **2007**, *315*, 493.
(199) Strasser, P.; Koh, S.; Anniyev, T.; Greeley, J.; More, K.; Yu, C.; Liu, Z.; Kaya, S.; Nordlund, D.; Ogasawara, H.; Toney, M. F.; Nilsson, A. *Nature Chem* **2010**, *2*, 454.
(200) McBain, J. W.; Sierichs, W. C. *J. Am. Oil Chem. Soc* **1948**, *25*, 221.

(201) Li, S. J.; Yamashita, Y.; Yamazaki, M. *Biophys. J* **2001**, *81*, 983.
(202) Angelova, A.; Angelov, B.; Mutafchieva, R.; Lesieur, S.; Couvreur, P. *Acc. Chem. Res* **2011**, *44 (2)*, 147.
(203) Ridell, A.; Ekelund, K.; Evertsson, H.; Engström, S. *Colloids and Surfaces A: Physicochemical and Engineering Aspects* **2003**, *228*, 17.
(204) Coleman, N. R. B.; Attard, G. S. *Microporous Mesoporous Mater* **2001**, *73*, 44.
(205) Gupta, M. *Manufacturing process for emulsifiers, Wiley, New York* **1996**.
(206) Lynch, M. L.; Ofori-Boateng, A.; Hippe, A.; Kochvar, K.; Spicer, P. T. *J. Colloid Interface Sci* **2003**, *260*, 404.
(207) Yaghmur, A.; Laggner, L.; Zhang, S.; Rappolt, M. *PLoS ONE* **2007**, *2*, No. e479.
(208) Alfons, K.; Engstrom, S. *J. Pharm. Sci* **1998**, *87*, 1527.